

On the Gravitational Wave Spectrum of Compact Relativistic Objects

Dissertation

der Mathematisch-Naturwissenschaftlichen Fakultät
der Eberhard Karls Universität Tübingen
zur Erlangung des Grades eines
Doktors der Naturwissenschaften
(Dr. rer. nat.)

vorgelegt von

Sebastian H. Völkel

aus Öhringen

Tübingen

2019

Gedruckt mit Genehmigung der Mathematisch-Naturwissenschaftlichen Fakultät der
Eberhard Karls Universität Tübingen.

Tag der mündlichen Qualifikation:	08.05.2020
Dekan:	Prof. Dr. Wolfgang Rosenstiel
1. Berichterstatter:	Prof. Dr. Kostas D. Kokkotas
2. Berichterstatter:	Prof. Dr. Wilhelm Kley
3. Berichterstatter:	Prof. Dr. Emanuele Berti

ON THE GRAVITATIONAL WAVE SPECTRUM OF
COMPACT RELATIVISTIC OBJECTS

DOCTORAL THESIS IN PHYSICS

BY

SEBASTIAN H. VÖLKE

UNIVERSITY OF TÜBINGEN

FACULTY OF SCIENCE

INSTITUTE FOR ASTRONOMY AND ASTROPHYSICS

THEORETICAL ASTROPHYSICS

FIRST SUPERVISOR: PROF. DR. KOSTAS D. KOKKOTAS

SECOND SUPERVISOR: PROF. DR. WILHELM KLEY

EXTERNAL REVIEWER: PROF. DR. EMANUELE BERTI

OCTOBER 2019

Preface

This doctoral thesis has been carried out at the University of Tübingen in the Institute for Astronomy and Astrophysics under supervision of my first supervisor Prof. Dr. Kostas D. Kokkotas and my second supervisor Prof. Dr. Wilhelm Kley. As the title suggests, the present work is on the gravitational wave spectrum of compact relativistic objects. In a series of projects, more specific questions in this context have been proposed and addressed. These have been reported in nine regular journal publications [1, 2, 3, 4, 5, 6, 7, 8, 9] and one proceedings [10]. For two of the publications, related blog articles in the accompanying blog of the journal have also been prepared [11, 12].

After acknowledgements, abstract, and table of contents, the thesis is organized into three main parts. Part I provides the theoretical foundations. Chapter 1 outlines the exciting field of general relativity and particularly gravitational wave physics suitable for any interested reader with a background in physics. Chapter 2 then provides a more detailed review of compact objects, while chapter 3 studies the perturbation equations describing gravitational waves. Chapter 4 explains the WKB methods for the direct and inverse spectrum problem. Part II is on applications and results. It contains the research output of this thesis and is based on the journal publications. Part III provides an overall discussion in chapter 13 and final conclusions in chapter 14.

Acknowledgments

Personal

As all good journeys come to an end, so too must my undergraduate and doctoral studies in Tübingen. After these great years of freedom and learning, I want to thank the many people that accompanied me.

First and foremost I express my deepest gratitude to my family, my brother Oliver and parents Heinz and Dorothea Völkel, for the continuous support and help on which I could always rely on. I am also indebted to Lisa-Marie Huber for the wonderful time we have spent together.

Clearly this thesis would not have been possible without my first supervisor Kostas Kokkotas. My Gratitude is not limited to his scientific experience that guided me towards the research projects, but also includes the possibilities for valuable and honest discussion. His liberal way of supervising provided me with various opportunities to follow my scientific interests and facilitated the many conferences and summer schools I visited. The scientific idea proposed by him to work on the inverse spectrum problem of compact objects ignited my creative urge and turned out to be a fruitful endeavour. At this point, I also have to include my second supervisor Wilhelm Kley, whose door has always been open for me. I want to thank both for their support in me, especially for the PhD scholarship Landesgraduiertenförderung and the 69th Lindau Nobel Laureate Meeting. From my times as undergraduate student, I also want to thank Andrea Santangelo, for the opportunity to work on a research project in his high energy astrophysics group. Furthermore, I thank him and Josef Jochum, for their trust in me in assisting them in their observational cosmology lecture. I will also not forget the (not quite) isospectral brass drums that David Wharam arranged for both of our curiosity.

During my years in the theoretical astrophysics group, many people came and left, but I always felt at home. The list of people that made this possible is (un)fortunately longer than I can acknowledge here. Nevertheless, I want to explicitly mention those that accompanied me for the longest time and helped me whenever I needed them. These are Andreas Boden, Gela Hämmerling, Severin Frank, Pantelis Pnigouras, János Schmidt, Christian Krüger, Andrew Coates, Dimitra Tseneclidou, Salvatore Vultaggio, Lorenzo Kuchler, Verena Krall, Panagiotis Herbe, Sourabh Nampalliwar, Andrea Maselli, Kostas Glampedakis, Daniela Doneva, Stoytcho Yazadjiev, Roman Konoplya, Jacopo Soldateschi, Arthur Suvorov, Zeljko Grljusic and more. Furthermore I want to thank Andrew Coates, Gela Hämmerling, and Andreas Boden for their valuable time to proofread parts of the manuscript of this thesis. Of course I am also indebted to Heike Fricke, especially for all the help and management of the bureaucratic issues in academia. Honest thanks also go to many members of the neighboring computational physics group of Wilhelm Kley. Here I want to particularly thank Christoph Schäfer for all the positivity, ski touring and hospitality. I wish him and his family all the best. From all the fellow students that I had the privilege to meet during my undergraduate studies, I explicitly want to thank Kevin Marolt, for all our coffee breaks and outdoor activities, as well as Lucas Jordan, Pit Burgbacher, Philip Wolf, Viktor Bach, Martin Bohnert, Timo Schössler, Patrick Müller, Timo Storzer, Manuel Nonnenmacher, Daniel Mieg, and Jonas Leister, for the countless hours inside and outside the university.

Finally, there are two friends from my early school days that strongly influenced my early academic interests and decisions. I thank Artur Lobanov for the many discussions and unique visits to his workplaces at CERN and at DESY. Speaking with him about physics, while he was already studying, motivated me a lot to pursue science. I also thank Patricia Wowra for coming up with the idea to visit the Institute for Astronomy and Astrophysics in Tübingen during a school internship (BOGY). It was a truly inspirational week and a key reason to study physics in Tübingen.

Funding

Besides acknowledging individual people, I also want to give credit to the different organizations and funding bodies that made this work and some of my trips possible. First, I acknowledge support of the PhD scholarship Landesgraduiertenförderung by the State Ministry of Baden-Württemberg for Sciences, Research and Arts, awarded through the University of Tübingen. Furthermore, I am indebted to the Baden-Württemberg Stiftung for the financial support of some research projects by the Eliteprogramme for postdocs of Daniela Doneva. I acknowledge support from the COST Action CA16104 “GWverse” and Cost Action MP1304 “NewCompStar”. I thank the Wilhelm and Else Heraeus Foundation for visiting seminars in the Physikzentrum Bad Honnef and partial support for the 69th Lindau Nobel Laureate Meeting. Hereby, I also acknowledge the support of the Nobel Laureate Foundation for attending this unique meeting. I received travel support from the Deutscher Akademischer Austauschdienst e.V. (DAAD) through the project on “Neutron Star Physics in the Era of Gravitational Wave Astronomy” for visits to Thessaloniki. Finally, the Kepler Center for Astro and Particle Physics at the University of Tübingen for attending repeatedly their PhD workshops.

Zusammenfassung

Kompakte Objekte sind für die Gravitationswellen-Astronomie, die in den letzten Jahren bedeutende Erfolge verbuchen konnte, von großem Interesse. Darunter befinden sich der erste direkte Nachweis von Gravitationswellen, welche von verschmelzenden Schwarzen Löchern und Neutronensternen stammen, sowie der dazugehörige Nobelpreis in Physik im Jahre 2017. Das erste mit elektromagnetischer Strahlung aufgenommene Bild eines supermassiven Schwarzen Lochs wurde 2019 der Weltöffentlichkeit vorgestellt. Die vorliegende Dissertation behandelt das Gravitationswellen-Spektrum von kompakten Objekten und basiert hierbei überwiegend auf Einsteins allgemeiner Relativitätstheorie. Die Dissertation umfasst mehrere Studien über unterschiedliche Aspekte axialer gravitativer Störungen sowie skalarer Testfeldern, welche in der Hintergrund-Raumzeit untersucht werden. Diese beschreiben Neutronensterne, Schwarze Löcher und verschiedene andere Modelle von extrem kompakten Objekten. Der überwiegende Teil dieser Arbeit widmet sich dem inversen Spektrum Problem, bei dem Eigenschaften einer Quelle anhand seines Spektrums rekonstruiert werden sollen. Darüber hinaus werden auch Studien über semi-klassische Eigenschaften Schwarzer Löcher behandelt. Bei diesen handelt es sich sowohl um Hawking Strahlung, als auch um die Theorie der Oberflächenquantisierung Schwarzer Löcher. Um semi-analytische Berechnungen durchführen zu können, liegt der Fokus hierbei auf sphärisch symmetrischen und statischen Raumzeiten. Für diese entkoppeln die zugrundelegenden Störungsgleichungen voneinander und ergeben eine Wellengleichung, ähnlich zur zeitunabhängigen Schrödingergleichung mit einem Potentialterm. Wegweisende Abhandlungen gehen hier auf Regge und Wheeler 1957, sowie Zerilli 1970 zurück. Beide haben zunächst nicht-rotierende Schwarze Löcher behandelt. Seitdem wurden auch Verallgemeinerungen für rotierende Schwarze Löcher und Neutronensterne gefunden. Das inverse Spektrum Problem wird im Rahmen der WKB Theorie untersucht. Hierbei werden Gleichungen hergeleitet, mit denen man das Potential in der Wellengleichung relativ einfach rekonstruieren kann. Darüber hinaus wird aufgewiesen, wie diese auch benutzt werden können, um weitere Eigenschaften zu rekonstruieren. Diese umfassen unter anderem Teile der Raumzeit und der Zustandsgleichung von Neutronensternen. Die Eindeutigkeit der mit der WKB Theorie rekonstruierten Potentiale ist in den Fällen möglich, in denen die äußere Raumzeit durch Birkhoffs Theorem gegeben ist. Im Fall von Hawking Strahlung wird gezeigt, wie die zugrundelegenden Potentiale nur teilweise rekonstruiert werden können. Obwohl die Beobachtung von Hawking Strahlung von astrophysikalischen Schwarzen Löchern in den nächsten Jahren sehr unwahrscheinlich ist, könnten die hier entwickelten Methoden für so-genannte analoge Experimente in Laboren nützlich sein. Ebenso wird der Frage nach der Eindeutigkeit des quasi-Normalmoden Spektrums von nicht-rotierenden Schwarzen Löchern in alternativen Gravitationstheorien nachgegangen. Hier-für wird ein bestimmtes Modell einer parametrisierten Metrik verwendet und das Spektrum eines skalaren Testfeldes untersucht. Auf die sich aufdringenden Schwierigkeiten in der Bestimmung der zugrundeliegenden Raumzeit wird weiter eingegangen. Zuletzt werden die Auswirkungen der Oberflächenquantisierung auf das Spektrum rotierender, astrophysikalischer Schwarzer Löcher untersucht. Hierbei wird die Möglichkeit einer prinzipiell beobachtbaren Überprüfung der theoriespezifischen Quantisierungsgröße gefunden und im Rahmen von Gravitationswellen-Messungen diskutiert.

Abstract

Compact objects are of great interest for gravitational wave astronomy, which has celebrated historical successes in recent years. Among them are the first direct measurements of gravitational waves from merging black holes and neutron stars, as well as the 2017 Nobel Prize in Physics. Using electromagnetic observations, the first image that resolves the close vicinity of a super massive black hole was presented to the world in 2019. The present thesis is about the gravitational wave spectrum of compact relativistic objects, mostly within general relativity. It combines several projects that focused on different aspects related to axial gravitational perturbations and test scalar fields in the background space-times of compact objects, such as neutron stars, black holes and various alternative ultra compact objects. Most of the work is on the inverse spectrum problem, where various properties of the source are constrained from a given spectrum. Projects on semi-classical and quantum aspects of black holes have been carried out as well, namely on Hawking radiation and black hole area quantization. In order to proceed with semi-analytic calculations, the focus is on spherically symmetric and static space-times, for which the full perturbation equations decouple from each other and some aspects of the full problem can be related to the time independent Schrödinger equation with an effective potential term. Seminal works were achieved by Regge and Wheeler in 1957, and Zerilli in 1970, for non-rotating black holes. Generalizations to rotating black holes, neutron stars and other compact objects have been carried out since then. To address the inverse spectrum problem, WKB theory is used as framework. Convenient relations to reconstruct properties of perturbation potentials from the spectrum have been derived. It is shown how they can be further used to reconstruct other properties, such as parts of the space-time and properties of the equation of state of neutron stars. The uniqueness of the reconstructed potentials using the WKB methods is possible in cases where the external space-time is known via Birkhoff's theorem, but not in general. It is demonstrated how these inverse methods can also be applied to constrain properties of the classical potentials from the spectrum of Hawking radiation. While observing it from astrophysical black holes in the foreseeable future is unlikely, the provided methods could be useful in the growing field of analogue gravity experiments, which deal with similar situations in laboratories. To study the question of the uniqueness of the quasi-normal mode spectrum of black holes in alternative theories of gravity, a project using parametrized space-times and test scalar fields has also been undertaken. Arising complications in the deduction of the underlying space-time are discussed. Finally, a study on the implications of black hole area quantization for spinning black holes in gravitational wave observations has been carried out. It is found that imprints of this quantum theory of black holes could still leave observable imprints for astrophysical black holes, which can be used to test area quantization itself.

List of Acronyms

In the following we provide a list of frequently used acronyms. Information in brackets indicates the context.

- ADM: Arnowitt-Deser-Misner (mass)
- BH: black hole
- BS: Bohr-Sommerfeld (quantization rule)
- BW: Breit-Wigner (potential)
- DS: Damour-Solodukhin (wormhole)
- EMRI(s): Extreme mass ratio inspiral(s)
- GR: general relativity
- GW: gravitational wave
- LIGO: Laser Interferometer Gravitational-Wave Observatory (detector)
- PN: post-Newtonian
- PPN: parameterized post-Newtonian (formalism)
- PT: Pöschl-Teller (potential)
- QNM: quasi-normal mode (spectrum)
- RZ: Rezzolla-Zhidenko (metric)
- TOV: Tolman-Oppenheimer-Volkoff (equations)
- WKB: Wentzel-Kramers-Brillouin (method)

Contents

I	Theory and Methods	1
1	Introduction	3
1.1	Einstein's Theory of General Relativity	4
1.2	Tests of General Relativity	8
1.3	Gravitational Waves	12
1.4	The Scope of this Thesis in a Nutshell	21
2	Compact Objects	23
2.1	Black Holes	23
2.2	Neutron Stars	26
2.3	Alternative Compact Objects	29
3	Perturbation Theory in General Relativity	35
3.1	Brief Historical Overview	35
3.2	Scalar Perturbations	37
3.3	Metric Perturbations	39
3.4	More Perturbation Potentials	43
3.5	Quasi-Normal Modes	44
3.6	Gravitational Wave Echoes	48
4	The WKB Method	51
4.1	Basics of WKB Theory	51
4.2	Bohr-Sommerfeld Rules	55
4.3	Inversion of Bohr-Sommerfeld Rules	60
4.4	Some Examples	68
II	Applications and Results	75
5	A Semi-Analytic Study of Axial Perturbations of Ultra Compact Stars	79
5.1	Introduction	79
5.2	Model for the Effective Potential	79
5.3	Applications	81
5.4	Results	82
5.5	Discussion	83
5.6	Conclusion	84
5.7	Supplementary Material	85
6	Ultra Compact Stars: Reconstructing the Perturbation Potential	87
6.1	Introduction	87
6.2	The Inverse Problem	88
6.3	Application and Results	90
6.4	Discussion	91
6.5	Conclusion	92
6.6	Supplementary Material	93

7	Wormhole potentials and throats from quasi-normal modes	95
7.1	Introduction	95
7.2	Inverse Spectrum Method	96
7.3	Wormhole Models	97
7.4	Reconstruction of the Potentials	98
7.5	Reconstructing the Throat	99
7.6	Comparison to Ultra Compact Star Potentials	100
7.7	Discussion	104
7.8	Conclusions	105
7.9	Supplementary Material	105
8	On the Inverse Spectrum Problem of Neutron Stars	109
8.1	Introduction	109
8.2	Perturbation Potential and Bohr-Sommerfeld Rule	110
8.3	Direct Spectrum Problem	111
8.4	Inverse Spectrum Problem	114
8.5	Results	116
8.6	Discussion	122
8.7	Conclusions	125
8.8	Supplementary Material	125
9	Scalar Fields and Parametrized Spherically Symmetric Black Holes: Can one hear the shape of space-time?	129
9.1	Introduction	129
9.2	Scalar Perturbations	131
9.3	Search for Isospectrality	132
9.4	Results	134
9.5	Discussion	135
9.6	Conclusions	136
9.7	Supplementary Material	137
10	Parameter Estimation of Gravitational Wave Echoes from Exotic Compact Objects	143
10.1	Introduction	143
10.2	The ECHO Templates	144
10.3	Data Analysis Procedure	146
10.4	Constraints on the echo's parameters	147
10.5	Conclusions	154
11	Inverse Problem for Hawking Radiation	157
11.1	Introduction	157
11.2	Hawking Radiation	158
11.3	Inverse Problem	160
11.4	Applications and Results	163
11.5	Discussion	164
11.6	Conclusions	166
11.7	Supplementary Material	166

12 Spectral Lines of Quantized, Spinning Black Holes and their Astrophysical Relevance	169
12.1 Introduction	169
12.2 Widths of non-spinning states	170
12.3 Including the Spin	172
12.4 Discussion and Conclusions	173
III Discussions and Conclusions	175
13 Discussion	177
13.1 Status of Compact Objects	177
13.2 WKB Method for the Inverse Spectrum Problem	179
13.3 Open Problems	180
14 Conclusions	183
14.1 Brief Conclusions of Individual Works	183
14.2 Final Remarks	185
Bibliography	189

Part I

Theory and Methods

1 | Introduction

It is no exaggeration to say that we live in exciting times for physics and astronomy. Over the last years, truly historical events have taken place. Gravitational waves, which are a substantial part and prediction of Einstein's theory of general relativity, were directly measured for the first time in 2015 by the advanced LIGO observatory [13]. This is one century after the theory was first presented [14], and it has not failed once. More direct detections have been made since, which are not limited black holes. Soon after the advanced Virgo observatory joined the hunt for gravitational waves, merging neutron stars were detected as well [15]. These breakthroughs have been honored by the awarding of the Nobel Prize in Physics of 2017 to three major pioneers of the field. The implications of these observations reach beyond gravitational physics and include astronomy, astrophysics, cosmology and fundamental physics. In addition, the Event-Horizon-Telescope Collaboration presented the first image of a supermassive black hole in 2019 [16], which was only possible by an enormous community effort. Both findings confirm Einstein's theory of general relativity as the prevailing theory of gravity. However, this marks not the end, but the beginning of exploring and testing the strong field regime of general relativity. With increasing accuracy and future detectors, like the space mission LISA [17], the hunt for the fine details of strong field gravity has just begun. And as history tells us, new windows to observe the Universe often lead to completely unexpected discoveries. If the 60's and 70's were the golden age of black hole physics, the decades ahead should be true diamonds, for the clear and valuable insights they will provide.

This thesis is about the gravitational wave spectrum of compact relativistic objects. We hereby refer to black holes and neutron stars, but also include alternative models of ultra compact objects. Black holes are among the most famous solutions of Einstein's equations of general relativity and describe dark objects that not even light can escape from. Neutron stars are the most compact stars we know in the Universe. As the name indicates, they are expected to be made up mostly of neutron matter, which in this form can only exist under extreme conditions. This makes neutron stars an ideal natural laboratory to study extreme phases of matter, which can not be probed in a laboratory on Earth. Their equation of state, which represents the complicated quantum physics, connects effectively classical quantities as density and pressure. It is not exactly known and therefore finding it is one of the big open challenges of current research. Since black holes themselves have quite exotic properties, such as a singular space-time hidden behind an event horizon, they might be the key to arriving at a quantum theory of gravity, which has been one of the biggest unsolved problems in theoretical physics for about a century. In this context, and further motivated by postulated new phases of matter, a long list of alternative compact objects exist as well. All of these systems can in principle be studied with gravitational waves. General relativity predicts them to be emitted by the dynamics of compact objects. As an observer far away from these objects, one can think of gravitational waves as tiny deformations of space-time. In simple words, the way clocks run and lengths are measured undergo tiny but, in principle, measurable changes. The details of these changes depend on the type of source. Among the strongest sources in the Universe are merging binary systems of black holes and neutron stars. Other sources which will produce characteristic signals include non-radial oscillations of isolated neutron stars, black holes, and potentially exotic alternatives. A simple analogy is the sound of different musical instruments. As different instruments produce characteristic sound waves that allow us to distinguish a guitar from a piano, so do the oscillations of different compact objects excite space-time in a characteristic way. Understanding these characteristics allows us to learn something about their internal structure and test whether general relativity remains the prevailing theory of gravity. For neutron stars, one of the most important problems here is to obtain the correct equation of state.

A problem for which the spectrum of a source is known, but not the physical parameters that describe the source, is called an inverse problem. In contrast to the prediction of the spectrum if the source is fully known, solving the inverse problem is in general more difficult. A simple but enlightening example is the question of

whether one can hear the shape of a drum. By this we mean is it possible to determine the shape of the boundary to which a two dimensional membrane is fixed, if only the characteristic spectrum is known. The answer is that it is in general not possible to find only one shape, but many different ones. In this example it is therefore impossible to find a unique relation between the spectrum and the source.

The equations relating the oscillations of compact relativistic objects with gravitational waves are given by general relativity and hydrodynamics, which makes them very complex. Even the direct problem of predicting the gravitational wave signal of compact objects is in general only solvable by using state-of-the-art numerical methods that solve the full non-linear, coupled set of Einstein's equations. Fortunately, there are different situations in which this very complex problem can be approximated and therefore simplified. By considering linear perturbations of objects whose equilibrium configuration is known, and by assuming spherical or axial symmetry, a set of linear coupled wave equations remain. Analytical and numerical approaches that solve these equations for different types of compact objects have been developed in the literature. The perturbation equations can be formulated in terms of an eigenvalue problem, whose solutions are called quasi-normal modes (QNMs). The spectrum of these complex eigenvalues describe the characteristic frequencies and damping times of gravitational waves and fields that propagate in these space-times.

The corresponding inverse problem, starting from a given QNM spectrum, is more complicated and therefore has received less attention. This thesis describes a new approach of how the inverse problem for different types of compact objects can be solved. In spherical symmetry and general relativity, it is shown how the axial QNM spectrum, as well as the spectrum of Hawking radiation (applies only for black holes), can be used to constrain fundamental properties of neutron stars, black holes, and different types of alternative compact objects. Among the reconstructed properties are the perturbation potential, which determines the gravitational wave dynamics, as well as the greybody factors of black holes. More results related to the direct spectrum problem and asteroseismology are reported as well. The final conclusion will show that this field has still open and fascinating, but also complicated problems waiting to be explored.

Before the technical aspects and results are outlined and discussed in the subsequent chapters, the remaining sections of this introductory chapter have the aim to familiarize any interested reader, whether being an expert in the field or not, to the overall subject of this work. In order to do so, it is less technical and of more qualitative character. We start in Sec. 1.1 by reviewing some basics of Newtonian gravity, before we outline key assumptions of Einstein's theory of general relativity. Its historical and modern tests are discussed afterwards in Sec. 1.2. Since this thesis is on gravitational waves, they receive special attention in Sec. 1.3. With this introductory knowledge at hand, we summarize the scope of this thesis in a renewed context in Sec. 1.4. Throughout this introductory chapter we explicitly write out Newton's constant G and the vacuum speed of light c , while we adopt geometric units in which $G = c = 1$ for the rest of the work.

1.1 Einstein's Theory of General Relativity

Like arguably no other physicist, Albert Einstein is considered to be one of humanity's greatest minds. His scientific achievements live on and are the reason why his name remains among the most renowned, not only to the general public, but also within the scientific community. During his lifetime, many of modern physics' most revolutionary ideas and theories have been developed by true pioneers, which settled the basis for various research fields and technological applications that are a crucial part of our modern society today. Like other great minds of that time, Einstein was interested in many different aspects of physics and had significant contributions. To name a few of them: quantum mechanics (the photoelectric effect [18], rate equations [19]), thermodynamics (Brownian motion [20]), special relativity [21], and of course gravity [14]. His works before proposing general relativity made him a respected and very successful physicist, but it was his revolutionary theory of gravity that clearly distinguishes him.

1.1.1 The Situation at the End of the 19th Century

To understand what Einstein's genius work is about, it makes sense to first outline the understanding of gravity at that time. At the end of the 19th century, the theoretical foundations were essentially the same as proposed by Isaac Newton centuries ago, in his theory of classical mechanics and his law of gravity. These historical milestones were published 1687 in his famous *Philosophiæ Naturalis Principia Mathematica* [22]. Here, the motion of bodies is determined by the sum of all forces that act on them. Gravity is a purely attractive force among massive bodies. Two masses m_1 and m_2 , which are separated by a distance r , attract each other by a force

$$F = G \frac{m_1 m_2}{r^2}, \quad (1.1)$$

where G is the gravitational constant, also called Newton's constant. This rather simple relation, in connection with Newton's laws of classical mechanics, allowed one to describe all observable gravitational phenomena of the time, at least in principle. While the form of the equations is rather simple, it is difficult to perform clean experiments on Earth. Such terrestrial experiments that probe gravity are plagued by all kind of environmental effects, because the gravitational force between test masses in a laboratory is extremely weak. In order to realize this we can think of a simple example. Note that it is the enormous mass of the Earth (around 6×10^{24} kg) which is pulling on us all the time, but the electro-magnetic forces that dominate chemical and biological processes allow birds to fly. It is therefore no surprise that the motion of planets in the solar system, for which electromagnetic forces are negligible, had for a long time been the only relevant possibility to see pure gravity at work.

With the framework of classical mechanics and Newton's law of gravity, it was possible to describe the motion of the planets from first principles, to confirm Kepler's law and to be in agreement with observations. Since almost all the mass of the solar system is contained in the Sun (weighting around 2×10^{30} kg), the motion of an individual planet is dominated by the influence of the sun, while the gravitational pull from the other planets can often be neglected. However, with increasing precision in astronomical measurements, it was possible to determine the trajectories of the planets with higher accuracy. In spite of the hard calculations at that time, astronomers were able to include the sub-dominant effects that other planets have on each other and the fact that the Sun is an oblate and extended body. Although celestial mechanics seemed to work without any serious problem, there was an increasing tension with the orbit of the innermost planet, Mercury. However, there was no urgent need to revolutionize the foundations of gravity, at this time. So what motivated Einstein to do this?

1.1.2 Special Relativity

As the name indicates, the first steps in the formulation of general relativity was the development of the theory of special relativity. Einstein published this theory in his famous work "Zur Elektrodynamik bewegter Körper" in 1905 [21]. The theory states that all physical laws take the same form in all non-accelerating frame of references, called inertial frames. Thus, inertial frames are frames of reference which can only move with a constant relative velocity to each other. The second important concept is that the measured speed of light in vacuum is the same for every observer, independent of the relative motion between the observer and the source. Both concepts are tightly connected to Maxwell's theory of electromagnetism and the Michelson Morley experiment. The latter rejected the contemporary idea of an aether, which was suggested to be the medium of electromagnetic waves and can also exist in vacuum. The existence of such a medium in the Universe would allow one to define an absolute reference frame, which is against the concept of relativity.

In order to change between two inertial systems, a coordinate transformation is necessary. In classical mechanics, this is achieved by the Galilean transformation intuitively adding velocities, while the new transformation in special relativity is called the Lorentz transformation. Both transformations depend on the relative velocity of the two inertial systems. They are approximately the same for relative velocities which are much smaller than the speed of light. Therefore, the non-relativistic Galilean case is included as limit for small velocities. For relative velocities close to the speed of light, the transformations are very different.

Among the most important implications of special relativity is the fact that the rate at which lengths are measured, as well as time, both depend on the observer. Observers in different inertial systems will only agree on these measurements after using a Lorentz transformation for conversion. One example here is the lifetime of muons which are created by high energy collisions of cosmic rays in the atmosphere and move with a high relative speed towards the Earth. Their lifetime seems longer than the one observed for slowly moving ones in a laboratory.

While special relativity is still a crucial part of modern quantum field theories, which in principle successfully describe all non-gravitational experiments on Earth, the question for non-inertial frames kept Einstein's mind busy for the subsequent decade.

1.1.3 General Relativity

Most scientists would probably agree with the following statement. A new theory that claims to take over the prevailing one calls for as many precise tests as possible, no matter how "elegant" or well motivated it is. First, it has to explain all existing observations, which are already explained by the old theory. Second, in order to be favorable, it has to explain observations that the old theory cannot explain or at least be simpler, by the means of Ockham's razor. When Einstein proposed general relativity, one might argue that the old theory was not able to explain Mercury's orbit properly ¹, but for sure his field equations can hardly be called a simplification of Newton's law of universal gravitation. However, two key observations of that time could be explained with Einstein's theory, and during the 20th century, the list of successful confirmations became longer and longer. Before we discuss this list in Sec. 1.2, let us first give an overview about the principles of general relativity.

General relativity is still the prevailing theory of gravitation. It is a metric theory that provides a quantitative connection between matter and space-time through the Einstein field equations, which are given by

$$R_{\mu\nu} - \frac{1}{2}Rg_{\mu\nu} + \Lambda g_{\mu\nu} = -\kappa T_{\mu\nu}. \quad (1.2)$$

Here one finds on the left hand side objects from differential geometry, such as the metric tensor $g_{\mu\nu}$, the Ricci tensor $R_{\mu\nu}$, and the Ricci scalar R . The right hand side introduces the role of matter through the energy momentum tensor $T_{\mu\nu}$ and $\kappa = 8\pi G/c^4$ is a constant. The free constants that have to be determined from observations are the speed of light c , Newton's constant G , as well as the cosmological constant Λ , which only plays a relevant role in cosmology. It is usually neglected for astrophysical applications and only shown here for completeness. The Einstein field eqs. (1.2) are of tensorial form, for which Greek indices take integer values from 0 to 3 (or 1 to 4, depending on convention). Simply speaking tensors are objects with special properties under a transformation of the coordinate system. A tensor equation will keep its structure under any valid coordinate transformation $x \rightarrow x'$.

The central object of general relativity is the metric tensor $g_{\mu\nu}$. It defines how time and space are measured and is related to the so-called line element via

$$ds^2 = g_{\mu\nu}d^\mu d^\nu. \quad (1.3)$$

The other objects in the fields equations, the Ricci tensor $R_{\mu\nu}$ and Ricci scalar R can be derived from it. Without giving an overview of differential geometry, which is beyond the scope of this introductory chapter, one should note that the generalization of derivatives of tensors in curved space-times requires the introduction of the Christoffel symbols $\Gamma^\mu_{\alpha\beta}$. They are related to the metric tensor via

$$\Gamma^\mu_{\alpha\beta} = \frac{1}{2}g^{\nu\mu} (\partial_\alpha g_{\nu\beta} + \partial_\beta g_{\nu\alpha} - \partial_\nu g_{\alpha\beta}), \quad (1.4)$$

¹Newton's law of gravity does not say anything about how many planets and other objects exist in our solar system. Dark objects that astronomers were simply not able to see, might have still explained the observation. One example of such a dark object is Neptune. Its position was predicted by the gravitational influence on Uranus, whose orbit was not in agreement with expectations of that time.

where $\partial_\mu \equiv \partial/\partial x^\mu$ correspond to the ordinary partial derivatives, respectively. Although the Christoffel symbols are labeled with Greek indices, they are no tensor. With the Christoffel symbols at hand, one can define the Riemann tensor

$$R^\delta{}_{\alpha\beta\gamma} = \partial_\beta \Gamma^\delta{}_{\alpha\gamma} - \partial_\gamma \Gamma^\delta{}_{\alpha\beta} + \Gamma^\epsilon{}_{\alpha\gamma} \Gamma^\delta{}_{\epsilon\beta} - \Gamma^\epsilon{}_{\alpha\beta} \Gamma^\delta{}_{\epsilon\gamma}, \quad (1.5)$$

which is a measure of the curvature. The Ricci tensor is given as contraction of the Riemann tensor

$$R_{\alpha\beta} \equiv R^{\gamma}{}_{\alpha\gamma\beta}, \quad (1.6)$$

and finally the Ricci scalar as contraction of the Ricci tensor

$$R = g^{\alpha\beta} R_{\alpha\beta} = R^\alpha{}_\alpha. \quad (1.7)$$

Note that the Einstein sum convention is used. It means that if two indices are the same, lower and upper, then there is an implicit sum over that index. Using the tensor relations given above shows that the field equations can also be completely expressed as a complicated nonlinear equation for the metric tensor $g_{\mu\nu}$ and its first and second derivatives. As it is evident from the involved equations above, finding exact solutions for $g_{\mu\nu}$ is quite challenging and can only be done analytically for very symmetric and physically simplified assumptions for the matter distribution. Assuming that one can find an exact solution for the metric tensor, how does matter behave in the respective space-time?

In Einstein's theory, the dynamics of a test particle in a gravitational field is not described by a force anymore, but determined by space-time itself. Test particles in the absence of external forces follow geodesics, which are the shortest paths between two points in space-time and thus the generalization of a straight line in flat space. Geodesics are described by the geodesic equation

$$\frac{d^2 x^\mu}{d\tau^2} + \Gamma^\mu{}_{\alpha\beta} \frac{dx^\alpha}{d\tau} \frac{dx^\beta}{d\tau} = 0, \quad (1.8)$$

where τ is the proper time and $\Gamma^\mu{}_{\alpha\beta}$ are the Christoffel symbols, which is related to the metric tensor $g_{\mu\nu}$ via eq. (1.4).

1.1.4 Equivalence Principle

General relativity fulfills the equivalence principle, which was one of the main aspects Einstein considered for his theory. Strictly speaking, there are several versions. The most well-known and oldest formulation is the Galilean equivalence principle, which states that the inertial mass and the gravitational mass are the same, also known as the universality of free fall. It is present in classical mechanics, where the gravitational mass is introduced through Newton's law of universal gravitation. Its consequence was impressively shown by a simple demonstration during the Apollo 15 mission on the Moon by astronaut David Scott. In vacuum he dropped a hammer and a feather, which both fell at the same rate.

There have since been more variations of the equivalence principle, which we summarize in the following. For more details we refer to Clifford Will's living review on "The Confrontation between General Relativity and Experiment" [23], from which the following definitions have been taken. The so-called weak equivalence principle is another name for the one discussed above. Another consequence of it is that the trajectory of a freely falling test body is independent of its internal structure and composition. The Einstein equivalence principle assumes the weak equivalence principle but additionally demands local Lorentz invariance and local position invariance. This means that the outcome of any local non-gravitational experiment is independent of the velocity of the freely-falling reference frame in which it is performed and is independent of where and when in the Universe it is performed. A slight but important difference is incorporated in the strong equivalence principle. It assumes the Einstein equivalence principle but extends it to gravitational experiments and self-gravitating bodies.

Since the different variations of the equivalence principle describe different physical assumptions, the experiments that test them are very different as well. They range from laboratory experiments to observations of binary pulsars. For a comprehensive discussion we refer again to [23]. In the following we briefly discuss a few of the many tests of general relativity. Some of them are connected to the equivalence principle as well.

1.2 Tests of General Relativity

Since Newton's law of gravity is much simpler than Einstein's theory and for most situations a very good approximation, it is still used today. This makes it a challenging task to observe effects that differ in both theories, especially in the early 20th century. Apart from the three classical tests, we also discuss some rather modern tests and finally gravitational waves. A recent standard reference that discusses the experimental status of general relativity, with many more details and references is again [23].

1.2.1 The Classical Tests

Perihelion Shift of Mercury

The first proof of a quantitative prediction of general relativity involves the trajectory of Mercury, the innermost planet in our solar system. Since it is closer to the Sun than any other planet, any deviation from Newtonian gravity that appears in strong gravitational fields should be more pronounced here. While Kepler's first law, which states that the trajectories of planets are ellipses, is in very good agreement with actually observed planetary motions, small deviations from it exist. The dominant deviation comes from the fact that Kepler's result is only valid within Newtonian gravity for a pure two body system, but the solar system consists of more than one planet. However, since almost all the mass of the solar system is concentrated in the Sun, describing planetary motion as a two body problem is a good approximation. Also, the Sun is slightly oblate, which gives an additional small correction.

It was Le Verrier who realized in 1859 that a careful analysis of Mercury's trajectory is not in agreement with the prediction of Newtonian theory [24]. Additional, so far unobserved planets might have been well justified assumptions of the time to approach the problem, no such planet has been found. The discrepancy could be explained later by Einstein in his new theory [14] and this solved the problem. The leading order effect for the relativistic shift of the orbit after one revolution is given by

$$\Delta\phi = \frac{6\pi GM}{a(1-e^2)c^2}, \quad (1.9)$$

where M is the mass of the Sun, a is the semi major axis and e the ellipticity [25]. At present, much more precise measurements of Mercury's orbit are still in precise agreement with general relativity [23].

Deflection of Light

The second classical test of general relativity is the deflection of light by massive bodies like the Sun. In Einstein's theory, light follows geodesics describing straight lines in space-time. For a curved space-time, as is the case around massive bodies, it seems that light gets deflected and bent towards the object. For small deflection angles $\Delta\varphi$ the effect is approximatively given by

$$\Delta\varphi = \frac{4GM}{c^2b}, \quad (1.10)$$

where M is the mass of the central object and b the impact parameter [25]. This effect was first observed by two expeditions under Arthur Eddington during the solar eclipse of May 1919 [26]. One team observed the solar eclipse from the island of Príncipe off the west coast of Africa, while the second team observed from Sobral in Brazil. A priori, three possible outcomes had been discussed. First, no deflection takes place, second, light

behaves like ordinary matter and follows the Newtonian result, and third, light behaves as predicted in Einstein's theory, which is by a factor of two different from the latter one. Although the measurements were later criticized by some for being not precise enough for such a bold confirmation, it was celebrated as a big success of Einstein's theory. The test has been successfully repeated many times with improved accuracy during other solar eclipses.

Gravitational Redshift

Another prediction of general relativity is the existence of gravitational redshift. The name comes, roughly speaking, from the fact that light comes in various colors, each identified with different frequencies. One result of general relativity is that the frequency of light traveling in a gravitational field will in general change. Photons emitted from the surface of a star of mass M seem to have a slightly lower frequency ν_R when observed far away from the star, than when they were emitted with ν_E . In a qualitative sense, the color of blue light is changed towards red, with the strength of the effect depending on the metric describing the space-time. For the space-time around a spherically symmetric object, the relation between these frequencies is given by

$$\frac{\nu_R}{\nu_E} = \left[\frac{1 - 2GM/(r_E c^2)}{1 - 2GM/(r_R c^2)} \right]^{1/2}, \quad (1.11)$$

where r_E and r_R are the radial coordinate for the emitted and received photons, respectively [25]. Gravitational redshift is also important for processes around black holes and neutron stars, e.g. accretion, but it is extremely difficult to measure on Earth. The first successful terrestrial experiment was performed by Pound and Rebka [27] in 1959 and was improved by Pound and Snider in 1965 [28]. The experiments used gamma-ray photons emitted via the Mößbauer effect, which describes resonant and recoil-free interaction of gamma quanta with atomic nuclei bound in a solid. In this way it was possible to precisely measure the frequency difference after the photons traveled about 20 m upwards Earth's gravitational field. These experiments confirmed the gravitational redshift effect to a 1 % level. This precision is remarkable, since the relative change is only of the order of 10^{-15} [29].

The first astronomical attempt to observe the gravitational redshift was conducted by Adams in 1925, who measured the spectral lines of the companion star of Sirius [30]. The first accurate measurements were taken around the same time as the terrestrial experiments were carried out, by Poper for 40 Eridani B in 1954 [31] and by Brault in 1962 [32] for the Sun.

1.2.2 Important Modern Tests

Shapiro Delay

The Shapiro delay is an effect that involves the geodesic motion of light and is also called the fourth test of general relativity. It was first proposed by Shapiro in 1964 as a test in the solar system [33] in which radar pulses are sent from Earth to Mercury or Venus, where they are partially reflected and then measured on Earth again. According to the geodesic motion of light predicted by general relativity, the path that light takes when the Sun is located between Earth and one of the planets becomes longer and the light takes more time. To lowest order one can express this additional time Δt for light rays passing close to the Sun as

$$\Delta t \approx \frac{4GM}{c^3} \left[\ln \left(\frac{r_E r_P}{r_0} \right) - 1 \right], \quad (1.12)$$

where M is the mass of the Sun, r_E and r_P are the distance of Earth and the second planet from the Sun, respectively, and r_0 is the closest approach of the light ray to the Sun [25]. The predicted effect for Earth to Venus and back is about $200 \mu\text{s}$ and was in experimental reach at that time. Using the MIT Haystack radar antenna, the successful realizations of this test were reported only a few years later [34, 35] and were in agreement with general relativity. Since the surface of a planet is clearly not a perfect mirror, due to non-trivial surface structure, there is a dispersion in the reflected pulses, which limits the overall precision of this method. More precise results

could be achieved when the second object was replaced by a spacecraft, as it was done, e.g., for the Viking orbiter and lander on Mars [36], and most precisely so far, for the Cassini spacecraft in 2002 [37]. The Shapiro delay is not limited to the solar system, but can also be observed in some binary pulsar systems. Since these systems are too far away to send radio pulses, one uses the precise pulsed radio emission of the pulsars themselves, e.g., in PSR B1855+09 [38]. While the solar system tests reached very high accuracies, the extra solar binary pulsar tests probe much stronger gravitational fields.

Compact Binaries: Hulse-Taylor Binary

Compact binary systems that consist of black holes or neutron stars provide unique opportunities for different types of precision tests of general relativity. Not only do the much stronger gravitational fields allow one to repeat some of the solar system tests in extreme environments, they also offer completely new kinds of tests. The historically first and most well-known system is the Hulse-Taylor binary discovered in 1974 by Russell A. Hulse and Joseph H. Taylor Jr [39]. The binary system consists of two neutron stars, where one of them is observable as a pulsar. Pulsars are rapidly spinning neutron stars with periodic radio emission (on the order of seconds to milliseconds) originating from the lighthouse effect. As the name suggests, the emission is directed and follows a rotational pattern, similar to a lighthouse. The precise radio observations of this system, which have been performed over many years now, allowed for the first time to indirectly verify the emission of gravitational waves [40, 41, 42, 43]. In contrast to Newtonian theory, Einstein's theory predicts that the orbits in a binary system should shrink slowly due to the emission of gravitational waves. For a circular binary with equal masses M , the change of the orbital period P can be approximated as [25]

$$\frac{dP}{dt} = -\frac{96}{5} 4^{1/3} \frac{\pi}{c^5} \left(\frac{2\pi GM}{P} \right)^{5/3}. \quad (1.13)$$

This effect is negligible in the solar system, but becomes measurable for relativistic objects in a small orbit. The orbital period in the Hulse-Taylor binary lasts less than 8 hours, which makes the system much more compact than the solar system. The discovery of this system was so important that Russell A. Hulse and Joseph H. Taylor Jr. received the Nobel Prize in Physics in 1993. The precise agreement between radio observations and the prediction from general relativity is shown in Fig. 1.1.

Accretion Discs around Compact Objects

Other types of astrophysical tests of general relativity use accretion discs around compact objects. One of the methods that has been established is the iron line technique, e.g., [44]. Accretion discs can contain iron, whose spectral lines can be observed. The properties of these lines are known both from theory and from experiments on Earth. The space-time around a black hole influences the structure of the disc, as well as the trajectories and redshift of photons. Models that try to incorporate the relevant astrophysical processes can therefore in principle relate the space-time with the observed spectrum. The spectrum of the iron line contains different features that can be used to extract information of the system. However, simulations and observations that involve such a complicated astrophysical system are more challenging to handle and are not as "clean" as some of the other tests. On the other hand, this technique can in practice be used to estimate the spin of the central black hole. Using this technique to study alternative theories of gravity is also possible [45].

Cosmology

In addition to relativistic effects in astrophysical systems, general relativity is also the prevailing theory when it comes to cosmology, the study of the history and evolution of the large scale structure of our Universe. The underlying metric that describes a homogeneous and isotropic background space-time has been found and explored multiple times in the literature, partially unaware of previous works. This pillar of cosmology is also called the Friedmann-Lemaître-Robertson-Walker metric, in order to account for the various early works that contributed

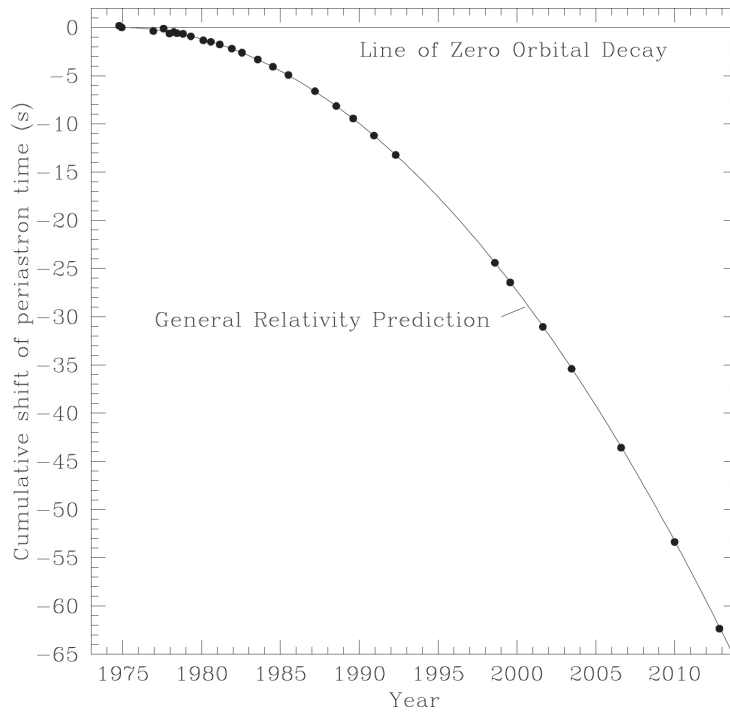


Figure 1.1: Orbital decay of the binary pulsar PSR B1913+16 through the emission of gravitational waves. The agreement of the measurements with the prediction of general relativity is excellent. Figure taken from “RELATIVISTIC MEASUREMENTS FROM TIMING THE BINARY PULSAR PSR B1913+16”, J. M. Weisberg and Y. Huang, *ApJ* 829 55, 2016, doi: <https://doi.org/10.3847/0004-637x/829/1/55>, [43]. ©AAS. Reproduced with permission.

[46, 47, 48, 49, 50, 51, 52, 53]. The line element is given by

$$ds^2 = -c^2 dt^2 + R^2(t) \left(\frac{dr^2}{1 - kr^2} + r^2 d\theta^2 - r^2 \sin^2(\theta) d\phi^2 \right), \quad (1.14)$$

where $R(t)$ is the so called scale-factor and $k = 0, 1$ or -1 for flat, spherical or hyperbolic spatial geometry respectively. The metric can be used to derive the Friedmann equations which connect the scale-factor describing the expansion of the Universe with the present matter and energy distribution. These equations are the basis for today’s standard model of cosmology, the Λ CDM model. By choosing a cosmological constant Λ and introducing cold dark matter it is able to describe various aspects of our evolving Universe. However, since this thesis is about compact objects and not about cosmology, we refer to [54] for a first introduction to cosmology.

Direct Observations of Gravitational Waves

A few years ago, before the first direct detection of the binary black hole merger GW150914 by the advanced LIGO observatory [55], it had not been possible to discuss direct observations of gravitational waves as successful test(s) of general relativity. The reason simply being that such waves are well known from theoretical works, but they are incredibly difficult to detect. For several aspects of general relativity, but also for astrophysics and cosmology, direct observations of gravitational waves are tremendously important for various reasons. Among them are tests of strong and highly dynamical gravitational fields, the very nature of black holes and the physics of neutron stars in connection with the nucleosynthesis of heavy elements in our Universe. Gravitational waves also offer a completely new window to observe the Universe, with great opportunities especially for its electromagnetically dark side. Therefore, and because this thesis is about gravitational waves, these aspects are discussed in more detail in the following Sec. 1.3.

1.3 Gravitational Waves

In this section we introduce gravitational waves, discuss possible sources and how they can be detected. The following discussion can be found in most text books on general relativity. Here, we refer the interested reader to [25].

1.3.1 What are Gravitational Waves?

Roughly speaking, gravitational waves can be described as small perturbations of space-time that propagate with the speed of light. For an observer on Earth, any gravitational wave passing by introduces tiny deviations in what one calls the background space-time. In many but not all situations, it is useful to discuss the concept of gravitational waves in the following way. One assumes that the actual metric $g_{\mu\nu}$ can be written in terms of a background metric $\bar{g}_{\mu\nu}$ and a small perturbation $h_{\mu\nu}$, which describes the gravitational wave

$$g_{\mu\nu} = \bar{g}_{\mu\nu} + h_{\mu\nu}, \quad (1.15)$$

with $|h_{\mu\nu}| \ll 1$. In our example for an observer on Earth, the background metric would correspond to the space-time on Earth, which is a small deviation from the Minkowski metric $\eta_{\mu\nu}$ of a flat and empty space-time. One can show that the first corrections to the Minkowski metric are related to the Newtonian gravitational potentials, which only enter as small term. In order to simplify further discussions, we neglect these influences.

In order to understand the connection between the Einstein field equations (1.2) and basic gravitational wave properties, we consider the simplest case of a Minkowski background metric

$$[\eta_{\mu\nu}] = \text{diag}(-1, 1, 1, 1), \quad (1.16)$$

with square brackets indicating the matrix representation of the tensor. With this background metric at hand, one can linearize the Einstein field equations (1.2) by computing the Ricci tensor eq. (1.6) and Ricci scalar eq. (1.7) on the left hand side with respect to

$$g_{\mu\nu} = \eta_{\mu\nu} + h_{\mu\nu}. \quad (1.17)$$

To further proceed in the calculation, one only keeps terms up to linear order in $h_{\mu\nu}$ and drops all higher orders. In order to simplify the rather lengthy terms, it turns out to be useful to study infinitesimal coordinate transformations of the kind

$$x'^{\mu} = x^{\mu} + \xi^{\mu}(x), \quad (1.18)$$

with four arbitrary functions $\xi^{\mu}(x)$ that are of the same order as $h_{\mu\nu}$. With these at hand, one adopts the following gauge transformation

$$h'_{\mu\nu} = h_{\mu\nu} - \partial_{\mu}\xi_{\nu} - \partial_{\nu}\xi_{\mu}, \quad (1.19)$$

and introduce the traceless tensor

$$\bar{h}'_{\mu\nu} = h'_{\mu\nu} - \frac{1}{2}\eta_{\mu\nu}h', \quad (1.20)$$

where h' is the trace of $[h'_{\mu\nu}]$. The linearized Einstein equations can then further be simplified by choosing

$$\square\xi^{\mu} = \partial_{\rho}\bar{h}^{\mu\rho}. \quad (1.21)$$

A straightforward calculation then yields

$$\boxed{\left(\frac{1}{c^2} \frac{\partial^2}{\partial t^2} - \nabla^2\right) \bar{h}_{\mu\nu} = -2\kappa T_{\mu\nu},} \quad (1.22)$$

where the notation of primes has been removed for simplicity. This is valid as long as $\partial_\mu \bar{h}^{\mu\nu} = 0$, which follows from the condition eq. (1.21).

Eq. (1.22) shows that the linearized version of Einstein's equations, written in some coordinate system, is a simple wave equation for the metric perturbations, with energy momentum tensor acting as a source term. We will extend this analysis in more detail in chapter 3, in which the background space-time will not be Minkowskian anymore. More information about this simple example can be found in most textbooks on general relativity, e.g. [25]. From there one would also arrive at the result that gravitational waves are transverse waves and have two polarizations. These are called plus and cross, which we demonstrate in Fig.1.2.

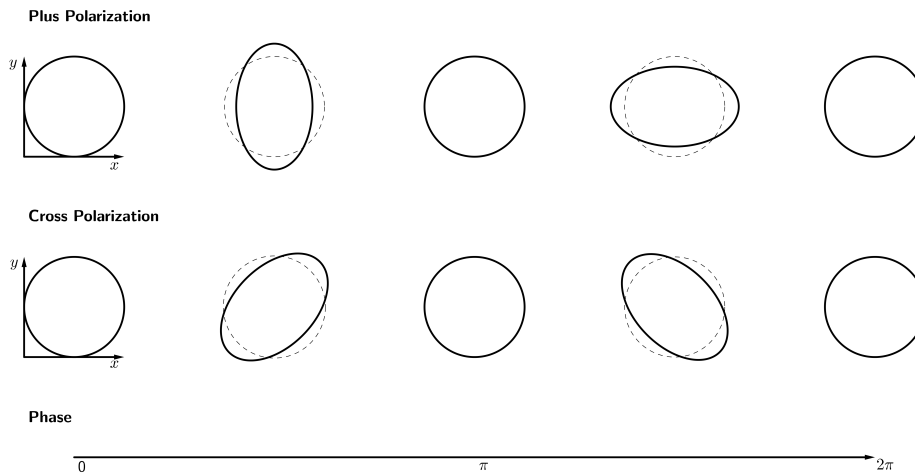


Figure 1.2: Qualitative visualization of the plus and cross polarization as function of the phase. The propagation direction of the wave is perpendicular to the $x - y$ plane shown here.

Let us make some further remarks here. In vacuum, where the energy momentum tensor is zero, the solutions for $\bar{h}_{\mu\nu}$ are freely propagating waves. In the presence of a source, solutions in the region where the energy momentum tensor is non-vanishing have to be matched with the vacuum solution. Also, due to the linearization the sum of two solutions of the linearized equations will again be a solution. Note that this is not true in the non-linear Einstein equations (1.2). There, the situation is more involved because the waves themselves act as a source. A common approximation to take this into account is a multiple step procedure. Here, one defines different orders of the perturbations $h_{\mu\nu}^{(i)}$. First the perturbations $h_{\mu\nu}^{(0)}$ are calculated from eq. (1.22). One can then define an energy momentum tensor $t_{\mu\nu}^{(0)}$, which includes the perturbations and takes into account the fact that gravitational waves in general carry energy and angular momentum from a source. In a second step, the wave equation is solved again for the next order in the perturbation $h_{\mu\nu}^{(1)}$, but this time $t_{\mu\nu}^{(0)}$ acts as additional source. This procedure can be repeated several times and potentially approximate non-linear effects. This is one example showing the technical difficulties that arise when working in general relativity and not Newtonian theory.

To complement this part, we want to mention the effect of a gravitational wave passing by. Since the metric tensor defines times and lengths, one expects that gravitational waves will influence this. The simplest solution of the wave equation (1.22) in the absence of sources are plane waves. A more detailed analysis, as demonstrated in [25], shows that the effect of a gravitational wave is the change of the separation of freely moving test masses, transversal to the direction of propagation of the wave. This induced length change will be the key concept used in gravitational wave detectors, as discussed in Sec. 1.3.4.

1.3.2 How are Gravitational Waves produced?

Gravitational waves are emitted by almost all accelerating mass distributions, so the actual question should be how strong is the gravitational wave emission of a given physical system? Since the exact answer involves the full treatment of the Einstein field equations, the situation is quite complicated. A very useful way around the full problem is to use certain approximations that allow one to simplify the non-linear coupled equations to something more tractable. Einstein himself provided one of these tools with the so-called quadrupole formula [56]. It is given by

$$\bar{h}_{ij} = -\frac{2G}{c^4 r} \frac{d^2}{dt^2} Q_{ij}^{\text{TT}} \left(t - \frac{r}{c} \right), \quad (1.23)$$

where Q_{ij}^{TT} is the quadrupole moment of the source expressed in the transverse-traceless gauge as

$$Q_{ij}^{\text{TT}} = \int dx^3 \rho(\vec{x}) \left(x_i x_j - \frac{1}{3} r^2 \delta_{ij} \right). \quad (1.24)$$

Here, the evolution of the system has to be provided through the mass density $\rho(\vec{x})$, which, e.g., can describe two point particles that approximate a binary system. The quadrupole formula is a widely used estimation and valid for systems that are not too relativistic. This means it is valid for small velocities and not very compact systems. In its simplest form one can use Newton's law of gravity to provide the trajectories and apply the quadrupole formula to estimate the emission of gravitational waves. By including backreaction effects and higher order corrections, it is possible to make more precise calculations. Here backreaction means that the emission of gravitational waves does in general change the trajectories.

1.3.3 Sources of Gravitational Waves

From Sec. 1.3.2 we have already motivated that almost all accelerated mass distributions, besides axial symmetric configurations, are a source of gravitational waves. However, a quick order of magnitude estimate already shows that the involved masses and accelerations have to be enormous to produce any observable effect at all. After all, this should not be surprising. Newtonian theory does not predict gravitational waves and only differs from general relativity in extreme situations or very precise observations. There is an enormous amount of literature that studies astrophysical and cosmological gravitational wave sources. In order to provide some overview, we discuss the main sources in the following. The basis of the following part is the living review by [57], if not otherwise stated. It includes an extensive list of literature for further reading.

The emission of gravitational waves is important for highly relativistic systems which usually consist of black holes or neutron stars, either as isolated objects or in binary systems with another compact object. While neutron stars can be thought of as extremely dense and compact stars, black holes are a completely new kind of object that has no real Newtonian analogue, although some qualitative discussions can be made. We introduce the details of different compact objects in chapter 2.

The most efficient events that produce gravitational waves are colliding black holes, which describe the natural evolution of a binary system of black holes. Also, mergers of neutron star binaries or black hole neutron star binaries are among the strongest sources. Other types of astrophysical relevant sources are isolated neutron stars, once they admit non-axially symmetric deformations, e.g., due to oscillation modes or possible deformations due to strong magnetic fields. Ordinary stars or even white dwarfs might only play an observable role when they orbit around a supermassive black hole. Also supernovae explosions can be sources of gravitational waves.

The following provides a short summary of the main astrophysical sources of gravitational waves as described in [57]. The subclass of compact objects that are object of the research in this thesis are discussed with more technical details in chapter 2.

Isolated Sources

As isolated gravitational wave sources one can consider neutron stars or black holes. The waves expected to be emitted by less compact stars would be too weak to be detected with current detectors. While black holes can in principle exist in all mass ranges, the astrophysics of stellar evolution and galaxy formation puts constraints on the actually possible black hole masses in nature. The lightest can be of the order of a few solar masses up to several tens of solar masses. The most massive black holes are so-called supermassive black holes and have been found with masses of around $10^6 - 10^{10} M_{\odot}$. Of course, it is expected that masses in between might have at some time been realized as well, which are called intermediate mass black holes and cover a range of around $10^3 - 10^4 M_{\odot}$. For neutron stars the situation is clearly different, since their allowed masses, constrained from observations and theory, can only be about one to two solar masses.

Black holes can only act as source of gravitational waves if surrounding matter or objects perturb the space-time. For neutron stars the situation is different. Since their complicated physics can allow for rapidly rotating non-axially symmetric matter configurations, even an isolated neutron star can be a source of gravitational waves. This can happen through various ways. Some neutron stars rotate very fast (millisecond pulsars), which can cause instabilities inside the neutron star to build up, which are then partially emitted in gravitational waves. A rich family of neutron star oscillation modes exist, see e.g. [58, 59] for two classical reviews of the field.

Also, neutron stars can have strong magnetic fields of around $10^{11} - 10^{12}$ T. Some of them, so-called magnetars, possess magnetic fields that might even be strong enough to deform the star from axial symmetry. This can happen if the axis of the magnetic field is not aligned with the axis of rotation. Due to the small expected amplitudes, these sources have not been measured yet.

Another class of isolated sources are supernovae explosions. Simulating these events is very challenging and they have not been observed by gravitational wave detectors so far.

Binary Systems

Binary systems are of great interest for gravitational wave physics and are the most promising sources. The most powerful sources are those that involve black holes or neutron stars, as proven by the repeated detections by the advanced LIGO and advanced Virgo detectors, which is discussed in Sec. 1.3.4. As has already been observed for a long time in the Hulse-Taylor binary and other binary pulsar systems, the orbits shrink and the binary systems are not stable on long time scales. Without external influences, there are three phases in the evolution of a relativistic binary system.

In the early phase, which is called inspiral, relativistic effects are weak. Here, it is possible to use post-Newtonian (PN) theory to include relativistic corrections to the classical Newtonian motion [60]. The amplitude and frequency of the emitted gravitational waves increase only slowly. Hereby the frequency is of the order of the orbital frequency and effects on the orbits are tiny. Depending on the initial separation, this phase can take in principle arbitrarily long. While the binary shrinks, the two body systems becomes more relativistic and the emission of gravitational waves more efficient. Just before the two object collide, the amplitude and frequency of the emitted waves increases strongly, it chirps. Since early emission is quite weak, detectors might only see the late part of this process.

The phase that describes the collision of the two objects is called merger. This phase is rather short compared to the previous timescales and can only be described by the numerical solution of the full, non-linear field equations. This is an extremely challenging task that requires state-of-the-art numerical relativity codes and significant computational resources. For binary black hole mergers, breakthrough results [61, 62, 63] have been reported from 2005 on. In the case of neutron stars it is necessary to use relativistic magneto-hydrodynamic simulations to describe how the matter evolves. The advantage of neutron star collisions is that electromagnetic radiation is produced as well, which can be used to gain more information about the source itself and its position.

The final phase is called ringdown. Depending on the initial objects, the final object is either a neutron star or a black hole. In both cases it has significant spin and the final space-time is highly excited. In the case of neutron stars, this also applies for the matter and thus a rich family of oscillations can be excited. The name ringdown

comes from the fact that the remaining perturbations are radiated away in the forms of gravitational waves and a linear description of the perturbations becomes possible. A possible analogy here is a ringing bell. The treatment at this stage can be similar to the one of an isolated source. A successful method that incorporates the different stages of a binary merger is the effective-one-body (EOB) formalism [64] introduced by Buonanno and Damour.

Since black holes exist in a wide range of masses, they are therefore present in different types of astrophysical systems. To start with, we note that the typical gravitational wave frequencies scale with the overall mass of the system. Particularly for binaries, the mass ratio of the two bodies indicates whether it is possible to use perturbative techniques (extreme mass ratio) or if full numerical relativity is necessary (similar masses). In the case of extreme mass ratio inspirals (EMRIs), in which the lighter object is a neutron star, it can be possible to observe the tidal deformations of the neutron star from the gravitational wave signal. This can be used as a tool to study the neutron star equation of state. EMRIs that involve a supermassive black hole might also be an opportunity to excite and observe the several gravitational wave QNMs of the Kerr space-time. This would be the most stringent test of the Kerr hypothesis which says that astrophysical black holes are described by the Kerr solution. In EMRIs where the smaller object is not a neutron star, the chances that the star gets disrupted by the tidal forces of the supermassive black hole are high. This is the case for normal stars and might also happen for white dwarfs, depending on the mass of the supermassive black hole. These are events that might not yet be directly observable with gravitational waves today, but at least would produce an electromagnetic signal.

Stochastic Background

Besides the previous examples of individual sources, it is also straightforward to expect a stochastic gravitational wave background, see [65, 66] for overviews. There are various processes that can contribute. First, the Universe is populated with compact binary systems which all emit gravitational waves in the inspiral phase. Since the emission is not very strong in this phase, but one expects many sources, they should add up to an unresolvable signals with stochastic properties, in contrast to the clean signal of an individual system. Measuring and analyzing such a background is valuable to study population models since they provide an imprint of the number and types of binary systems, at least in our cosmological neighborhood. Another contribution is expected from isolated sources, which in the case of millisecond pulsars might to a good approximation be monochromatic. Besides astrophysical contributions, for which the one from binary systems might be the most important one, there are also strong theoretical suggestions of a cosmological gravitational wave background. The origin of this background lies in the very early Universe and is discussed in the context of inflationary theories that determine the details.

1.3.4 Observing Gravitational Waves

Since gravitational waves describe small changes in the metric tensor, they can in principle be measured by keeping precise track of length or time intervals. A gravitational wave detector does exactly this, but in a very sophisticated way to make the tiny effects observable. Rough order of magnitude estimates predict that the relative length changes induced by a gravitational wave of realistic astrophysical origin could be of the order of $\Delta L/L \sim 10^{-20}$. In order to detect such tiny effects, it was not only necessary to develop new experimental technology, but also to push forward numerical simulations and data analysis schemes. So far, three different types of direct gravitational wave detection principles have been explored in a comprehensive way. These are resonance detectors, laser interferometers, and pulsar timing arrays. So far, only laser interferometers reached the required sensitivity for direct detections. Another attempt, which is intended to work for cosmological gravitational waves, is through observations of the B-mode polarization of the cosmological microwave background. Claims that this was observed had been made in 2014 [67] by the BICEP2 experiment. However, using more recent dust maps obtained by the Planck satellite, the claims have been withdrawn [68]. These results can be used to put limits on the strength of this type of gravitational wave background and therefore impose constraints on some inflationary models.

Resonance Detectors

The idea behind these type of detectors is that gravitational waves could be detected by exciting oscillations in a solid object. The pioneering work goes back to Joseph Weber who started to report results from the 1960s on [69, 70, 71]. Claims that direct detections were possible have mostly been rejected in the community. To attempt to measure gravitational waves, different aluminum cylinders with lengths of about 1 – 2 m and diameters of about 0.2 – 1 m were used. These were suspended in such a way that most of the environmental disturbances could be eliminated, while thermal noise was one of the limiting factors. If a gravitational wave passes through the detectors, oscillations should get excited. Excitations of the solids were read out using precise piezoelectric elements at their ends. However, this approach only works for gravitational wave frequencies close to the resonance frequencies of the detectors and can therefore only work in a narrow frequency window. To honor Weber's pioneering work in developing these early type of gravitational wave detectors, they are also called Weber bars.

Back in these early days of experimental gravitational wave physics, it was only possible to provide estimates for the expected waveforms, since the full Einstein equations could not be solved numerically and much of the underlying astrophysics was not well understood. With the experimental precision that was possible and without the powerful numerical simulations or data analysis techniques available today, it was not possible to measure gravitational waves.

More advanced realizations of resonance detectors have been developed and are still being improved, e.g., MiniGRAIL in Leiden, Netherlands [72]. A detailed overview on the past, present, and future of resonant gravitational wave detectors can be found in [73]. Besides larger detector masses, crucial improvements could be achieved by cooling these down to low temperatures in order to reduce thermal noise. Once the required sensitivities are reached, resonance detectors might be able to operate in a lower frequency window than that of the currently operating laser interferometer detectors, which are discussed next.

Laser Interferometers

The most sensitive, current gravitational wave detectors are huge, state-of-the-art laser interferometers. The setup is qualitatively similar to the Michelson interferometer, but of completely different size and level of technology. The basic principle is to measure the length difference between freely moving test masses, whose separations are changed when a gravitational wave passes through the setup in a suitable orientation. To do so, a powerful laser beam is split at a beam splitter into two directions. At each end, a freely hanging mirror reflects the light. The reflected light goes back through the beam splitter and is superimposed at a readout detector. In order to increase the sensitivity, Fabry-Pérot cavities can be used. Finally, when one of the arm lengths is changed relative to the other one, the wave nature of light will change the output signal due to interference. A gravitational wave passing by that changes the separation of the mirrors can therefore in principle be detected. An illustration of such an experimental setup is provided in Fig. 1.3, which shows some of the basic properties implemented in the advanced LIGO detectors. The requirements to observe gravitational waves are so high, that it took several decades from early developments until detections were possible. In order to achieve such outstanding precision, many smaller prototype detectors have been built throughout the world. Among the smaller detectors that have mainly been important in the development of different technologies are the GEO600 detector near Hanover, Germany, and the TAMA detectors at the Kamioka site in Japan. GEO600 was built in the 1990s as a British-German project, it is now operated by groups from different universities and the Max Planck Society. The successor of the TAMA detectors is the, currently under construction, Kamioka Gravitational Wave Detector (KAGRA), which should be ready to join the advanced LIGO and advanced Virgo detectors in 2019.

The first direct observation of gravitational waves was achieved in 2015 by the advanced LIGO [55] detectors. One detector is in Livingston, Louisiana, and the other one in Hanford, Washington, both in the United States. The first direct observation of a binary neutron star merger was possible in 2017 [15], together with the European detector advanced Virgo, which is located close to Pisa, Italy. Founded as a French-Italian project in the early 1990s, several other European countries have since joined the collaboration. The current advanced LIGO and advanced Virgo detectors have arm lengths of around 3 – 4 km and are the largest detectors so far.

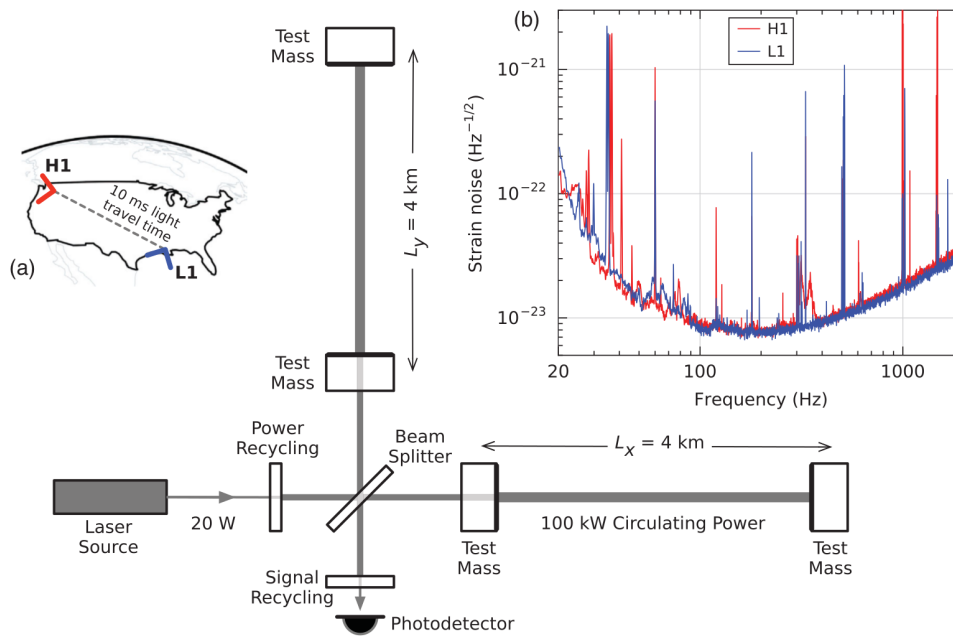


Figure 1.3: Simplified illustration of the advanced LIGO detector, as example of a laser interferometric gravitational wave detector. The top right plot illustrates the sensitivity of the both detectors as function of the gravitational wave frequency. Figure taken from B.P. Abbott et al. (LIGO Scientific Collaboration and Virgo Collaboration), Phys. Rev. Lett. 116, 061102, DOI: 10.1103/PhysRevLett.116.061102, 2016, [55]. It has been published under Creative Commons Attribution 3.0 License (<https://creativecommons.org/licenses/by/3.0/>)

Pulsar Timing Arrays

A completely different approach is followed by Pulsar Timing Arrays (PTAs), for which an extensive overview can be found in [74]. The basic idea is to use a known set of pulsars whose pulses can be tracked precisely through radio telescopes on Earth. As the name suggests, this type of rapidly spinning neutron stars sends very regular radio pulses. Analyzing and correlating the signals from many such pulsars allows one to constrain low frequency gravitational waves of the order of $10^{-9} - 10^{-6}$ Hz. If a low frequency gravitational wave travels between Earth and the pulsars, it will change the arrival times of the pulses. The reason for the low frequency sensitivity is that the effective “arm lengths” are the separation between Earth and the pulsars, which are many light years. The biggest PTA consortium is the International Pulsar Timing Array (IPTA), which consists of the European Pulsar Timing Array (EPTA), the North American Nanohertz Observatory for Gravitational Waves (NANOGrav), and the Parkes Pulsar Timing Array (PPTA). So far, it has not been possible to detect gravitational waves with this approach, but supermassive black hole binaries should exist and are expected to be measurable with further improvements in the future.

Future Detectors

There is a wide range of possible future gravitational wave detectors. While some of them will be improved ground-based detectors in a frequency range similar to the already existing ones, other proposals are space-based missions that will measure at lower frequencies. One of these space-missions is the Laser Interferometer Space Antenna (LISA) [17] which consists of three satellites with arm lengths of 2.5 million km. The project started as US-European collaboration between the North American Space Agency (NASA) and the European Space Agency (ESA). The project went through difficult times when NASA left in 2011. The original mission was planned with longer arm lengths, but was shrunk to reduce costs. However, after the LISA pathfinder mission was able to prove that essential parts of the technological problems can be solved, ESA selected the LISA mission in 2017 as a large-class mission in the cosmic vision program. It is expected to launch in 2034. The main observational targets will be events involving supermassive and intermediate mass black holes, as well as extreme mass ratio inspirals. Another space-based mission is the proposed Japanese DECi-hertz Interferometer Gravitational wave

Observatory (DECIGO), with shorter arm lengths of around 1000 km [75]. On Earth, there are ambitious plans for third generation detectors, such as the Einstein Telescope (ET) [76] and Cosmic Explorer [77].

Signal Extraction

Before we discuss the main insights from the recent gravitational wave detections, we should spend some time on how these signals are detected. Due to the required precision, data analysis schemes play a big role. Without going into detail about the limiting factors for the precision and explanations why gravitational wave detectors are only sensitive in a certain frequency window, we want to mention some basic principles for the signal detection. So far, the sensitivity of the detectors require sophisticated data analysis techniques [13]. One which is commonly used is matched filtering. Here, a theoretically computed waveform is used to look for a weak signal which is contaminated with noise and other contributions that are not from the actual source. If the expected waveform is present in the signal, this technique allows to extract it even if the true waveform is not clearly visible in the original signal. Since every gravitational wave signal depends on the parameters of the source as well as the relative orientation of the detector, this becomes quite challenging in practice. To address this problem, a huge bank of templates is used. Every template corresponds to a theoretically computed waveform that represents one physical system, e.g., a binary black hole merger with certain masses and spins. In order to detect a signal and reconstruct the parameters of the system, it is necessary to have a matching template. Since the total number of parameters is non-trivial, the total number of required templates to cover binary black hole or neutron star mergers is huge. As the precise computation of a single waveform is already computationally expensive, the use of computer clusters is mandatory. A direct inversion from the signal to the underlying system is an extremely complicated inverse problem, which is not possible at this time.

1.3.5 The Observational Status of Gravitational Waves

The repeated direct detections made by the advanced LIGO and advanced Virgo detectors has many interesting implications. The most obvious one is that all observed signals originate from binary systems of black holes or neutron stars. Isolated sources, such as continuously emitting rapidly rotating neutron stars or supernovae explosions, have not been measured so far. Also, there have been no unexpected signals from unknown sources. During the first observing run O1 of advanced LIGO, which lasted from September 2015 to January 2016, two binary black hole mergers were detected clearly [55, 78]. Fig. 1.4 shows the published reconstructed signals and waveform for the first event GW150914. It shows the reconstructed signal in the top panels, the best fit numerical relativity template along with the reconstructed wavelet and template in the middle panels, as well as the residuals in the panels directly below. The two bottom panels show the extracted frequencies of signal as function of time. All panels on the left are from the Hanford detector and the right ones from the Livingston detector. More details can be found in the original publication [55]. Advanced Virgo joined the observation campaign in the second observing run O2 in August 2017. Soon the first joint detection was possible [79], allowing for an improved localization of the source.

While a few more binary black hole mergers have been found in O2, the truly new discovery was the first direct detection of a binary neutron star merger [15]. Due to the observed optical counterparts [80], a vast amount of literature was released from collaborating groups observing at all kinds of wavelengths. Various interesting questions could be addressed. One of them is a completely new way to measure the Hubble constant [81], which was found to agree within the error margins with the known values from other methods [82]. This is especially interesting for more precise future observations since different methods in cosmology seem to give two slightly different values in recent years. This disagreement has become known as the Hubble tension. Another interesting aspect is the connection of gamma ray bursts with neutron star mergers [83]. With the improving sensitivity of the detectors the number of measured events is increasing. In the current observing run O3, which started on April 1st 2019, there has been roughly one detection per week.

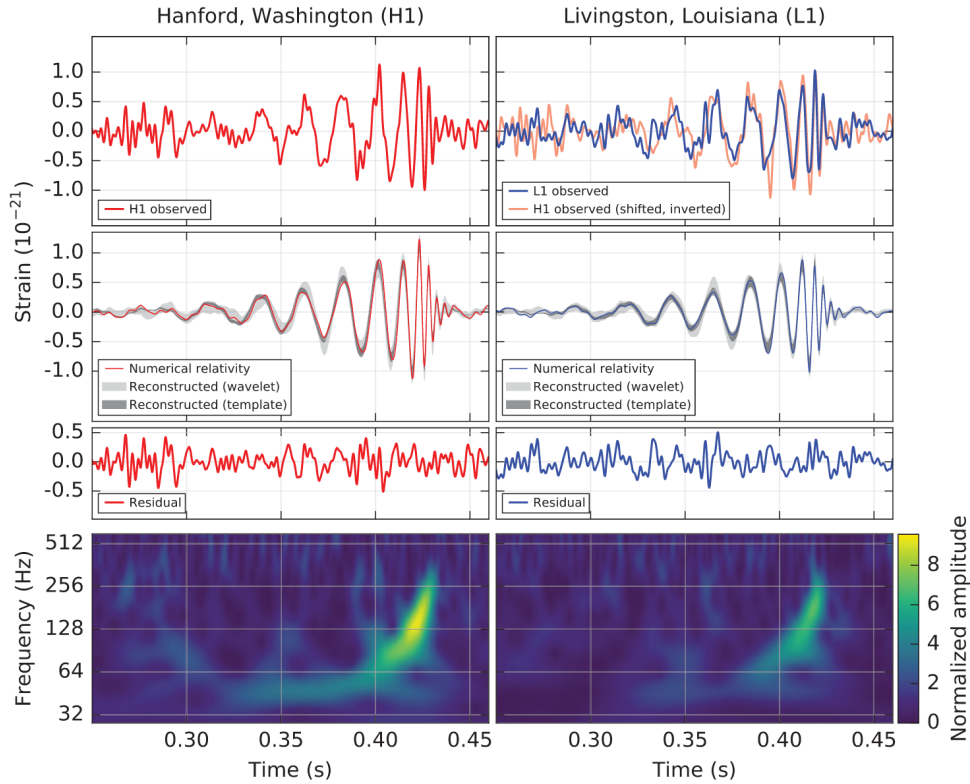


Figure 1.4: Published results of the first direct gravitational wave detection GW150914 by the advanced LIGO detectors. Figure taken from B.P. Abbott et al. (LIGO Scientific Collaboration and Virgo Collaboration), *Phys. Rev. Lett.* 116, 061102, DOI: 10.1103/PhysRevLett.116.061102, 2016, [55]. It has been published under Creative Commons Attribution 3.0 License (<https://creativecommons.org/licenses/by/3.0/>).

Gravitational Wave Tests of General Relativity

The observed gravitational wave signals from merging binary black holes and neutron stars allow one to put completely new constraints on general relativity and alternative theories of gravity. First of all, the observations have proven that gravitational waves really exist in nature. Furthermore, the fact that the measured signals of binary black hole mergers match to the prediction of general relativity is arguably the best proof that objects as compact as black holes really exist in nature. Thanks to the observed binary neutron star merger [83], Einstein’s prediction that the speed of gravitational waves and the speed of light are equal have been confirmed with very high precision. In addition, this provides new bounds on possible violations of the Lorentz invariance. The observation also provides a new test of the equivalence principle.

Therefore, it seems that Einstein was right again. However, there are some important remarks that need to be made with respect to alternative theories and the nature of black holes. First of all, unfortunately there is no comparable template bank for waveforms computed from still allowed alternative theories of gravity. We thus simply do not know how exactly such signals would look in alternative theories and can therefore not simply rule them out. Also, the conclusion that the merging objects necessarily must be black holes is challenged by various exotic models for ultra compact objects. Although most of these models are not on an equivalent theoretical level as neutron stars or black holes, simplified analysis show that there is room for such alternatives [84]. Moreover, many theorists have pointed out that black holes, although being the current standard paradigm, give rise to a series of conceptual issues. And testing the most characteristic property of a black hole, namely its event horizon, can conceptually not be done all the way down, neither by gravitational wave detectors nor by telescopes measuring electromagnetic waves.

With increasing sensitivity of detectors in the future, we will access more details of gravitational wave signals. One so far poorly constrained property is the QNM spectrum that is expected in the ringdown phase after a binary black hole merger. This is one of the main aspects of this thesis and will be discussed in detail in the subsequent

chapters. Comparable to atomic spectroscopy or seismology, knowing the details of a spectrum is a powerful tool to study the nature of the source or its composition. Since predictions in this regime of the merger are easier to compute, more insights from alternative ultra compact objects and alternative theories of gravity are available and wait to be tested. Confirming the QNM spectrum will be one of the next milestones in black holes physics and tests of general relativity.

1.4 The Scope of this Thesis in a Nutshell

After this introductory chapter on different aspects of general relativity, compact objects, and gravitational waves, one can present a more detailed scope of this thesis. As discussed in the previous Sec. 1.3.5, arguably the best evidence that black holes really exist in nature is the repeated detection of gravitational wave signals that match to general relativity's prediction of merging binary black holes. But, the era of this experimental part of gravity has only begun and many fine details have not been observed so far. However, exactly these details make the difference as to whether the observed object is a black hole or something more exotic that can behave and look like a black hole at first sight. The list of such alternative objects is long and we present some of them in chapter 2, but at the same time their physics might be oversimplified, speculative or poorly understood. Among the fine details that confirm or might falsify the existence of black holes in general relativity is their gravitational wave spectrum. Like musical instruments, the space-time of compact objects can have a particular "sound" when the object gets excited. The QNM spectrum, which describes the frequencies and corresponding damping times of the gravitational waves that we associate with a compact object, is quite characteristic. In principle, it provides the fascinating possibility of "*hearing*" the nature of compact objects by measuring their QNM spectrum.

The equations that govern these perturbations around spherically symmetric and non-rotating space-times have already been worked out in several pioneering works [85, 86, 87, 88] which are discussed in chapter 3. While the absence of rotation is a strong assumption for astrophysical objects, it is a necessary starting point in the study of the inverse spectrum problem, which is the main aspect of this work. While many techniques to solve the perturbation equations and obtain the QNM spectrum exist [58, 59, 89], much less is known about the inverse problem. Here, one starts with a given QNM spectrum and wants to reconstruct the properties of the compact object. For neutron stars, there is a lot of literature on empirical scaling relations of the kind initially discovered in the late 1990s [90, 91, 92]. Also, using the mass and radius of neutron stars as observables, it has been demonstrated how the unknown equation of state can be determined with the help of these relations [93, 94, 95, 96]. However, less has been done for the inverse QNM problem, where the knowledge of the complete spectrum is used in methods which reach beyond empirical relations. The main focus of this thesis is to investigate this aspect and to develop methods that can solve it. The underlying approach that is being used is based on the Wentzel-Kramers-Brillouin (WKB) method, which is a semi-analytic technique to obtain approximate solutions for some types of differential equations. These newly derived methods are discussed in chapter 4.

In contrast to the direct problem, the corresponding inverse problems often suffer from the fundamental issue that the reconstructed solutions are not unique. This is captured by the famous mathematical physics question: "Can one hear the shape of a drum?" [97]. As in the case of the drum question, the answer can be that more than one solution exists for a given spectrum [98]. The methods to solve the inverse problem depend on the qualitative type of compact object one studies. This originates in the structure of the effective potential that appears in the perturbation equations. In this context it was possible to adapt the inverse WKB method to different types of objects. If valid, Birkhoff's theorem can be used to find unique solutions for the reconstructed potentials. The applicability of the developed methods have been demonstrated in a series of publications [1, 2, 4, 5, 6, 10], which are the content of Part II of this thesis. Another project related to the QNM spectrum of parametrized black hole metrics has been carried out in [8]. Here, we study the QNM spectrum of test scalar fields and discuss how characteristic the Schwarzschild QNM spectrum is.

Apart from this main focus of this work, there are also related projects, some of which are in collaboration with a third author. These involve a parameter estimation study of parametrized waveforms for ultra compact

objects [3]. In this work, presented in chapter 10, we provide parametrized templates motivated by the time evolution of wavepackets scattered with ultra compact objects and study their value for parameter estimation using current and future gravitational wave detectors. In another project, we applied a part of the inverse WKB method to the inverse problem of Hawking radiation [7], as presented in chapter 11. Here, we demonstrate the reconstruction of greybody factors from the spectrum, which we then use to reconstruct properties of the classical perturbation potentials. As the last project of this thesis we discuss the implications of black hole area quantization for the observation of gravitational waves of spinning black holes [9]. It can be found in chapter 12.

2 | Compact Objects

This chapter is all about the different types of compact objects that are studied in the thesis. Before introducing black holes, neutron stars and exotic alternatives, we first discuss how the term compact object is meant in the context of this work. Unless otherwise stated, from now on through the rest of this thesis, we use geometric units $G = c = 1$, in order to match most of the literature and simplify the relations.

In order to categorize different types of astrophysical objects, one can define a property called compactness C . It is simply the ratio of the mass M over the radius R of a given object

$$C \equiv \frac{M}{R}. \quad (2.1)$$

Here one assumes that a spherical shape for the object under consideration is a good approximation, which is the case for stellar type objects. In geometric units, the compactness can reach a maximum of $1/2$, which is the case for a Schwarzschild black hole. In this case the Schwarzschild radius $R_{\text{Sch}} = 2M$ is used for R and M is the Arnowitt-Deser-Misner (ADM) mass of the space-time [99].

There are several physical properties of an object that are, at least qualitatively, related to its compactness. For example, in Newtonian theory the gravitational potential at the object's surface is proportional to C . Furthermore, it is a useful indicator to estimate whether the gravitational properties of the object can be sufficiently well described with Newton's theory of gravity or if general relativity is required. From main sequence stars to white dwarfs to neutron stars and finally to black holes, the compactness ranges over many orders of magnitude. The closer the compactness of an object is to the limit of $1/2$, the more important one expects the general relativistic corrections to be. For most of the physics related to gravitational waves, the two main classes of compact objects are black holes and neutron stars. White dwarfs do have relativistic features, but they are relatively mild and the expected gravitational wave effects are significantly smaller. Therefore, in the context of this thesis, we are only interested in objects of at least neutron star compactness, which depending on the equation of state and central density is about $C \approx 0.1 - 0.3$. For comparison, the compactness of the Sun is $C = 2 \times 10^{-6}$.

Although the history and physics of compact objects are related to each other, the structure of this chapter is that we first address black holes in Sec. 2.1, then neutron stars 2.2, and finally some of the alternative ultra compact objects in Sec. 2.3.

2.1 Black Holes

In this section we introduce arguably the most fascinating and extreme objects in physics. Black holes became not only an essential part of many fields in astronomy and astrophysics, but also of countless science fiction movies and books, that made them known to the general public. In Sec. 2.1.1 we first review some of the seminal works, before we discuss their actual metric tensors in Sec. 2.1.2.

2.1.1 A Brief History of Black Holes

Black holes are commonly described as objects whose gravitational attraction is so strong that even light can be trapped. Already in the late 18th century, it was first John Michell [100], and a few years later Pierre-Simon Laplace [101], who proposed the existence of objects with such properties. A historical discussion can be found in [102]. Using different assumptions for these dark objects, masses of today's intermediate mass and supermassive black holes were proposed, long before general relativity.

Today, the black holes we talk about are purely related to general relativity and described by a three parameter family of solutions for the metric tensor, whose history we describe in the following. Not that generalizations

in alternative theories of gravity exist as well, but we continue with those of general relativity. The simplest, non-rotating black hole solution is named after Karl Schwarzschild, who discovered it in 1916 [103], shortly after Einstein proposed his general theory of relativity. At that time there were no calculations that explicitly showed how black holes could form in nature. The creation of black holes as final fate of massive stars that ran out of fusion material was first studied by J. Robert Oppenheimer and Hartland S. Snyder in their 1939 seminal paper on the gravitational collapse of fluid spheres [104]. However, there were serious concerns about the formation of black holes and their singularity, as argued by Einstein himself [105].

Later, in 1958, it was David Finkelstein who discovered that the singularity at the Schwarzschild radius originates from the choice of coordinates. He identified this surface as a one way membrane, which is widely known as event horizon today [106]. The maximal extension of the solution was studied shortly after by Martin D. Kruskal [107].

The generalization of the Schwarzschild solution to rotating objects took almost half a century, although early approximate work for a rotating sphere was published in 1918 by Lense and Thirring [108, 109]. It was not before 1963, when Roy Kerr found the most relevant black hole solution for astrophysics. It is the two parameter family of rotating black holes [110], purely described by their mass and angular momentum. The generalization to the three parameter family, which also includes electrical charge, was reported two years later [111] and is now known under the name Kerr-Newman metric. Can there be even more general stationary black hole solutions in Einstein's theory? According to the commonly referred "no-hair theorem", the answer is no. It states that every black hole in general relativity, including the Maxwell equations of electrodynamics, should be described by these three parameters [29]. Note that the cosmological constant Λ is excluded here. The rigorous proof of such a statement is not easily possible and several works had proven different aspects of this theorem under more specific assumptions. Werner Israel proved it first for the Schwarzschild case [112] and non-rotating charged solution [113]. Brandon Carter proved the theorem for uncharged rotating black holes [114]. The nature of black hole singularities have been further studied by Roger Penrose, who formulated his famous singularity theorem in 1965 [115].

A somewhat unexpected field, black hole thermodynamics, was opened in the 1970s, by the seminal works of Werner Bekenstein, Brandon Carter, James Bardeen, Stephen Hawking and related works of other great minds of the time [116, 117, 118, 119]. They discovered analogies between the laws of thermodynamics and the properties of black holes. By studying quantum fields in curved space-times, Hawking found that black holes do evaporate. His famous result, known as Hawking radiation, shows that black holes should radiate particles with an approximate thermal spectrum. Therefore they should slowly evaporate by this mechanism and it is justified to assign them a real temperature, the so-called Hawking temperature. The emission is weaker the more massive a black hole is, which makes it probably impossible to detect this form of radiation for astrophysical black holes. However, this does by no means imply that these findings are not relevant for astrophysical black holes. Among the striking implications of black hole thermodynamics are questions regarding the quantum structure of black holes, their possible remnants, and how much information could possibly be stored. Different works addressing these questions resulted in the so-called information loss problem of black holes, see e.g. [120, 121, 122, 123], which is still an unsolved problem. It seems that demanding fundamental properties of quantum mechanics and general relativity at the same time causes inevitable unexpected consequences. A lot more than the aforementioned works have addressed the subtle consequences of both fundamental theories, but did not yield a satisfying answer yet. One of the directions led to the concepts of a holographic universe, as proposed by Gerard 't Hooft [124], Leonard Susskind [125], and Raphael Bousso [126]. Another striking aspect is the postulation of highly energetic firewalls instead of harmless event horizons [127]. Also Stephen Hawking, even 40 years after his seminal works, continued to work on solutions of the information loss problem [128].

While the previous discussion provided a brief theoretical review, there have of course also been important observational milestones. For a long time, the vast majority of the community did not consider black holes as real objects in our universe, but instead thought of them only as mathematical solutions. This changed due to advances in observational astronomy, when more and more different types of compact systems have been discovered. Some of them, called quasi-stellar objects, are extremely luminous compact sources. For a brief

early history of these objects and active galactic nuclei we refer the reader to [129]. From the 1960s on, detailed studies have been carried out and revealed that these objects can not be explained by ordinary stars. Black holes as driving mechanisms that interact with surrounding matter have been proposed to explain the extremely powerful emission. Another hint that something like black holes must exist, came from observations of the center of our galaxy. By observing the proper motion of stars around the radio source Sagittarius A* for several years, e.g. [130], it was possible to conclude that an object with a mass of around $4 \times 10^6 M_{\odot}$ has to exist in a relatively small region. A supermassive black hole seems to be the least exotic explanation for this. For less massive black holes, evidence has been found in compact binary systems and compact objects with accretion discs. The historically most important one is the galactic x-ray source Cygnus X-1 discovered in 1964 [131]. Its very strong X-ray emission and mass beyond those possible for neutron star can hardly be explained by other known objects. Again, due to the lack of alternative compact objects, one of the two objects in the binary has been conjectured to be a black hole. More recent studies show that the mass of this black hole must be around $14 M_{\odot}$ [132].

Most proofs of black holes are due to the lack of alternative explanations, and therefore indirect, but two more recent techniques changed this considerably. First, the direct detections of gravitational waves from merging binary black holes by the advanced LIGO and advanced Virgo detectors, as discussed in Sec. 1.3.5. Second, the direct image of the shadow of the supermassive black hole in M87 by the Event-Horizon-Telescope Collaboration [16] presented in 2019. While these observations provide best evidence so far for the existence of black holes, ultra compact alternatives are hard to disprove. In fact, various alternative ultra compact objects might be in agreement with the gravitational wave observations, see [84] for a current overview. Claims that such objects had actually been observed by the gravitational wave detections were reported [133, 134]. However, these claims are disputed and require more data for clarification [135, 136]. Thus, the quest to understand the most compact objects in the universe is an ongoing endeavor.

2.1.2 The Space-Time of Black Holes

In the following we briefly discuss the metric tensors of the Schwarzschild black hole and the Kerr-Newman black hole.

Schwarzschild Black Hole

The most famous solution of general relativity is probably the one found by Karl Schwarzschild [103]. It describes the vacuum solution of a spherically symmetric and asymptotically flat space-time with only one parameter, which can be understood as the mass M of the central object. Its line element can be written as

$$ds^2 = - \left(1 - \frac{2M}{r}\right) dt^2 + \left(1 - \frac{2M}{r}\right)^{-1} dr^2 + r^2 d\theta^2 + r^2 \sin^2(\theta) d\phi^2, \quad (2.2)$$

which immediately indicates two special values for the radial coordinate r . The metric functions g_{tt} and g_{rr} diverge at $r = 0$ and $r = 2M$, respectively, which suggests a special behavior of the solution there. While one can show that the singularity at $r = 2M$ is only the result of the choice of coordinates, the one at $r = 0$ can not be removed by such means [106]. The region at $r = 2M$ is called the event horizon, while $r = 0$ is the singularity of the black hole which is not part of the manifold. The tidal forces diverge and would ultimately disrupt any physical object in its vicinity. Due to Birkhoff's theorem, which we discuss in Sec. 2.2.4, the Schwarzschild metric also describes the external space-time of any spherically symmetric matter configuration. It is therefore widely used to describe relativistic effects, such as the gravitational redshift or time dilatation around the Earth or stars, which can be regarded as very slowly rotating.

The Kerr-Newman Metric

The most general black hole solution that describes a rotating and electrically charged black hole is described by the Kerr-Newman metric [111]. For astrophysical applications it is usually assumed that electrical charge Q is tiny and can be neglected, which then yields the Kerr solution [110]. If astrophysical black holes would be charged significantly, the common assumption is that they should discharge quickly with matter in the environment, simply because electromagnetic forces are much stronger than gravitational ones. Thus the no-hair theorem for astrophysical black holes, also called Kerr hypothesis, is that every astrophysical black hole should be uniquely described by its mass M and angular momentum J , also called spin. The line element written in Boyer-Lindquist coordinates is given by

$$ds^2 = -\frac{\Delta}{\rho^2} [dt - a \sin^2(\theta) d\phi]^2 + \frac{\sin^2(\theta)}{\rho^2} [(r^2 + a^2) d\phi - a dt]^2 + \frac{\rho^2}{\Delta} dr^2 + \rho^2 d\theta^2, \quad (2.3)$$

with

$$\Delta = r^2 - 2Mr + a^2 + Q^2, \quad \rho^2 = r^2 + a^2 \cos^2(\theta), \quad a = \frac{J}{M}. \quad (2.4)$$

For non-vanishing angular momentum J or charge Q , one finds that there are two event horizons, an inner one and an outer one. Another new feature, which is present for rotating black holes, is the so-called ergosphere. It describes a region around the black hole from where it is possible to extract rotational energy from the black hole. This was first discovered by Penrose and Floyd in 1971 [137] by using particles and around the same time for waves by Zel'Dovich [138, 139]. Here the so-called phenomenon of superradiance, allows to obtain high frequency waves from low frequency waves that scatter with the rotating black and thereby extract energy.

Another relativistic effect of rotating black holes and other rotating objects, is frame dragging [108, 109], also called Lense-Thirring effect. In Newtonian theory, a test body which is outside an axial symmetric matter distribution experiences the same force as if the central object is not rotating. An analysis of the geodesic equation eq. (1.8) for the Kerr space-time shows that the test body is affected by this. For example, an equatorial, initially purely radially in falling test particle will be dragged in the rotational direction [25].

2.2 Neutron Stars

While black holes are truly fascinating objects, they are in some regard quite simple. Following the no-hair theorem, one might be tempted to say that all there is to know are only three parameters. In clear contrast to this are neutron stars, which consist of matter under the most extreme conditions we know in the current universe. Neutron stars are ideal natural laboratories, which bring together multiple fields in physics and offer a rich complexity of unsolved problems. The name comes from the assumption that most of the matter is made up of degenerate neutrons, that similar to degenerate electrons in white dwarfs, balance the global gravitational attraction. From observations and theoretical considerations of reasonable equation of states, we know that they have masses between roughly one and two solar masses. However, all this mass is confined within a radius of about 10–15 km. In contrast to black holes, these objects have a material surface that emits light and can directly interact with in falling matter. After briefly reviewing the history of neutron stars in Sec. 2.2.1, we go through the relativistic structure equations in Sec. 2.2.2 and discuss two important theorems in Sec. 2.2.4 and in Sec. 2.2.5.

2.2.1 A Brief History of Neutron Stars

Although the history of the study of neutron stars is connected with the one of black holes, there are clear differences. In contrast to the three parameter solution of black holes, there is not a similar answer for neutron stars. Even from the simplest relativistic description discussed in Sec. 2.2.2, one always needs an equation of state to find a solution. Walter Baade and Fritz Zwicky proposed the idea of neutron stars in the 1930s [140]. They

assumed a star made up of neutrons, which had just recently been discovered by James Chadwick [141]. Also Lev Landau proposed one of the earliest works on neutron stars in 1932 [142]. However, translating this assumption in the correct equation of state is quite challenging, due to the complicated nature of quantum field theories that describe the microscopic interactions. Back in these days, the Pauli exclusion principle [143] was used as starting point. This deep quantum mechanical principle in its modern form states that two or more fermions can not be in the same state. Since neutrons are fermions, it implies that such a star must have a very strong internal pressure that might avoid the gravitational collapse. However, the original simple picture is not describing all underlying physics and finding the correct equation of state that incorporates this is thus sometimes called the holy grail of neutron star physics. It is this challenging connection to nuclear and particle physics that makes neutron stars so exciting from different points of view.

As it was the case for black holes, theoretical considerations existed before astronomical observations were available. In 1967, it had been Jocelyn Bell Burnell and Antony Hewish, who discovered the first pulsar [144]. These neutron stars are observable through very regular radio pulses, whose almost constant intervals can be of the order of seconds or milliseconds (millisecond pulsars). For some times in the past, these pulses were more precise than laboratory atomic clocks. The emission mechanism can be qualitatively understood as follows. Due to the very strong magnetic fields that neutron stars have, charged particles can travel along the field lines, where they get accelerated and produce radio emission. The emission is not isotropic, but roughly directed along the magnetic axis. The magnetic axis is not necessarily aligned with the rotational axis of the star, which allows for the lighthouse effect. Depending on the orientation relative to the pulsar, the radio beam can be observed as regular pulse. The precise track of the pulse intervals can show that the pulsar spins down, e.g. due to magnetic braking, or spins up through accreting surrounding matter. Some neutron stars, called magnetars, have even stronger magnetic fields, which can be up to $10^{14} - 10^{15} \text{ G}$ [145]. They have been first discovered in 1979 [146, 147] by measuring x-ray and soft gamma-ray flares. Another milestone discovery was the Hulse-Taylor binary system in 1974 [39], as discussed in detail in Sec. 1.2.2. The most recent important discovery was the direct detection of gravitational wave from a binary neutron star merger in 2017 [15], see Sec. 1.3.5.

2.2.2 The General Relativistic Structure Equations

In order to describe the stellar structure of compact stars, it is necessary to make use of general relativity. While main sequence stars, as well as to a large extent also white dwarfs, are well described with Newtonian gravity, neutron stars are truly relativistic objects. The correct way to describe strong gravitating spherically symmetric matter configurations in equilibrium is given by the Tolman-Oppenheimer-Volkoff (TOV) equations [148, 149, 150]. A derivation can be found in most textbooks in relativity, in the following we refer to [25].

To derive the TOV equations, one starts with a spherically symmetric line element

$$\boxed{ds^2 = -e^\nu dt^2 + e^\lambda dr^2 + r^2 d\theta^2 + r^2 \sin^2(\theta) d\phi^2,} \quad (2.5)$$

where $\nu = \nu(r)$ and $\lambda = \lambda(r)$. Furthermore one uses the energy momentum tensor of a perfect fluid

$$T_{\mu\nu} = (\rho + P) u_\mu u_\nu - P g_{\mu\nu}. \quad (2.6)$$

Here $\rho = \rho(r)$ is the density, $P = P(r)$ is the pressure, and u_μ is the four velocity. A straight forward calculation using eq. (2.5) and eq. (2.6) in the Einstein field equations, yields

$$e^\lambda = \left(1 - \frac{2m(r)}{r}\right)^{-1}, \quad (2.7)$$

where $m(r)$ is defined via

$$\boxed{\frac{dm}{dr} = 4\pi r^2 \rho.} \quad (2.8)$$

Although it looks like the integrated mass inside a sphere of radius r , note that it is not the same as the one that includes properly the volume element of the metric. Furthermore, applying the conservation law

$$\nabla_{\mu} T^{\mu\nu} = 0, \quad (2.9)$$

one finds

$$\frac{dP}{dr} = -\frac{\rho + P}{2} \frac{dv}{dr}, \quad (2.10)$$

which can alternatively be written in terms without the metric function v

$$\frac{dP}{dr} = -\frac{\rho + P}{r^2} [4\pi Pr^3 + m] \left[1 - \frac{2m}{r}\right]^{-1}. \quad (2.11)$$

In order to solve the structure equations, they must be closed by an additional relation. This is done by choosing an equation of state $P(\rho)$. This function takes into account what type of matter one considers and can not be derived from general relativity itself. For the densities and pressures that arise inside neutron stars, the properties of matter are not known and the exact form of the equation of state is among the most important open problems in neutron star physics. This is one of the reasons why these stars are such an exciting topic and interdisciplinary research object. Due to the technical complications in solving the full problem, many equations of states that take into account some aspects have been proposed. Among the simplest ones are polytropic equation of states

$$P = K\rho^{\gamma}, \quad (2.12)$$

where the two constants K and $\gamma = 1 + 1/n$, with polytropic index n , have to be provided [151]. The polytropic index measures how soft or stiff the matter behaves, which results in different compactness and maximum allowed masses. One improvement of this approach is to use piecewise polytropic equation of states, in order to treat the core differently than the outer regions. Finally, realistic equation of states calculated from nuclear and particle physics can only be provided numerically in tabulated forms. Only for very special choices for the equation of state, the TOV equations can be solved analytically, e.g. for constant density, discuss in Sec. 2.3.1. Fortunately it is straight forward to integrate the TOV equations numerically. For a given equation of state, one chooses a value for the central density or central pressure and integrates outwards. The pressure gradient dP/dr , as well as $m(r)$ are zero at the origin. The surface can be defined where pressure or density vanish, or at least are below a given threshold.

2.2.3 Mass and Radius

From the TOV equations for a given equation of state, one can derive a one parameter family of solutions by increasing the central density. This provides a relation between the radius and the mass of the neutron star. Thus, for a given equation of state, one can relate the mass of the star with its radius, and vice versa. Note that we do not discuss other effects, such as rotation or magnetic fields, which would introduce more complexity. Using observations, this can also be used to put constraints on the set of proposed equations of state. One can show that for reasonable equation of states, one arrives at a maximum central density, beyond which no stable neutron star exists. Analogue to the Chandrasekhar limit for white dwarfs, which is based on degenerate electron pressure [152], a similar limit exists also for neutron stars and is known under the TOV limit [149, 150]. However, since the exact equation of state is not known, there is not a clear answer yet. Current limits obtained by matching with observations allow a bit more than $2 M_{\odot}$ [153].

2.2.4 Birkhoff's Theorem

In Newtonian theory, the gravitational field outside an extended spherically symmetric matter distribution is equivalent to the one of a point particle in the center of mass having the same mass. In general relativity, a similar result for the space-time is stated by Birkhoff's theorem [154] in 1923. The theorem says that the space-time outside a general spherically symmetric matter distribution is given by the Schwarzschild solution. This implies that purely radial oscillations of stars do not change the exterior space-time and therefore be no source of gravitational waves.

2.2.5 Buchdahl's Theorem

A very important insight related to the question of how compact stars can be in general relativity, is provided by Buchdahl's theorem [155] from 1959. It states that for spherically symmetric stars, the maximum possible compactness allowing a static solution, is given by

$$\boxed{\frac{M}{R} = \frac{4}{9}} \quad (2.13)$$

This statement is true for any isotropic equation of states, but can be circumvented by assuming anisotropic stress. This however requires additional justification, to be considered as realistic property of neutron star matter. Note that the Buchdahl limit predicts a gap for the allowed compactness of stars and the Schwarzschild black hole, which is $M/R = 1/2$.

2.3 Alternative Compact Objects

There are many reasons why one could be interested in the question whether even more compact objects than neutron stars could exist or if black holes are the ultimate outcome. One motivation is that by going from ordinary stars to white dwarfs to neutron stars, there is a repetition in finding families of increasingly compact configurations. From nuclear fusion, to electron degeneracy pressure and the more complicated and not yet fully understood interactions in neutron stars, nature repeatedly finds different ways to form stable configurations. Since every increase in compactness introduces physics of smaller scales, it might not be surprising if history repeats itself in a yet unexplored regime. In the following we will discuss some of the models that have been proposed in the literature to describe ultra compact objects beyond neutron stars. Since the underlying physics of such objects is not as well understood as it is for neutron stars, these models have to be considered as toy models. They are justified to explore possible consequences of ultra compact objects and basic properties, but are not based on the same theoretical foundations as neutron stars. However, since most of the observational evidence can only be used to predict ultra compact objects, and thereby not uniquely features of the Kerr solution, some of the alternative models are conceptually hard to rule out. Black holes are thereby chosen by the lack of physically well motivated alternatives, which is to some extent also a personal question of style and background. For example, whether quantum mechanical effects are relevant to describe correctly the physics close to black hole horizons is an unsettled issue. With actual gravitational wave observations, these alternative models and theories can be tested in a much more significant way as before. While the direct detections so far are in agreement with black holes, some of the characteristic features like the QNM ringdown, have been poorly constrained so far. Fortunately, future observations are expected to provide more insights to actually confront exotic models with reality.

The list of models we discuss in the following are neither complete nor ordered with respect to viability. These are mainly the models that have been used in the projects carried out in this thesis, which are presented in Part II. We have chosen these models because they provide enough diversity to account for different types of ultra compact objects, but are at the same time technically tractable, which is especially important for the inverse spectrum problem. One popular model, which however is not further studied in this thesis, is the one of

boson stars. These are hypothetical objects constructed from scalar fields [156, 157, 158] and are an active field of research. For an extensive and recent review of this, and many other, ultra compact objects with respect to their observational status, we refer to [84].

2.3.1 Constant Density Stars

The simplest model of an ultra compact object is the incompressible fluid star found by Schwarzschild [159]. As the name tells, the star is assumed to be of uniform density, which is an extreme assumption for the equation of state. Besides the nice property that the TOV equations can be solved analytically, these stars can be as compact as the Buchdahl limit of $C = 4/9$. This makes them a suitable choice for analytic studies that represent an extremely stiff equation of state.

The constant density equation of state is given by

$$\rho(r) = \rho_0, \quad (2.14)$$

where ρ_0 is constant. The analytic solutions for this equation of state in the TOV equations are given by

$$m(r) = \begin{cases} \frac{4}{3}\pi\rho_0 r^3, & \text{for } r \leq R, \\ \frac{4}{3}\pi\rho_0 R^3, & \text{for } R < r, \end{cases} \quad (2.15)$$

where one defines $M \equiv m(R)$. The relation for the pressure inside the star can be integrated and yields

$$P(r) = \rho_0 \frac{(1 - 2Mr^2/R^3)^{1/2} - (1 - 2M/R)^{1/2}}{3(1 - 2M/R)^{1/2} - (1 - 2Mr^2/R^3)^{1/2}}, \quad \text{for } r \leq R. \quad (2.16)$$

The non-trivial components of the metric tensor $g_{\mu\nu}$ inside the star are given by

$$g_{00} = \frac{1}{4} \left[3 \left(1 - \frac{2M}{R} \right)^{1/2} - \left(1 - \frac{2Mr^2}{R^3} \right)^{1/2} \right]^2, \quad g_{11} = \left(1 - \frac{2Mr^2}{R^3} \right)^{-1}. \quad (2.17)$$

Since the star is spherically symmetric, Birkhoff's theorem states that the external solution is the Schwarzschild one with mass M , see Sec. 2.2.4. Note that the pressure vanishes continuously at the surface ($r = R$), while the density is of course discontinuous. Furthermore, we want to point out that the central pressure diverges in the limiting case of the Buchdahl compactness limit $M/R = 4/9$. For all less compact stars, the pressure remains finite for any finite choice of the density ρ_0 . Since constant density stars can not approach the Schwarzschild limit $M/R = 1/2$, light that is emitted from the surface has a finite redshift. Thus these stars can in principle always be distinguished from a black hole of the same mass.

2.3.2 Gravastars

Gravitational vacuum condensate stars (gravastars) have been proposed as alternatives to black holes by Mazur and Mottola [160, 161] in the early 2000s. These objects can be constructed to be as compact as Schwarzschild black holes and are therefore an interesting candidate to mimic black holes. The spherically symmetric model can be made up of different layers [162], but always features a de Sitter condensate, with $P = -\rho$, as core. The gravastar proposal features thermodynamic and quantum properties, which circumvent some of the problems related to classical black holes, such as the information loss problem. Beside thermodynamical stability, which was addressed in the original works, other types of perturbations have been investigated as well in [162, 163, 164, 165, 166]. Depending on the chosen equation of state for the shell, stable solutions were reported. Later in this thesis we will focus on the thin shell model, which matches the external Schwarzschild geometry with an internal de Sitter geometry at the surface. In order to circumvent the classical Buchdahl limit, gravastars have anisotropic pressure and are therefore quite different from normal stars [167]. The motivation of this anisotropic

features have been motivated in [168] in terms of a low energy effective field theory approach to include quantum effects.

Gravastars have an interesting connection to constant density stars, which has been pointed in [169]. The divergent pressure at the Buchdahl limit is integrable once a non-isotropic transverse stress surface tension is introduced. Going beyond the limit gives rise to negative energy density solutions which approach the original thin shell gravastar solution at the Schwarzschild compactness. The extension to slowly rotating configurations, which seem to be capable of mimicking slowly rotating black holes as well, has been reported in [170]. The non-rotating solutions are stable against radial perturbations [171] and axial non-spherical perturbations [172]. In another recent work it was argued that GW150914 did not produce a rotating gravastar [173].

2.3.3 Wormholes

Although wormholes are well known in science fiction as proposed portals to travel between distant galaxies or even different universes, they have been discussed as possible solutions of general relativity long before. Here they are a way to connect different space-times and questions regarding their formation, stability and traversability are still open problems. First works in this direction had already been done by Ludwig Flamm [174] in 1916 and Hermann Weyl [175] in 1921. Later, in 1935, Albert Einstein and Nathan Rosen published their work on the now famous Einstein-Rosen bridge [176], which is usually considered as the prototype of a wormhole. Back then, Einstein and Rosen introduced another interpretation of the Schwarzschild solution and tried to connect it with electromagnetism. However, the term wormhole was coined much later in 1957 by John A. Wheeler, in a joint work with Charles Misner [177]. The question whether wormholes could actually be traversable for light or observers was studied in 1962 by Robert W. Fuller and John A. Wheeler for the Schwarzschild solution [178], who found that the answer is no. Among the intriguing questions therefore is under what conditions traversable wormhole solutions might be possible. More work in this direction has been done by Homer G. Ellis [179] and Kirill Bronnikov [180]. Michael S. Morris, Kip S. Thorne and Ulvi Yurtsever showed that this is feasible with exotic forms of matter, violating energy conditions [181]. However, small quantities of such matter are known from quantum field theory. Despite their rather exotic nature, wormholes are among the commonly studied objects, not only in general relativity, but also in alternative theories of gravity.

Damour-Solodukhin Wormhole

The wormhole model studied in this thesis is the one proposed by Damour and Solodukhin (DS) [182]. It is an example of a Lorentzian wormhole and mimics the exterior Schwarzschild space-time arbitrarily well. Besides the mass M , it has only one additional parameter λ , which scales the deviation to the Schwarzschild black hole. Even for small values of λ , there is no event horizon, but a throat connecting two isometric, asymptotically flat regions. It is located close to where the event horizon would have been. Throughout this work we assume that λ is small, such that deviations far away are negligible. The line element is given by

$$ds^2 = - (g(r) + \lambda^2) dt^2 + \frac{dr^2}{g(r)} + r^2 (d\theta^2 + \sin^2(\theta)d\phi^2), \quad (2.18)$$

with $g(r) = 1 - 2M/r$. It will be convenient to set $r/M \rightarrow r$ and $r^*/M \rightarrow r^*$ for the later introduced tortoise coordinate. Since DS wormhole is explicitly mimicking the Schwarzschild black hole, it is of great interest in what properties it might be distinguishable. In the same work [182] it was shown that deviations for geodesic motion, as long as it does not happen close to the throat, is negligible, what can already be expected from the line element eq. (2.18).

2.3.4 Quantum Gravity Inspired Models

The previous examples of compact objects have all been discussed within general relativity, although some forms of matter are rather exotic, e.g. in the gravastar proposal in Sec. 2.3.2. While these objects can be discussed

in classical theories of gravity, there are also approaches that are more directly motivated by a quantum theory of gravity. These can be “fuzzballs”, which are supposed to describe black holes in string theory [183], but are difficult to treat in the context of this thesis. Another more recent proposal is the existence of so-called firewalls, which replaces the vicinity of a classical black hole event horizon with a region of high energy quanta [127]. It arises in the context of the information loss problem and states that certain basic principles of quantum field theory and general relativity can not all be true at the same time and predicts that black hole horizons are dramatically different from what is expected in classical general relativity.

Black Hole Area Quantization

One quantum mechanically inspired model that has been studied as one project in this thesis in Sec. 12 is black hole area quantization. It was proposed by Jacob Bekenstein and Viatcheslav F. Mukhanov in seminal works [184, 185, 186]. The basic idea is that the horizon of a black hole is not described by a smooth area A , but qualitatively speaking consists of quantized patches

$$A_n = \alpha \ell_p^2 n = 4\pi (2M)^2. \quad (2.19)$$

Here $\ell_p^2 = \hbar G/c^3$ is the Planck length and $2M$ the Schwarzschild radius. The last equality is only valid for the non-rotating Schwarzschild case, but can be generalized to include spinning black holes. The state of the black hole is labeled by n , which is an integer. α is a constant that is not known a priori and depends on the specific model of area quantization. Different proposals for α that have been made in the literature range from $4 \ln 2$ to 32π or even larger¹ [184, 185, 186, 187, 188, 189, 190]. The key implication is that inverting for the mass one finds a discrete spectrum for possible black hole masses. From this one would expect that not every incoming particle can be absorbed, but rather gives some non-zero reflectivity. This has been pointed out and connected to possible gravitational wave effects more recently [191, 192]. The generalization of this to the rotating case was one of the projects in this thesis and is discussed in Sec. 12.

2.3.5 Parametrized Space-Times

The last category of ultra compact objects we discuss in this chapter is conceptually quite different from most of the previous ones. If one is interested in extending the study of compact objects to alternative theories of gravity, one faces the problem that the underlying field equations are usually more complicated. Even constructing static or stationary background solutions might be challenging. Moreover, the equations describing perturbations of the solution in alternative theories is not always known. Even if all these things can be managed, it always depends on the gravitational theory that one has chosen, and there are many candidates.

An alternative way that avoids some of these problems, is to start from a parametrized metric, not a theory. Such a metric can have many advantages, but of course also disadvantages. If the underlying theory is not known, one is quite limited with the predictions one can actually make. However, there are a few properties that one can study for a broad range of theories directly from the metric without making very restrictive assumptions. One of them is the geodesic motion of test particles and light. While this can in principle be directly compared with actual observations, the question for the gravitational wave dynamics is conceptually more complicated. It is not surprising that an actual description of gravitational waves requires a specific choice of the field equations. Test fields on the other hand can give a qualitative behavior of what one might expect. One application of parametrized metrics is the determination of black hole shadows [193] and x-ray reflection spectroscopy [194, 195].

Choosing a parametrization for the metric does not guarantee that it really represents a viable solution of any known or unknown theory of gravity. Even if it is not an exact solution, an efficient parametrization might be very useful from a computational point of view, especially if it is justified to assume that a few parameters are sufficient to approximate an exact solution. A range of different parameterizations for non-rotating, as well as rotating, black hole solutions have already been proposed in the literature, e.g., [196, 197, 198, 199, 200]. A

¹In principle $4 \ln q$ for integer $q > 2$ is included in the literature but $q < 10$ has been the focus.

widely used approach is to introduce extra terms to the general relativity solutions, which are expected to capture possible deviations. However, without an underlying theory at hand, it is clear that not every choice for the parametrization will describe a reasonable physical solution and pathologies are possible. Caution is therefore required.

Rezzolla-Zhidenko Metric

Later in Sec. 9 we will study a parametrization of the metric as proposed by Rezzolla and Zhidenko (RZ) [198], from now on called RZ metric. In its original form it is valid for spherically symmetric black holes, but has been extended to include rotation more recently [199]. The basic properties are discussed in the following, but we refer to the original publication for all details [198].

The line element of the RZ metric is given by

$$\boxed{ds^2 = -N^2(r)dt^2 + \frac{B^2(r)}{N^2(r)}dr^2 + r^2d\Omega^2,} \quad (2.20)$$

with $d\Omega^2 = d\theta^2 + \sin^2\theta d\phi^2$. The two functions $N(r)$ and $B(r)$ describe the details of the space-time. It turns out to be useful to introduce the dimensionless variable

$$x \equiv 1 - \frac{r_0}{r}, \quad (2.21)$$

which maps the location of the event horizon r_0 to $x = 0$ and spatial infinity to $x = 1$. This coordinate and $N(x)$ are used to define another function $A(x)$

$$N^2 = xA(x), \quad (2.22)$$

which has the property $0 < A(x)$ for $0 \leq x \leq 1$. The actual parametrization appears now by introducing expansion coefficients, which determine $A(x)$ and $B(x)$. These are defined by

$$A(x) = 1 - \varepsilon(1-x) + (a_0 - \varepsilon)(1-x)^2 + \tilde{A}(x)(1-x)^3, \quad (2.23)$$

$$B(x) = 1 + b_0(1-x) + \tilde{B}(x)(1-x)^2. \quad (2.24)$$

The functions $\tilde{A}(x)$ and $\tilde{B}(x)$ should describe the metric near the horizon and at spatial infinity. In the original work [198] it is discussed how the parameterized post-Newtonian (PPN) expansion allows to constrain some of the parameters around $x \approx 1$ and relate them to the PPN parameters β, γ . It is shown that

$$\varepsilon = -\left(1 - \frac{2M}{r_0}\right), \quad a_0 = \frac{(\beta - \gamma)(1 + \varepsilon)^2}{2}, \quad b_0 = \frac{(\gamma - 1)(1 + \varepsilon)}{2}. \quad (2.25)$$

By using the experimentally constrained values for β and γ , it follows that $a_0 \sim b_0 \sim 10^{-4}$. As last step, the functions $\tilde{A}(x)$ and $\tilde{B}(x)$ are expressed with their Padé approximants as continued fractions

$$\tilde{A}(x) = \frac{a_1}{1 + \frac{a_2x}{1 + \frac{a_3x}{1 + \dots}}}, \quad \tilde{B}(x) = \frac{b_1}{1 + \frac{b_2x}{1 + \frac{b_3x}{1 + \dots}}}. \quad (2.26)$$

3 | Perturbation Theory in General Relativity

The rather complicated structure of Einstein’s theory makes it a very challenging task to study systems beyond axial symmetry or dynamical situations. However, these correspond to interesting astrophysical scenarios, like binary mergers of black holes and neutron stars or supernovae explosions. To find solutions here, one has to use numerical relativity. This field uses state of the art numerical codes to solve the full non-linear, coupled Einstein field equations, if necessary also including relativistic magnetohydrodynamics for the matter. Even using modern computers, the complicated structure of the equations require a lot of mathematical and numerical insights to be formulated in an actually stable and therefore computable way.

Besides all the great possibilities that modern numerical relativity offers, there are also some disadvantages. Understanding and applying these codes in practice requires a high degree of specialization, as it is the case for all complex codes. It also depends on the physical situation and timescales one is interested in. Simulating the whole life time of a neutron star after its formation is impossible, because simulations can in practice only run for relatively short times, due to finite computational resources and issues of numerical stability. While numerical relativity is currently the only tool to study the most violent part of a binary merger or a supernovae explosion, there are other situations which allow for different methods. In the context of the three stages of a binary merger, these are post Newtonian calculations for the inspiral part and a perturbative scheme for the last phase of the ringdown. Also, to study the stability of isolated compact objects, it can be sufficient to use perturbative techniques.

This chapter provides an introduction to some aspects of perturbation theory of compact stars and black holes in general relativity. We start with a review of important works in the literature in Sec. 3.1. For gravitational perturbations, which describe gravitational waves, we generalize the results for the Minkowski space-time discussed in Sec. 1.3 to curved, spherically symmetric space-times. This allows one to study the propagation and dynamics of weak gravitational waves around black holes, neutron stars, and other ultra compact objects. Before we discuss the more complicated case of gravitational perturbations in Sec. 3.3, we start with the simple case of a massless scalar test field in a spherically symmetric space-time in Sec. 3.2. This is a widely used approach to study the qualitative behavior of fields in a given space-time. It is especially useful for complicated space-times or theory agnostic studies, where the starting point is a metric but the underlying theory is unknown. For both types of perturbations, one encounters the general concept of QNMs, which are discussed in Sec. 3.5. Over the last years, a lot of interest in the community has been in so-called “echoes”. These are a phenomenon of the time evolution of perturbations around ultra compact objects. We outline them in Sec. 3.6.

3.1 Brief Historical Overview

The field of perturbation theory and QNMs of compact objects covers more than half a century of works. It is therefore not possible to provide a complete overview here. More details and discussions can be found in a series of review articles [58, 59, 89, 201]. In the following we provide a summary of key results, which are the most relevant in the context of this thesis.

The pioneering works that initiated the field of black hole perturbation theory go back to Regge and Wheeler in 1957 for axial perturbations [85], and Zerilli in 1970 for polar perturbations [86]. The precise meaning of axial and polar will be discussed in Sec. 3.3. These were the first works that studied metric perturbations of the Schwarzschild black hole. In the case of compact stars, it was Thorne and Campolattaro who derived the perturbation equations around non-rotating, relativistic stars in 1967 [87]. The next milestone was achieved by Teukolsky, who extended the perturbation equations to the Kerr solution in 1973 [202]. Deriving the perturbation equations is one part of the problem, but actually solving them to understand the observables is another

one. As we will see when discussing the perturbation equations, finding exact solutions in terms of simple known functions is not possible. Even when the full set of equations decouples, as in the case of black holes and approximately also for slowly rotating stars, the remaining equations are analytically complicated. Therefore a lot of work has been done to obtain approximate analytic solutions or to provide numerical methods.

In the context of black holes, seminal works were done in the 70s and 80s. Schwarzschild black hole QNMs were first computed by Vishveshwara in 1970 [203] and one year later by Press [204] by numerical time evolution of initial perturbations. QNMs have also been found in numerical calculations of particles that fall into black holes, for Schwarzschild [205] and Kerr [206, 207]. The idea to approximate the perturbation potential with a simpler analytic function was initiated by Chandrasekhar and Detweiler in 1975 for a rectangular potential barrier, who also demonstrated a numerical approach [208]. One decade later the analytic efforts were improved by using a parabolic approximation [209], the Eckart potential [210], and shortly afterwards the Pöschl-Teller potential [211, 212]. In these cases, the spectra of bound states of the inverted potentials, describing potential wells, are known and can be used in a clever way. Using coordinate and parameter transformations that switch between potential well and barrier, allow to transform the spectrum of bound states to the QNM spectrum and vice versa. In the same works, it was shown that this method also works for slowly rotating black holes. Another type of approach was carried out by Schutz and Will [213], who approximated the peak of the potential with a parabola and applied asymptotic matching. In all cases a simple analytical approximation is found, where the parameters describing the potential are related to its Taylor expansion around the maximum. In contrast to the previous approaches, the idea of Schutz and Will can be extended to higher order in WKB theory and higher order in the Taylor expansion of the potential [214, 215, 216, 217]. This approach has since been further improved [218]. The resulting WKB relation is a simple and popular tool for computing black hole QNMs in general relativity and alternative theories of gravity. Because the WKB method is approximate, and also for other technical reasons, it is not able to describe the whole QNM spectrum. An early work by Dunham on computing eigenvalues of a quantum mechanical system from 1932 [219], was rediscovered by Kokkotas in 1991 in the study of the QNMs of the Kerr black hole [220]. With this approach, one can in principle study the spectrum to all orders of the WKB expansion, but has to work with complex potentials. It also works for QNMs with large damping times. A method that is capable of providing the whole spectrum with great precision was demonstrated by Leaver in 1985 and is known as the continued fraction method [221]. Similar to earlier works for the hydrogen atom, a recurrence relation can be found, which allows for a precise numerical evaluation of the spectrum.

The situation of neutron stars is again more involved because of the presence of matter. In contrast to black holes, the full perturbative treatment of stars also requires one to study different types of matter perturbations. Since the original work of Thorne and Campolattaro [87], and further explorations by him and collaborators [222, 223, 224, 225, 226], extensive efforts have been made to describe and understand the emerging types oscillations. Some of the pioneering work here has been done by Lindblom and Detweiler [227] in 1983, and Cutler and Detweiler [228] in 1987. By studying a simplified model, new types of oscillation modes for compact stars were predicted by Kokkotas and Schutz in 1986 [229]. These space-time oscillations have been found in subsequent studies for different types of compact stars [88, 230, 231, 232, 233]. Another type of space-time modes, the w_{II} -modes, which are strongly damped low frequency modes, were found in [234]. For ultra compact systems of the kind introduced in Sec. 2.3, so-called trapped w -modes are another kind of space-time modes. They are long lived and correspond to trapped waves in the potential cavity [88, 231, 233, 235]. Back then the theoretical motivation for such systems was more of academic interest, but more recently they have received considerable attention in the study of black hole alternatives and possible quantum physics on the horizon scale, see [84] for a recent review. In order to study the excitation of these modes from astrophysical scenarios, the response of neutron stars to small perturbations introduced by test particles or ingoing radiation was first studied in [236, 237, 238]. By understanding the axial and polar oscillation modes it is possible to connect them with the unknown neutron star equation of state. The first systematic works date back to the 90s, [90, 92, 239, 240] and became important pillars of gravitational wave asteroseismology. Related works have been presented in a series of papers by Lindblom [93, 94, 95, 96, 241], who studied the inverse problem for the stellar structure of neutron stars by assuming that their masses and radii are known from observations.

Due to the technical complications of rotating neutron stars, most of the works have been for the idealized situation of spherically symmetric and non-rotating compact objects. Since this situation allows for semi-analytic treatments, they can contribute important insights to the more refined numerical approaches. This is particularly interesting for ultra compact objects of Sec. 2.3, whose underlying physics is less understood and in some cases might not even be sufficient for realistic dynamical simulations. The first works to construct rotating neutron star solutions go back to Hartle [242], and Hartle and Thorne [243]. Early works that studied r-modes, which are axial modes in rotating compact stars, had been reported by Andersson [244], and Friedman and Morsink [245] in the late 90s. There it was discussed that these modes can be unstable due to the Chandrasekhar Friedman Schutz (CFS) instability [246, 247]. Since the rotating case is not explicitly studied in this thesis, we only refer the reader to [248, 249] for comprehensive reviews.

3.2 Scalar Perturbations

Scalar test fields can be used to understand some aspects of gravitational perturbations, without working with the full set of field equations, at least to some extent. In the spherically symmetric Schwarzschild space-time, it turns out that studying scalar test fields results in an effective one-dimensional wave equation, which includes a potential term, similar to the one of axial and polar gravitational perturbations [85, 86]. While there are quantitative differences, they describe qualitatively a similar situation. Also, the boundary conditions and number of turning points are the same. In the eikonal limit (large l limit), both potentials approach each other. Although these features can in general not be expected in all alternative theories, it is still reasonable that they are present in some of them. This makes scalar test fields an interesting starting point to look for “smoking gun” effects and other qualitatively different properties of alternative black hole solutions and other space-times.

There are different ways to introduce the scalar test field to the space-time. One can start from the action and derive the equations of motion, alternatively one can start from the wave operator. In the following we demonstrate the second approach. We start with a general spherically symmetric background space-time, which can be written as

$$\bar{g}_{\mu\nu} = -A(r)dt^2 + B(r)dr^2 + r^2(d\theta^2 + \sin^2\theta d\phi^2). \quad (3.1)$$

The Klein Gordon equation describing the test scalar field ϕ in this space-time is in general given by [250]

$$\square_{\bar{g}}\phi = (-\bar{g})^{-1/2} \partial_{\mu} \left[(-\bar{g})^{1/2} \bar{g}^{\mu\nu} \partial_{\nu} \right] \phi. \quad (3.2)$$

Here \bar{g} is the determinant of $\bar{g}_{\mu\nu}$ and $\bar{g}^{\mu\nu}$ is the inverse of the metric tensor. The index of the wave operator $\square_{\bar{g}}$ indicates that it is defined in the background of the metric \bar{g} . Since we are interested in spherically symmetric space-times, eq. (3.2) can be further expanded

$$\square_{\bar{g}}\phi = (-\bar{g})^{-1/2} \left\{ \partial_0 \left[(-\bar{g})^{1/2} \bar{g}^{00} \partial_0 \right] + \partial_1 \left[(-\bar{g})^{1/2} \bar{g}^{11} \partial_1 \right] \right. \quad (3.3)$$

$$\left. + \partial_2 \left[(-\bar{g})^{1/2} \bar{g}^{22} \partial_2 \right] + \partial_3 \left[(-\bar{g})^{1/2} \bar{g}^{33} \partial_3 \right] \right\} \phi. \quad (3.4)$$

Since the background space-time is spherically symmetric, we will find that it is convenient to expand the scalar field ϕ into spherical harmonics $Y_{lm}(\theta, \phi)$

$$\phi(t, r, \theta, \phi) = \sum_{l,m} \frac{u_{lm}(t, r)}{r} Y_{lm}(\theta, \phi), \quad (3.5)$$

where the radial-time part $u_{lm}(t, r)$ remains to be determined. We proceed by focusing on the angular part of

the wave equation. Here we make use of the following relation

$$\frac{1}{\sin \theta} \partial_2 (\sin \theta \partial_2 Y_{lm}) + \frac{1}{\sin^2 \theta} \partial_3^2 Y_{lm} = -l(l+1) Y_{lm}. \quad (3.6)$$

Next we multiply the wave-equation with $Y_{l'm'}$ and integrate over the angular part using that the spherical harmonics are orthogonal

$$\int \int d\Omega Y_{lm} Y_{l'm'} = \delta_{ll'} \delta_{mm'}, \quad (3.7)$$

which simplifies the summation. It turns out that the radial part of the equations can be further simplified by introducing the so-called tortoise coordinate transformation

$$\partial_1 = \left(\frac{B}{A} \right)^{1/2} \partial_{1*}, \quad (3.8)$$

which we will see again when studying tensor perturbations. Using the expanded form of ϕ and the tortoise coordinate, we find for the radial part of the wave equation after a straight forward calculation

$$\boxed{[\partial_{1*}^2 - \partial_0^2 - V_l(r)] u_{lm}(t, r) = 0,} \quad (3.9)$$

with the effective potential $V_l(r)$

$$\boxed{V_l(r) = A \left(\frac{l(l+1)}{r^2} + \frac{1}{2Ar} \partial_1 \left(\frac{A}{B} \right) \right).} \quad (3.10)$$

After Fourier transforming u_{lm}

$$u_{lm}(t, r) = \int_{-\infty}^{+\infty} \frac{d\omega}{2\pi} \tilde{u}_{lm}(\omega, r) e^{-i\omega t}, \quad (3.11)$$

the wave equation eq. (3.9) becomes

$$[\partial_{1*}^2 + \omega^2 - V_l(r)] \tilde{u}_{lm}(\omega, r) = 0, \quad (3.12)$$

which has the same form as the time independent Schrödinger equation in one dimension with $E = \omega^2$, $\hbar^2/2m = 1$ and potential $V(x)$

$$\psi'' + [E - V(x)] \psi = 0. \quad (3.13)$$

In the special case of the Schwarzschild black hole the potential eq. (3.10) simplifies due to $A(r) = 1/B(r) = 1 - 2M/r$ and takes the simple form

$$V_l(r) = \left(1 - \frac{2M}{r} \right) \left(\frac{l(l+1)}{r^2} + \frac{2M}{r^3} \right). \quad (3.14)$$

Note that due to the tortoise coordinate transformation eq. (3.8), the potential evaluated in the tortoise coordinate r^* has a significantly more complicated form. For other space-times it can not, in general, be written explicitly in terms of the tortoise coordinate.

3.3 Metric Perturbations

3.3.1 Linearized Einstein Equations

The study of metric perturbations is technically more involved, since one has to deal with the full field equations of general relativity

$$R_{\mu\nu} - \frac{1}{2}Rg_{\mu\nu} = -\kappa T_{\mu\nu}, \quad (3.15)$$

where we have set the cosmological constant Λ to zero. Furthermore $G_{\mu\nu} \equiv R_{\mu\nu} - \frac{1}{2}Rg_{\mu\nu}$ is the Einstein tensor. Following the spirit of the analysis of flat space gravitational perturbations, as discussed in Sec. 1.3.1, we assume the actual metric $g_{\mu\nu}$ to be constructed from a background metric $\bar{g}_{\mu\nu}$ with small perturbations $h_{\mu\nu}$

$$g_{\mu\nu} = \bar{g}_{\mu\nu} + h_{\mu\nu}, \quad (3.16)$$

with $|h_{\mu\nu}| \ll 1$. Since we are interested in spherically symmetric and static space-times, the background metric $\bar{g}_{\mu\nu}$ is of the form

$$[\bar{g}_{\mu\nu}] = \text{diag}(-A(r), B(r), r^2, r^2 \sin^2 \theta). \quad (3.17)$$

With this metric at hand, one expands the Einstein tensor up to terms of order $h_{\mu\nu}$

$$G_{\mu\nu} = \bar{G}_{\mu\nu} + \delta G_{\mu\nu}. \quad (3.18)$$

To do so, one starts with the Christoffel symbol as defined in eq. (1.4) and finds

$$\Gamma^{\kappa}_{\mu\nu} = \frac{1}{2}g^{\kappa\alpha} (g_{\alpha\nu,\mu} + g_{\alpha\mu,\nu} - g_{\mu\nu,\alpha}) \approx \bar{\Gamma}^{\kappa}_{\mu\nu} + \delta\Gamma^{\kappa}_{\mu\nu}. \quad (3.19)$$

Here $\bar{\Gamma}^{\kappa}_{\mu\nu}$ is the Christoffel symbol with respect to the background space-time $\bar{g}_{\mu\nu}$ and $\delta\Gamma^{\kappa}_{\mu\nu}$ collects terms linear in $h_{\mu\nu}$. It is given by

$$\delta\Gamma^{\kappa}_{\mu\nu} = \frac{1}{2}\bar{g}^{\kappa\alpha} (h_{\alpha\nu;\mu} + h_{\alpha\mu;\nu} - h_{\mu\nu;\alpha}). \quad (3.20)$$

The semicolon represents the covariant derivative with respect to the unperturbed Christoffel symbol

$$h_{\mu\nu;\alpha} = h_{\mu\nu,\alpha} - \bar{\Gamma}^{\beta}_{\alpha\mu}h_{\beta\nu} - \bar{\Gamma}^{\gamma}_{\alpha\nu}h_{\mu\gamma}. \quad (3.21)$$

By using the linearized perturbed Christoffel symbol eq. (3.19) to compute the Riemann tensor eq. (1.5) one finds after contraction the perturbation of the Ricci tensor

$$\delta R_{\mu\nu} = \delta\Gamma^{\alpha}_{\mu\alpha;\nu} - \delta\Gamma^{\alpha}_{\mu\nu;\alpha}. \quad (3.22)$$

In vacuum it follows from the field equations that

$$\delta R_{\mu\nu} = 0, \quad (3.23)$$

while in the presence of matter, e.g., inside a neutron star, neither the energy momentum tensor nor its perturbation is zero. We discuss both cases separately and start with black holes in Sec. 3.3.2 and continue with neutron stars in Sec. 3.3.2. In general one has to include perturbations of the matter as well, which makes the full problem considerably more involved. Even in Newtonian theory, perturbations of the matter influence the gravitational potential and vice versa. A commonly used approximation here is the Cowling approximation [251], which ne-

glects the impact of the perturbed gravitational field to the matter. This idea can also be used in the relativistic equations, where it implies that perturbations of the metric are neglected [252]. Perturbed quantities of the matter are calculated with respect to the unperturbed background metric. Its counterpart is the inverse Cowling approximation [253], which neglects the influence of matter perturbations on metric perturbations. This means that perturbations of the metric are calculated with respect to the unperturbed matter. The inverse Cowling approximation has been motivated from earlier works that demonstrated that the space-time modes are weakly coupled with matter oscillations [232, 234, 254].

3.3.2 Spherical Harmonics and Parity

Since we are interested in spherically symmetric and static space-times, the perturbation equations can be further simplified by expanding $h_{\mu\nu}$ into tensor spherical harmonics. Motivated from our discussion of scalar field perturbations in Sec. 3.10, one might be tempted to expand each of the 10 independent functions of $h_{\mu\nu}$ individually in spherical harmonics Y_{lm} . However, this can not work, since tensors transform differently than scalars under rotation. For a spherically symmetric space-time, one can realize by studying rotational transformations, that the components of $h_{\mu\nu}$ transform as follows. h_{00}, h_{01} and h_{11} transform under rotations like a scalar, thus one can use ordinary spherical harmonics to decompose them. The components $(h_{02}, h_{03}), (h_{12}, h_{13}), (h_{20}, h_{30})$ and (h_{21}, h_{31}) transform like two dimensional vectors, while the four components $(h_{22}, h_{23}, h_{32}, h_{33})$ transform like a 2x2 tensor. From the explicit forms of the scalar, vector and tensor harmonics, it is useful to realize that they can be further split into two groups, depending on their behavior under parity transformations $\hat{\mathcal{P}}$

$$\theta \rightarrow \pi - \theta, \quad \phi \rightarrow \pi + \phi. \quad (3.24)$$

By explicitly inserting this into the definition of the scalar spherical harmonics Y_{lm} , it is straightforward to see that they behave like

$$\hat{\mathcal{P}}(Y_{lm}(\theta, \phi)) = (-1)^l Y_{lm}(\theta, \phi), \quad (3.25)$$

and are therefore all of the same type. However, for the vector and tensor harmonics, one finds that some of them also transform under parity transformation like $(-1)^{l+1}$. Thus it turns out one can categorize all three types of harmonics according to this behavior. The ones with $(-1)^l$ are from here on called to be of polar type and the ones with $(-1)^{l+1}$ are said to be of axial type. In the spherically symmetric case, these perturbations are decoupled and can be studied independently of each other

$$h_{\mu\nu} = h_{\mu\nu}^{\text{axial}} + h_{\mu\nu}^{\text{polar}}. \quad (3.26)$$

In the linearized theory for a spherically symmetric background metric, it is straightforward to see that eq. (3.26) together with eq. (3.20) also implies

$$\delta G_{\mu\nu} = \delta G_{\mu\nu}^{\text{axial}} + \delta G_{\mu\nu}^{\text{polar}}, \quad (3.27)$$

which simplifies the problem considerably. The explicit form of the vector and tensor harmonics can be found in the literature. We refer the reader to [250] for a comprehensive discussion and reference. In this thesis we are interested in the axial case and refer the reader interested in the corresponding discussion of polar perturbations to the same reference. Because the perturbation equations decouple, we can continue our discussion without explicitly studying the polar case.

It has been shown that the axial perturbations can be explicitly written in terms of

$$\left[h_{\mu\nu}^{\text{axial}} \right] = \begin{pmatrix} 0 & 0 & -h_0(t,r) \frac{1}{\sin(\theta)} \frac{\partial Y_{lm}}{\partial \varphi} & h_0(t,r) \sin(\theta) \frac{\partial Y_{lm}}{\partial \theta} \\ 0 & 0 & -h_1(t,r) \frac{1}{\sin(\theta)} \frac{\partial Y_{lm}}{\partial \varphi} & h_1(t,r) \sin(\theta) \frac{\partial Y_{lm}}{\partial \theta} \\ * & * & \frac{1}{2} h_2(t,r) \frac{1}{\sin(\theta)} X_{lm} & -\frac{1}{2} h_2(t,r) \sin(\theta) W_{lm} \\ * & * & * & -\frac{1}{2} h_2(t,r) \sin(\theta) X_{lm} \end{pmatrix}, \quad (3.28)$$

where the asterisks indicate the symmetry $h_{\mu\nu} = h_{\nu\mu}$ and the functions X_{lm} and W_{lm} are given by

$$X_{lm}(\theta, \varphi) = 2 \left(\frac{\partial}{\partial \theta} \frac{\partial}{\partial \varphi} Y_{lm} - \cot(\theta) \frac{\partial}{\partial \varphi} Y_{lm} \right), \quad (3.29)$$

$$W_{lm}(\theta, \varphi) = \left(\frac{\partial^2}{\partial \theta^2} Y_{lm} - \cot(\theta) \frac{\partial}{\partial \theta} Y_{lm} - \frac{1}{\sin^2(\theta)} \frac{\partial^2}{\partial \varphi^2} Y_{lm} \right). \quad (3.30)$$

One is thus left with three unknown function $h_0(t,r)$, $h_1(t,r)$ and $h_2(t,r)$ for each l and m .

As we have seen in the case of perturbations of the Minkowski space-time in Sec. 1.3.1, further simplification can be achieved by choosing a suitable gauge transformation. Under an infinitesimal coordinate transformation

$$x'^{\mu} = x^{\mu} + \eta^{\mu}, \quad (3.31)$$

the metric transforms like as follows

$$g'_{\mu\nu}(x') = g_{\mu\nu}(x) + \eta_{\mu;\nu} + \eta_{\nu;\mu} - g_{\mu\nu,\alpha} \eta^{\alpha} \quad (3.32)$$

$$= \tilde{g}(x') + h_{\mu\nu} + \eta_{\mu;\nu} + \eta_{\nu;\mu} \quad (3.33)$$

$$= \bar{g}_{\mu\nu}(x') + h'_{\mu\nu}. \quad (3.34)$$

The gauge vector η^{μ} must be chosen in such a way that the decomposition into tensor spherical harmonics and the parity properties still hold. We follow the frequently chosen Regge-Wheeler gauge. One can show that the following vector satisfies the desired conditions for axial modes

$$[\eta^{\mu}] = -\frac{1}{2} h_2(t, r) \left[0, 0, -\frac{1}{\sin(\theta)} \frac{\partial}{\partial \varphi} Y_{lm}, \sin(\theta) \frac{\partial}{\partial \theta} Y_{lm} \right]. \quad (3.35)$$

At this point one has to specify what type of spherically symmetric object one studies. We first discuss the vacuum black hole case in Sec. 3.3.2 and then continue with compact stars in Sec. 3.3.2.

Black Holes

The energy momentum tensor for black holes is vanishing for the background solution $\bar{G}_{\mu\nu} = 0$. The influence of test particles can be introduced by an energy momentum tensor, which will effectively appear as a source term to the perturbation equations. In the following we consider the source free case and refer the reader to [250] for more details.

In the absence of matter for the background, as well as for perturbations, the Einstein field equations become eq. (3.23)

$$\delta R_{\mu\nu} = \delta \Gamma^{\alpha}_{\mu\alpha;\nu} - \delta \Gamma^{\alpha}_{\mu\nu;\alpha} = 0, \quad (3.36)$$

where the perturbed Christoffel symbols are given by eq. (3.20). Using the Regge-Wheeler gauge eq. (3.35) and explicitly computing $\delta R_{\mu\nu}$ one finds three non-trivial relations. These are the $(t\phi)$, $(r\phi)$ and $(\theta\phi)$ components of the equation, which depend on two unknown functions $h_0(t,r)$ and $h_1(t,r)$. One can show that only two of the

equations are linearly independent. Combining the remaining two equations, introducing

$$Q(t,r) \equiv \frac{1}{r} A(r) h_1(t,r), \quad (3.37)$$

as well as the tortoise coordinate eq. (3.8), one finds

$$[\partial_{t_*}^2 - \partial_0^2 - V_{\text{RW}}(r)] h_1(t,r) = 0, \quad (3.38)$$

with the so-called Regge-Wheeler potential

$$V_{\text{RW}}(r^*) = \left(1 - \frac{2M}{r}\right) \left(\frac{l(l+1)}{r^2} - \frac{6M}{r^3}\right). \quad (3.39)$$

The tortoise coordinate transformation is explicitly given by

$$r^* = r + 2M \log\left(\frac{2M}{r} - 1\right), \quad (3.40)$$

and maps the external Schwarzschild space-time $r \in (2M, \infty)$ to $r^* \in (-\infty, \infty)$. The corresponding potential for polar perturbations was derived by Zerilli in 1970 [86]

$$V_{\text{polar}}(r) = \left(1 - \frac{2M}{r}\right) \frac{2\lambda^2(\lambda+1)r^3 + 6\lambda^2Mr^2 + 18\lambda M^2r + 18M^3}{r^3(\lambda r + 3M)^2}, \quad (3.41)$$

with $2\lambda = (l-1)(l+2)$.

Note that we found a very similar perturbation potential for massless scalar test fields in Sec. 3.2, given by

$$V_{\text{scalar}}(r) = \left(1 - \frac{2M}{r}\right) \left(\frac{l(l+1)}{r^2} + \frac{2M}{r^3}\right). \quad (3.42)$$

It looks very similar to the Regge-Wheeler potential eq. (3.39), besides the last term. Relative to the other contribution $l(l+1)/r^2$, the difference between these last terms is less important far away (for large r), as well as for increasing values of l . Close to the horizon $1 - 2M/r$ goes to zero, while the other terms are finite. Thus the potentials are also similar close to the horizon. Therefore one would expect the spectrum of QNMs for both types of perturbations at least to be qualitatively similar, which we follow up in Sec. 3.5.1.

Stars

In the following we extend the result found for black holes to the case of spherically symmetric stars. The key difference is to include a non-vanishing energy momentum tensor inside the object, which requires a bit more care. For a complete perturbative study one has also to include small oscillations of the star itself. The resulting equations that also take into account perturbations of the matter are considerably more involved. Fortunately, it has been shown that the axial perturbations decouple from these perturbations, unlike the polar perturbations. Their dynamics can be simplified if one chooses to work in the inverse Cowling approximation, where one neglects the matter perturbations.

The non-radial perturbation equations for spherically symmetric neutron stars were found in the series of seminal works by Thorne and collaborators [87, 222, 223, 224, 225, 226]. The axial perturbations have received renewed interest in the early mid 1990s by Chandrasekhar and Ferrari [88, 231] and Kokkotas [233]. In the aforementioned works, the potential for the axial perturbation is given by

$$V(r) = g_{00}(r) \left[\frac{l(l+1)}{r^2} + [\rho(r) - P(r)] - \frac{6m(r)}{r^3} \right], \quad (3.43)$$

Here the tortoise coordinate r^* remains in its general form

$$r^* = \int_0^r \sqrt{\frac{g_{11}(r')}{g_{00}(r')}} dr', \quad (3.44)$$

and can only be evaluated analytically in special cases. In chapter [6] a particularly simple approximation for the tortoise transformation is discussed. It allows for a much simpler analytic treatment of the wave equation. For the polytropic equations of state that have been used in one project presented in chapter 8, the TOV equations are integrated numerically to obtain the static background metric and the equations of stellar structure.

3.4 More Perturbation Potentials

While the previous section was on the derivation of the axial perturbation equations, the following one is on the different types of perturbation potentials. We explicitly discuss those that have been used in some of the projects in this thesis and provide the following list as reference for the thesis projects in Part II.

3.4.1 Ultra Compact Objects

In the following we discuss different cases for perturbations potentials of ultra compact objects.

Constant Density Stars

Found by Schwarzschild in 1916 [159], constant density stars are the prototypical toy model in the study of ultra compact relativistic objects [88, 231, 233]. The corresponding axial perturbation potential is a special case of eq. (3.43) with constant density

$$\rho = \rho_0. \quad (3.45)$$

For this choice for the equation of state, it is possible to find analytic solutions of the TOV equations for $m(r)$, $P(r)$, and $g_{00}(r)$, which are shown in Sec. 2.3.1. The axial mode potential for constant density stars is given by

$$V(r) = g_{00}(r) \left[\frac{l(l+1)}{r^2} + [\rho_0 - P(r)] - \frac{6m(r)}{r^3} \right], \quad (3.46)$$

here ρ and $P(r)$ are the density and pressure, respectively. An explicit analytic form for the tortoise transformation can be found in [255]. The appearance of a third classical turning point and the cavity is clearly visible. The discontinuity in the potential is always at the surface of star and is due to the discontinuity in the density profile. Due to Birkhoff's theorem, the external potential always coincides with the Regge-Wheeler potential eq. (3.39) with the similar mass M .

Thin Shell Gravastars

The potential for axial perturbations inside a thin shell gravastar is given by

$$V(r) = \left(1 - \frac{8\pi\rho}{3} r^2 \right) \frac{l(l+1)}{r^2}, \quad (3.47)$$

for which discussion can be found in [164]. The stability of different gravastar models against axial and other types of perturbations were studied in [163, 164, 256]. The tortoise coordinate inside the object can be found analytically and is given by

$$r^* = \sqrt{\frac{3}{8\pi\rho}} \operatorname{arctanh} \left[\left(\frac{8\pi\rho r^2}{3} \right)^{1/2} \right] + C, \quad (3.48)$$

where C is a constant of integration, when chosen by demanding that r^* continuously matches the usual exterior Schwarzschild tortoise coordinate

$$C = a + 2M \ln \left(\frac{a}{2M} - 1 \right) - \sqrt{\frac{3}{8\pi\rho}} \operatorname{arctanh} \left[\left(\frac{8\pi\rho a^2}{3} \right)^{1/2} \right], \quad (3.49)$$

with a being the Schwarzschild radius of the gravastar.

Damour-Solodukhin Wormhole

The potential of massless scalar perturbation around the DS wormhole [182] is given by

$$V(r) = \frac{l(l+1)f(r)}{r^2} + \frac{(f(r)g(r))'}{2r}, \quad (3.50)$$

with $f(r) = 1 - 2/r$ and $g(r) = 1 - 2(1 + \lambda^2)/r$, taken from [257]. In this case it is possible to find an explicit expression for the tortoise coordinate¹ x

$$x = \pm \left(\sqrt{(r-2)(r-2(1+\lambda^2))} + (2+\lambda^2) \cosh^{-1} \left[\frac{1}{\lambda^2} (r-2) - 1 \right] \right). \quad (3.51)$$

Later in this thesis we will consider the case of double barrier potentials, which appears for small values of λ . Under this circumstance one can find the following approximation

$$x \approx r + 2 \ln \left(\frac{r}{2} - 1 \right) + 2 \left(\ln \left(\frac{4}{\lambda^2} \right) - 1 \right). \quad (3.52)$$

Here one can relate the position of the throat, described by λ , with the distance L between the two maxima of the potential barriers

$$L \approx 4 \left(\ln \left(\frac{4}{\lambda^2} \right) - 1 \right), \quad (3.53)$$

Rezzolla-Zhidenko Metric

Although strictly speaking the RZ parametrization of spherically symmetric alternative black holes [198] does not directly correspond to a compact object, as the previous ones do, one can still study scalar fields, as discussed in Sec. 2.3.5. From our general approach of test scalar field perturbations in Sec. 3.2, we already know that the the perturbation potential from eq. (3.10). Here the metric functions $A(r)$ and $B(r)$ follow from the definitions provided in Sec. 2.3.5 for a given choice of the parameters.

3.5 Quasi-Normal Modes

In this section we introduce the concept of QNMs, which is one of the most important tools to probe the nature of compact objects with gravitational waves. However, let us start with a short reminder of normal modes in physical systems we are familiar with, e.g., a string of length L that is fixed at both of its ends. In an idealized situation, one can describe small oscillations $y(t,x)$ of the string from its equilibrium configuration with

$$\frac{d^2 y}{dt^2} - \frac{T}{\rho} \frac{d^2 y}{dx^2} = 0, \quad (3.54)$$

¹We here use x and not r^* to match the thesis project discussed in Sec. 7.

where ρ and T describe its density and tension, respectively. Using an expansion of the general solution into a superposition of modes for the time part, one finds

$$y(t, x) = \sum_{n=-\infty}^{\infty} c_n \exp(i\omega_n t) \Phi(x), \quad (3.55)$$

where ω_n is the normal mode spectrum and the constants c_n describe how much a given mode is excited in the solution. In order to determine a specific solution for $y(x)$, one has to provide boundary conditions, e.g. Dirichlet type [$y(t, x = 0), y(t, x = L)$] and initial conditions [$y(t = 0, x), y'(t = 0, x)$]. Here one can already identify a crucial difference between ω_n and c_n . The spectrum ω_n follows directly from the boundary conditions and is therefore independent of the initial conditions. The constants c_n are in some sense not describing a fundamental property of the system, but one of many initial configurations. To phrase it more concisely, there are many ways to excite the same system, but the set of possible modes, from which some will be excited, does not depend on this. It may happen that certain modes are not excited for some initial conditions, but it is not possible to excite modes that are not part of the spectrum. Therefore, if one is interested in studying fundamental properties of the system, e.g., the density or tension of a string, the knowledge of the mode spectrum ω_n is crucial.

Our conclusions in the simple example are only valid, because we know that the expansion into modes forms a complete set and any possible solution can be constructed from it. In contrast to any realistic system, the previous example does not take into account that internal friction, or couplings to the environment, introduce dissipative effects. The consequence is that such open systems loose energy and the modes decay in time. A pedagogical toy model that has been used to understand the QNM spectra of stars was proposed by Kokkotas in [229]. The new feature is that the spectrum of eigenvalues becomes complex, where the imaginary part is related to the damping time. In systems which are unstable, the sign of the imaginary part would be opposite and describe exponentially growing solutions.

3.5.1 Types of Quasi-Normal Modes

From the introduction to different types of perturbation potentials in Sec. 3.4, one might already expect that the corresponding spectra of QNMs can be quite diverse and feature a rich structure. This is the case and we will review the qualitative properties in the following, along with the boundary conditions.

Black Holes

According to the no-hair theorem in general relativity, astrophysical black holes are only characterized by their mass and spin. Since black holes are vacuum solutions, we have already seen in Sec. 3.3 that the perturbations equations are less involved than those of compact stars. While this general case is described by the Teukolsky equation [202], we are here particularly interested in the Schwarzschild solution. Although the analytic forms of the Regge-Wheeler potential (axial) eq. (3.39) and Zerilli potential (polar) eq. (3.41) are different, Chandrasekhar and Detweiler have proven that the corresponding QNMs are isospectral [208], which has more recently also been related to the Darboux transform [258].

The QNM boundary conditions for black holes are purely ingoing waves at the horizon ($r^* \rightarrow -\infty$, waves propagate into the black hole) and purely outgoing waves at spatial infinity ($r^* \rightarrow \infty$). These boundary conditions imply no emission from the event horizon, as well as no incoming radiation from infinity. In contrast to normal modes of mechanical systems or QNMs of compact stars, the black hole QNMs are quite different. Note that the fundamental mode is the least damped mode as one would expect, but counter-intuitively, for the first few overtones the black hole QNM frequency decreases. For all choices of l , there is one algebraic special mode with vanishing real part [259]. The higher overtones approach a constant real part and equidistant spacing for the imaginary part. Approximate relations for $n \leq l$ can be obtained by the WKB method [213, 214, 215, 216, 217, 218, 220, 260] or approximate potentials [209, 210, 211, 212]. An asymptotic relation for modes with very large imaginary parts has been reported by Nollert in [261].

Neutron Stars

From the derivation of the perturbation equations for neutron stars in Sec. 3.3 we have seen that even in the absence of rotation, oscillations of the matter couple to the polar perturbations. This introduces a technical complication for analytic studies, but is approachable with standard numerical methods as demonstrated in several works, see [58, 59] and references therein. On the other hand, we have seen that the axial perturbations are not coupled to the matter oscillations. The inverse Cowling approximation introduced in [253] neglects matter perturbations, which brings the polar perturbations to a similar form. In a more recent work it has been explicitly shown that polar perturbations decouple from the matter oscillations for high frequencies [262]. These space-time modes are clearly different from the ones of black holes. Even for the most compact stars, constant density stars approaching the Buchdahl limit, the two types of spectra do not become similar. One fundamental reason for that is that the internal boundary condition is completely different. For neutron stars one demands a regular solution at the origin ($r = 0$).

Ultra Compact Objects

The previous discussion on neutron stars in general also applies to ultra compact objects, as long as they are in general relativity. For axial and polar perturbations, similar space-time modes exist. In addition to that, there is a new family of space-time modes, which are called trapped modes or quasi-trapped modes [231, 233]. These correspond to semi-trapped states in the cavity of the potential, which can only exist in ultra compact space-times. The characteristic property of these modes are the exponentially small imaginary parts, which implies that these modes are very long lived. The real part follows a qualitatively similar spacing to the ordinary curvature w-modes. Since these modes can be thought of as modes in the cavity of the potential, there can only be a finite number of these modes. Since the potential barrier gets higher with larger values of l , the total number of trapped modes for higher values of l is larger. The imaginary part scales inversely with the height and width of the barrier, which implies that low lying modes have a considerably smaller imaginary part than the ones close to the peak of the barrier. Thus the low lying modes are the ones with the longest life-time.

Such long lived trapping of radiation can cause serious problems for rotating objects, for which the ergoregion stability becomes important and indicates that rotating ultra compact objects are not stable. For constant density stars or gravastars, the internal boundary conditions follows from regularity, but it is less clear for phenomenological proposals of firewalls. We discuss this in Sec. 13.1.2.

3.5.2 Computing Quasi-Normal Modes

Since the perturbation equations can usually not be solved analytically, a wide range of methods to obtain solutions has been developed. The results obtained in these ways are analytic and approximate or numerical and precise. In most cases, choosing a specific methods is beneficial with respect to some aspects, but will have disadvantages in others. As we will see, some methods only work for spherically symmetric cases, while others might only work for a certain part of the spectrum, and some others maybe for the whole spectrum, in principle, but have to be adapted laboriously when some property of the compact object is being changed. A quite popular and versatile approach is the Wentzel-Kramers-Brillouin (WKB) method, which we later use for the inverse spectrum problem. Therefore we devote the complete Sec. 4 to introduce and discuss these important results.

In the following we only explain those methods that are already known in the field. These are the numerical integration of the wave equation in the time domain, the numerical integration using the Wronskian method, and the higher order WKB formula for black hole QNMs. Comprehensive reviews of other methods can be found in [58, 59, 89, 201].

Integration in the Time Domain

The numerical integration of initial data $\psi(t = 0, x)$ and $\psi'(t = 0, x)$ in the time domain of eq. (3.12) has been widely applied in the literature, see [58, 59, 89, 201] and references. To extract QNMs from the time evolution,

they have to be excited first. To do so one can send in a Gaussian wavepacket from far away and read out the reflected radiation at a fixed spatial position far away. The critical aspect of this method is to extract the excited QNMs from the “observed” waveform. For black holes, there is one reflection which is typically dominated by the fundamental QNM $n = 0$ and some traces of overtones. To extract them, a superposition of exponentially decaying solutions can be fit to the signal. This typically provides good results for the fundamental mode, but fails for large overtones. In the case of ultra compact objects with a cavity in the potential, the trapped modes can be excited and leak out on a long time scale. Taking the Fourier transform of a long interval allows one to obtain the real part of the trapped modes quite precisely and with more work also the imaginary part. The method is not well suited to obtain short lived modes from a superposition of multiple modes.

Direct Integration with Wronskian

The numerical values which are used in some of the projects of this thesis have been obtained by a code that was first applied in [233] for constant density stars. It integrates the time independent Schrödinger equation numerically from the center to the surface, where it is matched with another integrated solution for the external region. The solution integrated from the center outwards has the form

$$\psi_{\text{in}} \sim r^{l+1}, \quad (3.56)$$

whose asymptotic form was reported in [216]. The outgoing solution is of the form

$$\psi_{\text{in}} \sim e^{-i\omega r^*}. \quad (3.57)$$

Next the Wronskian $W(\psi_{\text{in}}, \psi_{\text{out}})$ of the internal ψ_{in} and exterior ψ_{out} solution is computed at the surface

$$W(\psi_{\text{in}}, \psi_{\text{out}}) = \psi_{\text{in}} \frac{d\psi_{\text{out}}}{dr^*} - \psi_{\text{out}} \frac{d\psi_{\text{in}}}{dr^*}. \quad (3.58)$$

The eigenvalue ω is obtained by demanding that the Wronskian vanishes, which results in numerically finding the complex roots of the equation $W(\psi_{\text{in}}, \psi_{\text{out}}) = 0$. In the same work it was demonstrated that the method is capable of finding the standard curvature modes, as well as the long lived trapped modes for ultra compact stars [233].

Higher Order WKB Method

This method, first motivated by Schutz and Will and subsequently improved to obtain higher precision [213, 214, 215, 216, 217, 218, 220, 260], is based on the WKB method and a Taylor expansion of the potential barrier at the maximum. The WKB method is described in detail in Sec. 4, but for the present discussion can be regarded as general approximate method for some types of partial differential equations. The higher order WKB method incorporates the black hole QNM boundary conditions of purely ingoing waves at the horizon and purely outgoing waves at spatial infinity. Furthermore, it has been derived for the one-dimensional wave equation of the Schrödinger type with a potential barrier that admits two turning points². The extension of the method to rotating black holes requires more care, because the potential becomes complex, depending on which formulation one chooses. This has first been outlined in [217, 220] and demonstrated that the method can also be used to determine the fundamental QNMs of the Kerr black hole. Since we are interested in non-rotating objects, the following discussion assumes the simpler case. The popularity of the method comes from the fact that it is easy to use and provides good to excellent results for QNMs with $n \leq l$. The QNM spectrum ω_n is determined by

$$\boxed{\frac{iQ_0}{\sqrt{2Q_0''}} - \Lambda_2 - \Lambda_3 - \Lambda_4 - \Lambda_5 - \Lambda_6 = n + \frac{1}{2}}, \quad (3.59)$$

²Turning points are defined by $V(r^*) = \omega^2$ and are thus a function of ω .

with $Q(r^*) \equiv \omega_n^2 - V_l(r^*)$, which is evaluated at the maximum of potential [218]. The primes denote the derivative with respect to the tortoise coordinate, also evaluated at the maximum. Without the correction terms Λ_i , the parabolic result of Mashhoon [209]³, and Schutz and Will is recovered [213]⁴. The index of the correction terms show the order in the WKB expansion and are explicitly determined by the overtone number n , as well as derivatives of the potential with respect to the tortoise coordinate, evaluated at the maximum of potential. Because the explicit expression for the correction terms is rather long, we refer the interested reader to [218].

3.6 Gravitational Wave Echoes

The term gravitational wave echoes was coined and popularized in recent years in the context of exotic compact objects, which are speculated to show some kind of reflection of ingoing radiation close to their would be horizon [263, 264, 264]. It gained enormous attention after claims about tentative evidence for their presence in first gravitational wave detections were made [133, 134], although this is disputed [135, 136, 265] and not confirmed by the advanced LIGO and advanced Virgo collaborations. We want to use the following paragraph to point out some similarities and differences between echoes and QNMs, as well as to provide a brief historical comment.

Let us start by introducing gravitational wave echoes. Phenomenologically speaking these are repeated bursts of similar wavepackets that should be observable in ultra compact objects which admit some kind of internal reflectivity. A typical waveform that captures the relevant details is shown in Fig. 3.1. It corresponds to the expected gravitational wave signal measured by an observer far away from the source. Echoes appear in the time-evolution of Gaussian or similar wavepackets, which are localized on a scale that is as small as the size of the cavity in the potential. The size of the cavity is between the would be horizon or center of the object, and the $r \approx 3M$ potential barrier. In the case of some types of wormholes, the reflection originates from the second potential barrier on the other side. Due to the assumed internal reflection or regularity, wavepackets in the cavity bounce and are partially trapped. Whenever it scatters with the potential barrier, a part of it leaks to spatial infinity. These repeated bursts of radiation are called echoes. The time between consecutive echoes corresponds to twice the size of the cavity. Since ultra compact objects are necessary to form such a potential, they are not relevant for neutron stars or ordinary black holes (because of the ingoing boundary condition). Note that similar waveforms can also be produced by infalling test particles which excite radiation in the space-time. A Fourier transform of the waveform measured far away from the object shows the characteristic modes of the cavity with corresponding damping times. These correspond to the spectrum of trapped QNMs.

Gravitational wave echoes can thus be understood as the result of some type of initial data which is evolved by the linearized perturbation equations. As one would expect, these perturbations excite some of the QNMs of the space-time. Strictly speaking echoes are therefore not a fundamental property of the space-time, but only a consequence of special initial data in some ultra compact object space-times. Note that first discussions of this phenomenon, although not called echoes, was presented by Kokkotas in 1995 [236]. Subsequent works a few years later reported similar waveforms, while studying particle motion around ultra compact constant density stars as a possibility to excite them [237, 238]. With the growing interest in models for black hole alternatives and mimickers, such as gravastars or wormholes, similar result have been obtained in a great number of works, see [84] and references therein for the most recent overview. Similar outcomes have also been motivated by speculative new physics on the horizon scale, such as firewalls [127] or black hole area quantization [184, 185, 186].

³Using the bound states of the inverted parabolic potential.

⁴Using the parabolic barrier explicitly.

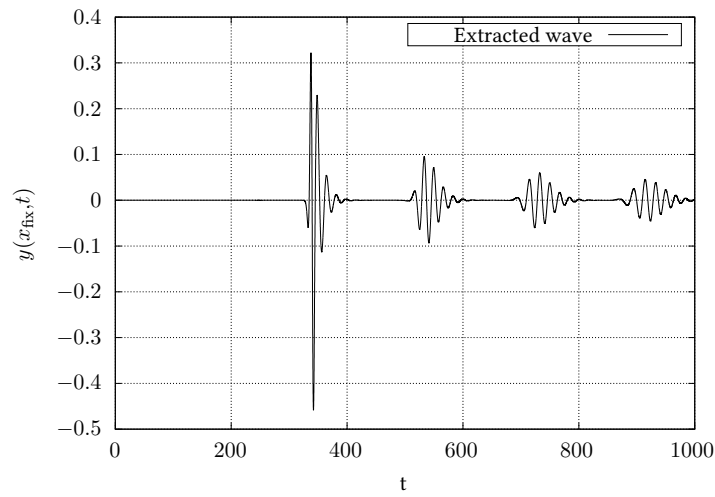


Figure 3.1: In this figure we show a qualitative example of a typical echo waveform. It has been computed by numerical integration of the wave equation with a Gaussian wavepacket as initial data. The position of the observer is at a fixed location far away from the source.

4 | The WKB Method

The WKB method or semi-classical theory, sometimes also called JWKB method or Liouville-Green method is a widely used method for finding approximate solutions to linear differential equations [266, 267, 268, 269, 270, 271, 272]. It became popular and is still widely used for the Schrödinger wave equation, but is not limited to quantum mechanics. It is suitable for linear differential equations where the highest derivative is multiplied with a small parameter. Since its early proposals, many extensions have been worked out and make it a very useful tool for analytical and semi-analytical calculations, see the textbook by Bender and Orszag [273] for a classical reference. Its main advantage is to reduce the complexity of the full differential equation to a more tractable framework of specific integral equations. Although being approximate and not always applicable, it provides great analytical power in many situations. In this thesis, such a situation is the inverse spectrum problem, which can not easily be addressed with most standard methods for the direct problem in a straight forward way. The fundamental nature of inverse problems often comes with serious technical and foundational questions whether a certain case is a well-posed problem or not. In the application and validity of the WKB method to the Schrödinger equation, one finds that different classes of potentials can be isospectral if their classical turning points fulfill certain relations [274, 275], which was also used in quantum mechanics [276, 277, 278, 279]. In the application to the direct problem of black hole QNMs, WKB theory is among the most widely used methods [213, 214, 215, 216, 217, 218, 220, 260].

This section is dedicated to a detailed introduction to the main concepts of WKB theory and shows some of the newly found results for the inverse problem that were found in this thesis. The basic derivation of the wave function in WKB theory as well as Kramer's matching relations are discussed in Sec. 4.1. With these tools in hand the classical Bohr-Sommerfeld rule as well as some of its important generalizations are then studied in Sec. 4.2. Their inversion, which is an important part of this thesis, is presented Sec. 4.3.

4.1 Basics of WKB Theory

4.1.1 Derivation of the Wave Function

The main assumption of the WKB method is that the change in the potential is small compared to the wavelength. It is therefore also called short wavelength approximation. In this work it is applied to the time independent Schrödinger equation

$$\frac{d^2}{dx^2} \Psi(x) + [E - V(x)] \Psi(x) = 0, \quad (4.1)$$

where $V(x)$ is the potential and E is the continuous or discrete energy. A standard reference for WKB theory is chapter 10 in the book of Bender and Orszag [273]. For the types of potentials studied here, another very useful reference is the textbook by Karnakov and Krainov [280], which summarizes a series of works on the application of WKB theory to examples in atomic physics. Additionally, a comprehensive list of applications of WKB theory and its related phase integral method can be found in the works of Fröman and Fröman [281]. The following introduction is closely related to the one reported in [273].

The heart of WKB theory is to make the following ansatz for the wave function

$$\Psi(x) \sim \exp\left(\frac{1}{\delta} \sum_{n=0}^{\infty} \delta^n S_n(x)\right), \quad (4.2)$$

where $S_n(x)$ is the phase, and $\delta \rightarrow 0$ is a small parameter that will become clear in a second. If the Schrödinger

equation can be written in the form

$$\varepsilon^2 \Psi''(x) = Q(x)\Psi(x), \quad Q(x) \neq 0, \quad (4.3)$$

one finds after inserting eq. (4.2) into eq. (4.3) the series

$$\varepsilon^2 \left[\frac{1}{\delta^2} \left(\sum_{n=0}^{\infty} \delta^n S'_n(x) \right)^2 + \frac{1}{\delta} \sum_{n=0}^{\infty} \delta^n S''_n(x) \right] = Q(x). \quad (4.4)$$

The next step is to set $\varepsilon = \delta$ and order terms in powers of ε . The first one is

$$S_0'^2 = Q(x), \quad (4.5)$$

and is called the eikonal equation and solved by

$$S_0(x) = \pm \int^x \sqrt{Q(x')} dx', \quad (4.6)$$

The next contribution is

$$2S_0'S_1' + S_0'' = 0, \quad (4.7)$$

and called transport equation. It is solved by

$$S_1(x) = -\frac{1}{4} \ln(Q(x)). \quad (4.8)$$

For terms with $n \geq 2$ one gets more complicated expressions

$$2S_0'S_n' + S_{n-1}'' + \sum_{j=1}^{n-1} S_j'S_{n-j}' = 0. \quad (4.9)$$

The corresponding solutions for S_n are more involved. They contain higher derivatives and combinations of $Q(x)$. Solutions for $S_n(x)$ up to order $n = 5$ are reported in Bender and Orszag. The general “standard” WKB solution is based on $S_0(x)$ and $S_1(x)$

$$\Psi(x) = c_1 Q^{-1/4}(x) \exp\left(\frac{1}{\varepsilon} \int_a^x \sqrt{Q(x')} dx'\right) + c_2 Q^{-1/4}(x) \exp\left(-\frac{1}{\varepsilon} \int_a^x \sqrt{Q(x')} dx'\right), \quad \varepsilon \rightarrow 0,$$

(4.10)

where c_1, c_2 are constants that follow from initial or boundary conditions and a is an arbitrary but fixed integration point.

4.1.2 Kramer's Matching Relations

The WKB solution derived in Sec. 4.1.1 is in general not valid in the entire region where $V(x)$ is considered. Especially at turning points, defined by $E = V(x)$, one can not use the WKB solution. The standard approach around this limitation is to split the whole domain up into different regions. Around a single turning point one finds two types of regions. The so-called classically allowed region with $E < V(x)$ and the classically forbidden region with $E > V(x)$. The name refers to the oscillatory or exponentially behavior of the wave function and has an obvious physical interpretation in quantum mechanics. In the WKB treatment of the problem, it makes sense to consider a third region, which overlaps with the other two around the turning point $E \approx V(x)$. WKB theory is not applicable in this region and one has to find the solution differently. A common approach is to solve the wave equation for the Taylor expansion of $V(x)$ around the turning point. This solution is then matched with the two

WKB solutions in the overlap interval and the boundary conditions are imposed. Due to its importance in the derivation of further WKB results in the subsequent sections, I will discuss the standard result for this approach here. The relations among the solutions that are being obtained for the linear expansion of the potential around the turning point are called Kramer's matching relations or matching conditions. The two possible cases for the one turning point problem are illustrated in Fig. 4.1. To derive the relations we first study the situation that corresponds to the right panel and then show the similar result for the other case.

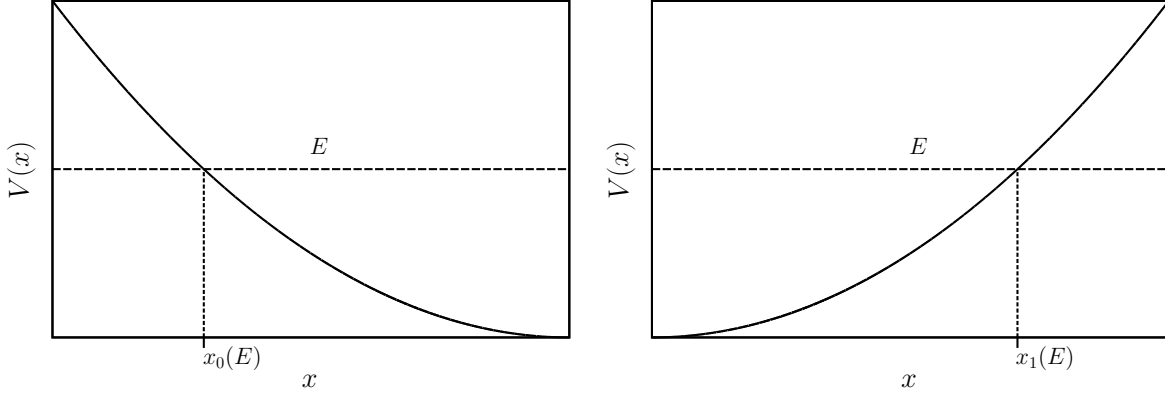


Figure 4.1: The two possible cases for the standard one turning point problem discussed in this section.

One starts with considering potentials $V(x)$ for which the linear Taylor expansion around the turning point x_1 gives a good approximation in the overlap region

$$V(x) \approx V_0 + V_1(x - x_1), \quad \text{with} \quad V_0 \equiv V(x) \Big|_{x=x_1}, \quad V_1 \equiv \frac{dV(x)}{dx} \Big|_{x=x_1}. \quad (4.11)$$

We define the classically allowed region for $x < x_1$ and label it with I, the overlap region around the turning point is labeled with II, and the classically forbidden region for $x_1 < x$ with III. Inserting eq. (4.11) in eq. (4.1) one finds

$$\frac{d^2}{dx^2} \Psi_{\text{II}}(x) - V_1(x - x_1) \Psi_{\text{II}}(x) = 0. \quad (4.12)$$

Since the allowed region exists for $x < x_1$, and the forbidden region for $x_1 < x$, it follows that $V_1 > 0$. Further note that by definition $V(x) = E$ at the turning point. The solutions of this differential equation are the Airy functions

$$\Psi_{\text{II}}(x) = A_{\text{II}} \text{Ai} \left(V_1^{1/3} (x - x_1) \right) + B_{\text{II}} \text{Bi} \left(V_1^{1/3} (x - x_1) \right), \quad (4.13)$$

with from matching and boundary conditions to be determined constants A_{II} and B_{II} . The WKB solution in the classically allowed region is

$$\Psi_{\text{I}} = \frac{A_{\text{I}}}{\sqrt{p(x)}} \exp \left(i \int_{x_1}^x p(x') dx' \right) + \frac{B_{\text{I}}}{\sqrt{p(x)}} \exp \left(-i \int_{x_1}^x p(x') dx' \right), \quad (4.14)$$

while the WKB solution in the classically forbidden region can be written as

$$\Psi_{\text{III}}(x) = \frac{A_{\text{III}}}{\sqrt{|p(x)|}} \exp \left(- \int_x^{x_1} |p(x')| dx' \right). \quad (4.15)$$

Here we already exclude the unphysical exponentially growing part of the general solution by setting the corresponding free constant B_{III} to zero. Note that the factor $1/\sqrt{p(x)}$ contains absolute value function and thus differs from the WKB solution effectively by a sign change inside $p(x) = \sqrt{E - V(x)}$. However, this sign change

can be absorbed in the constant A_{III} . With solutions in all three intervals, we are ready now for the matching procedure. We start with the overlap between region II and III. In this case the Airy functions are expanded for large positive arguments, which yields to leading order

$$\Psi_{\text{II}}(x) \approx \frac{A_{\text{II}}}{2\sqrt{\pi} \left(V_1^{1/3}(x-x_1)\right)^{1/4}} \exp\left(-\frac{2}{3} \left(V_1^{1/3}(x-x_1)\right)^{3/2}\right) \quad (4.16)$$

$$+ \frac{B_{\text{II}}}{\sqrt{\pi} \left(V_1^{1/3}(x-x_1)\right)^{1/4}} \exp\left(\frac{2}{3} \left(V_1^{1/3}(x-x_1)\right)^{3/2}\right). \quad (4.17)$$

Inserting the Taylor expansion of $V(x)$ into the WKB solution eq. (4.15) yields

$$\Psi_{\text{III}}(x) \approx \frac{A_{\text{III}}}{\left(V_1(x-x_1)\right)^{1/4}} \exp\left(-\frac{2}{3} \sqrt{V_1} (x-x_1)^{3/2}\right). \quad (4.18)$$

In the next step one compares the expanded Airy solution eq. (4.16) with the approximate WKB solution eq. (4.18) and finds

$$A_{\text{II}} = 2\sqrt{\pi} V_1^{-1/6} A_{\text{III}}, \quad \text{and} \quad B_{\text{II}} = 0. \quad (4.19)$$

A similar matching has also to be done between region I and II. Here the Airy solution are expanded for large negative argument, from which one finds

$$\Psi_{\text{II}}(x) \approx \frac{A_{\text{II}}}{\sqrt{\pi} \left(-V_1^{1/3}(x-x_1)\right)^{1/4}} \sin\left(\frac{2}{3} \left(-V_1^{1/3}(x-x_1)\right)^{3/2} + \frac{\pi}{4}\right). \quad (4.20)$$

This form has to be matched with the approximated Taylor expansion eq. (4.14), which is a sum of complex exponential functions. Instead of deriving an explicit expression for $A_{\text{I}}(B_{\text{I}})$, which will match the super-positioned sine and cosine WKB solution to the phase shifted sine solution. We follow [280] and show that A_{I} and B_{I} must be such that the approximated WKB solution takes the form

$$\Psi_{\text{I}}(x) \approx \frac{2A_{\text{III}}}{\left(-V_1(x-x_1)\right)^{1/4}} \sin\left(\frac{2}{3} \left(-V_1^{1/2}(x-x_1)\right)^{3/2} + \frac{\pi}{4}\right). \quad (4.21)$$

Using the previously found connection eq. (4.19), we find that this solution indeed matches exactly with eq. (4.20). The WKB solutions are thus given by

$$\psi_{\text{I}}(x) = A_{\text{III}} \frac{2}{\sqrt{p(x)}} \sin\left(\int_x^{x_1} p(x') dx' + \frac{\pi}{4}\right), \quad x < x_1, \quad (4.22)$$

$$\psi_{\text{III}}(x) = A_{\text{III}} \frac{1}{\sqrt{|p(x)|}} \exp\left(-\int_{x_1}^x |p(x')| dx'\right), \quad x_1 < x, \quad (4.23)$$

In this derivation we only considered the situation depicted in the right panel of Fig. 4.1. The second case that corresponds to the left panel of the same figure can be studied in a similar way. Following the same procedure yields for the WKB solutions

$$\psi_{\text{I}}(x) = B_{\text{I}} \frac{1}{\sqrt{|p(x)|}} \exp\left(-\int_x^{x_0} |p(x')| dx'\right), \quad x < x_0, \quad (4.24)$$

$$\psi_{\text{III}}(x) = B_{\text{I}} \frac{2}{\sqrt{p(x)}} \sin\left(\int_{x_0}^x p(x') dx' + \frac{\pi}{4}\right), \quad x_0 < x. \quad (4.25)$$

The solutions in eqs. (4.22), (4.23), (4.24) and (4.25) are called Kramer's matching relations or matching conditions.

They will be of crucial importance in the next Sec. 4.2, where we discuss the different types of Bohr-Sommerfeld rules and the Gamow formula. The matching conditions describe how two different types of WKB solutions are related to each other if their domain is separated with one classical turning point, where the potential can be well approximated with a linear Taylor expansion. In cases where this assumption is not valid, generalized matching conditions exist in the literature as well.

4.2 Bohr-Sommerfeld Rules

4.2.1 The Classical Bohr-Sommerfeld Rule

Among the standard problems in quantum mechanics is the time independent Schrödinger equation with a one-dimensional potential well. Despite the textbook examples of the infinite potential well or the harmonic oscillator, there is a list of well studied analytically solvable potentials that are being used to approximate different quantum mechanical systems. A similar situation emerges from the perturbation equations being studied in the context of this thesis. However, here it is technically more difficult to find exact solutions in most cases. In such situations, WKB theory can help to find approximate solutions in different ways. From the previous Sec. 4.1 it is known how the wave function $\Psi(x)$ can be written in terms of integral equations. If one is interested in the eigenvalue spectrum E_n , WKB theory can offer even more. The WKB solution for $\Psi(x)$ can be used to derive an integral equation for the spectrum E_n itself, which can be evaluated even without knowing $\Psi(x)$ explicitly. The most popular result is the so-called Bohr-Sommerfeld rule

$$\int_{x_0}^{x_1} \sqrt{E_n - V(x)} dx = \pi \left(n + \frac{1}{2} \right), \quad (4.26)$$

where (x_0, x_1) are the classical turning points and $n \in \mathbb{N}_0$. The result in eq. (4.26) is valid for potential wells $V(x)$ with two classical turning points and vanishing boundary conditions in the classically forbidden region. The situation is illustrated in Fig. 4.2. The spectrum is real valued and describes bound states. The following part shows the derivation of the classical Bohr-Sommerfeld rule eq. (4.26) and outlines the way how this result can be generalized to more involved types of potentials.

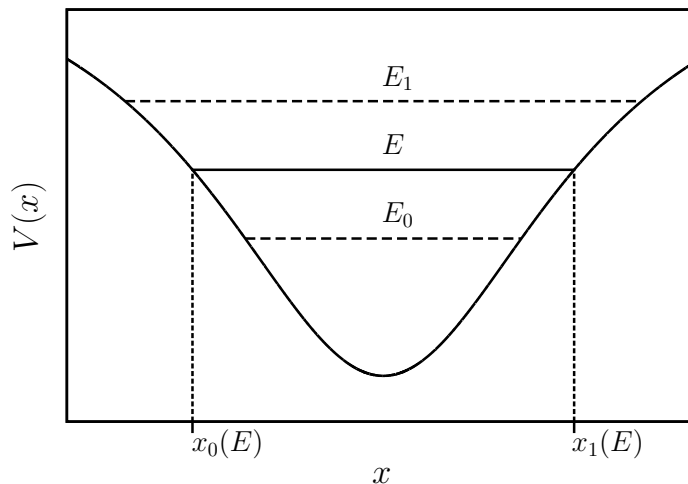


Figure 4.2: An example for a potential well $V(x)$ and the spectrum of bound states E_n . A given energy E implies two classical turning points x_0 and x_1 .

Deriving Bohr-Sommerfeld rules is in principle a straight forward approach. Depending on the type of potential, and possibly also on the range of E_n , one divides the full domain into multiple intervals. The intervals are defined based on the validity of the WKB solutions. As discussed in the previous Sec. 4.1.2 one can distinguish between classically allowed and forbidden regions, where the WKB solutions are valid. Of crucial importance

are as well the regions around the turning points, where the WKB solutions are not applicable and solutions have to be obtained in another way. The standard approach is to find solutions for the Taylor expansion of the potential, taken at each turning point. Finally, the solutions of each interval have to be matched to each other and incorporate the boundary conditions. Following this procedure then yields the equation for the eigenvalue spectrum.

With the detailed derivation of Kramer's matching relation in Sec. 4.1.2 it is fairly simple to obtain the classical Bohr-Sommerfeld rule. We split up the whole interval into 2 classically forbidden regions ($x < x_0$) and ($x_1 < x$), one classically allowed region ($x_0 < x < x_1$), and an overlap region around the two turning points (x_0, x_1). The WKB solutions in the classically forbidden region have two different constants, that will be determined by matching the two oscillatory WKB solutions in the classically allowed region. Following the explicit calculation in [280] we rewrite

$$B_{\text{I}} \frac{2}{\sqrt{p(x)}} \sin \left(\int_{x_0}^x p(x') dx' + \frac{\pi}{4} \right) = -B_{\text{I}} \frac{2}{\sqrt{p(x)}} \sin \left(\int_x^{x_1} p(x') dx' + \frac{\pi}{4} - \left[\int_{x_0}^{x_1} p(x') dx' + \frac{\pi}{2} \right] \right). \quad (4.27)$$

This looks similar to the relation for the other solution

$$A_{\text{III}} \frac{2}{\sqrt{p(x)}} \sin \left(\int_x^{x_1} p(x') dx' + \frac{\pi}{4} \right), \quad (4.28)$$

which can only coincide if the extra term in the square brackets in eq. (4.27) is equal to πk , which implies

$$\int_{x_0}^{x_1} p(x') dx' = \pi \left(k - \frac{1}{2} \right). \quad (4.29)$$

Since the integral is positive one can further restrict k , which can only be a positive integer. Thus we find

$$\int_{x_0}^{x_1} p(x') dx' = \pi \left(n + \frac{1}{2} \right), \quad (4.30)$$

with $n \in \mathbb{N}_0$. This implies for the matching of the coefficients

$$B_{\text{I}} = (-1)^n A_{\text{III}}. \quad (4.31)$$

Higher Order Correction

The classical result for the Bohr-Sommerfeld rule eq. (4.30) can be further improved by including higher order terms of the WKB method. The results, as shown in [280], has the form

$$\int_{x_0}^{x_1} \sqrt{E_n - V(x)} dx = \pi \left(n + \frac{1}{2} \right) + \frac{1}{24} \frac{\partial^2}{\partial E_n^2} \int_{x_0}^{x_1} \left(\frac{dV(x)}{dx} \right)^2 \frac{dx}{\sqrt{E_n - V(x)}}. \quad (4.32)$$

4.2.2 Quasi-Stationary States: Three Turning Points

A similar but more involved situation emerges if the potential has an additional turning point. This is the case for potentials of the type shown in Fig. 4.3. In such potentials, the spectrum is complex.

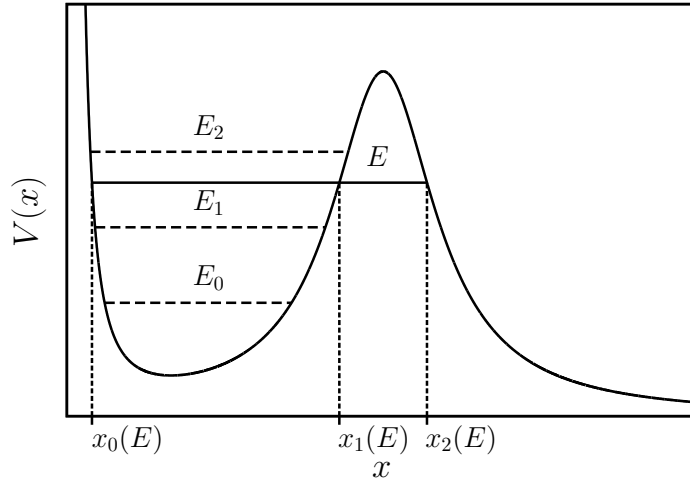


Figure 4.3: Representation of a potential $V(x)$ that has three classical turning points (x_0, x_1, x_2) and admits a spectrum of quasi-stationary states E_n .

In [282] it has been shown that quasi-stationary states located in the lower part of the potential well can be approximated with the following generalized Bohr-Sommerfeld rule

$$\int_{x_0}^{x_1} \sqrt{E_n - V(x)} dx = \pi \left(n + \frac{1}{2} \right) - \frac{i}{4} \exp \left(2i \int_{x_1}^{x_2} \sqrt{E_n - V(x)} dx \right). \quad (4.33)$$

The spectrum of quasi-stationary states E_n is complex valued. For the states in the potential barrier, the imaginary part is exponentially small. We start with splitting the complex E_n into its real part E_{0n} and imaginary part E_{1n}

$$E_n = E_{0n} + iE_{1n}, \quad \text{with} \quad |E_{1n}| \ll |E_{0n}|. \quad (4.34)$$

This property can be used to expand eq. (4.33) into two equations. After inserting eq. (4.34) in the lhs. of (4.33) one finds

$$\int_{x_0}^{x_1} \sqrt{E_{0n} + iE_{1n} - V(x)} dx \approx \int_{x_0}^{x_1} \sqrt{E_{0n} - V(x)} dx + \frac{iE_{1n}}{2} \int_{x_0}^{x_1} \frac{1}{\sqrt{E_{0n} - V(x)}} dx. \quad (4.35)$$

The same is done for the rhs.

$$\pi \left(n + \frac{1}{2} \right) - \frac{i}{4} \exp \left(2i \int_{x_1}^{x_2} \sqrt{E_{0n} + iE_{1n} - V(x)} dx \right) \quad (4.36)$$

$$\approx \pi \left(n + \frac{1}{2} \right) - \frac{i}{4} \exp \left(2i \left[\int_{x_1}^{x_2} \sqrt{E_{0n} - V(x)} dx + \frac{iE_{1n}}{2} \int_{x_1}^{x_2} \frac{1}{\sqrt{E_{0n} - V(x)}} dx \right] \right). \quad (4.37)$$

The contribution of the E_{1n} term in the exponential can be neglected, since it only adds an exponentially small correction. Ordering terms into real and imaginary part yields

$$\int_{x_0}^{x_1} \sqrt{E_{0n} - V(x)} dx = \pi \left(n + \frac{1}{2} \right), \quad (4.38)$$

and

$$E_{1n} = -\frac{1}{2} \exp \left(2i \int_{x_1}^{x_2} \sqrt{E_{0n} - V(x)} dx \right) \left(\int_{x_0}^{x_1} \frac{1}{\sqrt{E_{0n} - V(x)}} dx \right)^{-1}. \quad (4.39)$$

The reference energy for the classical turning points is only the real part E_{0n} , such that the integration remain on the real axis. Note that $\sqrt{E_{0n} - V(x)}$ is real valued between x_0 and x_1 and is imaginary valued between x_1

and x_2 .

The beautiful result of this expansion is a two step approach for the calculation of E_n . The real part E_{0n} is first determined by the classical Bohr-Sommerfeld rule eq. (4.38), while the imaginary part E_{1n} is directly connected to the Gamow formula [283] and follows from eq. (4.39) using E_{0n} .

4.2.3 One Turning Point with Discontinuity

Here we discuss the one turning point potential admitting one discontinuity as shown in Fig. 4.4. It has first been derived in the project presented in Sec. [6], from where the following derivation is taken.

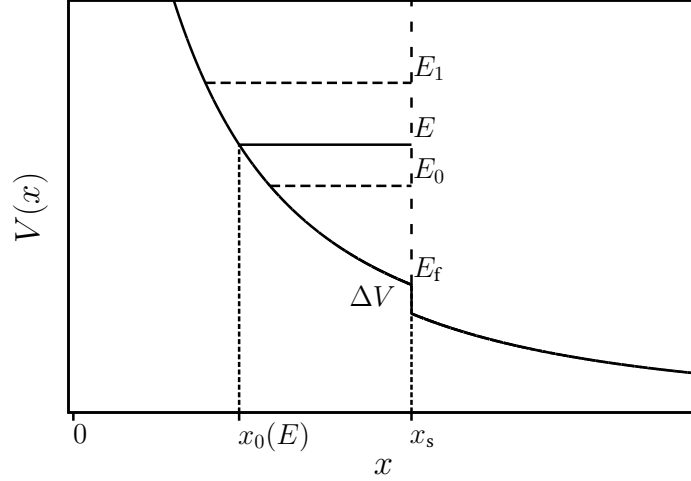


Figure 4.4: Example for a one turning point potential $V(x)$ with discontinuity ΔV . The spectrum of eigenvalues E_n that is approximated by eq. (4.52) is shown as E_n . In this approximation, the Bohr-Sommerfeld equation describes a similar situation as a potential well with the turning points x_0 and x_s .

Starting point is the time independent one-dimensional wave equation with potential $V(x)$. For some types of neutron stars one finds that the potential diverges at $x = 0$ and goes to zero for $x \rightarrow \infty$. It is further assumed that the potential admits one discontinuity at x_s , with $0 < x_s < \infty$, where the potential drops by the constant ΔV given by

$$\Delta V \equiv \lim_{x_- \rightarrow x_s} V(x) - \lim_{x_+ \rightarrow x_s} V(x). \quad (4.40)$$

Furthermore the potential is monotonically decreasing as function of x . In order to derive a new Bohr-Sommerfeld rule for this potential we start with the standard WKB solutions left and right of x_s , which can be written as

$$\Psi_1(x) = \frac{A_1}{\sqrt{p_1(x)}} \exp\left(i \int_{x_{0,1}}^x p_1(u) du\right) + \frac{B_1}{\sqrt{p_1(x)}} \exp\left(-i \int_{x_{0,1}}^x p_1(u) du\right), \quad (4.41)$$

$$\Psi_4(x) = \frac{A_4}{\sqrt{p_4(x)}} \exp\left(i \int_{x_{0,4}}^x p_4(u) du\right) + \frac{B_4}{\sqrt{p_4(x)}} \exp\left(-i \int_{x_{0,4}}^x p_4(u) du\right), \quad (4.42)$$

with

$$p_1(x) = \sqrt{E_n - V_1(x)}, \quad p_4(x) = \sqrt{E_n - V_4(x)}. \quad (4.43)$$

Here (A_1, A_4, B_1, B_4) and $(x_{0,1}, x_{0,4})$ are constants that will be determined by matching the solutions and using initial conditions. The WKB solution $\psi_1(x)$ is not valid at $E_n = V(x)$, but it can be shown by using Kramer's relations, that the WKB solution in the classically allowed region, defined by $V(x) < E_n$, can be written as

$$\Psi_1(x) = \frac{A_1}{\sqrt{p_1(x)}} \sin\left(\int_{x_{0,1}}^x p_1(u) du + \frac{\pi}{4}\right), \quad (4.44)$$

which is in agreement with a regular solution at $x = 0$. $x_{0,1}$ is the classical turning point that follows from $E_n = V(x_{0,1})$. The WKB solutions are not valid at the discontinuity itself, because the change in the potential is not small compared to the wavelength of our solution. In order to match the internal and external WKB solution, we can find exact solutions on a small interval around the discontinuity and match them with the WKB solutions. On a small interval around the discontinuity, we make a Taylor expansion of the potential. It is defined on the left and right of x_s and stop at zero order, since this is the interesting property of the discontinuity. The interval can be made arbitrarily small as long as it contains the discontinuity. In contrast to the standard matching of WKB solutions with exact solutions on some finite interval where WKB is not valid¹, the WKB solutions are valid arbitrary close to the discontinuity. By demanding the usual conditions that $\psi(x)$ and $\psi'(x)$ are continuous throughout the discontinuity x_s , one finds from the Wronskian

$$W(x) = \Psi_1(x)\Psi_2'(x) - \Psi_1'(x)\Psi_2(x) = 0, \quad (4.45)$$

now evaluated in the limit $x \rightarrow x_s$

$$\tan\left(\int_{x_{0,1}}^{x_s} \sqrt{E_n - V_1(u)} du + \frac{\pi}{4}\right) = i \frac{\sqrt{E_n - V_1(x_s)}}{\sqrt{E_n - V_4(x_s)}}, \quad (4.46)$$

where $V_1(x)$ and $V_4(x)$ are the internal and external potential, respectively. Note that derivatives of WKB solutions do not take into account the x dependency of the amplitude $1/\sqrt{p(x)}$. This would produce terms that are not valid within WKB theory, see [280] for a discussion on this circumstance. Regarding eq. (4.46) We can make two more comments. First, if the potential is smooth there are no solutions. Second, if the potential has a discontinuity there are discrete solutions, which are determined by

$$\boxed{\int_{x_{0,1}}^{x_s} \sqrt{E_n - V_1(u)} du = \pi\left(n - \frac{1}{4}\right) + i \tanh^{-1}\left(\frac{\sqrt{E_n - V_1(x_s)}}{\sqrt{E_n - V_4(x_s)}}\right)}. \quad (4.47)$$

This relation looks like a modified Bohr-Sommerfeld rule for a potential well between $(x_{0,1}, x_s)$ with an additional imaginary part described by $\tanh^{-1}(\phi)$ and $n \in \mathbb{Z}$. However, as we will argue in the subsequent section, there is a further restriction for this set that demands $n \in \mathbb{N}$.

We can further simplify our result, by assuming that E_n is either much larger than $(V_1(x), V_4(x))$ or that ΔV is small compared to E_n . Both assumptions are valid for the asymptotic behavior of the kind of spectra that we are interested in. Thus one can approximate the argument of $\tanh^{-1}(\phi)$ and find

$$\frac{\sqrt{E_n - V_1(x_s)}}{\sqrt{E_n - V_4(x_s)}} \approx 1 - \frac{1}{2} \frac{\Delta V}{E_n - V_4(x_s)}, \quad (4.48)$$

where we have used ΔV given by eq. (4.40). We can further expand $\tanh^{-1}(\phi)$ in the case of $\Delta V \ll E_n$ and obtain

$$\int_{x_{0,1}}^{x_s} \sqrt{E_n - V_1(u)} du = \pi\left(n - \frac{1}{4}\right) + i \left[\frac{1}{2} \ln\left(\frac{4(E_n - V_4(x_s))}{\Delta V}\right) - \frac{\Delta V}{8(E_n - V_4(x_s))} \right] \quad (4.49)$$

$$\approx \pi\left(n - \frac{1}{4}\right) + \frac{i}{2} \ln\left(\frac{4(E_n - V_4(x_s))}{\Delta V}\right). \quad (4.50)$$

From here we see that for high eigenvalues E_n , which correspond to large n , the rhs. of eq. (4.49) has a large real part, but the imaginary part only grows logarithmic. Thus, we expect that the complex eigenvalues for large n can be written in the form

$$E_n = E_{0n} + iE_{1n}, \quad (4.51)$$

¹Typically the WKB solution is not valid on a finite region around a turning point, where $E_n \approx V(x)$. In this case one matches the WKB solutions with an exact solution on this interval.

with $E_{1n} \ll E_{0n}$. Inserting this in the lhs. of eq. (4.49) and expanding the argument of the integral, we find two equations. The first one determines the real part E_{0n}

$$\int_{x_{0,1}}^{x_s} \sqrt{E_{0n} - V_1(u)} du = \pi \left(n - \frac{1}{4} \right), \quad (4.52)$$

while the imaginary part E_{1n} follows from the second one

$$E_{1n} = \left(\int_{x_{0,1}}^{x_s} \frac{1}{\sqrt{E_{0n} - V(u)}} du \right)^{-1} \ln \left(\frac{4(E_{0n} - V_4(x_s))}{\Delta V} \right). \quad (4.53)$$

In the last step we neglected small contributions to E_{0n} that are related to E_{1n} . Here the turning point $x_{0,1}$ is with respect to E_{0n} and real, which simplifies the otherwise complex integration. Note that the real part E_{0n} is closely related to the classical Bohr-Sommerfeld rule. For standard potential wells for which the classical Bohr-Sommerfeld rule applies, the phase is $\pi(n + 1/2)$, for $n = (0, 1, 2, \dots)$. Since the integral eq. (4.52) is greater or equal to zero, it now follows that $n \in \mathbb{N}_{>0}$. One can rewrite the phase

$$n - \frac{1}{4} \rightarrow n + \frac{3}{4}, \quad (4.54)$$

and start from $n = 0$ to match standard notation. In order to find E_{1n} , one first has to solve eq. (4.52) for E_{0n} and insert it into eq. (4.53). This is similar to the case of the Gamow formula for the transmission through a potential barrier.

4.3 Inversion of Bohr-Sommerfeld Rules

Here we discuss the inversion of the different Bohr-Sommerfeld rules and their answer for the inverse spectrum problem.

4.3.1 The Classical Bohr-Sommerfeld Rule

What happens if the standard quantum mechanics problem of finding the bound states in a given potential well is turned around? Can one find the potential well for a given spectrum of bound states? In general, this explicit example of an inverse problem, is in some sense harder to answer than the direct problem. In this section it is shown how the Bohr-Sommerfeld rule can be used to address the question. The here presented derivation is close to the one given by Wheeler [274]. In contrast to his derivation, the presentation here is a bit more explicit in the calculations for easier reading, but does not mention the connections to fractional calculus.

We start with some useful definitions. The first is the so-called inclusion

$$I(E) \equiv \int_{x_0}^{x_1} (E - V(x)) dx, \quad (4.55)$$

which corresponds to the area enclosed by the value of E and the function that describes the potential $V(x)$ between the two turning points (x_0, x_1) . The second relation is the so-called excursion, or “width²” of the potential well

$$\mathcal{L}(E) \equiv \int_{x_0}^{x_1} dx = x_1 - x_0. \quad (4.56)$$

It describes the width of the potential well as a function of energy. Its role in the inverse problem will be a crucial result of this section. Further, one can understand the classical Bohr-Sommerfeld rule as well for continuous

²In the following the term “width” is used to define the difference of the turning points. Also the notion of $\mathcal{L}(E)$ is used instead of $X(E)$, as being used in [274, 284].

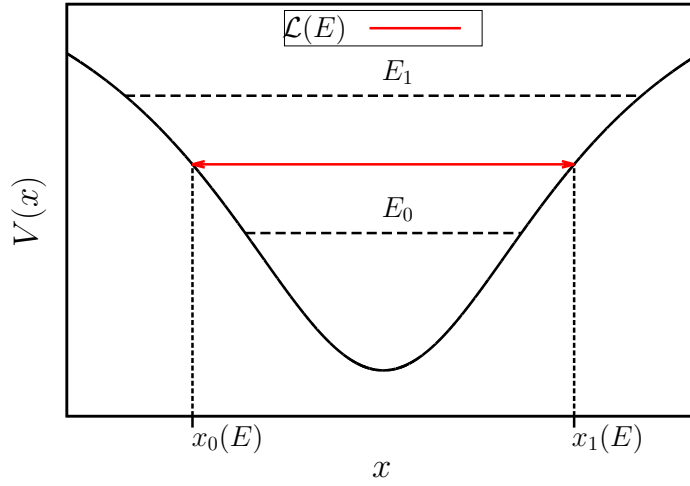


Figure 4.5: The two turning point potential $V(x)$ (black solid) and the width $\mathcal{L}_1(E)$ (red solid).

values of $n = n(E)$

$$\pi \left(n(E) + \frac{1}{2} \right) = \int_{x_0}^{x_1} \sqrt{E - V(x)} dx. \quad (4.57)$$

The spectrum of bound states E_n corresponds only to integer values of n , however in the WKB solution of the inverse problem, this “interpolation” becomes important. Note that this interpolation, if the spectrum is known as set of discrete numerical values and not as analytical function of n , is not unique. The minimum of the potential well $V(x)$, defined as E_{\min} , is interpolated from where the change in the phase is zero. This condition implies

$$n(E_{\min}) = -\frac{1}{2}. \quad (4.58)$$

The inversion of the Bohr-Sommerfeld rule eq. (4.57) works as follows. For continuous E , one multiplies both sides with $1/(E - E')^{1/2}$ and integrates over E'

$$\int_{E_{\min}}^E \frac{\pi \left(n(E) + \frac{1}{2} \right)}{\sqrt{E - E'}} dE' = \int_{E_{\min}}^E \frac{1}{\sqrt{E - E'}} \left(\int_{x_0}^{x_1} \sqrt{E - V(x)} dx \right) dE'. \quad (4.59)$$

Following Wheeler’s calculation [274], we examine the limits of integration. The x integration is between the two classical turning points (x_0, x_1) , which depend implicitly on E . This implies that we do not have any contribution in the case $E' < V(x)$, because this is outside the x integration. We can make explicit use of this observation by splitting the E' integration into two parts. The first from $(E_{\min}, V(x))$ and the second one from $(V(x), E)$

$$\int_{E_{\min}}^{V(x)} \frac{1}{\sqrt{E - E'}} \left(\int_{x_0}^{x_1} \sqrt{E - V(x)} dx \right) dE' + \int_{V(x)}^E \frac{1}{\sqrt{E - E'}} \left(\int_{x_0}^{x_1} \sqrt{E - V(x)} dx \right) dE'. \quad (4.60)$$

Since the x integration (keeping x fixed) does not contribute for $E' < V(x)$, the first part is zero. For the second part one can perform the E' integration explicitly (note that the turning points depend on E and not E') and finds

$$\int_{V(x)}^E \frac{1}{\sqrt{E - E'}} \left(\int_{x_0}^{x_1} \sqrt{E - V(x)} dx \right) dE' = \frac{\pi}{2} \int_{x_0}^{x_1} (E - V(x)) dx. \quad (4.61)$$

Here one identifies the inclusion eq. (4.55) times a numerical factor. The last step is now differentiate eq. (4.59) with respect to E and to multiply with $2/\pi$. Using eq. (4.61) for the rhs. one finds

$$\frac{d}{dE} \int_{x_0}^{x_1} (E - V(x)) dx = \left(\frac{\partial}{\partial E} + \frac{dx_0}{dE} \frac{\partial}{\partial x_0} + \frac{dx_1}{dE} \frac{\partial}{\partial x_1} \right) \int_{x_0}^{x_1} (E - V(x)) dx \quad (4.62)$$

$$= \left(\frac{\partial}{\partial E} + \frac{dx_0}{dE} \frac{\partial}{\partial x_0} + \frac{dx_1}{dE} \frac{\partial}{\partial x_1} \right) \left(E(x_1 - x_0) - \int_{x_0}^{x_1} V(x) dx \right) \quad (4.63)$$

$$= (x_1 - x_0) + E \left(-\frac{dx_0}{dE} + \frac{dx_1}{dE} \right) + \left(\frac{dx_0}{dE} V(x_0) - \frac{dx_1}{dE} V(x_1) \right) \quad (4.64)$$

$$= (x_1 - x_0) + \frac{dx_1}{dE} (E - V(x_1)) - \frac{dx_0}{dE} (E - V(x_0)) \quad (4.65)$$

$$= (x_1 - x_0). \quad (4.66)$$

Where first, the implicit dependence of the turning points on the energy was taken into account, and second, that $E - V(x_i)$ vanishes, since both terms are by definition equal at the turning points x_i . The final result for the inversion of the Bohr-Sommerfeld rule is

$$\mathcal{L}(E) = x_1 - x_0 = 2 \frac{d}{dE} \int_{E_{\min}}^E \frac{n(E) + \frac{1}{2}}{\sqrt{E - E'}} dE', \quad (4.67)$$

and calls for some comments.

In the following we will only consider potentials for which WKB theory is valid and that the result in eq. (4.67) is precise. By this we mean that the result is correct and we neglect possible deviations due to higher order corrections or possibly existing counterexamples for which WKB theory is not valid. Due to the very nature of approximate methods, this does not allow to study every possible function that one could use as a potential and might affect quantitative statements, but not their qualitative meaning. The inversion process revealed that given a spectrum of bound states E_n , it is in principle possible to reconstruct the width of the potential well $\mathcal{L}(E)$, which is the difference between the classical turning points x_0 and x_1 , but not the potential $V(x)$ itself. This means one is able to reconstruct one equation for two unknown functions. However, this is not a drawback of WKB theory, but simply one approximate way to realize that the inverse spectrum problem of bound states in a potential well is in general not unique. Different potentials can in principle admit the same spectrum. The simplest WKB answer to the inverse problem, shown in eq. (4.67), tells us that all potentials sharing the same width, admit the same spectrum. This implies that there are in general infinitely many potentials admitting the same spectrum. Constructing a family of isospectral potentials can be done by providing a valid function for one of the two turning points. A valid function is, if the resulting potential is a regular function. There are no “overhanging cliffs” in the potential well, as it was coined by Wheeler. Such so-called WKB equivalent potentials have been studied in the literature [276, 277, 278, 279].

4.3.2 The Gamow Formula

Besides the classical Bohr-Sommerfeld rule, another important and popular WKB result is the Gamow formula [283]. It has been used to describe tunneling problems in quantum mechanics, such as radio active decay involving alpha particles. The formula can be used to calculate the transmission probability of a wave through a potential barrier as function of energy. It can be derived with WKB theory and extended to higher orders for higher precision. Potential barriers in the context of this work appear for non-rotating or slowly rotating black holes, as well as for ultra compact stars and different exotic compact objects. In the first case one finds a two turning point potential barrier, while the second one is a combination of potential well and barrier(s) and yields quasi-stationary states. This case is discussed in a separate part.

The WKB description for the transmission for energies well below the barrier maximum is

$$T(E) = \exp \left(2i \int_{x_0}^{x_1} \sqrt{E - V(x)} dx \right). \quad (4.68)$$

Between the turning points we have $E < V(x)$, so the final result is real. In the literature it is known how the Gamow formula can be inverted to address the inverse problem where the transmission is being provided and one wants to find the potential [275, 285, 286]. This situation is addressed in this thesis in the case of Hawking

radiation in Sec. 11. The energy emission spectrum is related with a weighted sum over the classical transmission and reflection coefficients. It is shown how the individual transmissions can be reconstructed from the spectrum and in a second step, how these transmission can be used to address the inverse problem. Besides this, the Gamow formula is important for quasi-stationary states, which are treated here for different ultra compact stars and exotic compact objects.

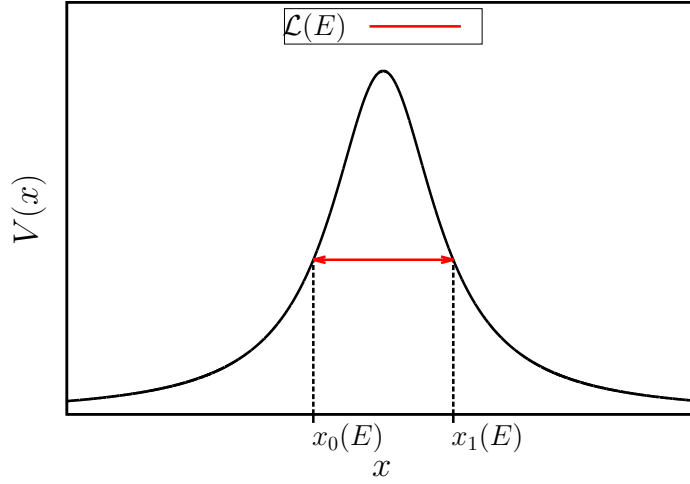


Figure 4.6: The two turning point potential $V(x)$ (black solid) and the width $\mathcal{L}_1(E)$ (red solid).

The inversion of the Gamow formula is discussed in the following. Here we follow the derivation reported in [286] but show a few more intermediate steps for easier reading and circumvent a discussion on Laplace transforms and Abel's equation that can be used here as well. We start with studying the total derivative of $T(E)$ with respect to E . Using eq. (4.68) and absorbing the imaginary unit by changing the position of E and $V(x)$ we arrive at

$$\frac{dT(E)}{dE} = \left(\frac{\partial}{\partial E} + \frac{dx_0}{dE} \frac{\partial}{\partial x_0} + \frac{dx_1}{dE} \frac{\partial}{\partial x_1} \right) \exp \left(-2 \int_{x_0}^{x_1} \sqrt{V(x) - E} dx \right) \quad (4.69)$$

$$= \left[\int_{x_0}^{x_1} \frac{1}{\sqrt{V(x) - E}} dx - \frac{dx_0}{dE} \sqrt{V(x_0) - E} + \frac{dx_1}{dE} \sqrt{V(x_1) - E} \right] \times \exp \left(-2 \int_{x_0}^{x_1} \sqrt{V(x) - E} dx \right) \quad (4.70)$$

$$= \left[\int_{x_0}^{x_1} \frac{1}{\sqrt{V(x) - E}} dx \right] \exp \left(-2 \int_{x_0}^{x_1} \sqrt{V(x) - E} dx \right). \quad (4.71)$$

Similar to the Bohr-Sommerfeld case we used that the terms with $E - V(x_i)$ vanish. Dividing with $T(E)$ we arrive at

$$\frac{1}{T(E)} \frac{dT(E)}{dE} = \int_{x_0}^{x_1} \frac{1}{\sqrt{V(x) - E}} dx. \quad (4.72)$$

Next we replace $E \rightarrow E'$, multiply with $1/\sqrt{E' - E}$ and integrate over E'

$$\int_E^{E_{\max}} \frac{1}{\sqrt{E' - E}} \left(\frac{1}{T(E')} \frac{dT(E')}{dE'} \right) dE' = \int_E^{E_{\max}} \frac{1}{\sqrt{E' - E}} \left(\int_{x_0}^{x_1} \frac{1}{\sqrt{V(x) - E'}} dx \right) dE'. \quad (4.73)$$

Here E_{\max} is the maximum of the barrier. Similar to the Bohr-Sommerfeld case it has to be interpolated. If eq. (4.68) is used it follows from

$$T(E_{\max}) = 1, \quad (4.74)$$

while it is $1/2$ if the more precise WKB formula is used. Note that $E < E_{\max}$ for the limits of integration. As in the Bohr-Sommerfeld case, we can split up the E' integration into the intervals with $E' < V(x)$ and $V(x) \leq E'$. We find that there is no contribution for $V(x) < E'$ and obtain

$$\int_E^{V(x)} \frac{1}{\sqrt{E' - E}} \left(\int_{x_0}^{x_1} \frac{1}{\sqrt{V(x) - E'}} dx \right) dE' = \pi \int_{x_0}^{x_1} dx = \pi(x_1 - x_0). \quad (4.75)$$

Combining eqs. (4.73) and (4.75) the solution of the inverse transmission problem is

$$\mathcal{L}(E) = x_1 - x_0 = \frac{1}{\pi} \int_E^{E_{\max}} \frac{(dT(E')/dE')}{T(E')\sqrt{E' - E}} dE'. \quad (4.76)$$

It is interesting that the answer to the uniqueness question of the solution is rather similar to the Bohr-Sommerfeld case. A given transmission $T(E)$ is not enough to uniquely reconstruct the potential barrier. Instead, one finds that potentials with the same width, the separation of the classical turning points, admit the same transmission. In general, one can only find a unique answer if one of the two classical turning point is provided.

4.3.3 Generalized Bohr-Sommerfeld Rules

The generalized Bohr-Sommerfeld rules for quasi-stationary states are more involved in the inversion process. However, as long as one considers energies below the barrier maximum, one can find an approximate answer which consists of a combination of the classical Bohr-Sommerfeld rule and the Gamow formula. In those three or four turning point potentials, one finds a similar answer for the uniqueness of the reconstruction.

One Turning Point with Discontinuity

The inversion of the one turning point potential with discontinuity is trivial in case one considers the real part only and makes use of the results that were derived for the classical Bohr-Sommerfeld rule. For the real part E_{0n} , this Bohr-Sommerfeld rule is given by

$$\int_{x_{0,1}}^{x_s} \sqrt{E_{0n} - V_1(u)} du = \pi \left(n + \frac{3}{4} \right). \quad (4.77)$$

The only difference is in the phase $3/4$ instead of $1/2$. However, this did not play any non-trivial role in the inversion process. In this case one can reconstruct the width

$$\mathcal{L}(E) = x_s - x_{1,0} = 2 \frac{d}{dE} \int_{E_f}^E \frac{n(E') + \frac{3}{4}}{\sqrt{E' - E}} dE', \quad (4.78)$$

where E refers to the real part only and E_f is the value of the potential on the left side of the discontinuity. If not provided, it can be extrapolated from there $n(E) = -3/4$. Note that in contrast to the classical Bohr-Sommerfeld rule, this generalized rule is more approximate and should not be trusted as much for small E_{0n} , since it was assumed that the imaginary part is negligible. Its actual precision in the application to some neutron star models has been studied as one project of this thesis in 8.

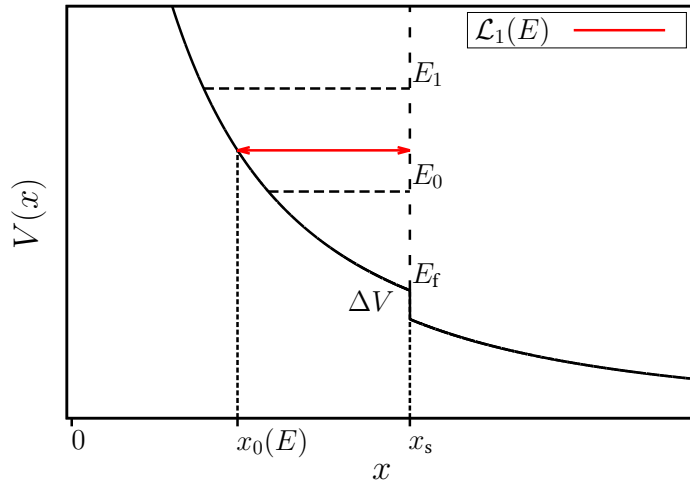


Figure 4.7: The one turning point potential $V(x)$ (black solid) and the width $\mathcal{L}_1(E)$ (red solid).

Three Turning Points

The expansion of the generalized Bohr-Sommerfeld rule eq. (4.33) into the classical Bohr-Sommerfeld rule eq. (4.38) and the Gamow formula (4.39) are the starting point for the inversion, which follows multiple steps.

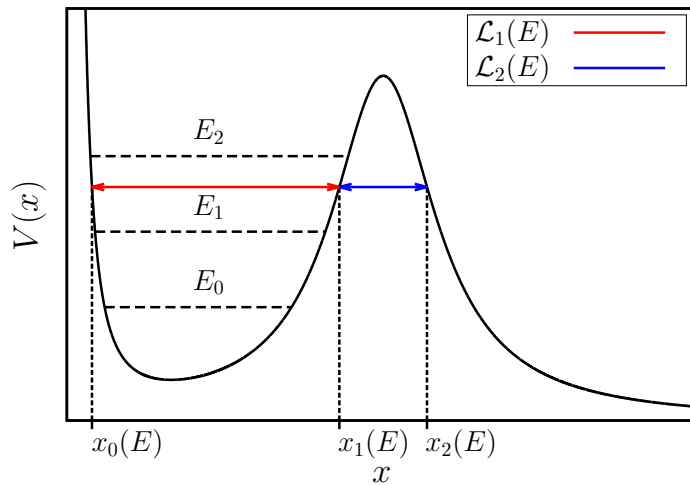


Figure 4.8: The three turning point potential $V(x)$ (black solid), the width $\mathcal{L}_1(E)$ (red solid), and the width $\mathcal{L}_2(E)$ (blue solid).

Assuming the complex spectrum of quasi-stationary states is being provided, one can invert the real part to get $n(E_{0n})$ and use the result eq. (4.67) for the classical Bohr-Sommerfeld rule. From this one knows the width of the potential well $\mathcal{L}_1(E)$.

The next step includes the imaginary part of the spectrum, which can be related to the transmission. This identification can be done by combining eq. (4.39) with eq. (4.68). From this one finds

$$T(E_{0n}) = -2E_{1n} \int_{x_0}^{x_1} \frac{1}{\sqrt{E_{0n} - V(x)}} dx, \quad (4.79)$$

which shows that the imaginary part E_{1n} can be related with T , but also depends on a second term. There the integration is carried out between the turning points that describe the unknown potential well $V(x)$. How should one proceed? Fortunately, it can be shown that the knowledge of $\mathcal{L}_1(E)$, which does not describe a unique $V(x)$ but in general infinitely many potentials, is enough, to obtain a unique result for the integral. This has been shown in the project presented in 6. The following calculation can be found in the appendix of the related publication

[2].

For all potentials being described with $\mathcal{L}_1(E)$, the classical Bohr-Sommerfeld rule has to give the same result, because $\mathcal{L}_1(E)$ had been constructed from it. In order to show that the integral is the same for all width equivalent potentials, we can choose the symmetric potential $V_S(x)$ and a second arbitrary $\bar{V}(x)$. Both are constructed from $\mathcal{L}_1(E)$ and fulfill the Bohr-Sommerfeld rule. We write the turning points as (x_{0S}, x_{1S}) for the symmetric potential and (\bar{x}_0, \bar{x}_1) for the arbitrary potential. Now we take the derivative of the continuous Bohr-Sommerfeld rule with respect to E . Using that each turning point implicitly depends on E as well, it follows that

$$\frac{d}{dE} \int_{x_0}^{x_1} \sqrt{E - V(x)} dx = \left(\frac{\partial}{\partial E} + \frac{dx_0}{dE} \frac{\partial}{\partial x_0} + \frac{dx_1}{dE} \frac{\partial}{\partial x_1} \right) \int_{x_0}^{x_1} \sqrt{E - V(x)} dx \quad (4.80)$$

$$= \frac{1}{2} \int_{x_0}^{x_1} \frac{1}{\sqrt{E - V(x)}} dx - \frac{dx_0}{dE} \sqrt{E - V(x_0)} + \frac{dx_1}{dE} \sqrt{E - V(x_1)} \quad (4.81)$$

$$= \frac{1}{2} \int_{x_0}^{x_1} \frac{1}{\sqrt{E - V(x)}} dx, \quad (4.82)$$

where we used $E - V(x_i) = 0$. It now follows that all potentials which have the same spectrum $n(E)$ and yield the same Bohr-Sommerfeld rule (4.57), will satisfy (4.82). The same calculation holds for $\bar{V}(x)$, thus we find

$$\int_{x_{0S}}^{x_{1S}} \frac{1}{\sqrt{E_n - V_S(x)}} dx = \int_{\bar{x}_0}^{\bar{x}_1} \frac{1}{\sqrt{E_n - \bar{V}(x)}} dx. \quad (4.83)$$

This proves that eq. (4.79) is the same for all width equivalent potentials. For actual calculations one can therefore choose a rather simple one, like the symmetric potential. Note that all steps assume that WKB theory is valid and that the interpolation to obtain the continuous $n(E)$ from E_{0n} already leaves room for small deviations in the potential. This underlines the circumstance that the integral character of WKB theory is not suitable to investigate small and local deviations in potentials, which happen to be smoothed via integration. The remaining width $\mathcal{L}_2(E)$ follows from using eq. (4.79) for the transmission $T(E)$ in eq. (4.76).

Symmetric Four Turning Points

The increasing number of turning points makes the explicit derivation of generalized Bohr-Sommerfeld rules more complicated. In this thesis there is a particular interest for four turning point potentials, which consist of two symmetric potential barriers. We show one of such potentials in Fig. 4.9.

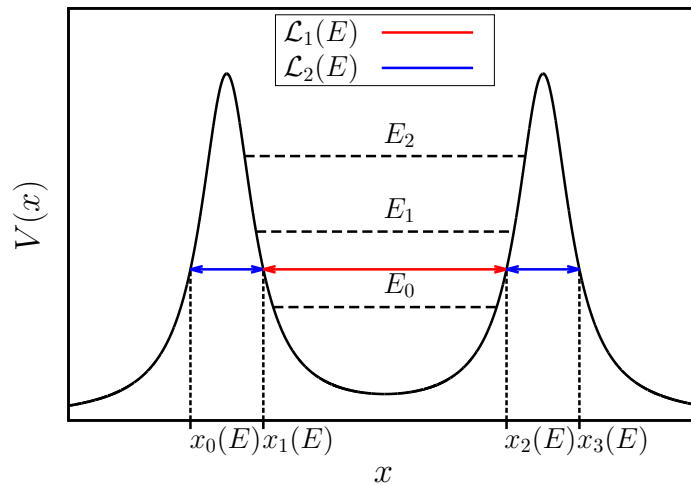


Figure 4.9: The four turning point potential $V(x)$ (black solid) and the width $\mathcal{L}_1(E)$ (red solid), and the widths $\mathcal{L}_2(E)$ (blue solid).

An alternative derivation of the generalized Bohr-Sommerfeld rule eq. (4.33) discussed in [280] shows that

for low lying quasi-stationary states, it is again possible to use the classical Bohr-Sommerfeld rule to determine the real part E_{0n} . The difference is that the transmission through the barrier can happen on both sides. One finds for the imaginary part

$$E_{1n} = -\frac{1}{2} [T_1(E_{0n}) + T_2(E_{0n})] \left(\int_{x_1}^{x_2} \frac{1}{\sqrt{E_{0n} - V(x)}} dx \right)^{-1}, \quad (4.84)$$

where (x_0, x_1, x_2, x_3) are the four classical turning points for the quasi-stationary case and $T_i(E)$ are the semi-classical descriptions for the transmission through the potential barriers

$$T_1(E_{0n}) = \exp\left(2i \int_{x_0}^{x_1} \sqrt{E_{0n} - V(x)} dx\right), \quad T_2(E_{0n}) = \exp\left(2i \int_{x_2}^{x_3} \sqrt{E_{0n} - V(x)} dx\right). \quad (4.85)$$

In the case of potentials that are symmetric around their minimum

$$V(x - x_{\min}) = V(-(x - x_{\min})), \quad (4.86)$$

the two integrals are identical and one finds an imaginary part that is two times larger than in the case with only one potential barrier

$$E_{1n} = -\left(\int_{x_1}^{x_2} \frac{1}{\sqrt{E_{0n} - V(x)}} dx \right)^{-1} \exp\left(2i \int_{x_0}^{x_1} \sqrt{E_{0n} - V(x)} dx\right). \quad (4.87)$$

The unknown integral between x_1 and x_2 can be calculated from the symmetric potential that can be constructed from $\mathcal{L}_1(E)$. Using the same inversion approach as in the case of the Gamow formula one finds the width of each potential barriers to be

$$\mathcal{L}_2(E) = x_1(E) - x_0(E) = \frac{1}{\pi} \int_E^{E_{\max}} \frac{(dT(E')/dE')}{T(E')\sqrt{E' - E}} dE', \quad (4.88)$$

where E_{\max} is the maximum of the potential barrier. The transmission $T(E)$ is obtained by combining eq. (4.85) with eq. (4.87). With the reconstruction of \mathcal{L}_1 and \mathcal{L}_2 one has two equations for four turning points (x_0, x_1, x_2, x_3) . However, in the case of a symmetric potential there is only one unique potential³. The turning points as function of the width are obtained via

$$x_0(E) = -\frac{\mathcal{L}_1(E)}{2} - \mathcal{L}_2(E), \quad x_1(E) = -\frac{\mathcal{L}_1(E)}{2}, \quad x_2(E) = -x_1(E), \quad x_3(E) = -x_0(E). \quad (4.89)$$

The reconstructed potential is found by inverting the turning points $x_i(E)$ for E , which might has to be done numerically.

4.3.4 Uniqueness of the Inverse Problem

The previous section revealed that the answer to the inverse spectrum or transmission problem in the standard WKB treatment is in general not unique. Even beyond WKB theory, this circumstance is well known and not a specific drawback of the underlying method. It is simply the fact that the input information does in general not correspond to only one potential. The more specific and approximate answer in WKB theory is that potentials fulfilling certain relations for the turning points are isospectral. The simple geometrical meaning, for the types of potentials being discussed in this thesis, is that the width of their potential well or potential barrier the same. This means potentials that are being “shifted” or “tilted” in this way still admit the same spectrum. Of course this finding does depend on the validity of WKB theory and is in general not exact, but can be of good value in

³Of course this potential can be shifted along the x -axis without changing the spectrum. But, this transformation is quite trivial and obvious.

practical calculations.

In order to obtain unique reconstructions, additional information about the potential is needed. In the case of the applications discussed in this thesis, one might be able to provide one of the turning points. One example is the use of Birkhoff's theorem that can provide the potential outside the compact object and thus constraints some of the turning points.

4.4 Some Examples

In the following we discuss some examples for the application of the inverse spectrum method to a few chosen spectra. These examples are taken from "*Inverse spectrum problem for quasi-stationary states*" by Sebastian H. Völkel, J. Phys. Commun. 2 025029, 2018, [4]. In this work the inverse spectrum method for three turning point potentials was applied to analytic spectra for the first time.

In the following we study analytic examples for the reconstruction of potentials by starting from a given function for the spectrum and analyze whether it leads to valid solutions for the potential or not. The first example is discussed in detail to demonstrate each step of the method. The subsequent examples follow the same procedure, thus only the results are summarized and discussed.

4.4.1 Spectrum I

To demonstrate the method we start with an analytic function for the spectrum given by

$$E_n = a \left(n + \frac{1}{2} \right) - ib \exp \left(-\frac{c}{n + 1/2} \right), \quad (4.90)$$

where (a, b, c) are three parameters that will be discussed later. We assume that eq. (4.90) describes a possible spectrum for quasi-stationary states, at least for $E_{0n} \in [E_{\min}, E_{\max}]$. It is not known to us as an exact solution for the spectrum of any potential. The inverse method allows now to find approximatively the corresponding potential. The real part of eq. (4.90) is described by the well known harmonic oscillator spectrum, while the imaginary part is exponentially small. Such a behavior can be expected for quasi-stationary states with $E_{0n} \in [E_{\min}, E_{\max}]$. Now we want to construct the widths $\mathcal{L}_1(E)$ and $\mathcal{L}_2(E)$. Afterwards we discuss the possible potentials that can be constructed from this knowledge.

First we calculate $\mathcal{L}_1(E)$. For this one needs to invert the real part of the spectrum

$$n(E) = \frac{E}{a} - \frac{1}{2}. \quad (4.91)$$

The minimum of the potential is extrapolated from $n(E_{\min}) + 1/2 = 0$ to be $E_{\min} = 0$. From this we can compute $\mathcal{L}_1(E)$ by using eq. (4.67)

$$\mathcal{L}_1(E) = 2 \frac{\partial}{\partial E} \int_{E_{\min}}^E \frac{n(E') + 1/2}{\sqrt{E - E'}} dE' = \frac{4}{a} \sqrt{E}. \quad (4.92)$$

In order to calculate \mathcal{L}_2 in the next step, one has to know the potential between (x_0, x_1) . As shown in Sec. 4.3.3, we can use any of the valid potentials constructed by \mathcal{L}_1 without loss of generality. Let us take the symmetric potential $V_s(x)$ with $x_{\min} = 0$ by inverting the left and right symmetric turning points

$$x_{s0}(E) \equiv -\frac{\mathcal{L}_1(E)}{2}, \quad x_{s1}(E) \equiv \frac{\mathcal{L}_1(E)}{2}, \quad (4.93)$$

from which we get

$$V_s(x) = \frac{a^2}{4} x^2. \quad (4.94)$$

This recovers, as might be expected from the form of the spectrum, the harmonic oscillator potential. Furthermore, it is worth to mention that this is only one specific solution for the potential well region. There are infinitely many other shifted or tilted potentials sharing the same $\mathcal{L}_1(E)$ and therefore the same spectrum, e.g., see [276, 277, 278, 279] for a discussion of so-called WKB equivalent potentials.

In the next step we calculate $\mathcal{L}_2(E)$, for which the following integral is needed

$$\int_{x_{s0}(E)}^{x_{s1}(E)} \frac{1}{\sqrt{E - V_s(x)}} dx = \frac{2}{a} \int_{-1}^{+1} \frac{1}{\sqrt{1 - u^2}} du = \frac{2\pi}{a}. \quad (4.95)$$

Now we can relate the transmission $T(E)$ with the imaginary part E_{1n} of the spectrum by using eqs. (4.79), (4.91) and (4.95)

$$T(E) = -2E_{1n} \int_{x_{s0}(E)}^{x_{s1}(E)} \frac{1}{\sqrt{E - V_s(x)}} dx = -\frac{4\pi}{a} E_{1n} = \frac{4\pi b}{a} \exp\left(-\frac{c}{n(E) + 1/2}\right) = \frac{4\pi b}{a} \exp\left(-\frac{ac}{E}\right). \quad (4.96)$$

Using this result for the transmission in eq. (4.88) we can finally calculate $\mathcal{L}_2(E)$

$$\mathcal{L}_2(E) = \frac{1}{\pi} \int_E^{E_{\max}} \frac{(dT(E')/dE')}{T(E')\sqrt{E' - E}} dE' \quad (4.97)$$

$$= \frac{ac}{\pi E_{\max} E^{3/2}} \left(\sqrt{E_{\max} - E} \sqrt{E} + E_{\max} \tan^{-1} \left(\frac{\sqrt{E_{\max} - E}}{\sqrt{E}} \right) \right). \quad (4.98)$$

The only unknown left is E_{\max} . It follows from $T(E_{\max}) = 1$ and takes the simple form

$$E_{\max} = \frac{ac}{\ln(4\pi b/a)}, \quad (4.99)$$

where we have used eq. (4.96). The parameters are not independent from each other, if they describe a spectrum related to our type of potentials. A necessary condition for them to be a valid solution is that E_{\max} has to be larger than E_{\min} . From this one finds (for positive c)

$$a < 4\pi b. \quad (4.100)$$

The number of states between E_{\min} and E_{\max} can be approximated from

$$n(E_{\max}) = \frac{c}{\ln(4\pi b/a)} - \frac{1}{2}. \quad (4.101)$$

We show \mathcal{L}_2 for different parameters in Fig. 4.10. It is interesting to see that different values of b have only little impact on \mathcal{L}_2 for small values of E , but become important when E approaches E_{\max} . Changing the parameter c strongly influences \mathcal{L}_2 for all values of E . The way how E_{\max} depends on (a, b, c) can be seen directly from eq. (4.99) and defines the intersection of $\mathcal{L}_2 = 0$ with the E -axis.

After reconstructing \mathcal{L}_1 and \mathcal{L}_2 we are left with choosing one of the three turning points in order to have a unique potential. To avoid any “overhanging cliffs” in the potential, \mathcal{L}_1 and \mathcal{L}_2 , as well as the turning points $(x_0(E), x_1(E), x_2(E))$, have to be strictly monotonically increasing/decreasing functions of E . This has to be taken into account when choosing one of the three turning points to obtain a specific potential.

To study a wide, but not complete, range of potentials $V_\chi(x)$, we can parameterize the relation between $(x_0(E), x_1(E))$ and \mathcal{L}_1 in the following way

$$x_0(E) = -\chi \mathcal{L}_1(E), \quad x_1(E) = (1 - \chi) \mathcal{L}_1(E), \quad (4.102)$$

with $\chi \in [0, 1]$ describing in a simple way how much the potential well is “tilted”. The symmetric potential is recovered for $\chi = 0.5$. For all values of χ it describes a piecewise potential made of two in general different parabolas. Other parameterizations that result in more complicated shapes of the potential, e.g. around the

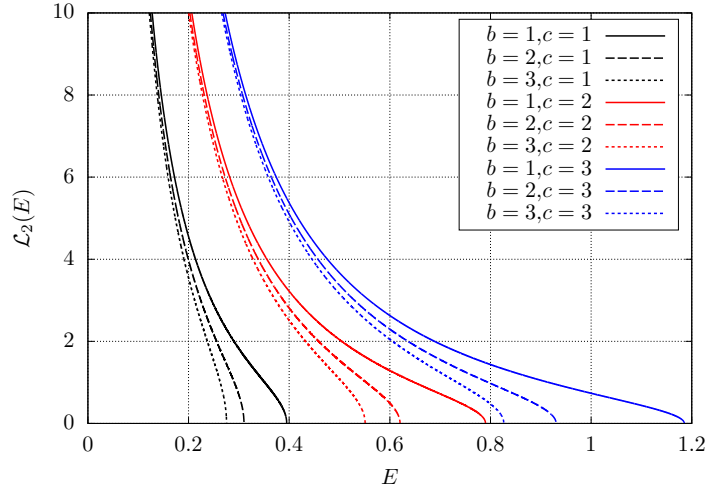


Figure 4.10: The width of the potential barrier $\mathcal{L}_2(E)$ for spectrum I shown in eq. (4.90) for different values of (b,c) and $a = 1$. Figure taken from [4].

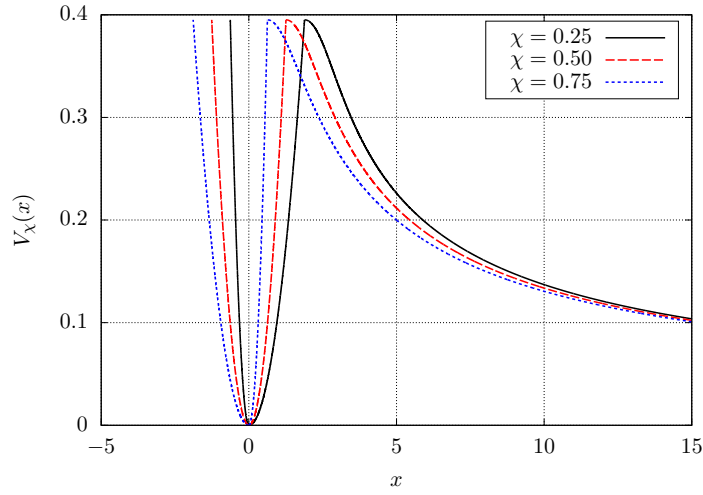


Figure 4.11: Reconstructed potential $V_\chi(x)$ for spectrum I shown in eq. (4.90) for different values of χ ; the other parameters are set to $a = b = c = 1$. Figure taken from [4].

potential barrier or $\chi = \chi(E)$, are possible. The turning point $x_2(E)$ is given by

$$x_2(E) = \mathcal{L}_2(E) + (1 - \chi) \mathcal{L}_1(E), \quad (4.103)$$

where we have used $\mathcal{L}_2(E) = x_2(E) - x_1(E)$ and eq. (4.102).

From the knowledge of the turning points we can now construct $V_\chi(x)$ by solving them for E . We show the reconstructed potential for different values of χ in Fig. 4.11 and a fixed choice of the parameters (a,b,c) .

With our choice for the parameterization, the turning points $(x_0(E), x_1(E))$ are by construction strictly monotonically decreasing and increasing functions of E , respectively. We can now determine what choices of χ are valid to guarantee that $x_2(E)$ is strictly monotonically decreasing by demanding

$$\frac{d}{dE} x_2(E; \chi, a, b, c) < 0, \quad \forall E \in (E_{\min}, E_{\max}). \quad (4.104)$$

This algebraic relation is too involved to be solved easily as a general function of (χ, a, b, c) , but can be checked numerically for a given choice of the parameters.

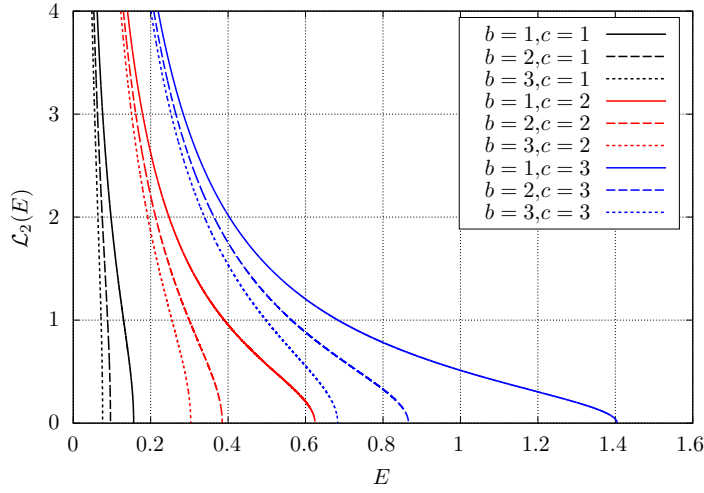


Figure 4.12: The width of the potential barrier $\mathcal{L}_2(E)$ for spectrum II shown in eq. (4.105) for different values of (b, c) and $a = 1$. Figure taken from [4].

4.4.2 Spectrum II

In this example we keep the same real part as in the first case but change the imaginary part

$$E_n = a \left(n + \frac{1}{2} \right) - ib \exp \left(-\frac{c}{\sqrt{n + 1/2}} \right). \quad (4.105)$$

Since the real part is the same, $\mathcal{L}_1(E)$ is given by eq. (4.92), but $\mathcal{L}_2(E)$ will be different because the transmission $T(E)$ takes another form

$$T(E) = \frac{4\pi b}{a} \exp \left(-\frac{c\sqrt{a}}{\sqrt{E}} \right). \quad (4.106)$$

The integration of eq. (4.88) to obtain $\mathcal{L}_2(E)$ is straightforward and leads to

$$\mathcal{L}_2(E) = \frac{c\sqrt{a}}{\pi} \frac{\sqrt{1 - E/E_{\max}}}{E}, \quad (4.107)$$

where E_{\max} is determined by $T(E_{\max}) = 1$ and given by

$$E_{\max} = \frac{ac^2}{[\ln(4\pi b/a)]^2}. \quad (4.108)$$

We show $\mathcal{L}_2(E)$ for different parameters in Fig. 4.12. One can check that $\mathcal{L}_2(E)$ describes a valid potential barrier by looking at the condition

$$\frac{d\mathcal{L}_2(E)}{dE} = \frac{c\sqrt{a}}{2\pi} \frac{E - 2E_{\max}}{E^2 E_{\max} \sqrt{1 - E/E_{\max}}} < 0, \quad \forall E \in (E_{\min}, E_{\max}). \quad (4.109)$$

This condition is always fulfilled (assuming $a > 0$), therefore $\mathcal{L}_2(E)$ is a valid solution to describe the width of the potential barrier. Using the same parameterization as for the first spectrum, we show the reconstructed potential $V_\chi(x)$ for a given choice of (a, b, c) in Fig. 4.13.

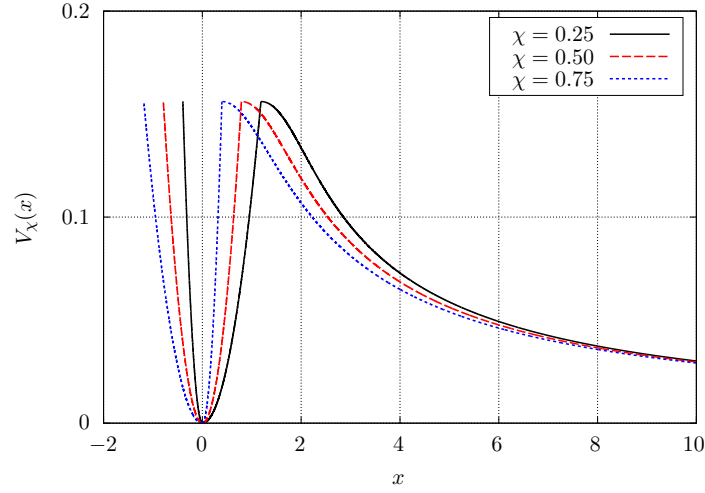


Figure 4.13: Reconstructed potential $V_\chi(x)$ for spectrum II shown in eq. (4.105) for different values of χ ; the other parameters are set to $a = b = c = 1$. Figure taken from [4].

4.4.3 Spectrum III

The third example shall be given by

$$E_n = a \left(n + \frac{1}{2} \right) - i \exp \left(- \left[N - b \left(n + \frac{1}{2} \right) \right] \right), \quad (4.110)$$

using the parameters (a, b, N) . Following the same procedure as in the previous examples one finds

$$T(E) = \frac{4\pi}{a} \exp \left(-N + \frac{b}{a} E \right), \quad \mathcal{L}_2(E) = \frac{2b}{\pi a} \sqrt{E_{\max} - E}, \quad E_{\max} = \frac{a}{b} \left[N + \ln \left(\frac{a}{4\pi} \right) \right]. \quad (4.111)$$

The special case of a symmetric potential barrier reveals that it is described by an inverted parabola with the maximum at E_{\max} . We show $\mathcal{L}_2(E)$ in Fig. 4.14 for $a = 1$ and different values of (b, N) .

Both functions, $\mathcal{L}_1(E)$ and $\mathcal{L}_2(E)$, are strictly monotonically increasing and decreasing functions of E for $E \in (E_{\min}, E_{\max})$, respectively. Nevertheless, if we choose to parameterize a subclass of the possible solutions for the potentials as done in the first example, something interesting happens. Because overhanging cliffs in the potential are not allowed, a quick analysis shows that only $\chi = 1$ gives a valid solution. For all other values of χ one finds overhanging cliffs for $E \rightarrow E_{\min}$. This can be seen by using eq. (4.103) to define $x_2(E)$, which has to be a strictly monotonically decreasing function of E , and check whether $dx_2(E)/dE$ changes sign. One finds that this is the case at a given value E_c , which is given by

$$E_c = \frac{E_{\max}}{1 + [b/(2\pi(1 - \chi))]^2}. \quad (4.112)$$

The parameter χ is defined in the interval $[0, 1]$. For $\chi \neq 1$ we therefore always find a value of E_c in the range (E_{\min}, E_{\max}) . This excludes all potentials described by $\chi \neq 1$ from being valid solutions.

4.4.4 Spectrum IV

In this last example we show that not every function for the spectrum leads to a valid solution for the potential. This is the case for the following spectrum

$$E_n = a \left(n + \frac{1}{2} \right) - i \exp \left(- \left[N - b \left(n + \frac{1}{2} \right)^2 \right] \right), \quad (4.113)$$

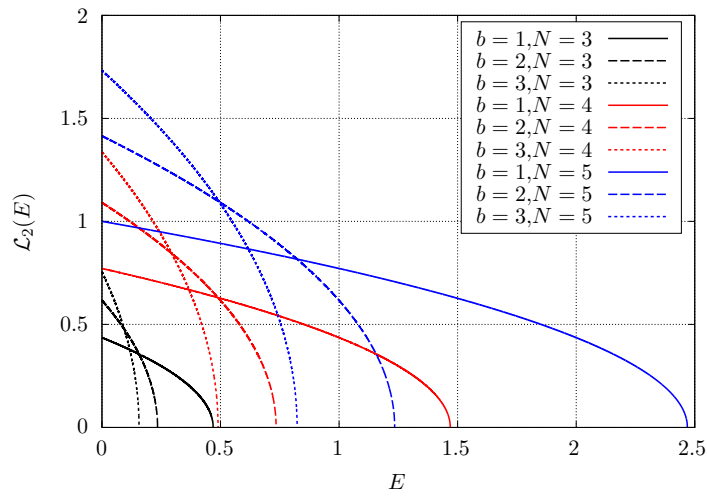


Figure 4.14: The width of the potential barrier $\mathcal{L}_2(E)$ for spectrum III shown in eq. (4.110) for different values of (b, N) and $a = 1$. Figure taken from [4].

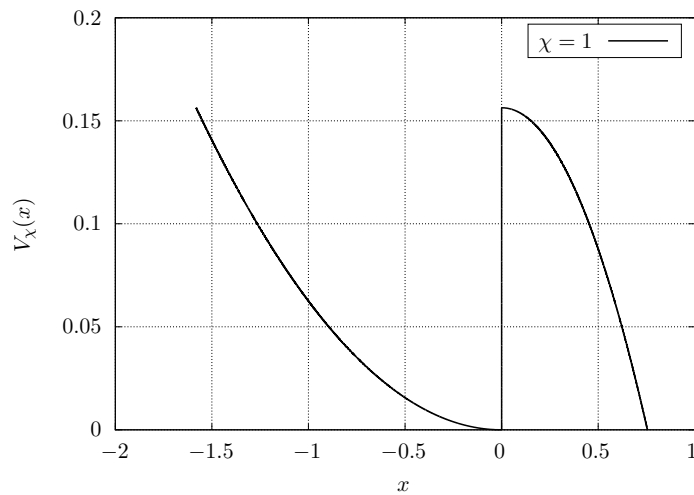


Figure 4.15: Reconstructed potential $V_\chi(x)$ for spectrum III shown in eq. (4.110) for the only valid value of $\chi = 1$; the other parameters are $a = 1, b = N = 3$. Figure taken from [4].

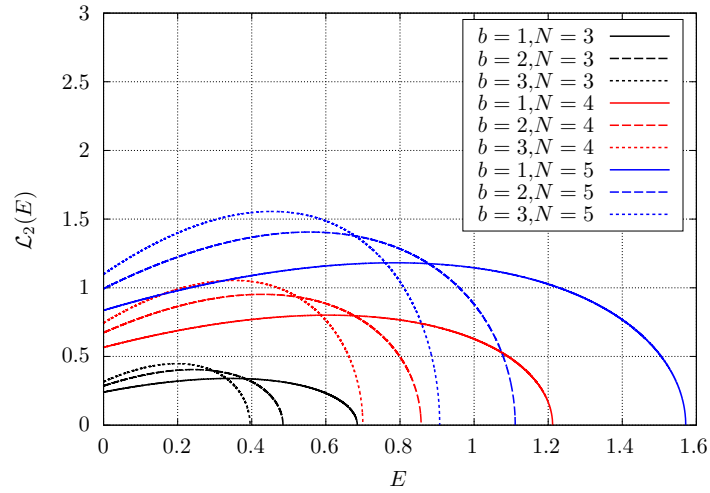


Figure 4.16: The reconstructed width of the potential barrier $\mathcal{L}_2(E)$ for spectrum IV shown in eq. (4.113) for different values of (b, N) and $a = 1$. Such a width can not be fulfilled by any potential. Figure taken from [4].

where we keep the same real part as in the previous examples but modified the imaginary part. The calculations are again straightforward and the important relations are found to be

$$T(E) = \frac{4\pi}{a} \exp\left(-\left[N - \frac{b}{a^2}E^2\right]\right), \quad \mathcal{L}_2(E) = \frac{4}{3\pi} \frac{b}{a^2} \sqrt{E_{\max} - E}(E_{\max} + 2E), \quad (4.114)$$

$$E_{\max} = \sqrt{\frac{a^2}{b} \left[N + \ln\left(\frac{a}{4\pi}\right)\right]}. \quad (4.115)$$

A quick look at $\mathcal{L}_2(E)$ shows that its derivative with respect to E is positive for $E \in E(E_{\min}, E_{\max}/2)$, which would cause overhanging cliffs for the potential barrier and is therefore clearly no valid solution for a potential. In this case we conclude that there exists no valid potential in our class of potentials that are described by the inverse method, which can have the given spectrum eq. (4.113). Nevertheless, we show the corresponding $\mathcal{L}_2(E)$ for $a = 1$ and different values of (b, N) in Fig. 4.16.

Part II

Applications and Results

Overview

After providing the theoretical background and methods in Part I, we now demonstrate the applications and results. These are the published works [1, 2, 3, 5, 6, 7, 8, 9], which we organize in two categories.

The first category summarizes works on the development and application of direct and inverse QNM spectrum methods to neutron stars, ultra compact objects, wormholes, and black holes:

- **Chapter 5**
A semi-analytic study of axial perturbations of ultra compact stars,
Sebastian H. Völkel and Kostas D. Kokkotas,
Class. Quantum Grav. 34, 125006, 2017
- **Chapter 6**
Ultra Compact Stars: Reconstructing the Perturbation Potential,
Sebastian H. Völkel and Kostas D. Kokkotas,
Class. Quantum Grav. 34, 175015, 2017
- **Chapter 7**
Wormhole potentials and throats from quasi-normal modes
Sebastian H. Völkel and Kostas D. Kokkotas,
Class. Quantum Grav. 35, 105018, 2018
- **Chapter 8**
On the inverse spectrum problem of neutron stars
Sebastian H. Völkel and Kostas D. Kokkotas,
Class. Quantum Grav. 36 115002, 2019
- **Chapter 9**
**Scalar Fields and Parametrized Spherically Symmetric Black Holes:
Can one hear the shape of space-time?**
Sebastian H. Völkel and Kostas D. Kokkotas
Phys. Rev. D 100, 044026, 2019

The second category are collaborative works including an author additional to my first supervisor. These are on parameter estimation [3], Hawking radiation [7], and black hole area quantization [9]:

- **Chapter 10**
Parameter estimation of gravitational wave echoes from exotic compact objects
Andrea Maselli, **Sebastian H. Völkel**, and Kostas D. Kokkotas
Phys. Rev. D 96, 064045, 2017
- **Chapter 11**
The Inverse Problem for Hawking Radiation
Sebastian H. Völkel, Roman Konoplya, and Kostas D. Kokkotas,
Phys. Rev. D 99, 104025, 2019
- **Chapter 12**
Spectral Lines of Quantized, Spinning Black Holes and Their Astrophysical Relevance
Andrew Coates, **Sebastian H. Völkel** and Kostas D. Kokkotas,
Phys. Rev. Lett. 123, 171104, 2019

Further publications prepared during the PhD work, which we *do not* explicitly present in the following, are on methodical aspects of the inverse spectrum method [4], because we included it already in Sec. 4.4, and the proceedings article for Domoschool 2018 [10], because results reported there have either been reported in our earlier works [1, 2, 5] or in much greater detail afterwards [6]:

- **Inverse spectrum problem for quasi-stationary states,**

Sebastian H. Völkel

J. Phys. Commun. 2 025029, 2018

- **Hearing the Nature of Compact Objects,**

Sebastian H. Völkel and Kostas D. Kokkotas

Einstein Equations: Physical and Mathematical Aspects of General Relativity, Domoschool 2018, Birkhäuser Basel, 2019

Each of the following chapters will summarize one work and is an adaption of the original publications. Since a comprehensive introduction has been provided in Part I, the following introductions and motivations sections are quite brief. Since some conventions for notation changes throughout the publications, but we want the reader to be able to follow original works, some notation also changes through the following chapters.

5 | A Semi-Analytic Study of Axial Perturbations of Ultra Compact Stars

Breakdown of Contributions

This chapter is based on the publication “*A semi-analytic study of axial perturbations of ultra compact stars*” by Sebastian H. Völkel and Kostas D. Kokkotas, *Class. Quantum Grav.* 34 125006, 2017, [1]. ©IOP Publishing. Reproduced with permission. All rights reserved. It contains several extensions of my work that I carried out in my master thesis. These new contributions are an improved analytical model for the effective potential, the effect of the next correction term to the classical Bohr-Sommerfeld rule, and a numerical implementation for the Bohr-Sommerfeld rules to apply them to the exact perturbation potentials. My contributions in this work are all analytic and WKB/Bohr-Sommerfeld related computations, while Kostas D. Kokkotas provided me with precise numerical values for verification by using a previously existing code. The paper writing was done by me, while Kostas D. Kokkotas assisted in the final editing of the manuscript.

Overview

In this work we find that the Bohr-Sommerfeld rules are a well suited method to study the trapped modes, which are a new family of QNMs that exists for ultra compact configurations only. The comparison to exact numerical values shows good precision for the analytic model and as expected higher precision for the numerical implementation of the next correction term. We conclude that the Bohr-Sommerfeld rules are a valuable tool for analytic and semi-analytic studies of trapped modes of ultra compact objects. Especially since the exact form of the perturbation potential does not simply allow for exact analytic solutions. This chapter is organized as follows. Since the theoretical background of compact objects and their axial perturbations are presented in chapter 2 and chapter 3, the introduction in Sec. 5.1 summarizes only the most important aspects. The analytical model for the effective potential is outlined in Sec. 5.2. The next correction term of the classical Bohr-Sommerfeld rule has been introduced in Sec. 4.2.1. Finally, the application of these methods can be found in Sec. 5.3 and the numerical results in Sec. 5.4. Discussion and conclusions are provided Sec. 5.5 and Sec. 5.6, respectively. Supplementary material can be found Sec. 5.7.

5.1 Introduction

In this work we revisit the problem of axial perturbations around ultra compact objects, in particular, constant density stars and gravastars, which we introduced and motivated in Sec. 2.3. The perturbation equations reduce to the one-dimensional wave equation and the effective potential admits three turning points, as discussed in Sec. 3.3. We show these potentials in Fig. 5.1 and Fig. 5.2. Exact analytic solutions for the QNM spectra are not known. In order to enhance the understanding of numerical results, we applied the generalized Bohr-Sommerfeld rule to this problem. Using different variations we find analytic and semi-analytic descriptions of the trapped QNM spectrum.

5.2 Model for the Effective Potential

Due to the complicated structure of the perturbation potential, it is reasonable to look for well justified simplifications, if analytical results should be obtained. Since this idea had successfully been investigated for black holes in the 70s and 80s [210, 211, 213, 213], it looks promising to follow a similar path. Different approaches to study

ultra compact objects can be found in the literature. Our aim in this work is to combine two approximations. Since the perturbation potential can be seen as a combination of one well and one barrier, we take this literally. Since these trapped modes are described as bound states with small decay, it is self-evident to find one approximation for the potential well and a another one for the potential barrier. The first is then responsible for the real part of ω_n^2 , while the second one introduces its imaginary part. In this way, the overall problem is split into two more tractable parts. The application of the generalized Bohr-Sommerfeld rule in the last step is a well suited tool to combine both parts properly.

5.2.1 Two Approximate Potentials

With the application to constant density stars and gravastars in mind, we introduce the quartic oscillator $U_Q(x)$ as approximation for the well, and the Breit-Wigner distribution function, from here on called Breit-Wigner potential $U_{BW}(x)$, for the barrier

$$U_Q(x) = U_0 + \lambda_0^2(x - x_{\min})^4, \quad U_{BW}(x) = \frac{U_1}{1 + \lambda_1(x - x_{\max})^2}. \quad (5.1)$$

Both functions altogether depend on six parameters. However, as we will show, the final result does not depend on (x_{\min}, x_{\max}) and therefore only on four of them $(U_0, U_1, \lambda_0, \lambda_1)$. The parameters are determined by matching with the exact perturbation potential. We consider U_0 to be the local minimum inside the well, while U_1 corresponds to the maximum of the barrier at x_{\max} . The remaining parameters are identified as follows. The second derivative V''_{\max} evaluated at the barrier maximum is matched with the second derivative of the Breit-Wigner distribution function and yields $\lambda_1 = -V''_{\max}/2V_{\max}$. Finding a suitable constraint to determine λ_0 is more involved, because the second derivative at the minimum does not yield an optimal overall description of the entire well. Here one should be more careful and consider the application one has in mind. For constant density stars we demand the quartic oscillator to be equal to the Regge-Wheeler potential at the surface of the star. However, for gravastars we keep $U_0 = V_{\min}$ but define x_{\min} , to be in the middle of the two x -values satisfying $V(x) = U_1$. Here λ_0 follows from demanding $U_Q(x_{\max}) = V_{\max}$. With a map in hand to determine all parameters for a given perturbation potential, we continue with the discussion on the computation of the eigenvalues.

5.2.2 Spectrum of Trapped Modes

As it was shown in chapter 4, the generalized Bohr-Sommerfeld rule can be expanded and yields the classical Bohr-Sommerfeld rule and the Gamow formula, for the real and imaginary part of E_n , respectively. Since we are using approximated potentials, most precision will be lost here, and not by the simplification of the generalized Bohr-Sommerfeld rule, as we show in Sec. 5.3. To find the solution for the complex spectrum $E_n = E_{0n} + iE_{1n}$, we first apply the classical Bohr-Sommerfeld rule to determine E_{0n} using the quartic oscillator. The integration can be carried out analytically. After rearranging terms one finds

$$E_{0n} = U_0 + \lambda_0^{2/3} \left(\frac{3\pi}{2\sqrt{2}\text{EllipticK}(1/\sqrt{2})} \left(n + \frac{1}{2} \right) \right)^{4/3}, \quad (5.2)$$

where $\text{EllipticK}(x)$ is the complete elliptic integral of the first kind. In the next step we insert the Breit-Wigner potential and the quartic oscillator into the Gamow formula to obtain E_{1n} . Again the integration can be done analytically and leads to

$$E_{1n} = -\frac{1}{4}\sqrt{\lambda_0} (E_{0n} - U_0)^{1/4} \frac{\Gamma(3/4)}{\sqrt{\pi}\Gamma(5/4)} \exp \left(4i\sqrt{\frac{U_1 - E_{0n}}{\lambda_1}} \text{EllipticE} \left(i\sqrt{\frac{U_1}{E_{0n}}} - 1, i\frac{\sqrt{E_{0n}/U_1}}{\sqrt{1 - E_{0n}/U_1}} \right) \right), \quad (5.3)$$

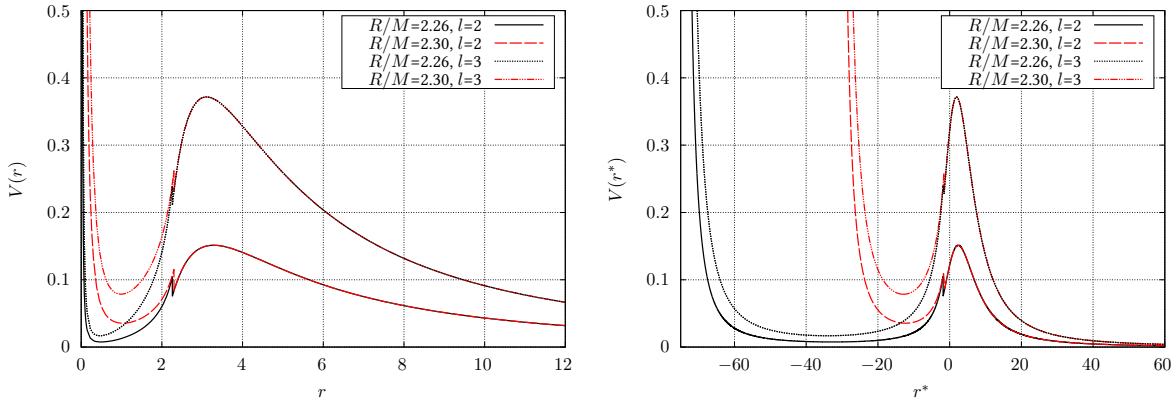


Figure 5.1: The effective potential for constant density stars for different R/M and l . **Left panel:** with respect to the r coordinate. **Right panel:** with respect to the tortoise coordinate r^* . Figure taken from [1].

where $\text{EllipticE}(x,y)$ is the elliptic integral of the second kind and $\Gamma(x)$ is the gamma function. We provide further details in Sec. 5.7. Finally, the QNM spectrum is given by

$$\omega_n = \sqrt{E_n} = \sqrt{E_{0n} + iE_{1n}}. \quad (5.4)$$

This is the fully analytic approximate result for all trapped modes in such potentials.

5.3 Applications

Here we present the application of the previously discussed methods to two different systems. First to constant density stars in Sec. 5.3.1, which can be seen as standard toy model for ultra compact stars. Second to thin shell gravastars in Sec. 5.3.2, which can be considered as theoretical alternative to black holes and are more exotic. Since an extensive introduction to these objects is presented in chapter 2.3, we only summarize the most important points here.

5.3.1 Constant Density Stars

Constant density stars are the ideal starting point in the study of ultra compact object dynamics. Due to the simplicity, they have been used extensively in the literature. First works on their QNM spectrum are [231, 233], while the time evolution of test particles around these objects have been studied in [236, 237, 238]. Recently they are in the focus of more efforts, see for example [166, 287]. The perturbation potential inside a constant density star has the form

$$V(r) = \frac{e^{2\nu}}{r^3} [l(l+1)r + r^3(\rho - P(r)) - 6M(r)], \quad (5.5)$$

where ρ is the density of the star, $P(r)$ its pressure and $M(r)$ the mass inside r . The tortoise coordinate r^* in which the wave equation appears is defined as

$$r^* = \int_0^r e^{-\nu+\mu} dr, \quad (5.6)$$

where $e^{2\nu}$ and $e^{2\mu}$ are the g_{00} and g_{11} components of the metric tensor $g_{\mu\nu}$. An explicit analytic expression for r^* can be found in [255]. We show the potential described by (5.5) in Fig. 5.1 for both coordinates. It is evident that the compactness determines the width of the potential well, while l has a strong impact on the height of the barrier. Both effects will become clearly visible in the trapped QNM spectrum.

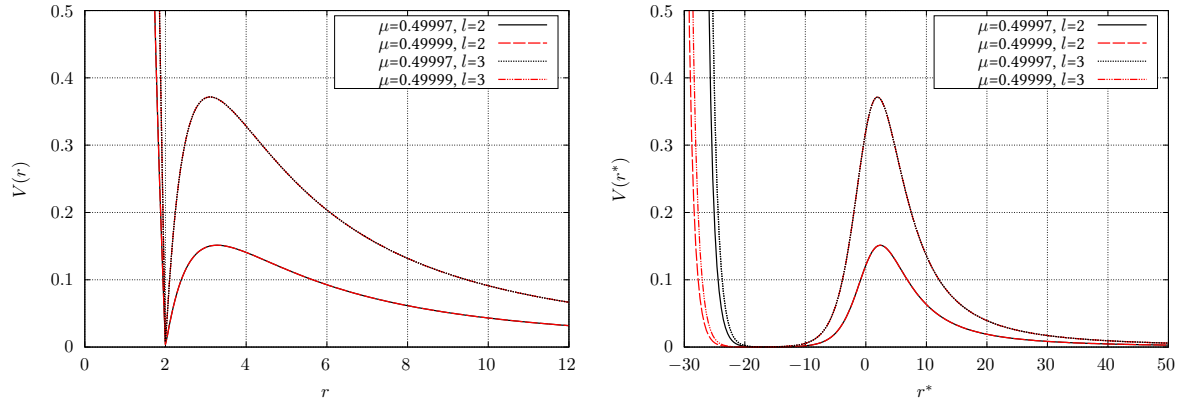


Figure 5.2: Effective potential for gravastars for different values of $\mu = M/a$ and for $l = 2$ and 3 . **Left panel:** with respect to the r coordinate. **Right panel:** with respect to the tortoise coordinate r^* . Figure taken from [1].

5.3.2 Gravastars

In this work we choose the thin shell model of a gravastar to demonstrate the efficiency of the Bohr-Sommerfeld rule. It describes an infinitely thin shell at radius a separating a de Sitter core from the external Schwarzschild space-time. The interior perturbation potential is given by

$$V(r) = \left(1 - \frac{8\pi\rho}{3}r^2\right) \frac{l(l+1)}{r^2}. \quad (5.7)$$

This case has a specific equation of state in the shell with zero surface density. In the case of axial perturbations studied here, there is no coupling to matter. Therefore our results also apply to other thin shell models and would differ in their polar oscillations. The relation of the tortoise coordinate to the metric is the same as for constant density stars, but the metric of course differs. We show the effective potential in both coordinates for different parameters in Fig. 5.2.

5.4 Results

In this section we present our results. We show the numerical values for a constant density model with the parameters $R/M = 2.26$ and $l = 2$ and 3 in Table 5.1. The application to a gravastar model with parameters $\mu = 0.49997$ and $l = 2$ and 3 is presented in Table 5.2. More tables can be found in the appendix of the corresponding publication [1]. The first column, named “BS Fitting”, shows the analytic model of Sec. 5.2. The second column, named “BS Low”, shows the low order Bohr-Sommerfeld result, while the third column, named “BS High”, includes the next correction term to the classical Bohr-Sommerfeld rule. The fourth column named “Numerical” shows the full numerical result based on the code used in [233]. For the smallest imaginary parts at $n = 0$ there is limited accuracy in the gravastar case, and potential errors in the imaginary part of the order of 10-20 % are possible. Since the potential of both objects are qualitatively similar, most of the findings apply to both.

Concerning the overall scaling of the trapped QNMs, one finds that their real and imaginary parts scale completely different. The real part is roughly equally spaced, while the imaginary part grows exponentially over many orders of magnitude. For constant density stars, all methods agree on percent level in the real part, while the imaginary parts show larger deviations. In the case of gravastars, the value of the fundamental mode with $n = 0$ is less precise. This might also be due to the fact that the chosen configuration admits less trapped modes.

For both values of l , the analytical model gives the correct number of trapped modes. The comparison to the results of the same Bohr-Sommerfeld rule applied to the exact perturbation potential shows in most cases larger deviations than the other methods compared to each other. From this we conclude that the deviation between the approximated potentials and the exact ones has a stronger impact than the use of the Bohr-Sommerfeld rule

Table 5.1: Results for three versions of the Bohr-Sommerfeld method for uniform density stars with $R/M=2.26$ and $l = 2$ and 3. The results listed in the first column are derived by using fitting to the true potentials, while the second and third column refer to numerical evaluation of the low and higher order BS rule. In the fourth column the fully numerical results of [233] are listed for comparison. Table taken from [1].

$l = 2$								
n	BS Fitting		BS Low		BS High		Numerical	
	Re(ω_n)	Im(ω_n)						
0	0.1060	2.88e-09	0.1068	1.01e-09	0.1091	1.29e-09	0.1090	1.24e-09
1	0.1530	9.54e-08	0.1462	3.16e-08	0.1485	3.73e-08	0.1484	3.95e-08
2	0.1970	1.14e-06	0.1856	4.13e-07	0.1879	4.72e-07	0.1876	5.47e-07
3	0.2377	7.92e-06	0.2251	3.47e-06	0.2274	3.88e-06	0.2267	4.85e-06
4	0.2756	3.97e-05	0.2646	2.28e-05	0.2668	2.52e-05	0.2654	3.23e-05
5	0.3114	1.60e-04	0.3040	1.40e-04	0.3063	1.52e-04	0.3036	1.72e-04
6	0.3453	5.54e-04	0.3411	5.51e-04	0.3441	6.14e-04	0.3410	7.30e-04
7	0.3778	1.71e-03	0.3784	2.00e-03	0.3752	1.81e-03	0.3777	2.30e-03
$l = 3$								
n	BS Fitting		BS Low		BS High		Numerical	
	Re(ω_n)	Im(ω_n)						
0	0.1474	3.46e-13	0.1494	1.34e-13	0.1506	1.56e-13	0.1508	1.52e-13
1	0.1949	1.99e-11	0.1886	6.70e-12	0.1901	7.61e-12	0.1901	7.76e-12
2	0.2422	4.62e-10	0.2279	1.37e-10	0.2294	1.52e-10	0.2293	1.62e-10
3	0.2869	5.82e-09	0.2671	1.71e-09	0.2686	1.87e-09	0.2686	2.08e-09
4	0.3292	4.88e-08	0.3064	1.54e-08	0.3079	1.67e-08	0.3078	1.93e-08
5	0.3694	3.09e-07	0.3457	1.10e-07	0.3472	1.18e-07	0.3469	1.42e-07
6	0.4078	1.59e-06	0.3850	6.54e-07	0.3865	6.99e-07	0.3860	8.79e-07
7	0.4447	6.98e-06	0.4243	3.45e-06	0.4257	3.66e-06	0.4249	4.72e-06
8	0.4802	2.71e-05	0.4636	1.83e-05	0.4650	1.93e-05	0.4636	2.25e-05
9	0.5146	9.54e-05	0.5019	7.32e-05	0.5075	8.93e-05	0.5019	9.64e-05
10	0.5479	3.09e-04	0.5403	2.83e-04	0.5404	2.84e-04	0.5397	3.63e-04
11	0.5803	9.36e-04	0.5782	1.03e-03	0.5768	9.82e-04	0.5768	1.15e-03

compared to the full numerical method.

There are different aspects of WKB theory and the type of potential that influence the accuracy when applied to the exact potential. For low n , WKB theory is usually expected to be least precise. We can observe this trend when comparing the relative errors for the first few n , which improve with growing n . For eigenvalues close to the peak of the barrier, the validity of the next correction term, which is valid for a two turning point potential, becomes less justified. The correction term to the classical Bohr-Sommerfeld rule then yields worse results. For all n , despite the ones approaching the peak of the barrier, including the next correction term yields excellent improvements in the accuracy.

5.5 Discussion

The numerical results reported in tables 5.1 and 5.2 can be discussed to demonstrate various points.

By using the next correction term of the classical Bohr-Sommerfeld rule for bound states, one finds significant improvements in the accuracy for the low lying trapped QNMs. Here the applicability of the bound state problem to determine the real part of ω_n^2 first, is well justified by the exponentially small imaginary part of the same. The technically more difficult treatment of higher order corrections to the full three turning point problem makes the success of this rather simple approach interesting. It is also useful because the classical Bohr-Sommerfeld rule is in general less accurate for modes in the bottom of the potential barrier (small n), while its accuracy improves for larger values of n .

We report that both version of the Bohr-Sommerfeld rule give an improved description of the spectrum, when the total number of trapped modes is large. One way to increase this number is to study large l . Comparing two eigenvalues with similar real part for two different l , the one corresponding to higher l has a significantly smaller

Table 5.2: Results for three versions of the Bohr-Sommerfeld method for gravastars with $\mu = 0.49997$ and for $l = 2$ and 3. The results listed in the first column are derived by using fitting to the true potentials, while the second and third column refer to numerical evaluation of the low and higher order BS rule. In the fourth column we show the fully numerical results of [233]. Table taken from [1].

$l = 2$								
n	BS Fitting		BS Low		BS High		Full Num.	
	Re(ω_n)	Im(ω_n)						
0	0.1195	3.04e-08	0.1098	6.14e-08	0.1307	2.11e-07	0.1312	2.39e-07
1	0.2482	3.60e-05	0.2433	3.98e-05	0.2495	5.09e-05	0.2500	6.89e-05
2	0.3488	1.77e-03	0.3534	2.26e-03	0.3520	2.15e-03	0.3527	2.63e-03
$l = 3$								
n	BS Fitting		BS Low		BS High		Full Num.	
	Re(ω_n)	Im(ω_n)						
0	0.1400	7.05e-13	0.1277	8.42e-12	0.1491	3.62e-11	0.1500	4.44e-11
1	0.2903	2.08e-08	0.2763	3.07e-08	0.2841	4.37e-08	0.2848	5.29e-08
2	0.4080	4.62e-06	0.4021	5.47e-06	0.4058	6.29e-06	0.4059	7.79e-06
3	0.5105	2.36e-04	0.5145	3.16e-04	0.5151	3.23e-04	0.5149	3.90e-04

imaginary part and is therefore better described as bound state. The second way to increase the number of trapped modes is to consider more compact configurations of the same family, e.g. constant density stars or gravastars.

Comparing the results of both families of objects, one finds that gravastars have to be significantly more compact than constant density stars to admit a similar number of trapped modes. While the Buchdahl limit of $R/M = 9/4$ for constant density stars seems to be much less than the possible compactness of gravastars that can be arbitrarily close to $R/M = 2$, it is the difference in the tortoise coordinate transformation, that can still account for a similar kind of spectrum. While the height of the potential barrier is determined from the external Regge-Wheeler potential, it only depends on l , but not of the compactness. This causes the same frequency and damping time range of the modes of both objects for a given l . It is the compactness that then determines the number of possible states (keeping l fixed) and therefore the spacing of modes.

Lastly, we want to discuss the performance of the analytic model for the perturbation potential presented in Sec. 5.2. Since it approximates the exact potential with only a few parameters, one can not expect it to be quantitatively as good as the application of the same Bohr-Sommerfeld rule to the exact potential. However, the model is able to give an excellent approximation of the spectrum of trapped modes. Errors in the real part are usually on percent level. The imaginary part is more tricky due to its range over many orders of magnitude for a given potential, but still useful. Comparing it with the overall precision of similar approaches for black holes, we conclude that this method for ultra compact objects is at least comparable in the overall precision. Since we report analytic formulas for the spectrum in eq. (5.2) and eq. (5.3) that can be easily fitted to a given exact perturbation potential, our approach is simple to use and sufficient for qualitative investigations of the object's spectrum.

5.6 Conclusion

This work has shown that the Bohr-Sommerfeld rule rules are a reliable tool in the study of trapped QNMs of ultra compact objects. For their analytic simplicity, we have chosen constant density stars and thin shell gravastars to demonstrate the method. After introducing an effective model that approximates the full perturbation potential as combination of a potential well with a potential barrier, we have used the classical Bohr-Sommerfeld rule and the Gamow formula to find an analytic result for the QNM spectrum. Also, we have numerically studied the expansion of the generalized Bohr-Sommerfeld rule to the exact perturbation potentials. Finally, we have considered the next correction term of the classical Bohr-Sommerfeld rule to see how the precision of the trapped modes increase. For both objects and different approaches we report good agreement with full numerical results that can be considered as exact for the comparison. Using the higher order correction term, there is a significant

improvement in the results for small n , for which WKB theory and the Bohr-Sommerfeld rules are usually expected to be worst. The precision of the analytic result of the effective potential model is mostly limited by how good the effective potential matches the exact one, and not mostly by the use of the classical Bohr-Sommerfeld rule and Gamow formula. This has been checked by comparing the results of the same method applied to the exact perturbation potential.

Although full numerical and therefore more precise methods for the QNM calculation are available, we argue that the Bohr-Sommerfeld rule adds a valuable contribution. Its is easier to implement than most other full numerical methods, because the numerical solution of the complicated boundary value problem reduces to simple integral evaluation and root finding. Especially the ability to find approximate, but full analytic results is appealing. They allow for an enhanced qualitative understanding how different parameters of a given object shape its spectrum.

5.7 Supplementary Material

Here we provide details for the calculation of the integrals appearing in the analytic toy model in Sec. 5.2.

The integral of the classical Bohr-Sommerfeld rule applied to the quartic oscillator (5.1) is given by

$$\pi \left(n + \frac{1}{2} \right) = \int_{x_0}^{x_1} \sqrt{E_{0n} - U_Q(x)} dx = \int_{x_0}^{x_1} \sqrt{E_{0n} - U_0 - \lambda_0^2 (x - x_{\min})^4} dx. \quad (5.8)$$

After introducing $u \equiv \lambda_0^{1/2} (x - x_{\min}) / (E_{0n} - U_0)^{1/4}$ one finds

$$\int_{x_0}^{x_1} \sqrt{E_{0n} - U_Q(x)} dx = \frac{(E_{0n} - U_0)^{3/4}}{\lambda_0^{1/2}} \int_{u_0=-1}^{u_1=+1} \sqrt{1 - u^4} du. \quad (5.9)$$

$$= \frac{(E_{0n} - U_0)^{3/4}}{\lambda_0^{1/2}} \frac{2}{3} \sqrt{2} \text{EllipticK} \left(\frac{1}{\sqrt{2}} \right). \quad (5.10)$$

Here the limits of integration are ± 1 . These follow from the definition of turning points $E_{0n} - V(x) = 0$, for $x = x_0, x_1$ and that x_0, x_1 are real. Rearranging terms to solve for E_{0n} gives

$$E_{0n} = U_0 + \lambda_0^{2/3} \left(\frac{3\pi}{2\sqrt{2} \text{EllipticK}(1/\sqrt{2})} \left(n + \frac{1}{2} \right) \right)^{4/3}. \quad (5.11)$$

The other integrals come from the Gamow formula. First we determine the integral between x_0 and x_1 , which is with respect to the quartic oscillator (5.1). Here we find

$$\int_{x_0}^{x_1} \frac{1}{\sqrt{E_{0n} - U_Q(x)}} dx = \frac{1}{\lambda_0^{1/2} (E_{0n} - U_0)^{1/4}} \int_{u_0=-1}^{u_1=+1} \frac{1}{\sqrt{1 - u^4}} du \quad (5.12)$$

$$= \frac{1}{\lambda_0^{1/2} (E_{0n} - U_0)^{1/4}} \frac{2\sqrt{\pi} \Gamma(5/4)}{\Gamma(3/4)}. \quad (5.13)$$

Lastly we evaluate the integral between x_1 and x_2 with respect to the Breit-Wigner potential (5.1)

$$\int_{x_1}^{x_2} \sqrt{E_{0n} - U_{BW}(x)} dx = \int_{x_1}^{x_2} \sqrt{E_{0n} - \frac{U_1}{1 + \lambda_1 (x - x_{\max})^2}} dx. \quad (5.14)$$

Introducing $v \equiv \lambda_1^{1/2} (x - x_{\max})$ and $\tilde{E}_n \equiv E_{0n} / U_1$ it can be written as

$$\int_{x_1}^{x_2} \sqrt{E_{0n} - U_{BW}(x)} dx = \left(\frac{U_1}{\lambda_1} \right)^{1/2} \int_{v_1}^{v_2} \sqrt{\tilde{E}_n - \frac{1}{1 + v^2}} dv, \quad (5.15)$$

with the new limits of integration $v_{1,2} = \mp\sqrt{1/\tilde{E}_n - 1}$, which again follow from the definition of turning points. Using $0 < \tilde{E}_n < 1$ one arrives at

$$\int_{v_1}^{v_2} \sqrt{\tilde{E}_n - \frac{1}{1+v^2}} dv = -i \frac{\sqrt{\frac{\tilde{E}v^2 + \tilde{E} - 1}{v^2 + 1}} \sqrt{v^2 + 1} (\tilde{E} - 1) \sqrt{\frac{\tilde{E}v^2 + \tilde{E} - 1}{\tilde{E} - 1}}}{\tilde{E}v^2 + \tilde{E} - 1} \times \text{EllipticE} \left(iv, i\sqrt{\frac{\tilde{E}}{1 - \tilde{E}}} \right) \Big|_{v_1}^{v_2}. \quad (5.16)$$

Inserting the limits of integration and using $\text{EllipticE}(-x, y) = -\text{EllipticE}(x, y)$ one finds

$$\int_{v_1}^{v_2} \sqrt{\tilde{E}_n - \frac{1}{1+v^2}} dv = 2\sqrt{1 - \tilde{E}} \text{EllipticE} \left(i\sqrt{\frac{1}{\tilde{E}} - 1}, i\sqrt{\frac{\tilde{E}}{1 - \tilde{E}}} \right). \quad (5.17)$$

Thus the final result is

$$\int_{x_1}^{x_2} \sqrt{E_{0n} - U_{\text{BW}}(x)} dx = 2\sqrt{\frac{U_1 - E_{0n}}{\lambda_1}} \text{EllipticE} \left(i\sqrt{\frac{U_1}{E_{0n}} - 1}, i\sqrt{\frac{E_{0n}/U_1}{1 - E_{0n}/U_1}} \right). \quad (5.18)$$

6 | Ultra Compact Stars: Reconstructing the Perturbation Potential

Breakdown of Contributions

This chapter is based on the publication “*Ultra compact stars: reconstructing the perturbation potential*” by Sebastian H. Völkel and Kostas D. Kokkotas, *Class. Quantum Grav.* 34 175015, [2]. ©IOP Publishing. Reproduced with permission. All rights reserved. My contributions are all the analytic and WKB/Bohr-Sommerfeld related computations. The numerical values to start the inverse problem have been provided by Kostas D. Kokkotas with the same code as in the previous work [1]. The paper writing was done by me, while Kostas D. Kokkotas assisted in the final editing of the manuscript.

Overview

Here we present a novel way how the Bohr-Sommerfeld rule and the Gamow formula can be combined to reconstruct the perturbation potential if the spectrum of trapped QNMs is provided. As in most inverse problems, one can in general not expect to obtain only one unique solution, but more likely constraints that describe multiple possible solutions. However, by using Birkhoff’s theorem as additional physical assumption and assuming that the underlying potential admits three turning points, the method we present here provides a unique reconstruction. As in our previous work in chapter 5, we consider axial perturbations of spherically symmetric and non-rotating constant density stars and gravastars, as example to demonstrate the method. Since the presented method is easy to implement and rather general, we expect it also to be interesting in other fields in which inverse spectrum problems are studied, e.g., quantum physics and molecular spectroscopy.

The structure of this chapter is as follows. For the theoretical background of the problem, we refer the reader again to chapter 2 and chapter 3. The inversion method in full details can be found in Sec. 4.3. We outline the motivation of this work in Sec. 6.1 and summarize the novel method in Sec. 6.2. The results obtained by applying the method to different constant density stars and gravastars are being presented in Sec. 6.3. We discuss these findings in Sec. 6.4 and conclude this work in Sec. 6.5.

6.1 Introduction

The compact objects studied in this work are constant density stars and gravastars, as in chapter 5. In the first work we determined semi-analytically the spectrum of trapped axial QNMs by using the Bohr-Sommerfeld rule in different variations. This type of problem can be called a direct problem, because the properties of the physical system are assumed in the beginning and the spectrum follows. These problems are studied more frequently and different techniques to obtain the spectrum have been developed in the literature, see [58, 59] and references therein. The opposite case is the inverse problem, where the spectrum is provided initially and the task is to reconstruct the properties of the source. In this work we will show how the knowledge of the spectrum of trapped QNMs can be used to constrain the perturbation potential of the underlying object. Here, the generalized Bohr-Sommerfeld is quite powerful, because most direct problem techniques can not easily be adapted to the inverse problem. To our best knowledge, this is the first time that the reconstruction of the perturbation potential from the knowledge of the trapped QNM spectrum is studied. If compact, horizonless objects of this type really exist, one would be interested to study their nature. The here presented method could in principle help if the spectrum can be extracted from a signal. Since the theoretical framework assumes spherical symmetry and no rotation, it is clear that it might be limited in real astrophysical scenarios, such as binary mergers. However, even as

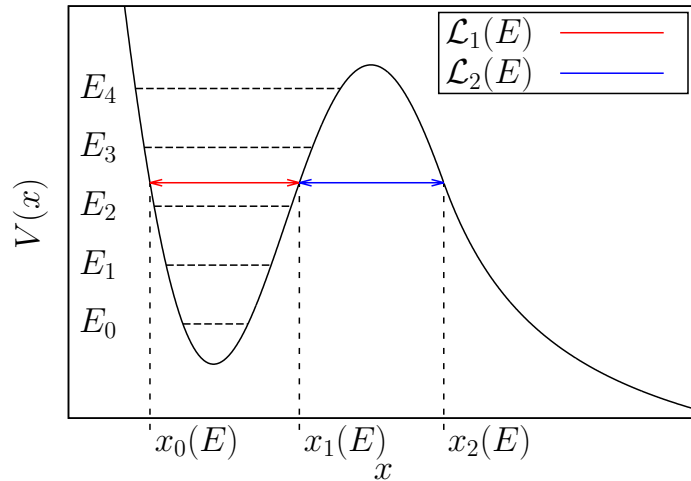


Figure 6.1: Typical potential for quasi-stationary states: shown is the potential $V(x)$, the three classical turning points (x_0, x_1, x_2) for a given state E_n together with the width of the bound region $\mathcal{L}_1(E)$ and potential barrier $\mathcal{L}_2(E)$ at $E = E_n$. Figure taken from [2].

a simplified problem, it is of theoretical and academic interest, because inverse problems of this kind are less studied. For instance, questions regarding the uniqueness of the object that produced the spectrum are usually not discussed in related works. Also, the ongoing discussion of the possible detection of so-called echoes in the late time signal of the measured advanced LIGO and advanced Virgo detections makes the present approach appealing, see our discussion in Sec. 3.6.

6.2 The Inverse Problem

Here we summarize the theoretical framework by reminding the reader that for spherically symmetric, non-rotating and asymptotically flat space-times, the problem of axial perturbations reduces to the time independent Schrödinger wave-equation with potential $V(x)$ where the eigenvalues are the QNMs ω_n^2 . While the direct problem is to determine ω_n for a given $V(x)$, the inverse problem studied here is to start with ω_n and reconstruct $V(x)$. The details for the inverse method, which is based on the inversion of the Bohr-Sommerfeld rule and the Gamow formula, can be found in Sec. 4.3.3. We show the type of potential we study in this work in Fig. 6.1. This type of inverse problem is in general not uniquely solvable, even if the given spectrum is determined from a reasonable potential. The type of perturbation potential admitting trapped modes for the objects studied here has three classical turning points. Due to the assumptions mentioned in the beginning of this section, and because we focus on ultra compact objects, the potential outside the object is given by the Regge-Wheeler potential eq. (3.39). The potential for $r < R$ depends crucially on the type of object one studies.

Our approach to solve the inverse problem for these type of potentials is motivated by our findings of the first work in chapter 5. Here we confirmed that the expansion of the generalized Bohr-Sommerfeld rule into the classical rule and the Gamow formula give accurate results (using $E_n = E_{0n} + iE_{1n}$ and assuming $|E_{1n}| \ll |E_{0n}|$). From this we conclude that the inverse problem might also be treated successfully in a similar way, which reconstructs the potential in multiple steps. Since this procedure was presented in chapter 4.3.3 we only summarize the main steps here.

6.2.1 Potential Well

The first step is to use the result for the potential well part, which is described by the turning points (x_0, x_1) . From the knowledge of the spectrum and using suitable interpolation, the reconstructed width of the potential

well $\mathcal{L}_1(E)$ is given by

$$\mathcal{L}_1(E) = x_1 - x_0 = \frac{\partial}{\partial E} I(E), \quad (6.1)$$

with the so-called “inclusion”

$$I(E) = 2 \int_{E_{\min}}^E \frac{n(E') + 1/2}{\sqrt{E - E'}} dE', \quad (6.2)$$

and E_{\min} is the minimum of the potential. Since this information is not directly known from the spectrum, it is approximated from $n(E_{\min}) + 1/2 = 0$.

6.2.2 Potential Barrier

The second step is to reconstruct the potential barrier, which is defined by the two turning points (x_1, x_2) . If the given information would not be the spectrum, but the classical transmission $T(E)$ through the potential barrier, one could directly apply the inversion of the Gamow formula. However, as shown in chapter 4.3.3 it is possible to replace the transmission with knowledge related to the bound states in the potential well. Here the non-trivial result is that although the potential well is not uniquely determined in the first step, all of these “width” equivalent potentials give the same result. Therefore, the result of the first step is enough to determine the width of the barrier

$$\mathcal{L}_2(E) = x_2 - x_1 = \frac{1}{\pi} \int_E^{E_{\max}} \frac{(dT(E')/dE')}{T(E')\sqrt{E' - E}} dE', \quad (6.3)$$

where E_{\max} is the maximum of the potential barrier. E_{\max} is not known from the spectrum but can be extrapolated similar to the minimum. Our previously mentioned, non-trivial result is that the semi-classical approximation for the transmission $T(E)$ can be written as

$$T(E_{0n}) = -2E_{1n} \int_{x_0}^{x_1} \frac{1}{\sqrt{E_{0n} - V(x)}} dx, \quad (6.4)$$

where all of the width equivalent potentials $V(x)$ from the first step give the same result here. Otherwise the problem could not be solved in this way. Note that this relation yields discrete values for the transmission, thus interpolation is required to use it in the integration in eq. (6.3).

6.2.3 The Combined Solutions

With the results of the previous two steps we obtained two functions $(\mathcal{L}_1, \mathcal{L}_2)$ that constrain three turnings points (x_0, x_1, x_2) . Without further input it is in general not possible to find one unique potential. As already known for single potential wells and single potential barriers, we should not expect one unique solution. The generalization to the three turning problem gives us a similar result regarding the uniqueness. Without providing one more turning point, the problem has no unique solution. However, this statement only concerns the properties of the spectrum and the assumption that the potential has three turning points. In this work, there is a way out. For ultra compact objects, we know that the external potential is the Regge-Wheeler potential. This provides us with the external turning point x_2 and we can conclude that there is only one unique solution, determined by

$$x_1(E) = x_2(E) - \mathcal{L}_2(E), \quad x_0(E) = x_1(E) - \mathcal{L}_1(E). \quad (6.5)$$

Strictly speaking we have to know the mass of the object, but in practice there are different ways of how this parameter can be determined. In this theoretical study we therefore assume it is provided from now on.

In case that the potential well admits negative values, our approach would not lead to a unique solution in this region, because there is no corresponding third external turning point. However, for the type of objects we

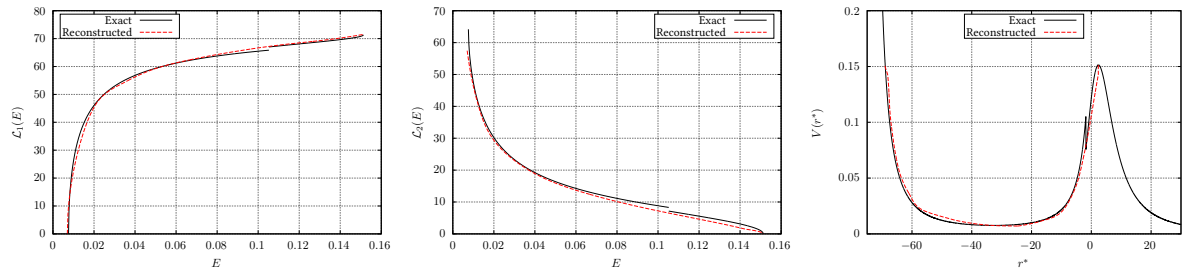


Figure 6.2: Constant density star with $R/M = 2.26$ and $l = 2$, there are 8 trapped modes. **Left panel:** width of the bound region $\mathcal{L}_1(E)$ for the exact potential (black) and the reconstructed one (red dashed). **Central panel:** width of the potential barrier $\mathcal{L}_2(E)$ for the exact potential (black) and the reconstructed one (red dashed). **Right panel:** exact axial mode potential (black) vs the reconstructed one (red dashed). Figures taken from [2].

study such regions do not exist and would be the signal of instabilities. It is therefore reasonable to exclude such objects from our analysis.

Lastly, we note that the here presented method and result is obviously only approximate, because of the underlying WKB method and the interpolation of the spectrum. Thus it can only be trusted if both approximations are valid, which in practice demands a reasonable number of trapped modes. We investigate the precision in the next Sec. 6.3.

6.3 Application and Results

In this section we demonstrate the inverse method by applying it to two different ultra compact objects. We start with constant density stars as standard object of this kind, whose oscillations have intensively been studied in [88, 233, 235, 236, 237, 238, 288] and in our previous work in chapter 5. We complement with thin shell gravastars as additional application, which are of more exotic nature [160, 161]. Their oscillations were studied in [163, 164, 165, 166]. Our tabulated numerical values have been obtained by the full numerical code discussed in [233].

6.3.1 Constant Density Stars

Starting with constant density stars, we remind the reader that the perturbation potential under consideration is given by

$$V(r) = g_{00}(r) \left[\frac{l(l+1)}{r^2} + [\rho_0 - P(r)] - \frac{6m(r)}{r^3} \right], \quad (6.6)$$

For details we refer to our discussion in Sec. 2.3.1. Here l is the harmonic index from the expansion of the metric perturbation in tensor harmonics. ρ and $P(r)$ are the density and pressure, respectively. $m(r)$ is the integrated mass function from the center of the star to r . The tortoise transformation is known analytically and can be found in [255]. Note that the most compact configuration is bounded by Buchdahl's limit of $R/M = 9/4$.

The results of the inverse method are presented in Fig. 6.2 and Fig. 6.3, with $R/M = 2.26$ and $l = 2, 3$. Additional results for $R/M = 2.28$ can be found in the appendix of the original publication [2]. Every figure has three panels and is organized as follow. The widths of the potential well $\mathcal{L}_1(E)$ and barrier $\mathcal{L}_2(E)$ are shown in the left and central panel, respectively. The right panel combines the two widths assuming Birkhoff's theorem to provide the external turning point $x_2(E)$ from the Regge-Wheeler potential. Black solid curves describe the exact potential, while the red dashed curves shows our reconstruction. The total number of trapped modes that entered the inverse method for each potential is mentioned in the caption.

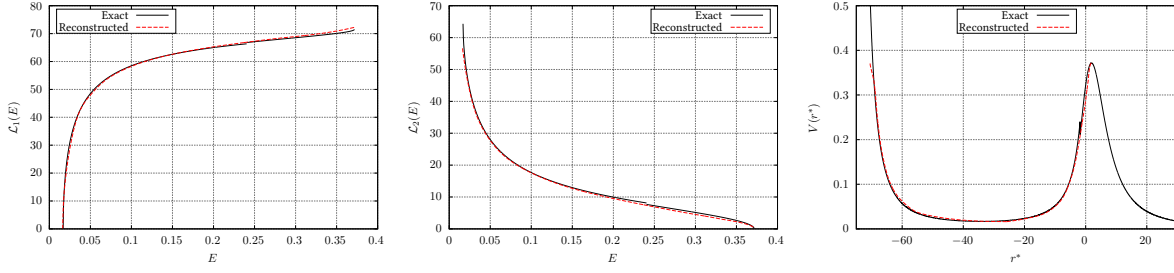


Figure 6.3: Constant density star with $R/M = 2.26$ and $l = 3$, there are 12 trapped modes. **Left panel:** width of the bound region $\mathcal{L}_1(E)$ for the exact potential (black) and the reconstructed one (red dashed). **Central panel:** width of the potential barrier $\mathcal{L}_2(E)$ for the exact potential (black) and the reconstructed one (red dashed). **Right panel:** exact axial mode potential (black) vs the reconstructed one (red dashed). Figures taken from [2].

6.3.2 Gravastars

In the following we discuss the results of the inverse method applied to thin shell gravastars. More details of this rather exotic type of object can be found in Sec. 2.3.2. The thin shell model describes a de Sitter condensate with $p = -\rho$ that is separated by an infinitely thin shell located at $r = a$, while the external space-time is Schwarzschild. Related work about their physics and oscillations can be found in [160, 162, 163, 164, 165, 166, 173] and our previous work [1]. The potential is given by

$$V(r) = \left(1 - \frac{8\pi\rho}{3}r^2\right) \frac{l(l+1)}{r^2}. \quad (6.7)$$

This model corresponds to the specific equation of state in the shell with zero surface density. The analytic form of the tortoise coordinate transformation is given by

$$r^* = \sqrt{\frac{3}{8\pi\rho}} \operatorname{arctanh} \left[\left(\frac{8\pi\rho r^2}{3} \right)^{1/2} \right] + C. \quad (6.8)$$

The constant of integration C is chosen by demanding continuity of r^* with the exterior Schwarzschild tortoise coordinate

$$C = a + 2M \ln \left(\frac{a}{2M} - 1 \right) - \sqrt{\frac{3}{8\pi\rho}} \operatorname{arctanh} \left[\left(\frac{8\pi\rho a^2}{3} \right)^{1/2} \right]. \quad (6.9)$$

Naturally the compactness of these objects is parametrized with $\mu = M/a$.

The results of the inverse method can be found in Fig. 6.4 for $\mu = 0.499999$ and $l = 3$. Further details can be found in the supplementary material of the original publication [2]. We start with $l = 3$, because the number of trapped modes for $l = 2$ with this compactness is too small to allow for a good reconstruction. The organization of the figure is similar to the one showing the results for constant density stars. We note that the unphysical deformation in the reconstructed potential arise because the absolute error for the reconstructed widths in this energy range are too large. We discuss this in Sec. 6.4.

6.4 Discussion

We observe the general trend that the inverse method gives reasonable results for both widths $\mathcal{L}_1(E)$ and $\mathcal{L}_2(E)$. The accuracy improves significantly for potentials admitting larger number of trapped modes. This is expected, because for these potentials the splitting into the classical Bohr-Sommerfeld rule and the Gamow formula is more justified. Also, the interpolation of the spectrum and transmission is more precise in such cases. Since the results for constant density stars and gravastars are comparable, taking into account the number of trapped modes in each potential, we expect the method to be applicable to other compact objects as well.

The number of trapped modes increases with increasing l and for more compact configurations. This universal

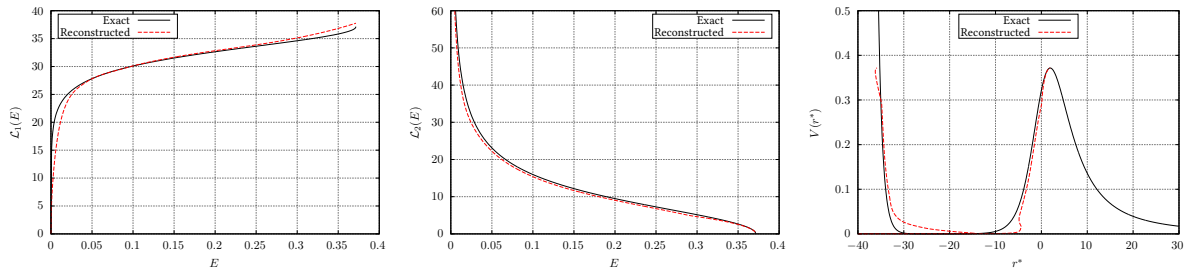


Figure 6.4: Gravastar with $\mu = 0.499999$ and $l = 3$, there are 6 trapped modes. **Left panel:** width of the bound region $\mathcal{L}_1(E)$ for the exact potential (black) and the reconstructed one (red dashed). **Central panel:** width of the potential barrier $\mathcal{L}_2(E)$ for the exact potential (black) and the reconstructed one (red dashed). **Right panel:** exact axial mode potential (black) vs the reconstructed one (red dashed). Figures taken from [2].

behavior of the spectrum is known, e.g. from chapter 5, and means that the inverse method is well suited for these cases. Especially in the eikonal limit of large l , the inverse method should perform excellent. We confirm this trend by comparing the $l = 2$ and $l = 3$ examples. Unfortunately, it is numerically challenging to compute the spectrum for very large l , because the imaginary part scales exponentially and becomes extremely small.

For less compact configurations the number of trapped modes becomes too small and we report larger errors for the reconstructed widths $\mathcal{L}_1(E)$ and $\mathcal{L}_2(E)$. Unfortunately, it is not straight forward to find a reliable estimate of the error, due to WKB theory and the interpolation itself.

Regarding the barrier width $\mathcal{L}_2(E)$ we observe that it is systematically underestimated around the peak of the barrier. The discrepancy decreases with an increasing number of trapped modes. We note that in our previous study in chapter 5, in which we describe the direct problem, we observe a similar trend regarding the imaginary part. Since the Gamow formula is not valid close to the peak of the barrier, but it is extended to this regime, we trace the limited accuracy back to this. We thus conclude that it does not originate from the details of the interpolation.

Since we used two types of ultra compact objects, it is worth to compare the results. Overall, we find better results for constant density stars than for gravastars. Here we comment three aspects. First, the number of trapped modes for this choice of parameters was smaller for gravastars. This means we already expect the method to perform less precise. Second, in our previous work in chapter 5, we observed that the fundamental gravastar mode is underestimated. We can find a similar effect also in the inverse problem, because the width $\mathcal{L}_1(E)$ is underestimated for small E . Third, the extrapolated minimum in the gravastar case is less precise. Since the potential decreases exponentially in the well region, it is very difficult to be reconstructed from the interpolation. As consequence, this has very sensitive impact on the barrier width $\mathcal{L}_2(E)$. Due to the form of the external potential, it has to diverge for $E \rightarrow 0$. At the same time $\mathcal{L}_1(E)$ goes to zero. For reconstructed potentials this scaling means that even small relative errors will cause unphysical deformations for small E . This effect should be disregarded as artifact for small E .

Another property of the WKB treatment of the problem is that “fine structure” in the potential, which is much smaller than the typical region between consecutive modes, can not be resolved. Such a behavior originates from the integral equations, where small deviations are easily averaged out. In the inverse problem one relies in practice on the interpolation of the spectrum, which makes such details not feasible. For the same reason, the extrapolated minimum of the potential well has to be regarded carefully.

6.5 Conclusion

In this work we developed and demonstrated a new method to address the inverse spectrum problem of different types of ultra compact objects. We studied the axial perturbations of non-rotating and static constant density stars and gravastars, as models for ultra compact objects. The inverse method is based on WKB theory and combines the inversion of the classical Bohr-Sommerfeld rule and the Gamow formula in a multiple step procedure.

The real and imaginary parts of the complex eigenvalue spectrum ω_n^2 are used to reconstruct the widths of the potential well and the potential barrier, respectively. This provides two relations for three unknown functions. By assuming Birkhoff's theorem, we have shown that a unique solution can be found. Since the method is based on WKB theory, it is not exact, but stands and falls with its general applicability.

The accuracy of the method has been demonstrated by applying it to the numerically obtained axial QNM spectra of non-rotating constant density stars and gravastars. Depending on the number of trapped modes, the inverse method is able to provide good reconstructions of the widths and the potential itself. However, less precise results are found in situations where our WKB related approximations are not valid. This is the case around the minimum of the potential well and the maximum of the potential barrier. This is not surprising and confirms the findings of our previous study in chapter 5, where we used similar approximations to calculate the QNM spectrum. Because the inverse method is valid for three turning point potentials, we think it could be useful in various other physical situations and is therefore of general interest.

Regarding the astrophysical aspects of our work, the assumption of non-rotating objects is a strong simplification. This is known from works that study the direct spectrum problem and are able to report numerical results for the spectrum. However, there are various technical problems which are not trivial in the context of the inverse problem. First, including rotation changes the simple structure of the Schrödinger equation due to coupling to polar perturbations [164, 165, 235, 288]. Second, for a rotating object, the external space-time is in general not known. A generalized version of Birkhoff's theorem does not exist. Also, polar perturbations itself are more difficult to describe and have a richer spectrum, because of coupling to fluid oscillations. If this type of inverse method can be extended to coupled wave equations, these problems can in principle be addressed in the future.

Finally, we want to relate our work to the ongoing discussion of gravitational wave echoes, that we introduced in Sec. 3.6. If echoes would really be confirmed in future observations, they would be related to ultra compact objects whose underlying physics is not well understood at the time. Since the QNM spectrum can in principle be extracted from the signal, it is in general possible to study the inverse problem. The here presented method and possible extensions could be a viable tool.

6.6 Supplementary Material

6.6.1 Notes about the Implementation

The QNM spectrum of the trapped modes is a discrete set of complex numbers which has to be inter- and extrapolated in the integration schemes. For all systems we studied, the spectrum is well-behaved and allows for such a treatment. If not mentioned differently, we use splines of degree three where interpolation is required.

The maximum of the potential barrier E_{\max} is taken from the Regge-Wheeler potential for the corresponding harmonic index l . For the transmission $T(E)$ we use again splines to interpolate between the first and last trapped mode. Furthermore, we assume that it extrapolates to 1 at E_{\max} and is equal to zero for $E = 0$. The last assumption comes from the fact that the integral in equation (6.4) diverges for $E \rightarrow 0$, because the Regge-Wheeler potential falls off like $1/r^{*2}$ for large r^* . Since the transmission grows exponentially, we use the logarithmic spline interpolation.

Gravastars have an exponentially small $E_{\min} > 0$, but it can happen that the standard extrapolation $n(E_{\min}) + 1/2 = 0$ yields $E_{\min} < 0$. This is only due to the specific choice of extrapolation and we assume a very small, but positive value for $E_{\min} = 1e - 5$. The influence of this choice for larger values of E is negligible. Once again we note that the results for very small E should not be trusted. A negative region in the potential signals the presence of instabilities thus we excluded such cases in the present work. Even though, for the reconstruction of the width $\mathcal{L}_1(E)$ negative values are in general no problem for the method. However, if the external potential has the Regge-Wheeler form, one would not be able to find a unique solution for $V(r^*) < 0$, because there is no third turning point for $E < 0$. Since most potentials of alternative models do not have negative regions, we do not consider such cases here.

For $\mathcal{L}_2(E)$ we additionally take into account the behavior around the minimum and close to the top of the barrier. For the values $E = [E_{\min}, E_0]$ we use $\mathcal{L}_2(E) \approx a + b/\sqrt{E}$. We choose this extrapolation because it takes into account that the Regge-Wheeler potential is proportional to $1/r^{*2}$ for large values of r^* . This corresponds to small values of E and provides the dominant contribution in the width of the Regge-Wheeler barrier. In this case the left side of the barrier falls off much faster than the right side (exponentially). The extrapolation is valid for small E as long as $\mathcal{L}_2(E)$ is much larger as $\mathcal{L}_1(E)$. For the values $E = [E_N, E_{\max}]$, where E_N is the largest trapped mode, we use a simple parabola for $\mathcal{L}_2(E)$. In both cases the parameters are determined from the neighbouring trapped modes.

7 | Wormhole potentials and throats from quasi-normal modes

Breakdown of Contributions

This chapter is based on the publication “*Wormhole potentials and throats from quasi-normal modes*” by Sebastian H. Völkel and Kostas D. Kokkotas, *Class. Quantum Grav.* 35 105018, 2018, [5]. ©IOP Publishing. Reproduced with permission. All rights reserved. My contributions are all the analytic and WKB/Bohr-Sommerfeld related computations. The numerical values to start the inverse problem have been provided by Kostas D. Kokkotas with the same code as in the previous works [1, 2]. The paper writing was done by me, while Kostas D. Kokkotas assisted in the final editing of the manuscript.

Overview

In this work we address the inverse spectrum problem of symmetric double barrier potentials, which appear in multiple non-rotating wormhole models. The inverse spectrum method presented here is an extension of our previous works discussed in chapter 5 and in chapter 6. It is derived in Sec. 4.3.3. We apply the method to the trapped scalar QNM spectrum of the Damour-Solodukhin wormhole [182] and the double Pöschl-Teller potential to demonstrate the precision of the method. Here, we also reconstruct the single parameter λ , which defines this wormhole model. Finally, we also discuss the connection to ultra compact stars, which have a similar QNM spectrum, but a different type of potential. We find that using the trapped QNM spectrum alone, it might not be possible to distinguish both types of objects from each other, but one requires precise knowledge of additional modes. Since the here presented method is valid in the context of the time independent Schrödinger equation with symmetric double barrier potentials, we think it can be of interest for other fields too.

This chapter is organized as follows. After a short introduction in Sec. 7.1, we briefly summarize the inverse method in Sec. 7.2. In Sec. 7.3 we discuss the Damour-Solodukhin wormhole model and the double Pöschl-Teller potential. The application of the inverse method along with the results for the reconstructed throat is shown in Sec. 7.4 and Sec. 7.5. We compare our results with the ones for ultra compact stars in Sec. 7.6. The discussion and conclusions of our findings can be found in Secs. 7.7 and 7.8. We provide additional material in Sec. 7.9.

7.1 Introduction

Wormholes are exotic solutions of general relativity, which also receive attention in the study of gravitational waves from compact objects. We discussed their theoretical motivations in Sec. 2.3.3 and introduced the scalar perturbations of the here studied Damour-Solodukhin (DS) wormhole in Sec. 3.4.1. In this work we use the trapped QNM spectrum of the DS wormhole to reconstruct the effective potential that appears in its wave equation for scalar perturbations. From this we can further recover the position of the wormhole throat, which in the DS wormhole is characterized by a single parameter λ . For some parameter range of λ , the external wormhole geometry approximates the one of the Schwarzschild black hole, which makes the DS model an interesting candidate for a black hole mimicker. The here presented inverse method is an extension of what we developed for ultra compact stars to some type of wormholes. As a proof of principle to demonstrate the inverse method, we apply it to the QNM spectra of the exact DS wormhole potential, as well as to the double Pöschl-Teller (PT) potential, which can be used as an analytical approximation. The QNM spectrum of both potentials have recently been studied [257], where it was shown that the trapped QNM spectrum is encoded in the so-called “echo” signal of the object. Echo signals of this kind are expected to be emitted from a wide range of ultra compact objects, as

we outlined in Sec. 3.6.

The inverse method we present is not limited or specially designed for the study of wormholes. We point out that it is a general inverse method to reconstruct a symmetric double barrier potential $V(x)$ that appears in the one-dimensional wave equation, where E_n is the given spectrum and describes quasi-stationary states. It is of approximate character because it is based on the “inversion” of the classical Bohr-Sommerfeld rule and the Gamow formula, which can be derived from WKB theory, see Sec. 4.3.3. Besides presenting and applying the inverse method, *we also address the uniqueness of the reconstruction and the question under what conditions one can distinguish such a wormhole potential from the typical potential of ultra compact stars.*

7.2 Inverse Spectrum Method

In this section we describe the method being used to reconstruct a symmetric double barrier potential of the type shown in Fig. 7.1, which is derived in Sec. 4.3.3. The potential is assumed to have one local minimum in the potential well and only two global maxima at the barrier. It is possible to use the inverted Bohr-Sommerfeld rule to reconstruct the width of the potential well $\mathcal{L}_1(E)$. The same can be done with the inverted Gamow formula, in combination with $\mathcal{L}_1(E)$, to reconstruct the width of the potential barrier $\mathcal{L}_2(E)$. It corresponds to the width of one of the symmetric potential barriers, if the barriers are not symmetric, the problem is more involved. The new

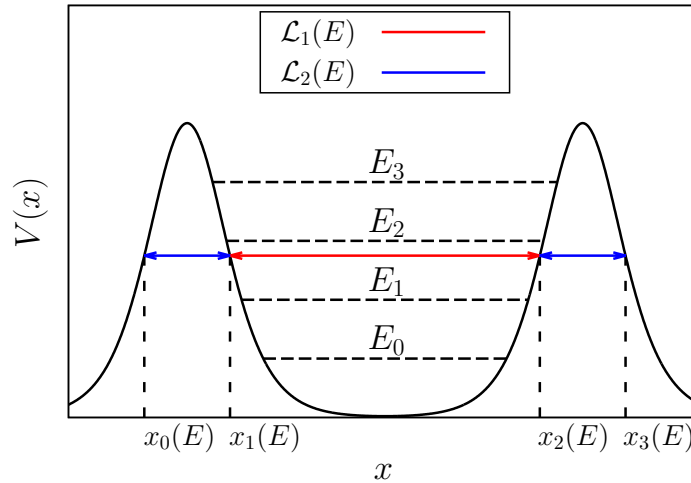


Figure 7.1: Here we show a typical symmetric double barrier potential studied in this work. The red and blue arrows denote the width of the potential well $\mathcal{L}_1(E)$ and individual potential barrier $\mathcal{L}_2(E)$, respectively. The corresponding turning points at the value E are indicated with broken lines. The real parts of the spectrum are shown as E_i . Figure taken from [5].

inverse method is applicable to the one-dimensional wave equation with a symmetric double barrier potential $V(x)$, in which E_n is the corresponding spectrum of quasi-stationary states, see 4.3.3. We again adopt the notation $\omega_n^2 \equiv E_n$. Since we are interested in the trapped modes, one faces an exponentially small imaginary part E_{1n} , while the real part E_{0n} is between the potential well minimum and the maxima of the barriers. Because of this property, one can expand the generalized Bohr-Sommerfeld rule [280, 282] and finds the classical Bohr-Sommerfeld rule describing the real part E_{0n} from the potential well only

$$\int_{x_1}^{x_2} \sqrt{E_n - V(x)} dx = \pi \left(n + \frac{1}{2} \right), \quad (7.1)$$

where (x_1, x_2) are the classical turning points defining the potential well and $n \in \mathbb{N}_0$. The imaginary part E_{1n} then follows from the Gamow formula, which depends on the potential barrier and E_{0n} . Since the real part E_{0n} can again be approximated with the classical Bohr-Sommerfeld rule, the result for the width of the potential well $\mathcal{L}_1(E)$ remains the same as in the case with one barrier eq. (4.67). From here on we again denote E as continuous

real part of E_n and E_{\min} is the minimum of the potential well. If the spectrum is not known as analytic function of n , one has to interpolate it. E_{\min} is not directly known from the spectrum, but can again be approximated from the value where $n(E_{\min}) + 1/2$ extrapolates to zero [274, 284].

To generalize the method to the double barrier potential problem, one has to take into account the contribution of the second potential barrier to the imaginary part E_{1n} , as shown in [280]. The Gamow formula now takes the form

$$E_{1n} = -\frac{1}{2} (T_1(E) + T_2(E)) \left(\int_{x_1}^{x_2} \frac{1}{\sqrt{E_n - V(x)}} dx \right)^{-1}, \quad (7.2)$$

where (x_0, x_1, x_2, x_3) are the four classical turning points for the quasi-stationary case and $T_{1,2}(E)$ are the semi-classical descriptions for the transmission through the potential barriers, respectively. Since the potentials studied in this work are symmetric, the two transmissions are identical and one finds an imaginary part that is two times larger than in the case with only one barrier eq. (4.39). Now one can apply the same inversion of the Gamow formula shown in [285, 286]¹ and finds that the width of one of the potential barriers is given by

$$\mathcal{L}_2(E) = x_1(E) - x_0(E) = \frac{1}{\pi} \int_E^{E_{\max}} \frac{(dT(E')/dE')}{T(E')\sqrt{E' - E}} dE', \quad (7.3)$$

where E_{\max} is the maximum of the potential barriers, which can be extrapolated from $T_{1,2}(E_{\max}) = 1$ or provided otherwise. The transmission is obtained by combining eqs. (4.85) and (4.87). If the spectrum is not known analytically, but as a discrete set of complex numbers, one has to interpolate between the states in order to obtain a discrete function for $T(E)$. From here one can already expect that the accuracy of the reconstruction improves for potentials with a large number of trapped modes compared to ones with a smaller number, as reported in chapter 6.

With the reconstruction of $(\mathcal{L}_1, \mathcal{L}_2)$ one has two equations for four turning points (x_0, x_1, x_2, x_3) . Without additional assumptions that provide two turning points, one can not find a unique reconstruction of the turning points and from this the potential $V(x)$. It actually implies that infinitively many potentials, which must have the same $(\mathcal{L}_1, \mathcal{L}_2)$, yield exactly the same spectrum within the accuracy of the underlying WKB method.

In the case of a symmetric potential, which was assumed to derive the above results, we can use the symmetry to reconstruct a unique potential. For a potential being symmetric around $x = 0$, the turning points are given by²

$$x_0(E) = -\mathcal{L}_1(E)/2 - \mathcal{L}_2(E), \quad x_1(E) = -\mathcal{L}_1(E)/2, \quad x_2(E) = \mathcal{L}_1(E)/2, \quad x_3(E) = \mathcal{L}_1(E)/2 + \mathcal{L}_2(E). \quad (7.4)$$

The reconstructed potential is simply found by inverting the turning points $x_i(E)$ for E .

7.3 Wormhole Models

We have introduced the DS wormhole model in Sec. 3.4.1, but want to connect it here with the double Pöschl-Teller potential that can be used to approximate the perturbation potential. In the case of scalar perturbations of the DS wormhole, one finds that the effective potential of the DS wormhole is given by

$$V_l(r) = \frac{l(l+1)f(r)}{r^2} + \frac{(f(r)g(r))'}{2r}, \quad (7.5)$$

with $f(r) = 1 - 2/r$ and $g(r) = 1 - 2(1 + \lambda^2)/r$. To obtain the form of a double barrier potential, one has to choose small values of λ . In this range of λ , we remind from Sec. 3.4.1 that the following simplification gives a

¹Note that the imaginary part E_{1n} in eq. (4.87) requires the knowledge of the potential between the barriers between the classical turning points (x_1, x_2) , which is not known from the spectrum. However, in the appendix of [2] it was shown that the knowledge of $\mathcal{L}_1(E)$, within the accuracy of the Bohr-Sommerfeld rule, is enough to uniquely describe E_{1n} by choosing any valid potential constructed from $\mathcal{L}_1(E)$.

²If the minimum of the potential well is not located at $x_{\min} = 0$, the derived turning points are all shifted by x_{\min} . The spectrum is of course independent of such a shift.

good approximation for the tortoise coordinate

$$r^* \approx r + 2 \ln \left(\frac{r}{2} - 1 \right) + 2 \left(\ln \left(\frac{4}{\lambda^2} \right) - 1 \right). \quad (7.6)$$

In this case one can relate the position of the throat, described by λ , with the distance L between the two maxima of the potential barriers

$$L \approx 4 \left(\ln \left(\frac{4}{\lambda^2} \right) - 1 \right). \quad (7.7)$$

The Pöschl-Teller potential has a notable history in the study of QNMs of black holes and other compact objects, because it allows for explicit analytical calculations, we refer to [211, 212, 257, 289, 290, 291, 292] for some examples. It has also been used to approximate the QNM spectrum of the DS wormhole [257]. For large separations between the potential barrier, one can treat the full potential either as two single Pöschl-Teller potentials, defined piecewisely on each side, or as their sum, defined on the full range. This three parameter potential can be written as

$$V_{\text{PT}}(x) = \frac{V_0}{\cosh^2(a(x + L/2))} + \frac{V_0}{\cosh^2(a(x - L/2))}, \quad (7.8)$$

where V_0 is the maximum of the potential barrier(s), L is the difference between the two barrier maxima, and a scales the second derivative at the barrier maximum. All three parameters can easily be obtained from the full effective potential of a given model for a given l and λ

$$V_0 \equiv V(r_{\text{max}}^*), \quad a \equiv \sqrt{-\frac{1}{2} \frac{V''(r_{\text{max}}^*)}{V(r_{\text{max}}^*)}}, \quad L \equiv 2r_{\text{max}}^*. \quad (7.9)$$

The parameters (a, V_0) depend strongly on the value of l in the effective potential, while L is a measure for the position of the throat and related to λ , see eq. (7.7). An implicit equation for the analytic solution of the QNM spectrum ω_n is provided in the appendix of [257]

$$e^{-i\omega_n L} = e^{-i\pi n} \frac{\Gamma(1 + i\omega_n/a) \Gamma(\xi - i\omega_n/a) \Gamma(1 - \xi - i\omega_n/a)}{\Gamma(1 - i\omega_n/a) \Gamma(\xi) \Gamma(1 - \xi)}, \quad (7.10)$$

with $\xi \equiv \left(1 \pm i\sqrt{4V_0/a^2 - 1} \right) / 2$.

7.4 Reconstruction of the Potentials

In this section we first briefly show the results of the inverse method applied to the QNM spectrum of the exact DS wormhole potential, as well as to the spectrum of the double Pöschl-Teller potential. In the subsequent Sec. 7.5 we show how the parameter λ , which appears in the wormhole metric and is related to the position of the throat, can be recovered. The extended discussion of our results can be found in Sec. 7.7.

7.4.1 Damour-Solodukhin Wormhole

Here we show the results for the reconstruction of the exact DS wormhole potential with the inverse method. The QNMs being used for the reconstruction are tabulated in Sec. 7.9.2 and have been produced with a modified code that was first presented in [233]. The subsequent Fig. 7.2 shows our result for the reconstructed potential for $\lambda = 10^{-5}$ and $l = 1, 2$. Additional results for $l = 3$ are provided in Sec. 7.9.1.

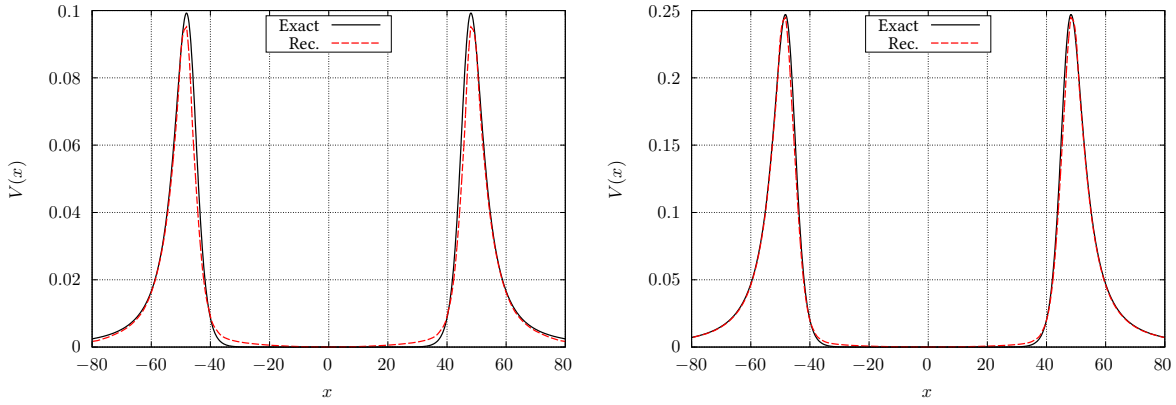


Figure 7.2: In this figure we compare the exact DS potential (black solid) with our results for the reconstructed potential (red dashed) for $\lambda = 10^{-5}$ and different values of l . **Left panel:** Here we show our result for $l = 1$, there are 9 trapped modes. **Right panel:** Here we show our result for $l = 2$, there are 14 trapped modes. Figures taken from [5].

7.4.2 Double Pöschl-Teller Potential

Although the double Pöschl-Teller potential is not a specific wormhole model, it is worth to apply the inverse method to this potential as well, to see how well one can reconstruct it from its trapped QNM spectrum. The QNMs being used for the reconstruction are tabulated in Sec. 7.9.2 and have been obtained by solving eq. (7.10) for ω_n numerically. Fig. 7.3 shows our result for $\lambda = 10^{-5}$ and $l = 1, 2$. The case of $l = 3$ is provided in Sec. 7.9.1. The panels are organized in the same way as for the DS potential in Sec. 7.4.1.

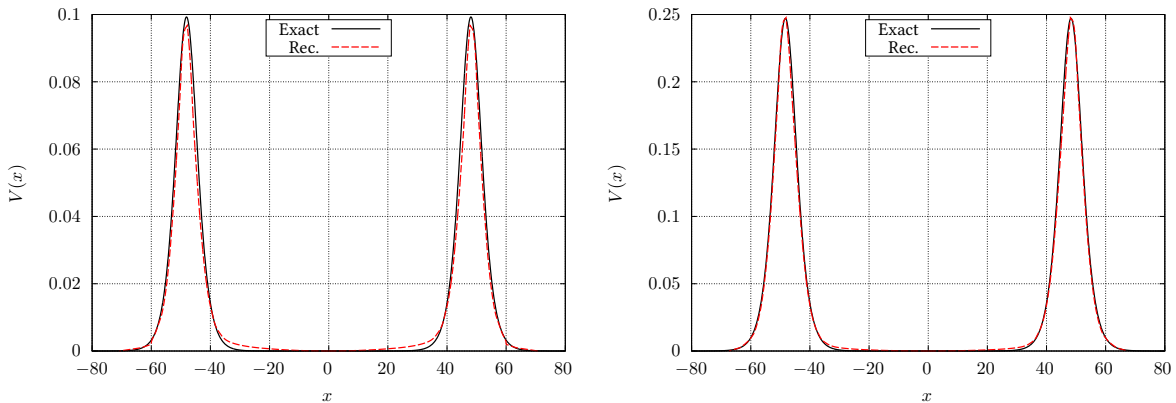


Figure 7.3: In this figure we compare the double PT potential (black solid) with our results for the reconstructed potential (red dashed) for $\lambda = 10^{-5}$ and different values of l . **Left panel:** Here we show our result for $l = 1$, there are 9 trapped modes. **Right panel:** Here we show our result for $l = 2$, there are 14 trapped modes. Figures taken from [5].

7.5 Reconstructing the Throat

Once the DS potential has been reconstructed, we can recover the position of the throat being characterized by the parameter λ . So far we did not have to identify any specific property of the wormhole model for the inverse method³. However, deriving λ from our results only makes sense, if one assumes that the underlying model for the wormhole is now the DS model.

To recover λ in a simple way from the potential, we have chosen to use the distance $\mathcal{L}_1(E)$ evaluated at $E = E_{\max}/2$, which is defined for every l and λ . One can expect that the reconstructed potential is most precise around this region. For small values of E the classical Bohr-Sommerfeld rule is less precise, while for values

³Besides the symmetric double barrier shape.

around the peak of the barriers, the Gamow formula becomes unreliable. For fixed values of $E = E_{\max}/2$ and a given l , we define the following one-dimensional function

$$L_l(\lambda) \equiv x_{2,l}(\lambda) - x_{1,l}(\lambda), \quad (7.11)$$

which for a given l only depends on λ . Here $(x_{1,l}(\lambda), x_{2,l}(\lambda))$ are the classical turning points for a given l at $E = E_{\max}/2$ as function of λ . We can use $L_l(\lambda)$ to bijectively relate the reconstructed width of the potential barrier with the corresponding value of λ . We show $L_l(\lambda)$ for the range of λ being studied in this work in the left panel of Fig. 7.4. The function depends only weakly on l . In order to recover λ from the reconstructed potentials, one only has to solve the following equation for a given reconstructed width of the potential well $\mathcal{L}_1(E)$ (for given l)

$$L_l(\lambda) = \mathcal{L}_1(E_{\max}/2). \quad (7.12)$$

This identification is a simple one which we use to demonstrate the precision one can expect from the method. In principle one could also reconstruct λ with more refined methods, e.g. via χ^2 fitting of the full functions for the reconstructed widths $(\mathcal{L}_1(E; \lambda), \mathcal{L}_2(E; \lambda))$ with the exact ones calculated directly from the DS potential as function of λ . We show the results for the reconstructed values of $\lambda_{\text{rec.}}$ for different parameters in the right panel of Fig. 7.4. Since the number of trapped modes increases with l , it is not surprising that the relative error becomes smaller with increasing l . We provide the tabulated values of the reconstructed values $\lambda_{\text{rec.}}$ along with the relative error in table 7.4 in Sec. 7.9.2. Concluding we want to note, as it is discussed in [182], that the time any perturbation takes to be reflected in the potential well, and thus excite the trapped QNMs, is increasing with smaller values of λ . Thus one should keep in mind that for too small values of λ , the trapped QNMs might be undetectable, since any observation can only cover a finite time interval.

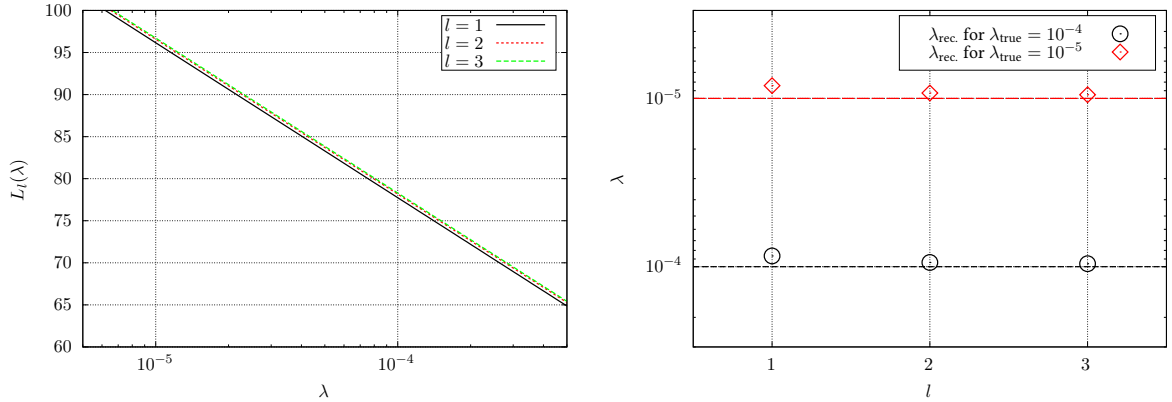


Figure 7.4: Left panel: Here we show the width of the potential well at $E_{\max}/2$ as function of λ for different values of l . Note that the λ -axis is in logarithmic scale. **Right panel:** Here we show the reconstructed values $\lambda_{\text{rec.}}$ (black circles and red diamonds) in the cases of $\lambda_{\text{true}} = 10^{-4}$ (black dashed) and $\lambda_{\text{true}} = 10^{-5}$ (red dashed). The y-axis is in a logarithmic scale, the tabulated values including the errors are provided in Sec. 7.9.3. Figures taken from [5].

7.6 Comparison to Ultra Compact Star Potentials

In this section we discuss and go beyond our results for the reconstructed wormhole potentials from Secs. 7.4 and 7.5. We compare them with similar results for ultra compact star potentials, reconstructed in chapter [2], and ask whether one can distinguish both type of objects from the trapped QNM spectrum only. More precisely, we want to study the following two cases: first case, only the trapped QNMs are known; second case, additional information from the time evolution related to the scattering at the black hole like potential barrier is provided. To answer the question, we first discuss the general case of the two different type of potentials, before we embed

it into the context of echoes from wormholes and ultra compact stars.

Trapped Modes Equivalence

The qualitative behavior of the trapped QNM spectrum for a double barrier potential is the same as for a single potential barrier next to a potential “wall”, which is the situation for ultra compact stars. We call this kind of potential now to be of type I. The double barrier potentials are now called type II. The similarities between the two spectra is self-evident by looking at the Bohr-Sommerfeld rule eq. (7.1) and the Gamow formula for each problem⁴. Thus it seems interesting to ask the following question, for which the spectrum ω_n containing the trapped modes and potentially also the first scattered modes is known. *Can one find two potentials, one of type I and one of type II, that admit the same trapped modes?* In the case of type II potentials studied in this work, we assume the potential to be symmetric around $x = 0$. This assumption for the symmetry allows to reconstruct one unique potential. But without this symmetry, “shifted” or “tilted” potentials with the same widths $(\mathcal{L}_1(E), \mathcal{L}_2(E))$ would also have the same spectrum ω_n . This is valid within the underlying first order WKB theory. The situation for type I potentials is similar. Without the knowledge of one of the three turning point functions, one can find infinitely many different potentials with the same widths and therefore the same spectrum. However, in both cases this non-uniqueness is “just” within the same type of potential. *But, is the same also true between the two different types of potentials? Can one find two potentials of type I and type II that describe the same spectrum?*

To investigate this question, within the accuracy of the underlying WKB methods being used in this work, we can start from a given spectrum ω_n that contains all the trapped modes and potentially the first few scattered modes. Then we insert it into the two inverse methods. If we can construct pathology free widths $(\mathcal{L}_1(E), \mathcal{L}_2(E))$ in both cases, and from this provide at least one specific potential of each type, one can not distinguish the two different types of potentials from the knowledge of their trapped modes only. Again this is only valid within first order WKB theory, but can be seen as a strong hint that exact potentials, which are quite similar, exist as well.

Note that by only looking at the full QNM spectrum (trapped modes and scattered modes), it is not obvious where exactly the trapped modes end and the scattered modes begin. Using the inverse methods, we can extrapolate the maximum of the potential barrier E_{\max} from the point where the semi-classical description of the transmission $T(E)$ extrapolates to 1⁵. Since the Gamow formula for the imaginary part E_{1n} differs by a factor of 2 for the two different types of potentials, see Sec. 7.2, one should expect slightly different values for the maximum E_{\max} . From this it directly follows that one might find a slightly different definition of which modes of the spectrum still belong to the trapped modes and which are the first scattered modes.

With all the previous thoughts in mind, we now show two *trapped spectrum equivalent potentials* in Fig. 7.5. The order of the panels is the same as in the previous Sec. 7.4. We can make several comments. First, due to the different Gamow formulas being used to approximate the transmission, the maximum of the potential barrier(s) differs slightly for both potentials. The maximum of the single barrier type is smaller than the one with two barriers. Second, since the real part is in both cases described by the same Bohr-Sommerfeld rule, it is not surprising that the width of the potential well $\mathcal{L}_1(E)$ is almost the same in both cases, it only differs by how far it is defined with respect to E_{\max} and deviates close to it. Third, the width of the potential barrier(s) $\mathcal{L}_2(E)$ differs close to the barrier maximum, but approaches each other with decreasing E . Note that the type I potential, shown in dashed blue in the right panel, goes only up to E_{\max} . For type I potentials the left side continues to larger values, but it can not be reconstructed with the present method. For this one would need to generalize the inverse method for scattered modes, which is beyond the scope of this work. To summarize this section, *we have shown that two different type of potentials (type I and type II) can have the same trapped mode spectrum.* They differ in the width of the potential barrier(s) and have a slightly different value for the barrier maximum. It might happens that the total number of trapped modes is not the same, e.g. the first scattered mode of type I can be the last trapped mode of type II. All calculations and conclusions are only valid within the precision of the underlying first order WKB method. It would be interesting to verify whether this kind of equivalence is also

⁴Only the imaginary part E_{1n} is modified by a factor of two for symmetric barriers.

⁵The semi-classical description of the transmission $T(E)$ becomes less precise close to the top of the barrier, still it is a useful approximation to extrapolate the peak of the barrier.

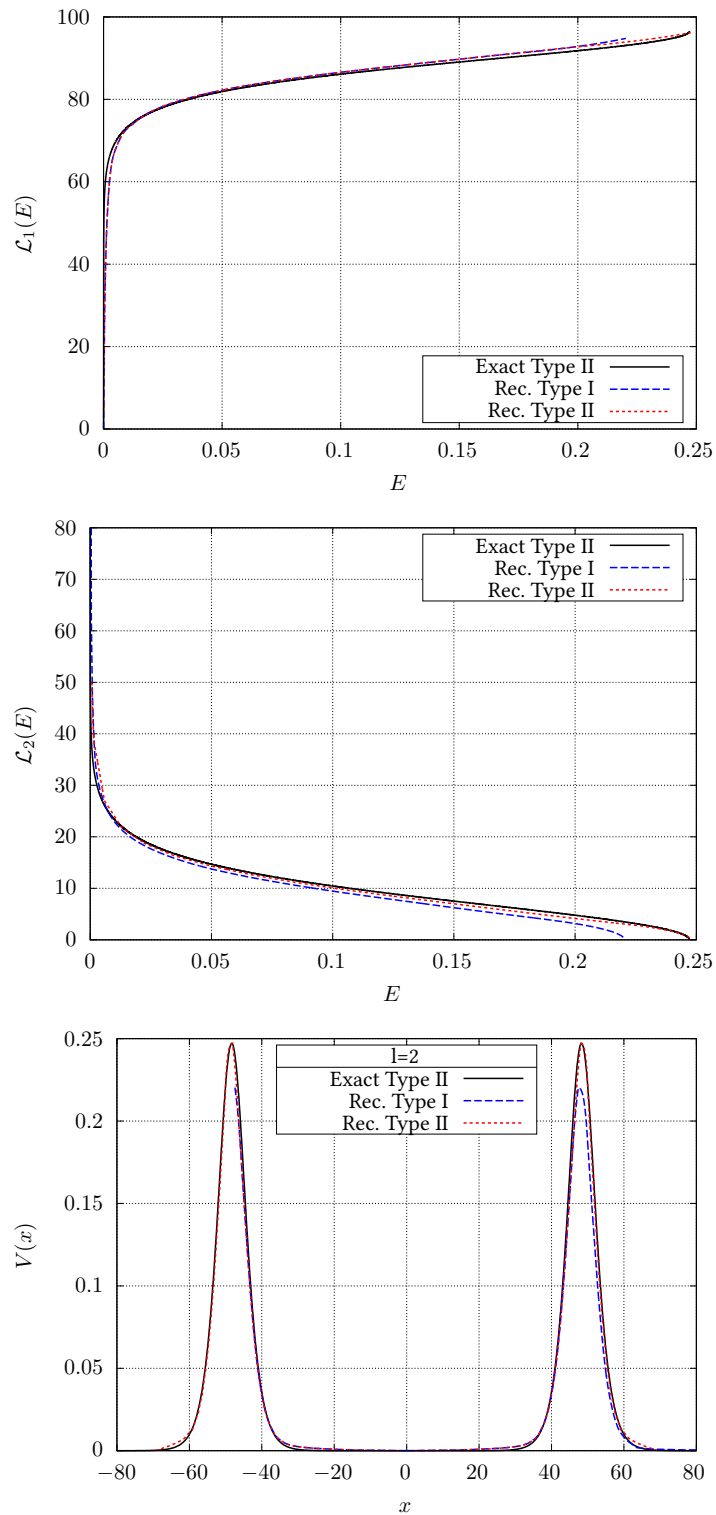


Figure 7.5: Results for the *trapped modes equivalent potentials*, one of potential type I, the other one of type II. The spectrum was obtained from the exact double Pöschl-Teller potential for $\lambda = 10^{-5}$ and $l = 2$, there are 13 trapped modes for type I and 14 trapped modes for type II. The exact Pöschl-Teller case is shown in solid black, the one of type I in dashed blue, and the one of type II in dashed red. **Left panel:** width of the bound region $\mathcal{L}_1(E)$. **Central panel:** width of the potential barrier $\mathcal{L}_2(E)$. **Right panel:** Exact potential and the two reconstructed trapped modes equivalent potentials of type I and II. Figures taken from [5].

true for higher scattered modes and how the exact equivalent potential looks like, but beyond the scope of this work. Since the Bohr-Sommerfeld rule and Gamow formula can be used to obtain quite precise spectra for both type of potentials, one should expect that the exact spectrum equivalent potentials are close to the ones we have presented in this work.

Echoes from Wormholes vs. Ultra Compact Stars

Now we can study the results of the previous section within the question whether one can distinguish a wormhole like object from an ultra compact star like object, if one only knows the trapped QNM spectrum contained in the expected echo signal. The QNMs in the echo signal are in principle all the trapped modes, but eventually also the first few scattered modes. It might also happen, that the last trapped mode coincides with the maximum of the potential barrier and thus could also be interpreted as first scattered mode. Therefore, it is in general not clear which part of the spectrum strictly belongs to the trapped modes and which describes the first scattered modes. Consequently, it might not be clear how many modes one has to use in the reconstruction. Choosing it by the value where the constructed transmission $T(E)$ (for both types of potentials) extrapolates to 1, can lead to two different choices for the last trapped QNM.

Combining all the considerations from the previous section, *one has to conclude that the two types of potentials can not be distinguished without additional information.* However, in the usual discussion of the expected echo signal, one knows that the first pulse of the echo signal is a direct reflection at the (first) potential barrier. This corresponds very well with the fundamental BH QNM⁶ that can be approximated with the Schutz-Will formula [213, 214] or alternative descriptions [210, 211, 212]

$$\omega_n^2 = V_{\max} - i \left(n + \frac{1}{2} \right) \sqrt{-2V''_{\max}}, \quad (7.13)$$

where V_{\max} and V''_{\max} are the values of the potential barrier at the maximum and its corresponding second derivative. The most dominant mode is the fundamental one with $n = 0$. None of the reflected modes is part of the exact QNM spectrum of the ECO, but has to be understood as additional information related to the scattering at the potential barrier. With this additional information one can approximate the maximum of the potential barrier and its second derivative in an independent way and check which of the two reconstructed trapped mode equivalent potentials is the right one. However, precise knowledge of the reflected mode would be required to exclude one of the two potentials.

The situation becomes even more clear, if one allows for additional physical assumptions. For example, in many ECO models, the modifications of the space-time become only important very close to the corresponding Schwarzschild radius, which can be at much smaller distances than the position of the barrier maximum. Thus one would expect most part of the barrier to be similar to the Schwarzschild case and can check which of the two reconstructed barriers fit.

Wormholes vs. Black Holes

Another fundamental question is whether black holes and wormholes (or other ultra compact objects) can in general be distinguished from each other. It has been addressed several times in the literature, see [163, 173, 263, 264, 293, 294, 295] for some examples and the references given in [296]. Some of the findings might seem to be contradicting on the first view, but this is more due to the different types of wormholes being studied. The situation becomes rather clear in cases where an effective perturbation potential can be shown. Wormholes of the DS type, within the parameter range studied in this work, have an effective perturbation potential consisting of a potential well between two potential barriers. It is evident that the QNM spectrum is drastically different compared to a Schwarzschild black hole, whose perturbation potential is a single potential barrier. Therefore one can distinguish these objects from the late time behavior of emitted perturbations. However, there are also other

⁶If the expected barrier is the same as for a BH. This has not to be the case in general, but the methods presented in [210, 211, 213, 214] are valid for any type of potential barrier that can be approximated around the maximum.

wormhole models like the Bronnikov-Ellis wormhole [179, 180], where the effective potential is a single potential barrier, which indeed can mimic the QNM spectrum and late time behavior of regular black holes [294, 295].

7.7 Discussion

In this section we discuss the accuracy of the inverse method from the results we obtained in the previous sections and give a brief outlook regarding actual observations using gravitational wave detectors.

7.7.1 Accuracy

The accuracy is similar to the case of ultra compact stars that we reported in chapter 6. For the reconstructed widths ($\mathcal{L}_1(E)$, $\mathcal{L}_2(E)$) one has to take into account the following aspects. First, the inverse method is a result of the WKB method and therefore *intrinsically* approximate. Second, the total number of trapped modes. Closely related to this is the expectation that the WKB method can become very precise for high values of n , but less precise for small n .⁷ Something similar is true for the semi-classical description of the transmission. It can be quite precise for energy values far below the barrier maximum but becomes less precise if the energy approaches the value of the maximum. We thus observe that the overall accuracy of the reconstructed widths ($\mathcal{L}_1(E)$, $\mathcal{L}_2(E)$) increases with the total number of trapped modes that exist in the potential, but has to be treated with caution close to the minimum of the potential well and close to the maximum of the barrier. Indeed, this behavior has been found in Sec. 7.4. In cases where the widths are reconstructed without any pathologies⁸, it can still happen that the reconstructed potential is unphysical due to “overhanging cliffs”, which can come from the very large values of $\mathcal{L}_2(E)$ for small values of E around E_{\min} .

So far it was assumed that the trapped QNM spectrum is known with pristine accuracy. Unfortunately, any real observation would come with an error which would also influence the reconstruction. Also, by analyzing the time-evolution of echoes, one finds that only the highest trapped QNMs are clearly visible, it will be more difficult to detect the lower ones. However, due to the approximative WKB method and the non-trivial integral equations that have to be solved, it is not obvious how exactly the final result is affected by initial errors on the spectrum. For small errors, which are also always present if one uses numerically obtained spectra, this effect does not play an important role. This view is supported by comparing the reconstructed results from the trapped QNM spectrum of the DS wormhole and the corresponding double Pöschl-Teller potential. In both cases the reconstructed potentials look quite similar. Nevertheless, one essential part of the reconstruction is the inter-/extrapolation being used to define the continuous spectrum $n(E)$ and transmission $T(E)$. These functions can not be arbitrary but must fulfill several conditions to describe a physical system. In the semi-classical description they must be strictly monotone increasing functions of E . As soon as these conditions are not fulfilled, the reconstructed widths can become unphysical, which is a clear sign that the spectrum is erroneous, not originating from this type of potential or the inter-/extrapolation insufficient. A detailed study for cases where the errors are not negligible is a non-trivial task that remains to be done in the future.

7.7.2 Gravitational Wave Detections

Our last discussion is on how well current and next generation gravitational wave detectors could be used to recover the trapped QNM spectrum from the expected echo signal of ultra compact objects. This question has been addressed in recent work of us [3], which we discuss in chapter 10. Here, a parameter estimation for phenomenological echo templates is done. The type of objects studied there are ultra compact stars, not wormholes, but the phenomenological templates that describe the echo signals are similar in both cases [263, 264]. Therefore one can also apply the key results from there to the wormhole case and state that current and next generation gravitational wave detectors are in principle able to detect a few of the trapped QNMs, with non-negligible errors, but probably not all. It will be more complicated to detect the lower trapped modes than the higher ones.

⁷For the bound states in a potential well described by the Bohr-Sommerfeld rule.

⁸E.g. not being strictly increasing/decreasing functions of E .

Because of this, but also due to the lack of concrete physical models that additionally also take into account rotational effects and deviations from axial symmetry, much more work has to be done, if one wants to make realistic statements about ECOs.

7.8 Conclusions

In this work we have successfully extended the inverse spectrum method, which we developed to reconstruct the effective perturbation potentials of ultra compact stars in chapter 6. The inverse method allows to reconstruct symmetric double barrier potentials from the knowledge of the trapped QNM spectrum. We applied the method to reconstruct the effective potential for scalar perturbations of the DS wormhole, which is characterized by symmetric double barriers. Starting from the trapped QNM spectrum of the exact DS wormhole and the double Pöschl-Teller potential approximation, we were able to reconstruct both potentials for different parameters. In the subsequent step we assumed that the underlying wormhole model is the one by Damour and Solodukhin and recovered the λ parameter, which describes the position of the throat, within a few percent.

We also addressed the question whether it is possible to distinguish in principle the double barrier potential of some wormhole models from the potential well with a single barrier that appears for ultra compact stars and gravastars, by using only the trapped modes of the spectrum. To address the question we were able to explicitly reconstruct one potential of each type from the same QNM spectrum. Both potentials have the same trapped QNM spectrum within the accuracy of the underlying WKB theory, and are therefore indistinguishable. However, using that the first pulse of the expected echo signal is independent and additional information being related to the shape of the potential barrier, we argue that one can in principle distinguish them. Note that this additional information is not related to the QNM spectrum of the object, but follows from the time evolution of the scattering at the potential barrier.

The inverse method is approximate since it is based on WKB theory, but has the advantage that it should be possible to extend it to different classes of potentials in the future and to include higher order correction terms for more precise reconstructions. We want to close our conclusions by emphasizing that the presented method is not limited to the study of ultra compact objects, but is applicable to reconstruct symmetric double barrier potentials in one-dimensional wave equations from the knowledge of the quasi-stationary states. Thus it should potentially find applications in other fields as well.

7.9 Supplementary Material

In the following we provide additional results from the reconstruction of the potentials in Sec. 7.9.1 and the tabulated QNMs being used for the reconstruction in Sec. 7.9.2. The tabulated values for the reconstruction of the throat parameter λ , including relative errors, are shown in Sec. 7.9.3.

7.9.1 Additional Figures

Here we provide additional results for reconstructed potentials for $\lambda = 10^{-5}$ and $l = 3$. The reconstruction of the DS and double PT potentials are shown in Fig. 7.6.

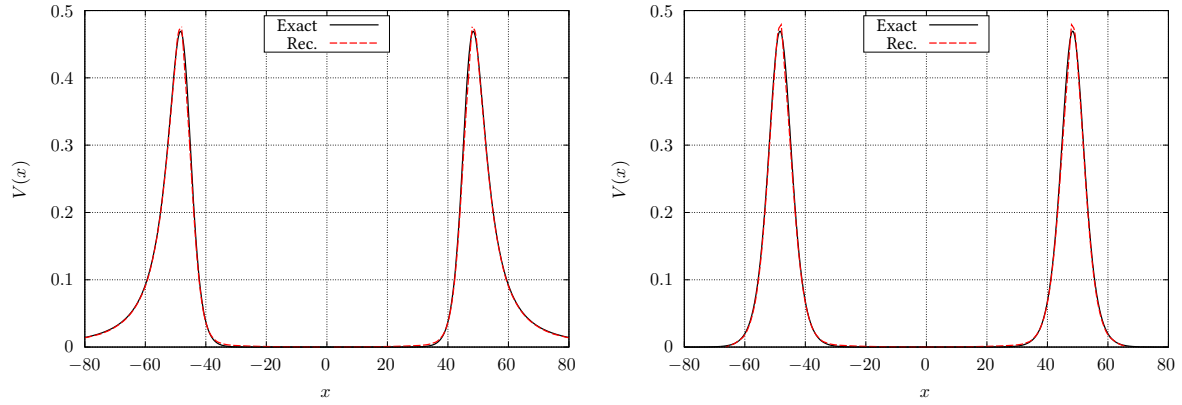


Figure 7.6: In this figure we compare the exact DS potential and double PT potential (black solid) with our results for the reconstructed potential (red dashed) for $\lambda = 10^{-5}$ and $l = 3$. There are 20 trapped modes in both cases. **Left panel:** Here we show our result for the DS potential. **Right panel:** Here we show our result for the double PT potential. Figures taken from [5].

7.9.2 Tabulated quasi-normal modes

In the subsequent tables 7.1, 7.2 and 7.3 we provide the tabulated QNMs that we used in the inverse method. The numerical values of the DS potential were produced by a modified numerical code first introduced in [233], while the spectrum of the double Pöschl-Teller potential can be obtained by solving an implicit equation as shown in [257].

Table 7.1: The trapped QNM spectrum for the DS potential for different values of l and $\lambda = 10^{-5}$. Table taken from [5].

n	$l = 1$		$l = 2$		$l = 3$	
	Re(ω_n)	Im(ω_n)	Re(ω_n)	Im(ω_n)	Re(ω_n)	Im(ω_n)
0	0.0350	1.96e-08	0.0367	6.44e-13	0.0378	6.70e-18
1	0.0698	4.44e-07	0.0731	5.26e-11	0.0755	2.78e-15
2	0.1043	3.30e-06	0.1092	9.03e-10	0.1127	1.10e-13
3	0.1382	1.62e-05	0.1449	8.05e-09	0.1496	1.72e-12
4	0.1715	6.28e-05	0.1801	4.99e-08	0.1859	1.64e-11
5	0.2041	2.08e-04	0.2148	2.47e-07	0.2218	1.18e-10
6	0.2358	6.01e-04	0.2490	1.06e-06	0.2572	6.92e-10
7	0.2667	1.52e-03	0.2827	4.07e-06	0.2922	3.51e-09
8	0.2968	3.30e-03	0.3159	1.43e-05	0.3267	1.58e-08
9			0.3485	4.64e-05	0.3609	6.47e-08
10			0.3805	1.41e-04	0.3947	2.48e-07
11			0.4118	3.95e-04	0.4280	8.90e-07
12			0.4423	1.01e-03	0.4610	3.02e-06
13			0.4721	2.30e-03	0.4936	9.77e-06
14					0.5257	3.02e-05
15					0.5573	8.88e-05
16					0.5884	2.48e-04
17					0.6187	6.45e-04
18					0.6483	1.53e-03
19					0.6773	3.22e-03

Table 7.2: The trapped QNM spectrum for the DS potential for different values of l and $\lambda = 10^{-4}$. Table taken from [5].

n	$l = 1$		$l = 2$		$l = 3$	
	Re(ω_n)	Im(ω_n)	Re(ω_n)	Im(ω_n)	Re(ω_n)	Im(ω_n)
0	0.0441	6.66e-08	0.0467	3.38e-12	0.0486	9.13e-17
1	0.0877	1.69e-06	0.0929	3.55e-10	0.0967	3.31e-14
2	0.1304	1.44e-05	0.1384	7.04e-09	0.1440	1.47e-12
3	0.1719	7.92e-05	0.1828	7.15e-08	0.1903	2.70e-11
4	0.2121	3.37e-04	0.2263	5.10e-07	0.2355	3.03e-10
5	0.2506	1.16e-03	0.2687	2.92e-06	0.2799	2.52e-09
6	0.2876	3.22e-03	0.3102	1.43e-05	0.3234	1.72e-08
7			0.3506	6.16e-05	0.3662	1.00e-07
8			0.3898	2.36e-04	0.4082	5.21e-07
9			0.4277	7.94e-04	0.4494	2.45e-06
10			0.4642	2.26e-03	0.4898	1.06e-05
11					0.5295	4.23e-05
12					0.5681	1.56e-04
13					0.6056	5.24e-04
14					0.6418	1.54e-03
15					0.6769	3.84e-03

Table 7.3: The trapped QNM spectrum for the double Pöschl-Teller potential for different values of l and $\lambda = 10^{-5}$. Table taken from [5].

n	$l = 1$		$l = 2$		$l = 3$	
	Re(ω_n)	Im(ω_n)	Re(ω_n)	Im(ω_n)	Re(ω_n)	Im(ω_n)
0	0.0362	7.28e-07	0.0385	1.70e-09	0.0402	3.67e-12
1	0.0720	3.83e-06	0.0766	9.46e-09	0.0799	2.10e-11
2	0.1071	1.31e-05	0.1139	3.49e-08	0.1189	8.12e-11
3	0.1415	3.91e-05	0.1505	1.14e-07	0.1569	2.80e-10
4	0.1751	1.09e-04	0.1863	3.57e-07	0.1941	9.23e-10
5	0.2077	2.91e-04	0.2213	1.08e-06	0.2306	2.96e-09
6	0.2394	7.26e-04	0.2556	3.19e-06	0.2664	9.26e-09
7	0.2701	1.66e-03	0.2893	9.22e-06	0.3016	2.85e-08
8	0.3000	3.41e-03	0.3224	2.61e-05	0.3363	8.60e-08
9			0.3547	7.18e-05	0.3704	2.56e-07
10			0.3864	1.91e-04	0.4041	7.50e-07
11			0.4173	4.87e-04	0.4373	2.17e-06
12			0.4474	1.16e-03	0.4700	6.15e-06
13			0.4767	2.49e-03	0.5022	1.72e-05
14					0.5340	4.70e-05
15					0.5651	1.25e-04
16					0.5957	3.22e-04
17					0.6255	7.84e-04
18					0.6545	1.76e-03
19					0.6830	3.53e-03

7.9.3 Reconstructed Throat Parameter λ

In table 7.4 we provide the tabulated values for the reconstruction of the throat parameter λ as described in Sec. 7.5. The relative error is defined as $\Delta_\lambda \equiv |\lambda - \lambda_{\text{rec}}|/\lambda$ and provided in the last row.

Table 7.4: The table shows the reconstructed values $\lambda_{\text{rec.}}$ of $\lambda = (1\text{e-}4, 1\text{e-}5)$ obtained by relating the width of the true potential well at $E_{\text{max}}/2$ with the reconstructed one for $l = (1,2,3)$. The corresponding relative error Δ_λ is given in the last row. Table taken from [5].

λ	1e-4			1e-5		
l	1	2	3	1	2	3
$\lambda_{\text{rec.}}$	0.863e-4	0.944e-4	0.960e-4	0.840e-5	0.929e-5	0.951e-5
Δ_λ	0.137	0.056	0.040	0.160	0.071	0.049

8 | On the Inverse Spectrum Problem of Neutron Stars

Breakdown of Contributions

This chapter is based on the publication “*On the Inverse Spectrum Problem of Neutron Stars*” by Sebastian H. Völkel and Kostas D. Kokkotas, *Class. Quantum Grav.* 36 115002, 2019, [6]. ©IOP Publishing. Reproduced with permission. All rights reserved. My contributions are all the analytic and WKB/Bohr-Sommerfeld related computations, as well as the parts on numerical fitting. The numerical values to start the inverse problem have been provided by Kostas D. Kokkotas with a previously existing code. The paper writing was done by me, while Kostas D. Kokkotas assisted in the final editing of the manuscript.

Overview

In this work we revisit axial perturbations of spherically symmetric and non-rotating neutron stars. Although this topic has been object of many studies, it still offers new insights that are of potential interest for more realistic scenarios or in the study exotic compact objects, which have drawn much attention recently. By using WKB theory, we first derive a new Bohr-Sommerfeld rule that allows to investigate the QNM spectrum and address the inverse spectrum problem. The pure analytical treatment of the wave equation is rather involved, because it requires the solution of the TOV equations and the non-trivial tortoise coordinate transformation depending on the underlying space-time. Therefore we provide an easy way to construct potentials that simplifies the analytical treatment, but still captures the relevant physics. The approximated potential can be used for calculations of the axial perturbation spectrum. These results are also useful in the treatment of the inverse problem. We demonstrate this by reconstructing the time-time component of the metric throughout the star and constraining the equation of state in the central region. Our method also provides an analytical explanation of the empirically known asteroseismology relation that connects the fundamental QNM and radius of a neutron star with its compactness.

This chapter is organized as follows. In Sec. 8.1 we first provide a short introduction that summarizes the discussion of the related sections of this thesis. In Sec. 8.2 we review the perturbation potential and the new Bohr-Sommerfeld rule. Its implications for the axial QNM spectrum is then discussed in Sec. 8.3, before we use it to address the inverse spectrum problem in Sec. 8.4. The results we obtain from applying the previously derived methods to constant density stars and polytropes are found in Sec. 8.5. These findings are then discussed in Sec. 8.6. Our conclusions are presented in Sec. 8.7. Sec. 8.8 shows the details for some of the calculations carried out in the main paper.

8.1 Introduction

As motivated in Sec. 2.2, neutron stars are among the most versatile and extreme objects being studied in modern physics. These ultra compact stars confront and join different fields of modern physics, ranging from nuclear and particle physics in their center, up to gravitational and mathematical physics to describe their space-time. With the groundbreaking rise of observational gravitational wave physics using sensitive gravitational wave detectors as LIGO and Virgo [15, 55, 78, 79, 297], there are novel ways to extract information about these objects in addition to electromagnetic observations. The characteristic oscillations of neutron stars, which are going to be measured with increasing precision in the future, can be used in asteroseismology to reconstruct their properties. Along with their typical masses and radii, there is even more interestingly the prospect to constrain the still unknown equation of state in their central regions. It is obvious that the full problem is extremely complicated and not traceable with analytical methods only. Rotation and the absence of axial symmetry lead to complicated

coupled system of equations and non-linear effects call for state of art numerical relativity techniques to simulate oscillating neutron stars, which can currently only be done on short time scales. The unique reconstruction of the underlying equation of state by matching simulations to current and future observations is one of the biggest open problems in neutron star physics, but in reach with current and future gravitational wave detectors.

In the present work we follow a semi-analytic approach, which does not aim to solve the full problem, but to focus and enhance our understanding of the theoretical minimum. The minimum, but still physically reasonable setup, is to study linear perturbations of spherically symmetric and non-rotating neutron stars within general relativity, which we introduced in Sec. 3.3. In this case one finds two types of perturbations, the axial and polar ones. The axial perturbations decouple from the fluid perturbations, which simplifies the analytical treatment, and are therefore the ideal starting point for our studies. In contrast to the fluid oscillations, axial perturbations do not have a Newtonian analogue and are pure oscillations of the space-time [231, 232, 233, 234].

Relating axial and polar perturbations to the unknown neutron star equation of state has also first been studied systematically in the 90s [90, 92, 239, 240], which is related to the field of gravitational wave asteroseismology. A lot of work has also been done in a series of papers by Lindblom [93, 94, 95, 96, 241], who studied the inverse problem for the stellar structure of neutron stars. His approach is not based on the QNM spectrum itself, but on the assumption that the mass radius curve for many neutron stars will be estimated from future observations.

8.2 Perturbation Potential and Bohr-Sommerfeld Rule

As discussed in Sec. 3.3.2, the study of axial perturbations of spherically symmetric and non-rotating stars leads to the one-dimensional wave equation with an effective potential $V(r)$ and w-mode QNM spectrum $\omega_n^2 = E_n$. The potential is characteristic for the underlying type of object and given by

$$V(r) = g_{00}(r) \left(\frac{L}{r^2} + 4\pi (\rho(r) - P(r)) - \frac{6m(r)}{r^3} \right), \quad (8.1)$$

with density $\rho(r)$, pressure $P(r)$, integrated mass $m(r)$, metric function $g_{00}(r) = \exp(2\nu(r))$, and $L \equiv l(l+1)$. The relevant radial coordinate, in which the wave equation takes the simple form, is the tortoise coordinate

$$r^*(r) \equiv \int^r \sqrt{\frac{g_{11}(r')}{g_{00}(r')}} dr', \quad (8.2)$$

where the transformation from r to r^* depends on the metric functions g_{00} and g_{11} . We expand on this relation in Sec. 8.3. The typical axial perturbation potential for neutron stars admits only one classical turning point and the spectrum is complex valued. It is valid for potentials with the qualitative behavior of the type shown in Fig. 8.1. To determine any type of QNM spectrum, appropriate boundary conditions are required emanating from the specific physics of the problem under study. The common ones used for neutron stars are regular solutions at the center and purely outgoing waves at infinity. The perturbation potential of a neutron star with mass M and radius R with $R/M \geq 3$ can qualitatively be described by a purely repulsive potential that diverges at the center of the star and falls off proportional to $\sim 1/r^2$ far away from the object. For stars with constant density or solid crust, $V(x)$ has a discontinuity at the surface, which plays an important role for the QNM spectrum. We show such a potential in Fig. 8.1¹. Note that all other physical properties of the star, such density or pressure are well behaved. The role of discontinuities in the potential has been investigated and pointed out in different works that are related to the QNM spectra of compact stars and black holes [15, 262, 298] and has implications for the significance of QNMs as well as the completeness of the obtained solutions to describe arbitrary perturbations.

¹Here x acts as tortoise coordinate, for which the location where the potential diverges is shifted to $x = 0$.

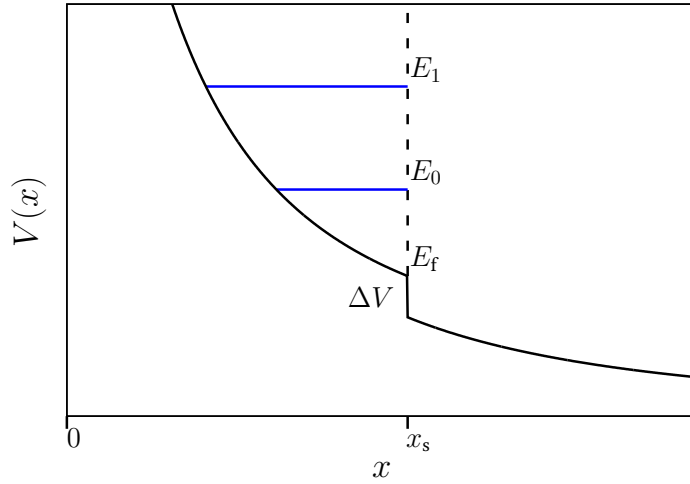


Figure 8.1: The type of axial perturbation potentials being studied in this work. It appears for simple neutron star models. The potential admits a discontinuity ΔV at the surface. As we demonstrate in Sec. 4.2.3, the real part of E_n can effectively be approximated as bound states inside the star. Figure taken from [6].

The Bohr-Sommerfeld rule that we derived in this work for the type of potential shown in Fig. 8.1 has been discussed in Sec. 4.2.3. The derivation can be summarized as follows. The typical potential shown in Fig. 8.1 is split up into one internal region $x \leq x_s$ and one external region $x_s < x$. We write the standard WKB solution for $\Psi(x)$ separately in the two regions and demand that the Wronskian at $x = x_s$ vanishes. This condition, together with the QNM condition of purely outgoing waves and regularity at $x = 0$ determines discrete eigenvalues, if the potential is discontinuous at x_s . Using this procedure yields the complex valued equation

$$\int_{x_0}^{x_s} \sqrt{E_n - V_1(u)} du = \pi \left(n + \frac{3}{4} \right) + i \tanh^{-1} \left(\frac{\sqrt{E_n - V_1(x_s)}}{\sqrt{E_n - V_4(x_s)}} \right), \quad (8.3)$$

where $V_1(x_s)$ and $V_4(x_s)$ are the values of the potential on each side of the discontinuity and $n = (0, 1, 2, \dots)$. It is well known for neutron stars that high eigenvalues grow linearly in the real part, but seem to saturate for the imaginary part. Under this condition one can further simplify the above relation. Assuming a much larger real than imaginary part for E_n , as well as $\Delta V \ll E_n$, one can expand eq. (8.3) into one equation for the real part E_{0n} and a second one for the imaginary part E_{1n}

$$\int_{x_0}^{x_s} \sqrt{E_{0n} - V_1(u)} du = \pi \left(n + \frac{3}{4} \right), \quad E_{1n} = \left(\int_{x_{0,1}}^{x_s} \frac{1}{\sqrt{E_{0n} - V(u)}} du \right)^{-1} \ln \left(\frac{4(E_{0n} - V_4(x_s))}{\Delta V} \right).$$

(8.4)

The relation for the real part looks similar to the classical Bohr-Sommerfeld rule for potential wells, while the second equation predicts a logarithmic scaling for the imaginary part. In contrast to the classical Bohr-Sommerfeld rule, our type of potential admits only one classical turning point $x_0(E_{0n})$ and the upper limit of integration is constant, which followed from the purely outgoing QNM boundary condition. The similarity between both Bohr-Sommerfeld rules is in contrast to the underlying type of potential. This result shows that the real part of the QNMs $E_n = \omega_n^2$ are closely related to the bound states of a potential well contained inside the star, with an infinitely high barrier at the surface.

8.3 Direct Spectrum Problem

In this section we investigate the new modified Bohr-Sommerfeld rule eq. (8.4) and its implications for the axial QNM spectrum of neutron stars.

8.3.1 General Implications

The new Bohr-Sommerfeld eq. (8.4) rule allows to draw some straight forward conclusions about the QNM spectrum. Since the upper turning point always coincides with the surface of the star, and it is known that the potential diverges in the center, the domain of integration for high eigenvalues is confined on a range given by

$$\mathcal{R} \equiv r^*(R) - r^*(0), \quad (8.5)$$

which we call the tortoise radius of the star. For high eigenvalues one can therefore expect a potential independent scaling of the kind ²

$$E_{0n} \sim \frac{\pi^2 n^2}{\mathcal{R}^2}. \quad (8.6)$$

This spectrum looks qualitatively like the one of the infinite box potential with width \mathcal{R} . It is also straightforward to see that the spacing of the real part of $\omega_n = \sqrt{E_n}$ should become constant and scale like

$$\Delta\omega \equiv \frac{\pi}{\mathcal{R}}. \quad (8.7)$$

Exactly this scaling has been found for the asymptotic high frequency behavior of axial and polar modes in [262] by using an alternative WKB analysis. In the same work, it was also shown how discontinuities in the derivatives of the potential can affect the QNM spectrum. In contrast to our result, no Bohr-Sommerfeld rule has been reported, but a direct approximation for high eigenvalues. We want to emphasize that the modified Bohr-Sommerfeld rule eq. (8.4) can also be applied to lower eigenvalues. In addition, it is very versatile for analytic studies related to the inverse spectrum problem, because it can be inverted to constrain the potential from the QNM spectrum.

The appearance of \mathcal{R} instead of R calls for two comments. First, for less compact stars, both scale similar and the difference is only logarithmic. Increasing R corresponds to increasing \mathcal{R} . This situation has been discussed in the literature [235] and one might think of \mathcal{R} as quantitative correction. Second, the more compact the object is, the stronger is not only their quantitative difference, but also their qualitative behavior. Going to very compact objects, which means decreasing R (fixed M), changes the behavior and results in increasing \mathcal{R} at a critical value, which depends on the equation of state (because the tortoise transformation given by eq. (8.2) inside the star depends on it). We discuss this observation in detail in Sec. 8.5.3 and in Sec. 8.8.1, where we also introduce a linear relation for the tortoise transformation $r^*(r)$ that turns out to be very useful for normal neutron star compactness.

8.3.2 Universal Relation

In the literature it is well known that the real part of the fundamental axial QNM follows a simple universal scaling that can be described as

$$\text{Re}(\omega_f)R = A - B\frac{M}{R}, \quad (8.8)$$

where (A, B) are constants whose numerical values do not follow from first principles. Such a linear behavior has been reported for polar and axial QNMs [90, 240]. This has been done for neutron stars using different equations of state, in general relativity, as well as alternative theories of gravity [299, 300]. The explanations for the scaling are of qualitative character, e.g. the coupled string toy model presented in [229] or considering the modes to be trapped in the star, due to the space-time curvature and being partially reflected at the potential discontinuity that appears at the surface [235]. The new Bohr-Sommerfeld rule can improve the situation a bit and we can provide a more satisfying reason for the scaling. Since the QNM spectrum is obtained from integrating the potential

²If one neglects terms of the order $\sim V(x)/E_n$ and higher.

inwards, starting at the surface, one would expect that the real part of the fundamental QNM should be close to the surface value of the potential. Unfortunately our Bohr-Sommerfeld rule is not able to find a precise value for the fundamental QNM. The derivation of the rule only applies for QNMs that are related to the region above the discontinuity, but does not allow to make any conclusion of possible QNMs that exist around this value or below. On the other hand, one can argue that the value of the fundamental mode $\text{Re}(\omega_f^2)$ should also not be too far away from the value of the potential at the surface, because one knows from numerical results reported in the literature that the eigenvalues of the spectrum follow a systematic pattern. Since one might not trust the WKB method in this delicate situation, we have treated the internal and external potential regions with two potentials that have the right asymptotic $1/r^2$ behavior for small and very large values of the tortoise coordinate, and might be matched smoothly or discontinuously at the surface. Applying the standard QNM conditions along with the Wronskian at the surface, one finds an involved equation, which however, can be solved numerically once the parameters of the model are provided. With this approach we can locate the fundamental QNM that is found numerically, but is missing within the Bohr-Sommerfeld rule. We can confirm that its real part is close to the surface value of the potential. Making the identification that it should correspond to the value of the Regge-Wheeler potential at the surface, the predicted universal scaling between the fundamental mode and the compactness M/R follows directly and is given by

$$R\sqrt{\text{Re}(\omega_f^2)} = \sqrt{\left(1 - \frac{2M}{R}\right)\left(L - \frac{6M}{R}\right)} \approx \sqrt{L} - \left(\frac{3+L}{\sqrt{L}}\right)\frac{M}{R} + \mathcal{O}\left(\left(\frac{M}{R}\right)^2\right), \quad (8.9)$$

which is functionally closely related to the empirical relation eq. (8.8). In the linear case and assuming that $\sqrt{E_f} \approx \text{Re}(\omega_f)$, the functional form coincides. We show results for this prediction in Sec. 8.5.2.

8.3.3 Approximate Potential

One major difficulty in the pure analytic treatment of the perturbation problem is that the simple form of the wave equation only appears in the tortoise coordinate. Making explicit use of it is almost impossible, since it is related to an integral over the metric functions g_{00} and g_{11} , which for most equations of state can only be obtained numerically by solving the TOV equations. In this section we show how the perturbation potential can be simplified significantly, without affecting the spectral properties to a good precision. To do so we make use of three things. First, for the compactness of normal neutron stars, the tortoise coordinate transformation can be approximated very well with a linear function and is explicitly known, once \mathcal{R} has been obtained. Second, only the first few QNMs correspond to the region of the potential far away from the center. Especially the internal classical turning point of the asymptotic part of the spectrum is located very close to the center. Third, in the central region one can expand all functions that appear in the potential and keep only dominant terms. Details for these approximations and calculations are provided in Sec. 8.8.1 and in Sec. 8.8.2. Making use of all three observations allows one to write the wave equation explicitly in a shifted³ tortoise coordinate u^* in the very simple form

$$V(u^*) = C_0 + \frac{C_2}{u^{*2}}, \quad (8.10)$$

with

$$C_0 = e^{2\nu_0} [v_2 L - 4\pi(\rho_0 + P_0)], \quad \text{and} \quad C_2 = L e^{2\nu_0} \left(\frac{\mathcal{R}}{R}\right)^2, \quad (8.11)$$

where ν_0, v_2, ρ_0 and P_0 come from the expansion of the metric potential $\nu(r)$, defined via $g_{00} = e^{2\nu(r)}$, the density ρ , and the pressure P , in the center of the star. We provide details of the expansion in Sec. 8.8.2. For central potentials one can use the Langer correction [280] to push the precision for small l , which means to

³The coordinate is shifted such that the potential diverges at $u^* = 0$, which simplifies the following calculations.

replace the factor $L = l(l+1)$ with $(l+1/2)^2$. Applying the new Bohr-Sommerfeld rule eq. (8.4) to the potential eq. (8.10) yields

$$\sqrt{(E_{0n} - C_0)\mathcal{R}^2 - C_2} + \sqrt{C_2} \left(\arctan \left(\frac{\sqrt{C_2}}{\sqrt{(E_{0n} - C_0)\mathcal{R}^2 - C_2}} \right) - \frac{\pi}{2} \right) = \pi \left(n + \frac{3}{4} \right). \quad (8.12)$$

It can either be solved for E_{0n} numerically for a given value of n or be expanded for high eigenvalues. The latter one predicts a polynomial behavior

$$E_{0n} \approx An^2 + Bn + C, \quad (8.13)$$

with

$$A \equiv \frac{\pi^2}{\mathcal{R}^2}, \quad B \equiv A \left(\sqrt{C_2} + \frac{3}{2} \right), \quad C \equiv C_0 - \frac{C_2}{\mathcal{R}^2} + A \left(\frac{C_2}{4} + \frac{3\sqrt{C_2}}{4} + \frac{9}{16} \right). \quad (8.14)$$

From this it is straight forward to see that the scaling for very high eigenvalues is to leading order as expected from eq. (8.6). Especially the relation eq. (8.7) for the spacing of the real part of the QNMs $\Delta\omega_n = \Delta\sqrt{E_n}$ converges to π/\mathcal{R} , as found in [262]. The results of this section applied to polytropes are shown in Sec. 8.5.

8.4 Inverse Spectrum Problem

In this section we discuss the inverse spectrum problem, which aims to reconstruct parameters of the source from the knowledge of the spectrum. It is split up in three parts. In Sec. 8.4.1 we first discuss the inversion of the new Bohr-Sommerfeld rule to find the underlying perturbation potential. The second part in Sec. 8.4.2 uses the results obtained from the approximated potential to reconstruct the fundamental parameters related to the potential. Finally, in 8.4.3 we show how the previously obtained results can be used to recover the g_{00} component inside the star, and how the equation of state can be constrained.

8.4.1 Inverting the Bohr-Sommerfeld Rule

As we have shown in Sec. 4.3, different types of Bohr-Sommerfeld rules can be used to constrain the widths of potential wells, barrier, and some combinations. For the present case demonstrated in Sec. 4.3.3, the inversion yields the distance $\mathcal{L}(E)$ from the surface of the star r_R^* , which is the same for all E , to the internal turning point $r^*(E)$ as

$$\mathcal{L}(E) \equiv r_R^* - r^*(E) = 2 \frac{\partial}{\partial E} \int_{E_{\min}}^E \frac{n(E') + \frac{3}{4}}{\sqrt{E - E'}} dE', \quad (8.15)$$

where $n(E)$ is the spectrum written as function of E . We use the lowest provided eigenvalue for E_{\min} , which corresponds to $n(E_{\min}) = -3/4$. Once the discrete spectrum is provided, $n(E)$ has to be interpolated. This introduces some non-uniqueness to the problem, but the spectrum is usually well behaved and different interpolations do not cause major differences. For more details we refer to the discussions presented in chapter 6 and in chapter 7. This observation is in agreement with the integral character of the Bohr-Sommerfeld rule, which is “blind” to small deviations in the potential, if they average out between consecutive n .

The associated turning point $r^*(R)$ at the surface of the star is uniquely determined from the external tortoise coordinate transformation if (M, R) are known. In this case, the perturbation potential inside the star follows uniquely from inverting eq. (8.15) for E , which can also be done numerically. Therefore, within the approximations being done to derive the Bohr-Sommerfeld rule, the perturbation potential is in principle explicitly known, if the QNM spectrum is provided. In Sec. 8.5 we show the results for the reconstructed potentials of constant density stars and polytropes.

8.4.2 Recovering Fundamental Parameters

The previously presented inversion of the Bohr-Sommerfeld rule transforms consecutive QNMs, starting from the fundamental one, to the potential. Because it was derived on rather general properties of the potential, it requires a precise knowledge of the spectrum, due to the involved interpolation. An alternative approach for applications in neutron stars, where additional properties of the potential can be imposed, is described in the following.

In Sec. 8.3.3 we presented an approximation for the perturbation potential and showed its Bohr-Sommerfeld spectrum. Using this result it is possible to reconstruct the fundamental parameters of the potential (\mathcal{R}, C_0, C_2) from the spectrum, if (M, R) are provided. Because the number of parameters is small, it is not necessary to assume that many QNMs are known. Since the Bohr-Sommerfeld spectrum is not exact, one expects that the reconstructed parameters differ slightly. As it is evident from the polynomial expansion of E_{0n} in eq. (8.13), one would expect that the parameters related to (A, B, C) might not be reconstructed equally well, since the precision of the underlying WKB method is more precise for high eigenvalues, where A dominates, and not very precise for small n , where C is important. Using $n(E_{0n})$ to fit a given spectrum, instead of the polynomial expansion, yields better results and is given by

$$n(E_{0n}) = \frac{1}{\pi} \left(-\frac{3}{4} + \sqrt{(E_{0n} - C_0)\mathcal{R}^2 - C_2} + \sqrt{C_2} \left[\arctan \left(\frac{\sqrt{C_2}}{\sqrt{(E_{0n} - C_0)\mathcal{R}^2 - C_2}} \right) - \frac{\pi}{2} \right] \right). \quad (8.16)$$

The reconstruction of (\mathcal{R}, C_0, C_2) imposes stringent constraints on the underlying equation of state. It is highly unlikely that for fixed (M, R) two different equation of states, which are intersecting in the mass-radius diagram, will also agree for these reconstructed properties. While \mathcal{R} is an averaged property obtained by integrating $\sqrt{g_{11}/g_{00}}$ throughout the whole star, C_2 can directly be used to obtain the g_{00} component of the metric at the center $r = 0$. The knowledge of C_0 allows in principle to relate the central pressure as function of the central density. We show results for this in in Secs. 8.5.5 and 8.5.6.

8.4.3 Recovering $P(r)$ and $\nu(r)$

In the previous section we have shown how the perturbation potential can approximately be reconstructed from the QNM spectrum. As it was recently discussed in [301], the knowledge of the potential has crucial implications for the stellar structure, which is described by the TOV equations. This system of equations is usually solved by integrating from the center of the star towards the surface, where the metric is matched with the external Schwarzschild solution. This requires the equation of state throughout the star, as well as the central pressure or density. Now, if the perturbation potential is known and used in the rewritten TOV equations, the stellar structure, as well as the equation of state can be determined by integrating the TOV equations inwards (assuming (M, R) are also known). Although our method allows to reconstruct the perturbation potential from the spectrum, it might turn out not to be precise enough for such a treatment and then requires a more refined study, which is beyond the scope of this work. Nevertheless, we are able to show that the equation of state in the central region can be constrained by assuming that (M, R) are known and ν_0 has been reconstructed to good precision from the spectrum, as described in the previous section. A close look on $\nu(r)$, obtained from the TOV equations for different neutron stars, suggests that the expansion shown in [227] could be a good approximation throughout the whole star, as long as there are no local effects. From (M, R) one can directly provide the metric functions $\nu_R \equiv \nu(R)$ and $\nu'_R \equiv \nu'(R)$ at the surface, by matching it with the external Schwarzschild space-time. Using the reconstructed value of ν_0 , one can directly deduce (ν_2, ν_4) , which imprint information of the equation of state in the central region

$$\nu_2 = \frac{4}{R^2} (\nu_R - \nu_0) - \frac{\nu'_R}{R}, \quad \nu_4 = \frac{2\nu'_R}{R^3} - \frac{4}{R^4} (\nu_R - \nu_0). \quad (8.17)$$

Table 8.1: Parameters of the studied polytropic neutron star models. Table taken from [6].

Model	M [km]	M [M_{\odot}]	R	C	K	γ	ρ_c
Poly A	2.0666 km	1.3991 M_{\odot}	14.1466 km	0.1461	100	2	8.925×10^{14} gr/cm ³
Poly B	2.4161 km	1.6357 M_{\odot}	11.3831 km	0.2123	100	2	2.482×10^{15} gr/cm ³

Once v_2 is known, one has an approximation for the central pressure P_0 as function of the central density ρ_0 , as well as the pressure $P(r, P_0)$ in the central region

$$P_0(\rho_0) = \frac{v_2}{4\pi} - \frac{\rho_0}{3}, \quad P(r, P_0) = P_0 - r^2 \left(\frac{3v_2^2}{8\pi} - P_0 v_2 \right). \quad (8.18)$$

Note that this reconstruction leaves some ambiguity, since it only allows to reconstruct a combination of central pressure and density, not their absolute values. However, it allows to approximate an upper limit for the central pressure, which appears for $\rho_0 = 0$, as well as an upper limit for the central density, which appears for $P_0 = 0$. They are given as

$$P_{0,\max} = \frac{v_2}{4\pi}, \quad \rho_{0,\max} = \frac{3v_2}{4\pi}. \quad (8.19)$$

We show the results for the here discussed approach in Sec. 8.5.6.

8.5 Results

In this section we present the results of the semi-analytic methods that were derived in the previous sections. In most cases we show two different polytropes and provide in some cases constant density stars as toy model for ultra compact stars. The basic parameters of the polytropes can be found in Table 11.1. The precise numerical data for the QNM spectra is provided from a code first presented in [233]. The polytropic equation of state is defined as

$$P = K\rho^\gamma. \quad (8.20)$$

8.5.1 Calculating the Spectrum

In the following we compare the predicted spectrum of the new Bohr-Sommerfeld rule eq. (8.4) by using the approximated potential eq. (8.12) with precise numerical data. The left panels of the subsequent Figs. 8.2, 8.3 show the spectra of two different polytropes, each for $l = 2$ and $l = 3$. The relative errors are defined as usually and shown in the right panel of the same figures. As it is expected from WKB theory, the overall accuracy improves for increasing n . The approximated potential resembles the true potential more and more for large l , thus the precision also increases for larger l . It is surprising that the method provides quite accurate predictions even for small n and l where the performance of the method is worst.

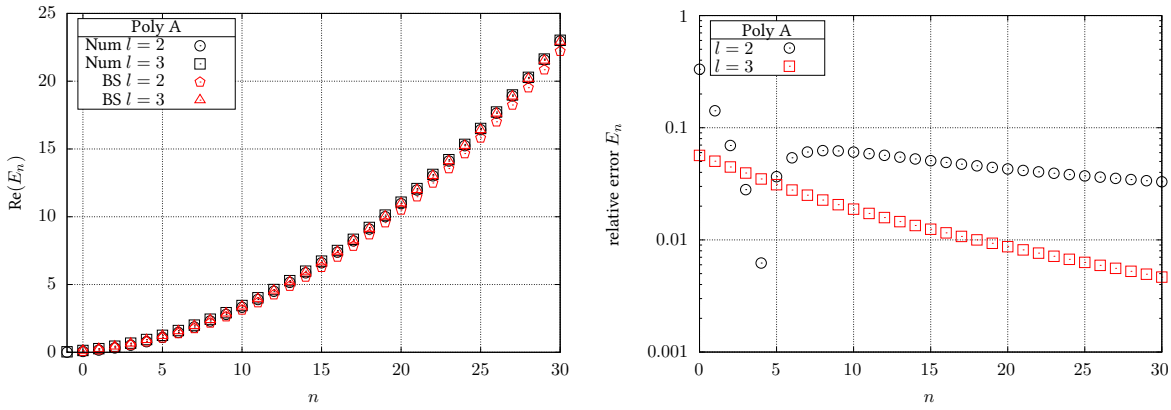


Figure 8.2: Left panel: Shown is the real part of the spectrum E_n for $l = 2$ and 3 for the polytrope model A, precise numerical values (black symbols) are compared to the Bohr-Sommerfeld prediction (red symbols). **Right panel:** The relative error of the spectrum is shown for $l = 2$ (black circles) and $l = 3$ (red boxes). Figures taken from [6].

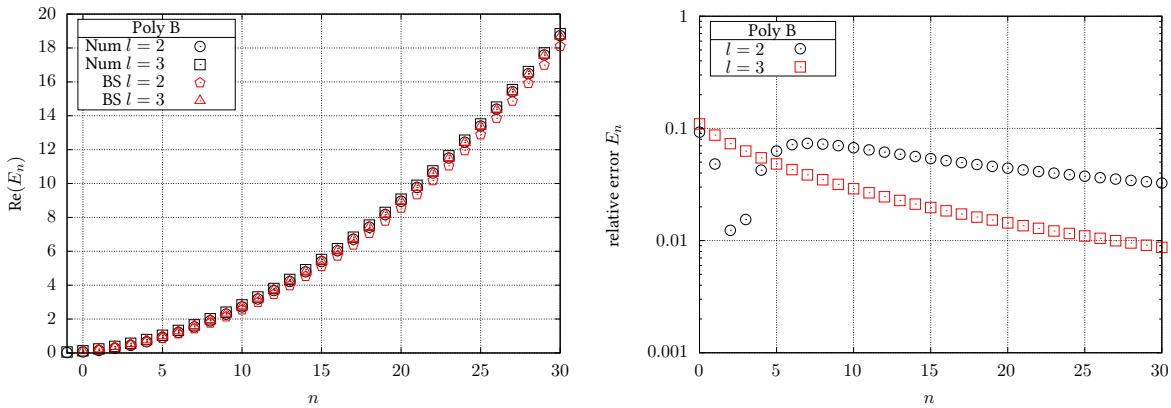


Figure 8.3: Left panel: Shown is the real part of the spectrum E_n for $l = 2$ and 3 for the polytrope model B, precise numerical values (black symbols) are compared to the Bohr-Sommerfeld prediction (red symbols). **Right panel:** The relative error of the spectrum is shown for $l = 2$ (black circles) and $l = 3$ (red boxes). Figures taken from [6].

8.5.2 Universal Relation

Here we compare the proposed universal relation for the fundamental axial QNM eq. (8.9) with exact values for different compact stars. The results are shown in Fig. 8.4. We recall that the distribution of numerical values around the empirically known fitting formula shows that the relation depends slightly on the equation of state and is not exact. For $l = 2$ we compare the empirical fit [240] with some examples for constant density stars, polytropes and the realistic equation of states used in the same work. Considering that the exact values are not exactly described by the empirical linear fit, our analytic estimate yields a good prediction and also takes into account the non-linear slope for large compactness, which is shown for constant density stars. This non-linear scaling with respect to the compactness, described in eq. (8.9), becomes more significant for higher l , both in our analytic estimate and for constant density stars. Overall, our relation slightly underestimates the true values. However, the estimate goes beyond the linear approximation, which was found only empirically in the literature [90, 240, 299, 300], and explains that the fundamental axial QNM can be approximately “identified” with the value of the perturbation potential at the stellar surface.

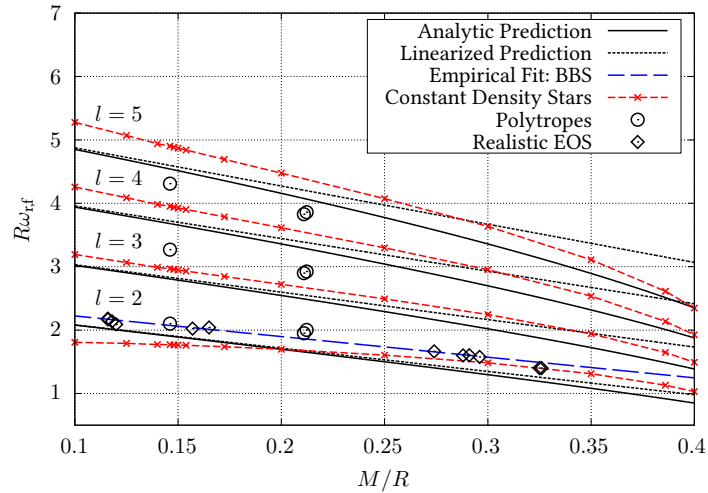


Figure 8.4: In this figure we show the universal relation (black solid) described in eq. (8.9) as well as its linearized form (black dashed) for $l = 2, 3, 4$ and 5 . The data points correspond to precise numerical values for different constant density stars (red dashed), polytropes (black circles), and different realistic equation of states (black diamonds) taken from [240]. The empirical fit for $l = 2$ (blue dashed), known from [240], is shown with the corresponding realistic equation of state results (black diamonds) used in the same work. Figure taken from [6].

8.5.3 Spacing of Modes

The π/\mathcal{R} spacing of modes is an interesting property and was first found in [262] using another WKB approach. In the same work, polar oscillations are considered as well. Including them in the Bohr-Sommerfeld rule is not straight forward, due to the coupling to fluid oscillations. However, the authors report that for large eigenvalues a similar scaling appears. In this section we verify the asymptotic spacing of the polytrope QNM spectra by using numerical data, we show that the spacing of modes should first increase with increasing compactness, as it is known in the literature, but then shrinks again for ultra compact stars. To our best knowledge, this varying behavior for ultra compact systems has not been pointed out anywhere.

Test of the Constant Spacing

In Fig. 8.5 we verify the constant spacing relation $\Delta\omega = \pi/\mathcal{R}$ for high eigenvalues. The left panel shows the absolute numbers for two different polytropes, while the right panel contains the relative errors. For comparison we include the rough estimate π/\mathcal{R} , which is known in the literature [235] for less compact systems. As it is evident, the π/\mathcal{R} spacing of modes is by far only a rough estimate, the deviations compared to \mathcal{R} are significant. Note that it predicts a larger spacing for Poly B compared to Poly A, while the opposite is true. Since the π/\mathcal{R} estimate is valid for less compact objects, it is not surprising that it fails completely for compact objects. However, the π/\mathcal{R} prediction is extremely precise fulfilled. The saturation of the relative errors is around 0.1 % for $n = 30$ and might indicate the precision for the high eigenvalues that were obtained numerically. Note that the spacing for the $l = 3$ modes is already around 0.1 – 1 % for $n = 5$.

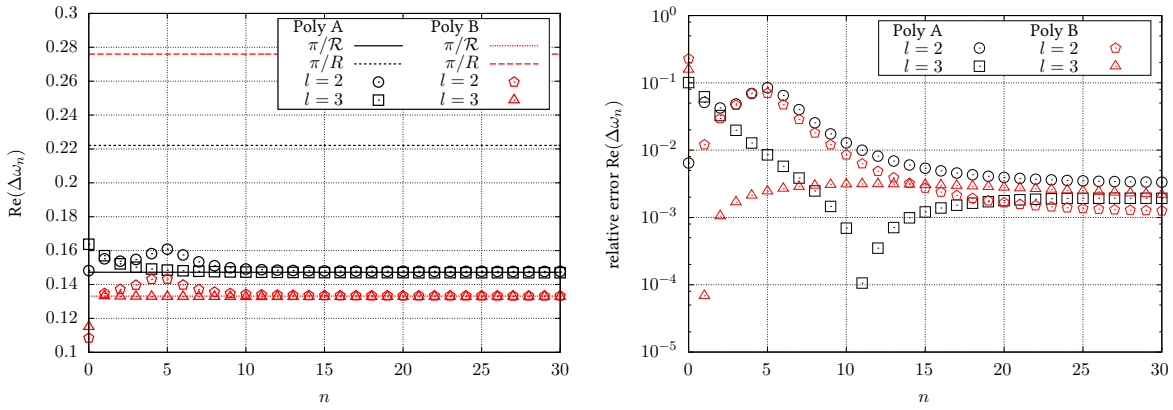


Figure 8.5: Here we compare the predicted spacing of neighboring modes for two polytrope models A and B for $l = 2$ and 3 modes. **Left panel:** The Bohr-Sommerfeld prediction (solid lines) is compared with the rough estimate from the literature (dashed lines) and numerical data (symbols). **Right panel:** The relative error between the Bohr-Sommerfeld prediction and the numerical data. Figures taken from [6].

Predicted Maximum Spacing of Modes

As discussed in Sec. 8.3.1, we expect that the asymptotic spacing as function of \mathcal{R} should have a maximum, because for fixed mass, $\mathcal{R}(R)$ is likely to have a minimum for very compact configurations. Verifying this expectation in a general case is not easy, since \mathcal{R} depends on the solutions of the TOV equations, which have to be obtained numerically in most cases. However, for constant density stars, which can exist for any radius larger than the Buchdahl limit of $R/M = 9/4$, it can easily be confirmed. We show the explicit result for constant density stars in Fig. 8.6. In this case one can analytically find the relation for $\mathcal{R}(R)$, which is shown in the left panel and follows from $r^*(r)$ derived in [255]. The right panel shows the predicted spacing for large modes, along with numerical data for different compactnesses. The asymptotic behavior for non-compact stars is already known in the literature as $\Delta\omega \approx \pi/R$ and was reported in [235]. The agreement in the ultra compact case is excellent and beyond the approximative nature that might be expected. The maximum value appears for $R \approx 3.86$, which seems not to be related to any special physical property of the star or the potential. Trapped modes, for which the potential admits a quasi-bound region, start to appear for more compact stars. Note that the spacing alone can not be used to uniquely determine the compactness of a star, since there are two possibilities, but their fundamental modes are significantly different. The two possible values for the tortoise radius \mathcal{R} that correspond to the same spacing $\Delta\omega$ can therefore in practice be distinguished by considering their fundamental mode, as discussed in Sec. 8.5.2.

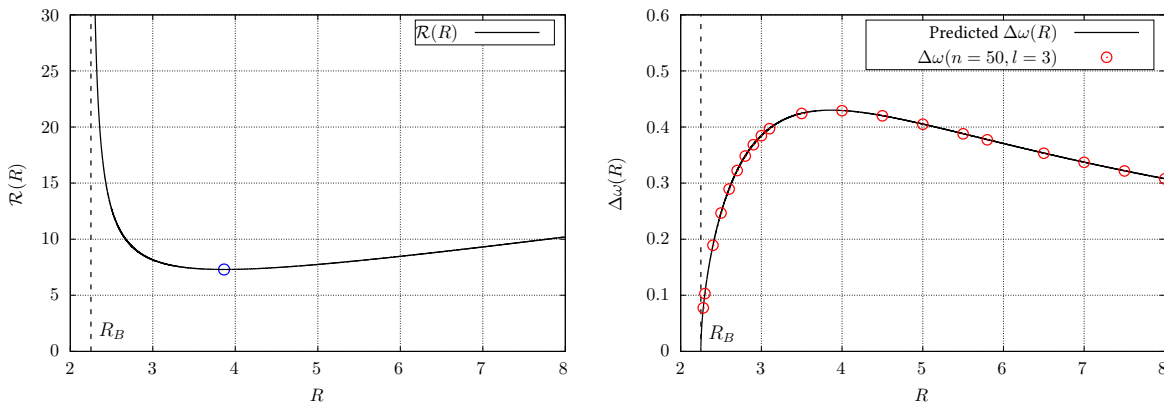


Figure 8.6: In this figure we show a sequence of constant density stars with $M = 1$. The Buchdahl limit R_B is indicated in both panels as dashed line. **Left panel:** The exact relation for $\mathcal{R}(R)$ is provided along with the minimum value of \mathcal{R} as blue dot at $R \approx 3.86$. **Right panel:** Here we compare the predicted spacing $\Delta\omega = \pi/\mathcal{R}$ with numerical values for different R and $l = 3$, evaluated at $n = 50$. Figures taken from [6].

8.5.4 Reconstruction of the Potential

By inverting the Bohr-Sommerfeld rule it is possible to reconstruct the internal perturbation potential once the spectrum is known. Here we show the results for an ultra compact constant density star and one of the polytropes. In the left panel of Fig. 8.7 we show the reconstructed potential for the constant density star with $R = 3M$. The right panel of the same figure contains the reconstructed potential of Poly A. Deviations to the true potential are visible, but small. The steep rise at $r^*(0)$ is precisely captured.

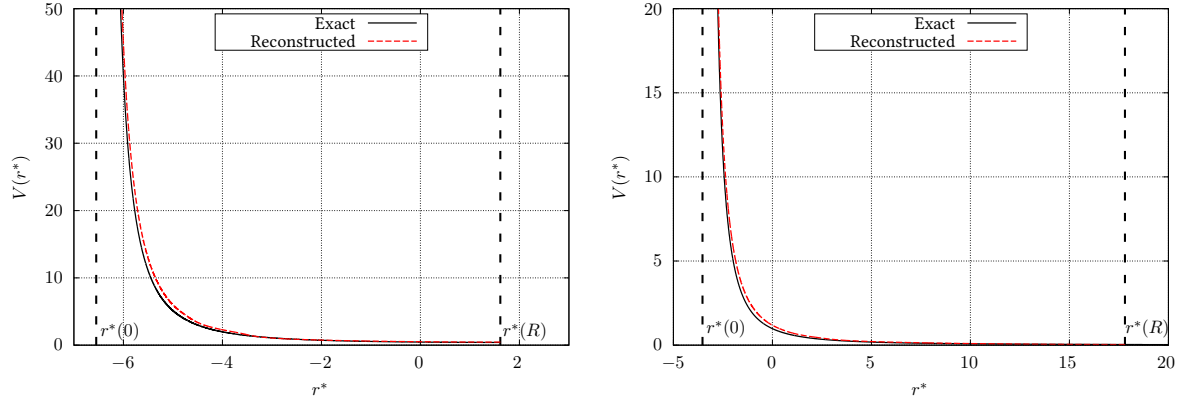


Figure 8.7: Reconstructed axial perturbation potentials (red dashed) are compared to the exact ones (black solid) for $l = 3$. The center and surface value of r^* is provided as well (black dashed). **Left panel:** The case of a constant density star with $R = 3M$. **Right panel:** The polytrope model A. Figures taken from [6].

8.5.5 Reconstruction of \mathcal{R} and v_0 from the Spectrum

As introduced in Sec. 8.4.2, one can use the analytic result for $n(E)$ in eq. (8.16) to find the parameters (\mathcal{R}, v_0) , as well as potentially $P_0 = P(\rho_0)$, from spectrum fitting. Since the analytic Bohr-Sommerfeld result for $n(E_{0n})$ does not include the fundamental mode, we start from the $n = 1$ mode, both for $l = 2$ and $l = 3$. Fig. 8.8 shows the reconstruction of \mathcal{R} in the left panel, while the relative errors are provided in the right panel. In Fig. 8.9 we present the corresponding results for v_0 . On the x-axis we report the number of used modes for the fitting of the spectrum. The relative errors for \mathcal{R} decrease when more modes are included. This is expected since it appears as only parameter that determines the $\sim n^2$ scaling for high eigenvalues. Something similar is initially found for v_0 , however the precision for $l = 2$ drops again. Note that the overall accuracy, both for \mathcal{R} and v_0 , is crucially better for $l = 3$ modes compared to the ones for $l = 2$. This is in agreement with the previous results for the direct spectrum prediction in Sec. 8.5.1.

Although it is possible to fit the parameter C_0 within a few percent error for $l = 3$, it is not close to the true value, calculated from eq. (8.11) and the method thus fails to reconstruct a useful relation for $P(\rho_0)$. Looking at the numerical values of (\mathcal{R}, C_2, C_0) , it turns out that C_0 is typically much smaller and contributes only to low eigenvalues, where the present method is least precise. However, note that (\mathcal{R}, v_0) are implicitly related to the equation of state through the TOV equations and our results thus still impose strong constraints on it.

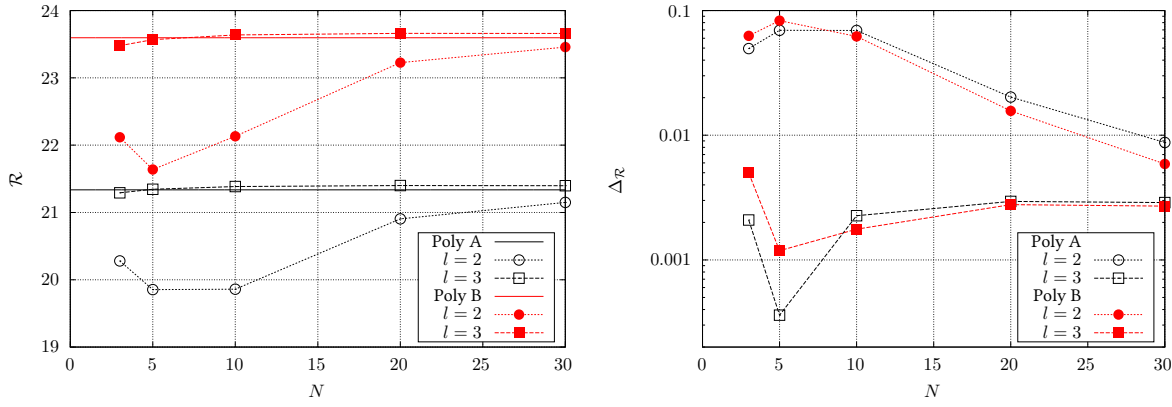


Figure 8.8: Here we present the reconstruction of \mathcal{R} as function of the number of included eigenvalues N for the spectrum fitting of the two polytrope models A and B for $l = 2$ and 3. **Left panel:** The reconstruction of \mathcal{R} (black and red symbols) compared to the true values (black and red solid line). **Right panel:** The relative errors for the reconstruction of \mathcal{R} . Figures taken from [6].

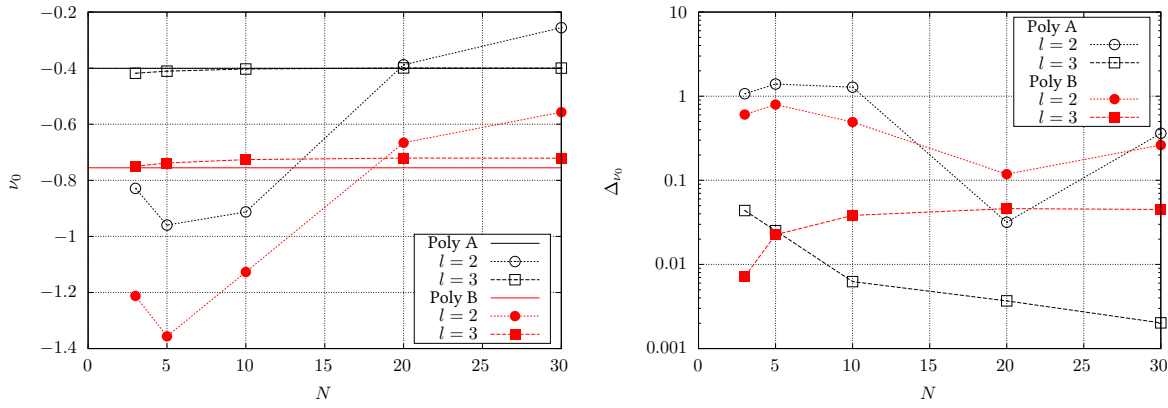


Figure 8.9: Here we present the reconstruction of ν_0 as function of the number of used eigenvalues N , for fitting the spectra of the two polytrope models A and B for $l = 2$ and 3. **Left panel:** The reconstruction of ν_0 (black and red symbols) compared to the true values (black and red solid line). **Right panel:** The relative errors for the reconstruction of ν_0 . Figures taken from [6].

8.5.6 Constraining the Equation of State in the Center

Using the spectral fitting result for ν_0 of the previous Sec. 8.5.5 allows one to approximate the equation of state at the center, as described in Sec. 8.4.3. Although the approach is approximate, the actual reconstruction yields useful results, as we demonstrate in Fig. 8.10. In the left panel we show the reconstructed value of ν_2 , while in the right panel the relation for the central pressure P_0 as function of central density ρ_0 is presented. For both polytropes we have used the $l = 3$ modes, since ν_0 obtained from the $l = 2$ modes has too large errors, as long as not many modes are included. We show the number of used modes in the reconstruction of ν_0 by using different dashed lines. Surprisingly, we find a quite good approximation if a small sample of modes is used, for both polytropes, while the asymptotic value is better for the less compact Poly A model. It does not converge to the right value for the Poly B model, but is still clearly distinguishable from the other model.

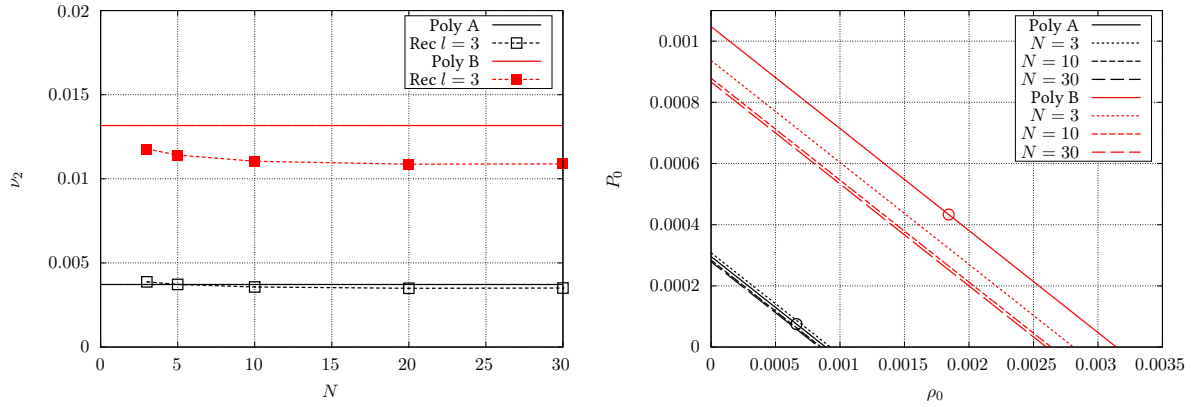


Figure 8.10: Here we show the results for the reconstruction of ν_2 and $P_0(\rho_0)$ for the two polytrope models A and B. **Left panel:** The reconstructed values for ν_2 , by using different numbers of modes (boxes), are compared to the exact value (solid lines). **Right panel:** The relation for $P(\rho_0)$ obtained from the true relation (solid lines) along with the reconstructed ones using different number of modes (dashed lines). The exact values (P_0, ρ_0) are shown as circles. Figures taken from [6].

From the reconstruction of ν_0 and ν_2 it is possible to approximate $\nu(r)$ throughout the whole star and $P(r, P_0)$ in the central region. Our results for this are shown in the left and right panel of Fig. 8.11 for both polytropes. While the reconstruction of $\nu(r)$ is quite robust, considering the involved approximations, $P(r, P_0)$ is only valid in the central region. The parameterization with respect to P_0 has negligible influence on the slope, but clearly shifts the absolute values. The relation for the expanded density $\rho(r)$, as it was derived in [227], also includes the adiabatic index, which introduces another unknown parameter to the problem, thus we do not consider it here.

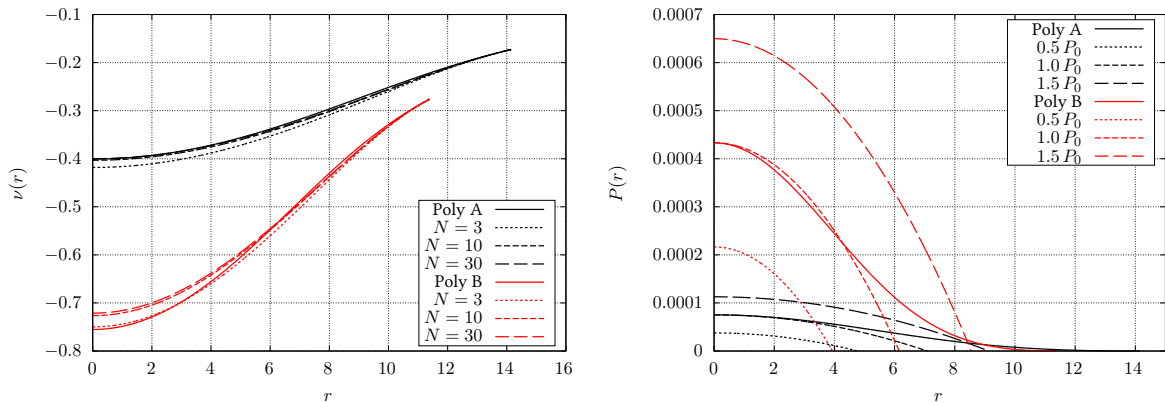


Figure 8.11: Here we show the reconstructed functions for $\nu(r)$ and $P(r, P_0)$ for the two polytrope models A and B. **Left panel:** The reconstructed metric functions $\nu(r)$ using a different number of modes (dashed lines) are compared to the exact functions (solid lines). **Right panel:** The reconstructed pressures parameterized by P_0 (dashed lines) are compared to the exact ones (solid lines). Figures taken from [6].

8.6 Discussion

In this section we discuss our previously shown results and their implications. Sec. 8.6.1 covers the direct spectrum problem, while Sec. 8.6.2 addresses the inverse problem.

8.6.1 Direct Problem

We start our discussion with the findings that are directly related to the precision of the Bohr-Sommerfeld description of the spectrum, before we continue with the universal relation of the fundamental axial QNM mode. The maximum value for the spacing of neighboring QNMs and the role of the discontinuity follow afterwards.

Accuracy of the Method

We have calculated the real part of ω_n^2 for the QNM spectrum of different polytropes and constant density stars with the new Bohr-Sommerfeld rule derived in Sec. 8.2. Using a linearized tortoise coordinate transformation and an approximation of the axial perturbation potential, we were able to derive an analytic formula for the spectrum eq. (8.16) and found a polynomial expansion for moderate and high eigenvalues eq. (8.13). Keeping in mind the various approximations being made to derive this result and the approximations for the potential that was used in Sec. 8.3, the method turns out to be a good approximation for the real part of the spectrum. Even low eigenvalues, for which the underlying WKB method and the approximated potential can not be expected to work reliable, are approximatively captured. The accuracy improves significantly for increasing n and l , which is expected from WKB theory and shows that our semi-analytic approach could be a powerful tool to determine very high eigenvalues, where numerical codes might face problems. For moderate n we find relative errors around $\sim 1 - 10\%$, while this improves below 1% for $l = 3$ and high eigenvalues. Since the method was derived for QNMs that are “located” above the discontinuity, it missed the fundamental mode, but works for all other QNMs.

Universal Relation

The universal asteroseismology relation for the fundamental axial and polar QNM, known empirically from [90, 235, 240], has been motivated analytically for the axial case in Sec. 8.3.2. The proposed relation was compared with the actual QNMs of polytropes, constant density stars and more realistic neutron star models in Sec. 8.5.2. Although the universal relation is only approximate, the analytical form provides a satisfying explanation of the scaling, since it relates the fundamental mode with the value of the Regge-Wheeler potential at the surface of the star, which is universal for all objects. The relation also includes ultra compact objects, which are effected by higher order corrections in M/R that also follow from our result. Since the relation does only depend on the star’s mass and radius, it is blind to the details of the underlying equation of state, as long as they produce a star with similar mass and radius. As a consequence, only higher modes should embed details of the equation of state, since they correspond to potential regions inside the star that are sensitive to it. Following the integral character of the Bohr-Sommerfeld rule, it is evident that only higher modes, which are explicitly related to the potential inside the star, can in principle contribute significantly to the reconstruction of the detailed equation of state.

Maximum Spacing of Neighboring quasi-normal modes

The predicted spacing of moderate and large neighboring QNMs as $\Delta\omega_n \approx \sqrt{\Delta E_n} = \pi/\mathcal{R}$, has first been found in [262] using another WKB approach to approximate the high frequency regime of axial and polar QNMs. The spacing of modes is not only extremely simple, but also very precise throughout different polytropes and constant density stars. We have verified this result for our neutron star models by comparing numerically obtained QNM spectra with the predicted spacing. Afterwards, in Sec. 8.5.3 we have shown that the scaling also holds for ultra compact constant density stars being close to the Buchdahl limit. This has to be surprising since these potentials are qualitatively different. We recovered the known result that the spacing first grows (for fixed mass), if one considers increasingly compact stars, but then has a maximum at $R \approx 3.86$, before it rapidly decreases again. We do not find any special properties of the star or the potential at this value. Trapped modes appear for more compact configurations. For general neutron stars, the exact position depends on the equation of state. This is because \mathcal{R} depends on the integrated metric functions g_{00} and g_{11} , which have to be determined from the TOV equations. For the internal tortoise coordinate $r^*(r=0)$ to take large negative numbers, configurations close or above realistic neutron star compactnesses are needed.

The Role of the Surface Discontinuity

The discontinuity of the perturbation potential at the stellar surface is necessary to derive discrete eigenvalues in our approach. Without the discontinuity, the surface of the star plays no special role and demanding outgoing

QNM at this matching point is arbitrary. Although the potential of constant density stars and the ones of neutron stars with a crust are not continuous, the ones for polytropes can be. From this point of view one would not expect the Bohr-Sommerfeld rule to be valid, but the predicted QNMs are found with similar precision compared to constant density stars. Note that the expanded Bohr-Sommerfeld rule for the real part of E_n does not explicitly depend on the discontinuity value ΔV , but the imaginary part of E_n does. It depends explicitly on ΔV and diverges in the limit of a continuous potential. A detailed discussion on the importance of discontinuities in higher derivatives of the potential can be found in [262], where also rapid changes of the equation of state close to the surface can be found and potentially be applied for further studies.

Here we also want to recall related results for the gravitational perturbations of black holes, where introducing small discontinuities in the potential changed the overall QNM spectrum significantly. In [298] the Regge-Wheeler barrier has been replaced by fitted step potentials with different numbers of steps, which extended earlier work [208]. It was found that the related QNM spectrum did not approach the exact one, when the number of potential steps being used was increased. The qualitative behavior of the obtained QNM spectrum is always much closer to the ones for neutron stars. Increasing the number of steps increased the density of QNMs, but not significantly their alignment on the complex plane. Somehow counterintuitive or at least remarkable, it was found that the time-evolution of scattered waves at the step potentials becomes close to the ones scattered at the exact potential. The actual QNMs only contributed weakly to the scattering. A more technical discussion on the significance of QNMs has been presented in [302]. The role of environmental effects around black holes lead in a related toy model to similar effects [303, 304].

8.6.2 Inverse Problem

Here we discuss our results related to the inverse problem. We start with the reconstruction of the perturbation potential from the inversion of the Bohr-Sommerfeld rule, before we continue with the reconstruction of the fundamental properties by fitting our analytic result to the spectrum.

Reconstruction of the Potential

By inverting the new Bohr-Sommerfeld rule, we have shown that it is possible to reconstruct the internal perturbation potential from the knowledge of the QNM spectrum. The reconstruction is approximate and not exact, because of the underlying WKB method and approximations being involved. In contrast to the non-uniqueness inherited in the inversion of the classical Bohr-Sommerfeld rule for pure potential wells, the reconstruction of the internal potential for typical neutron stars turns out to be unique. This is because the upper limit of integration corresponds to the surface of the star and the problem reduces to the one turning point problem. The method recovers the internal potential by using consecutive modes and approaches the central region for high eigenvalues. In practice one will be limited by a finite number of modes, which means that the potential can only be known from the surface inwards close to the center. Fortunately it turns out that one approaches the central region quite fast, while modes related to high eigenvalues are only interesting for the region extremely close to the center. However, in the reconstruction procedure it was assumed that the QNM spectrum is known with pristine accuracy and other effects are neglected.

As it was pointed out recently in [301], knowing the perturbation potential can be used to determine the equation of state and solve the inverse problem for the stellar structure. The here presented methods allows a simple, but approximate reconstruction of the potential. Whether its accuracy is sufficient for the suggested approach could be investigated in future work.

Reconstruction of Crucial Parameters and Metric Function

With the analytic result for $n(E)$ eq. (8.16), which we obtained by applying the new Bohr-Sommerfeld rule to an approximated version of the perturbation potential, it was possible to reconstruct with very good precision two of the three parameters that describe the potential by fitting the exact QNM spectrum. Compared to the inversion

of the Bohr-Sommerfeld rule, only a minimum number of three modes is required. The recovered parameters translate to the tortoise radius of the star \mathcal{R} , as well as ν_0 , which is the central value of the metric function $\nu(r)$. By using the expanded version of $\nu(r)$, which was derived in [227], we were able to approximate it to good accuracy throughout the whole star. Also we were able to approximate $P(r, P_0)$ in the central region, which is not unique, but parameterized by the central pressure P_0 . However, the slope of $P(r)$ is only slightly influenced by the choice of P_0 and can be clearly distinguished for both polytropes.

8.7 Conclusions

In this work we have studied several aspects of the axial QNM spectrum of spherically symmetric and non-rotating neutron stars and used it to constrain their space-times and equations of state. We also motivated an analytic approximation being closely related to the empirically known universal scaling relation for the fundamental axial QNM. Some of our results even extend to ultra compact stars, which can be seen as a toy model for exotic compact objects.

By using standard WKB theory, we first derived a new Bohr-Sommerfeld rule which looks similar to the classical one for potential wells, but is modified by an additional imaginary part. In contrast to potential wells, the relevant potential for neutron stars admits only one classical turning point, which changes the problem significantly. We demonstrated how the new Bohr-Sommerfeld rule can be used to approximate the real part of the axial QNM spectrum of different polytropes with good precision. Especially for large n and l , where numerical codes might face problems, it could be of general interest.

Making use of several well justified approximations, we were able to show that the spacing of moderate and large neighboring QNMs has to be a constant, which our method predicts to be π/\mathcal{R} , where $\mathcal{R} = r^*(R) - r^*(0)$ is the ‘‘tortoise radius’’ of the star, and coincides with the result reported in [262]. We have also concluded that this scaling predicts a maximum possible spacing, which depends on the radius (for fixed mass). For constant density stars this was shown explicitly. Furthermore, as a useful approximation in the study of the gravitational perturbations of normal neutron stars, we have demonstrated that the tortoise coordinate transformation can be approximated very well with a linear function. It only depends on the mass, the radius and the tortoise radius of the star and simplifies the perturbation equations significantly.

Even more interesting are the implications of our results for the inverse spectrum problem. The new Bohr-Sommerfeld rule can be inverted to reconstruct approximatively the perturbation potential from a known spectrum and potentially be used to determine the equation of state throughout the star [301]. This approach requires the knowledge of many modes. As an alternative and more robust solution being tailored to the perturbation potential of neutron stars, we have also shown how a minimum number of 3 modes, for the same l , are enough to reconstruct fundamental parameters of the star. These are the tortoise radius and the value of the time-time component of the metric in the center. Both parameters can be obtained with good precision and play the dominant role in characterizing the spectrum. We were also able to approximate the time-time component of the metric throughout the whole star and provide a linear relation between central pressure and central density, which constrains any equation of state significantly. Future work in this direction will include a direct reconstruction of the underlying equation of state in these systems.

8.8 Supplementary Material

In the following we provide additional information about the linear tortoise transformation 8.8.1 and the approximated axial perturbation potential 8.8.2.

8.8.1 Approximate Tortoise Transformation

The tortoise coordinate transformation $r^*(r)$ is essential in obtaining the simple structure of the wave equation that appears in the perturbations of spherically symmetric and non-rotating space-times. Although its details

depend on the metric functions g_{00} and g_{11} via the integral

$$r^*(r) = \int^r \sqrt{\frac{g_{11}(r')}{g_{00}(r')}} dr', \quad (8.21)$$

it is possible to make some general remarks for stars that are not ultra compact. In this case the ratio in eq. (8.21) is approximatively constant inside the star and can be matched with the external exact tortoise transformation known from Schwarzschild. In the limit of $M/R \rightarrow 0$ one finds $r^* \approx r$. Here we show, as an educated guess, how the tortoise transformation inside the star can be written as a linear function and demonstrate that it is an accurate description for polytropes and constant density stars, as long as one is not interested in compactnesses beyond normal neutron stars. The linear relation we propose is given by

$$r^*(r) \approx \left[R + 2M \ln \left(\frac{R}{2M} - 1 \right) - \mathcal{R} \right] + \frac{\mathcal{R}}{R} r, \quad (8.22)$$

with $\mathcal{R} = r^*(R) - r^*(0)$. Note that $r^*(R) = R + 2M \ln (R/(2M) - 1)$ is the standard Schwarzschild result, which we use for matching at $r = R$. The relation in eq. (8.22) recovers the exact values of $r^*(r)$ at $r = 0$ and $r = R$. Its linearity makes it trivial to make explicit use of it in the perturbation equation, which then simplifies significantly. In Fig. 8.12 we show the accuracy of the linear approximation for the two polytropes studied in this work, as well as for constant density stars with different compactness. The result clearly shows that the linear approximation is a useful for analytical studies.

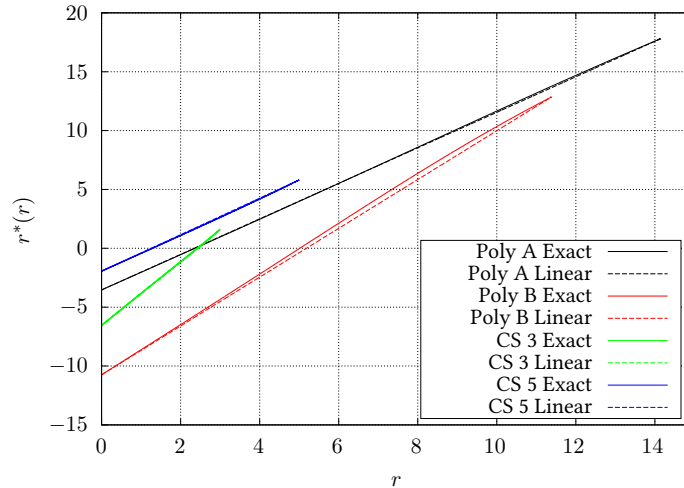


Figure 8.12: Here we compare the exact tortoise transformation (solid lines) inside the star with the linear approximation (dashed lines). We show results for the two polytrope models A and B along with constant density stars with compactness $R/M = 3$ and 5 with $M = 1$. Figure taken from [6].

8.8.2 Approximate Potential Calculation

Here we provide additional information for the derivation of the approximated axial mode potential in spherically symmetric and non-rotating neutron stars. As it was shown in [227], it is possible to expand all functions that appear in the TOV equations as series for small r . The expanded relations for $(\rho(r), P(r), v(r), m(r))$ are then given by

$$\rho(r) = \rho_0 + \frac{1}{2} \rho_2 r^2, \quad (8.23)$$

$$P(r) = P_0 + \frac{1}{2} P_2 r^2 + \frac{1}{4} P_4 r^4, \quad (8.24)$$

$$v(r) = v_0 + \frac{1}{2} v_2 r^2 + \frac{1}{4} v_4 r^4, \quad (8.25)$$

$$m(r) = \frac{4\pi}{3} \rho_0 r^3, \quad (8.26)$$

where $m(r)$ directly follows from $\rho(r)$. In the same paper it was shown how the series coefficients are related to the equation of state for small r . For our application we need the relation for v_2 , which is given as

$$v_2 = \frac{4\pi}{3} (\rho_0 + 3P_0), \quad (8.27)$$

for the notation $g_{00} = e^{2v(r)}$, while the factor is $8\pi/3$ for $g_{00} = e^{v(r)}$, as it was used in [227]. Inserting the series expansions into $V(r)$ and ordering in powers of r , one finds

$$V(r) = e^{2v(r)} \left(\frac{L}{r^2} + 4\pi (\rho(r) - P(r)) - \frac{6m(r)}{r^3} \right) \quad (8.28)$$

$$\approx \frac{e^{2v_0} L}{r^2} + \exp(2v_0) (v_2 L - 4\pi(\rho_0 + P_0)) + \mathcal{O}(r^2). \quad (8.29)$$

Making use of the linearized tortoise transformation presented in Sec. 8.8.1, it is possible to find explicitly $V(r^*)$. To simplify further calculations we introduce a temporary coordinate u^* , which shifts $r^*(0)$ to $u^* = 0$. The wave equation does not change under such a coordinate shift and the resulting potential is given as

$$V(u^*) \approx \left(\frac{\mathcal{R}}{R} \right)^2 \frac{e^{2v_0} L}{u^{*2}} + e^{2v_0} [v_2 L - 4\pi(\rho_0 + P_0)]. \quad (8.30)$$

This potential can now be used in the new Bohr-Sommerfeld rule eq. (8.4) to obtain a simple relation for the spectrum $n(E_n)$. The integration is straightforward and yields the result presented in eq. (8.12).

9 | Scalar Fields and Parametrized Spherically Symmetric Black Holes: Can one hear the shape of space-time?

Breakdown of Contributions

This chapter is based on the publication “*Scalar Fields and Parametrized Spherically Symmetric Black Holes: Can one hear the shape of space-time?*” by Sebastian H. Völkel and Kostas D. Kokkotas, Phys. Rev. D 100, 044026, 2019, [8]¹. My contributions are all the computations and paper writing, while Kostas D. Kokkotas assisted in discussions and editing the final manuscript.

Overview

Here we study whether parametrized spherically symmetric black hole solutions in metric theories of gravity can appear to be isospectral when studying perturbations. From a theory agnostic point of view, the test scalar field wave equation is the ideal starting point to approach the QNM spectrum in alternative black hole solutions. We use a parametrization for the metric proposed by Rezzolla and Zhidenko, as well as the higher order WKB method in the determination of the QNM spectra. We look for possible degeneracies in a tractable subset of the parameter space with respect to the Schwarzschild QNMs. Considering the frequencies and damping times of the expected observationally most relevant QNMs, we find such degeneracies. We explicitly demonstrate that the leading Schwarzschild QNMs can be approximated by alternative black hole solutions when their mass is treated as free parameter. In practice, we conclude that the mass has to be known with extremely high precision in order to restrict the leading terms in the metric expansion to currently known limits coming from the PPN expansion. Possible limitations of using the QNM ringdown to investigate black hole space-times are being discussed.

This chapter is organized as follows. In Sec. 9.1 we provide a short introduction. In Sec. 9.2 we briefly outline the Rezzolla-Zhidenko parametrization along with the scalar wave equation. Our framework for the study of the QNM spectrum of different black hole space-times is explained in Sec. 9.3. Our results are then presented in Sec. 9.4 and discussed in Sec. 9.5. Finally, we conclude in Sec. 9.6. The figures we produced for the results are shown in Sec. 9.7.

9.1 Introduction

In Einstein’s theory of general relativity the field equations determine the metric tensor, which is related to the present energy and matter. With the metric tensor at hand, different types of perturbations on this background can be studied and eventually lead to QNM spectra, as discussed in Sec. 3. In same section we explained that the QNM spectrum of a certain type of perturbation is an important and characteristic property connecting linear oscillation phenomena with compact objects. The simplest perturbation is a scalar test field, described by the massless Klein-Gordon equation, which we introduced in Sec. 3.2. It is the simplest example, because once the background metric is known, there is no direct connection to the rather complicated field equations of general relativity. This is different for gravitational perturbations, which are obtained by expanding the field equations in terms of a small perturbation of the metric tensor. In this case, even at linearized order, the field equations determine how perturbations evolve. The importance of this key difference becomes crucial if one starts to be interested in alternative metric theories of gravity. Although general relativity has been passing all tests for more

¹Reprinted parts with permission from Sebastian H. Völkel and Kostas D. Kokkotas, Phys. Rev. D, 100, 044026, 2019. Copyright 2019 by the American Physical Society.

than 100 years [23], the strong field regime around black holes only became accessible recently, via gravitational waves [13, 305] and black hole shadows [16].

It is also possible that different field equations admit a subclass of similar solutions, see [306] for a discussion on scalar tensor theories and [307] for the gravitational perturbations of the Kerr solution in $f(R)$ theories. However, since the field equations differ, the evolution of gravitational perturbations will in general be different. This implies that even if a metric tensor is provided or assumed, it is necessary to know the underlying theory if one is interested in gravitational waves. This is in strong contrast to the test scalar field evolving independent of the field equations. Of course, one could also imagine the rather exotic case that two alternative theories yield slightly different solutions for the background, but evolve perturbations in such a way that the observations are too similar to be distinguishable. Thus, if one is agnostic about the underlying theory of gravity, but interested in describing gravitational waves, one faces a fundamental problem.

In general relativity, scalar test fields behave qualitatively to a large extent similar to gravitational perturbations. In the Schwarzschild space-time, scalar and gravitational perturbations are both described by an effective one-dimensional wave equation that includes a potential term, see our discussion in Sec. 3.2 and Sec. 3.3.2. The explicit form of the potential differs quantitatively, but is qualitatively very similar. Moreover, by going to the eikonal limit (large l limit), both potentials approach each other. Although such similarities can clearly not be expected in every alternative theory, it is still reasonable that they are encoded in some of them. Therefore, as long as one is aware of this circumstance and restricted to such theories, this connection is a promising starting point to study the qualitative gravitational wave behavior in alternative black hole solutions.

Instead of picking a few explicit examples from specific theories, we here are interested in parametrized black hole metrics. Such a parametrization might or might not be an exact solution in a known or unknown theory. In any case, it can be an effective approximation and therefore serves as useful tool in explicit calculations. Different parameterizations for non-rotating, as well as rotating, black hole solutions have been proposed in the literature, e.g. [196, 197, 198, 199, 200]. The idea is to introduce extra terms that can capture possible deviations from the Kerr solution [110]. Following such approaches can be promising even beyond oscillation phenomena, because they can also be applied to the geodesic motion of test particles, the determination of black hole shadows [193], and x-ray reflection spectroscopy [194, 195]. However, it is clear that not every parametrization will be a reasonable physical solution and pathologies might arise.

In this work we use the proposal by Rezzolla and Zhidenko [198], which can be used for non-rotating black hole solutions. The advantage of this parametrization is that a small number of parameters can be used to describe deviations from the Schwarzschild solution in an explicit way that incorporates proper conditions at spatial infinity and at the horizon. Moreover, it was demonstrated [198, 308] that this proposal allows for a precise and fast converging approximation for exact solutions in alternative theories.

With this background information at hand, and some inspiration from Marc Kac's question whether one can hear the shape of a drum [97], the motivation of our work is the following. From a theory and metric agnostic point of view, one can ask the following question:

How uniquely is the QNM spectrum related to the theory and metric under consideration?

Since the answer in the case of gravitational perturbations involves the underlying field equations, it can not be answered explicitly. Connecting QNM spectra with compact objects has led to the field of black hole spectroscopy [309]. Now, if one makes the assumption that the underlying field equations are very similar, and only introduces changes in the metric, a study on the time evolution of axial perturbations has been done in [310]. A perturbative framework, which relates small, parametrized deviations from different perturbation potentials to their QNM spectrum, has been proposed in [311] and extended to coupled wave equations [312] arising in alternative theories of gravity. Related approaches using the eikonal limit can be found in [313, 314].

As another approach, at least for scalar test fields, one could start with an efficient parametrization for different space-times and study the related eigenvalue problem. Even on the level of scalar fields, there is a rich complexity that can arise in the possible black hole space-times. Therefore, it is a priori not trivial to answer whether the same QNM spectrum can originate from different space-times. Since the complete QNM spectrum is infinite in general relativity, one can also rephrase the question in a more observation driven context:

Assuming that observations would provide the first few QNMs within a finite error, how likely is it that the reconstructed parameters determine these eigenvalues uniquely?

It is clear that the underlying theory of gravity is needed to describe actual gravitational wave observations. However, test scalar fields will at least in some theories behave qualitatively similar and do not require more than the background space-time. Therefore, we consider a scalar test field evolving in the background of the parametrized Rezzolla-Zhidenko (RZ) metric as a theory agnostic way to study the qualitative behavior of fields and their QNM spectra. We are particularly interested in the QNM properties, because at least for moderate deviations from Schwarzschild, they are strongly influenced by the metric around the lightning ($\sim 3M$). This is much closer to the horizon than accretion discs and therefore potentially more sensitive to deviations.

9.2 Scalar Perturbations

The starting point in this work is the RZ parametrization for spherically symmetric black hole metrics [198], which has been introduced in Sec. 2.3.5. We remind the reader that the line element for spherically symmetric black holes described by the RZ metric takes the form

$$\boxed{ds^2 = -N^2(r)dt^2 + \frac{B^2(r)}{N^2(r)}dr^2 + r^2d\Omega^2}, \quad (9.1)$$

with $d\Omega^2 = d\theta^2 + \sin^2\theta d\phi^2$. All details of the space-time are encoded in the two functions $N(r)$ and $B(r)$. The dimensionless variable

$$x \equiv 1 - \frac{r_0}{r}, \quad (9.2)$$

maps the location of the event horizon r_0 to $x = 0$ and spatial infinity to $x = 1$. The simplest, but also gravitational theory independent wave equation is the Klein-Gordon equation, as discussed in Sec. 3.2

$$\frac{d^2}{dr^{*2}}\psi + (\omega_n^2 - V_l(r))\psi = 0. \quad (9.3)$$

The effective perturbation potential $V_l(r)$ of the RZ metric takes the form

$$V_l(r) = \frac{l(l+1)}{r^2}N^2(r) + \frac{1}{r} \frac{d}{dr^*} \frac{N^2(r)}{B(r)}. \quad (9.4)$$

The tortoise coordinate r^* is related to the parametrized metric via

$$\frac{dr^*}{dr} = \frac{B(r)}{N^2(r)}. \quad (9.5)$$

The shape of $V_l(r)$ of the Schwarzschild black hole is the one of a two turning point potential barrier, with a maximum located around $3M$.

For the computation of QNMs later in this work, we use the higher order WKB method [213, 214, 215, 216, 217, 218, 220], which is discussed in Sec. 3.5.2. We remind that the QNM spectrum ω_n is determined by

$$\frac{iQ_0}{\sqrt{2Q_0''}} - \Lambda_2 - \Lambda_3 - \Lambda_4 - \Lambda_5 - \Lambda_6 = n + \frac{1}{2}, \quad (9.6)$$

with $Q(r^*) \equiv \omega_n^2 - V_l(r^*)$, which is evaluated at the maximum of potential [218]. The primes denote the derivative with respect to the tortoise coordinate, also evaluated at the maximum. The index of the correction terms show the order in the WKB expansion and are explicitly determined by the overtone number n , as well as derivatives of the potential with respect to the tortoise coordinate, evaluated at the maximum of potential. Since their explicit form is rather long, we refer to [218].

The main advantage of eq. (9.6) is that all terms can be evaluated, once the potential and the tortoise transformation are being provided. The method is expected to give accurate results for $n \leq l$. The overall performance improves with increasing l and decreases with increasing n . As long as the general criteria for the validity of the WKB method are fulfilled [273], and the potential barrier has two turning points, the method provides a quick and robust determination of the leading QNMs. Luckily, these are the ones which are dominant in the ringdown phase and therefore of key importance from an observational point of view.

9.3 Search for Isospectrality

The purpose of our work is to study how the QNM spectrum and the parametrized metric are connected to each other. More specifically, we want to investigate whether different metrics can yield the same QNM spectrum. This would imply that the effective potentials are either exactly the same or differ, but are still isospectral. At the same time, we also want to relate the question to the situation that only some part of the QNM spectrum is provided, but with finite errors. In this case we then want to know if a degeneracy in the parameter space of alternative black hole solutions with respect to the Schwarzschild solution can arise.

In order to address both questions, we find ourselves at the crossroads of following a more mathematical inspired path or a more applied one. By mathematical we mean e.g. to apply the Darboux transform, as it was recently done in [258], to confirm the already known isospectrality of the Regge-Wheeler and Zerilli potentials of gravitational perturbations in general relativity. The more applied path we chose is to start with a finite set of parameters that describe the metric and search in the parameter space for degeneracy by solving the eigenvalue problem explicitly for reasonable combination of parameters.

In the following we outline our approach to study the parameter space of different metrics and how we relate it with a given spectrum.

9.3.1 Provided Spectrum

[13, 305] In order to study isospectrality, one needs to define a potential or a spectrum as reference first. The canonic choice for a spherically symmetric black hole is the Schwarzschild solution. We will use its QNM spectrum as reference and define the relative error for the real (r) and imaginary (i) parts of ω as

$$\delta\omega_{r,i} \equiv \frac{\omega_{r,i}^{\text{Sch}} - \omega_{r,i}^{\text{param}}}{\omega_{r,i}^{\text{Sch}}}, \quad (9.7)$$

where the explicit choice of n and l , as well as the parameters are suppressed. In order to combine the knowledge of the real and imaginary part of a given mode, we also define a combined relative error as

$$\delta\omega_c \equiv \sqrt{\delta\omega_r^2 + \delta\omega_i^2}, \quad (9.8)$$

where $\delta\omega_{r,i}$ are the standard relative errors defined in eq. (9.7).

A parametrized potential is isospectral to the Schwarzschild potential, if $\delta\omega_{r,i} = 0$, for all l and n . Since there are infinitely many eigenvalues, the full problem can in practice not be studied numerically. However, coming back to the connection to observations, one can only measure a finite set of eigenvalues. A reasonable choice is to start with the knowledge of the fundamental QNMs for moderate l and include a finite set of eigenvalues by increasing l and n . One can then compute the relative errors explicitly in the parameter space. Since the QNM spectrum is complex valued, it is also interesting to see how its real and imaginary parts separately depend on the parameter space, as well as their combination.

9.3.2 Studied Parameter Space

In [198] it was demonstrated that the parametrized metric has very good convergence properties with respect to the number of included parameters. Thus, even including a relatively small set of parameters can yield accurate results, which implies that many alternative black hole solutions are being included. This is an important observation for our work. A large set of free parameters makes it likely that a small set of observables can more easily be explained than if the set of free parameters is small and therefore less favored.

The whole parameter space of the most general metric is infinitely large. However, since we are only interested in those space-times that can be well approximated with a few terms, we consider a finite parameter space. As such, we choose the ADM mass M and only the leading terms for $[a_i, b_i]$

$$\mathcal{P} \equiv [M, a_0, a_1, b_0, b_1], \quad (9.9)$$

while all other parameters $[\varepsilon, a_i, b_i]$, with $2 \leq i$ are set to zero. The deviation of the horizon location, described by ε , is set to zero as well. Allowing for more non-zero parameters is in principle interesting as well, but the number of combinations becomes less tractable. We set ε to zero in this work, because it appears in the lowest order of the expansion and the next higher order terms $[a_0, b_0]$ are already constrained to be small.

Note that not all actual values for the parameters can be chosen arbitrarily. Naturally the ADM mass M is positive. Furthermore, in order to keep the signature of the metric, the expansion parameters describing $\tilde{A}(x)$ have to be chosen such that $0 < A(x)$, for $0 \leq x \leq 1$. Also, since we are using the WKB method, we have to make sure that all effective potentials in the parameter space being considered are actually two turning point potential barriers.

9.3.3 Higher Order WKB and Numerical Implementation

For every choice of the parameters \mathcal{P} one has to solve the eigenvalue problem. In practice we are interested in the leading QNMs with moderate l and $n < l$. First, these modes are the most relevant ones from an hypothetical observational point of view. Second, for these modes it is justified to use the WKB method for numerical results. Applying the WKB method is in principle trivial, but there are some practical aspects we want to note. Obviously, it gets computationally expensive, once the parameter space is investigated with high resolution. For a given computational time, there is a clear trade-off between the QNM precision, by including more higher order WKB terms Λ_i , and the resolution of the parameter space \mathcal{P} . The reason being that going one order higher in the WKB method requires two more higher order derivatives of the potential, evaluated in the tortoise coordinate. In the case of a general parametrized metric, this becomes more and more involved. At the same time, keeping a smaller number of WKB terms yields slightly less precise numerical results, but allows to study the parameter space in more detail.

For the explicit numerical calculations we wrote a code. The derivatives of the potential at the maximum are computed with finite differences. Here we avoid the explicit computation of the tortoise coordinate and instead use an iterative scheme

$$\frac{d}{dr^*} = \frac{N^2(r)}{B(r)} \frac{d}{dr}, \quad (9.10)$$

to obtain the derivative of the potential. The advantage is that we reduce numerical errors arising from the coordinate transformation, but pay the price that higher order derivatives become numerically more expensive. In principle computer algebra software like Maple or Mathematica can compute the derivatives analytically, but the number of involved terms grows rapidly, limiting the overall performance when studying a large parameter space with high WKB order. We choose the third order WKB method for the reasons being mentioned.

9.4 Results

In the following we discuss our results for the studied parameter space \mathcal{P} eq. (9.9). We consider the fundamental modes ($n = 0$), as well as the first overtone ($n = 1$), for $l = 2$ and $l = 3$, to make the qualitative connections to gravitational perturbations. This section is organized in different parts. In Sec. 9.4.1 we compare the properties of the QNM spectrum by varying $[a_0, b_0]$ and $[a_1, b_1]$ with respect to the Schwarzschild case. In Sec. 9.4.2 we show what precision in the black hole mass M is required, in order to determine $[a_0, b_0]$ and how this depends on the number of provided modes. We do the same analysis for $[a_1, b_1]$ in Sec. 9.4.3. We discuss how these results change if one considers the first overtone ($n = 1$) in Sec. 9.4.4. Finally, we show some of the reconstructed potentials in Sec. 9.4.5. Note that parameters not being explicitly varied are set to zero.

9.4.1 Parameters $[a_0, b_0]$ and $[a_1, b_1]$

Here we show our results for the relative errors for the fundamental ($n = 0$) QNM for $l = 2$ (top panels) and $l = 3$ (bottom panels) for $[a_0, b_0]$ in Fig. 9.1 and for $[a_1, b_1]$ in Fig 9.2. The reference value to which the relative error is obtained is the $M = 1$ Schwarzschild case for the same n and l , computed with the WKB method. The relative errors in the real part ω_r are shown in the left panels and the ones for the imaginary part ω_i in the central panels. Finally, the combined relative errors ω_c are shown in the right panels. The color scaling shows the logarithm of the absolute value of the relative errors, respectively. The contour lines show integer values for this logarithm.

It is evident that the role of $[a_0, b_0]$ and $[a_1, b_1]$ is very similar for both l . Both can effectively influence each other in such a way that the real and imaginary parts remain unchanged compared to the Schwarzschild case. It is remarkable that the knowledge of only the real or imaginary parts for two different l can hardly be used to constrain $[a_0, b_0]$ or $[a_1, b_1]$, because the scaling is very similar in both cases. It is by far more useful to connect the real and imaginary part of the same mode, which we show in the combined relative errors in the right panels. However, comparing this for both l , it is evident that merging both results is of limited usefulness in the more precise determination of the parameters. Also, note that the real part is almost blind to changes in b_0 and b_1 , while the imaginary part is sensitive to both.

9.4.2 Parameters $[M, a_0, b_0]$

In this section we investigate up to which extent a change in the mass M can allow the fundamental QNMs of non-vanishing a_0 and b_0 to mimic the pure Schwarzschild modes with reference mass $M = 1$. Since it is more involved to visualize the contours of the now three-dimensional parameter space, we decided to show slices of constant M in the a_0 and b_0 parameter plane. These two dimensional slices through the three dimensional parameter space are orthogonal to the M -axis and have a similar color map representation as used in the previous Sec. 9.4.1. This is shown in the top panels of Fig. 9.3.

The similar scaling of the combined relative errors for $l = 2$ and $l = 3$ is remarkable. It shows that changing the mass by 1 % allows values for $[a_0, b_0]$ of around ± 0.04 , assuming the relative error would be 10^{-2} . Since the scaling for both l is very similar, merging the two parameter ranges can hardly be used to constrain the mass. The relative errors for the real and imaginary parts scale also very similar, which we do not show explicitly here.

9.4.3 Parameters $[M, a_1, b_1]$

In the bottom panels of Fig. 9.3 we show our results for repeating the analysis from Sec. 9.4.2 with varying a_1 and b_1 . Now a_0 and b_0 are set to zero. Qualitatively we arrive at a very similar result. Again it is possible to find non-zero values for the parameters through modifying the black hole mass. But, since the combined error areas enclosed by the same contour are larger here, compared to the $[a_0, b_0]$ case, the combination $[a_1, b_1]$ requires higher precision to be constrained.

9.4.4 Investigating the First Overtone $n = 1$

The analysis of the previous subsections can also be done for the first overtone $n = 1$, which we show in Fig. 9.4, Fig. 9.5, and Fig. 9.6. We find that the overtone changes the scaling of the real part (left panels), it is now more sensitive to changes in b_0 and b_1 . The change in the imaginary part (central panels) seems to be more stable towards the first overtone n . However, unless pristine precision is available, the combined error contours (right panels) overlap significantly in all studied cases and can hardly be used to constrain the parameters $[a_0, b_0]$ to be within their PPN limits or $[a_1, b_1]$ to be of similar order.

9.4.5 The Effective Potentials

In order to verify that changing the mass parameter M can actually recast the Schwarzschild fundamental QNMs, although $[a_0, b_0]$ and $[a_1, b_1]$ are non-zero, we show specific effective potential barriers in Fig. 9.7. These serve as verification that the application of the WKB formula is well justified, because the potential barriers have two turning points and very similar behavior to the well established Schwarzschild case.

From all panels one can deduce that changing the mass by 1% around the reference value of $M = 1$ leads to clearly distinguishable potential barriers for Schwarzschild (solid lines). This is expected and will change the QNMs in the same order. In all panels, we also show multiple realizations of the RZ metric (dashed lines), where we choose $[a_0, b_0]$ and $[a_1, b_1]$ to be the ones that minimize the combined errors $\delta\omega_c$ (here for $n = 0$). Note that these values slightly differ from $l = 2$ to $l = 3$ and are not exactly the same. However, since the contours are almost the same for both l , the values are very close to each other, as shown in Fig. 9.3.

For large r^* , all potentials go to zero, as expected from construction of the metric. Around the peak of the barrier, which is the region of the potential that determines the properties of the fundamental QNMs, the RZ potentials match the Schwarzschild reference potential extremely well, although their mass parameter is different. At the same time, the other Schwarzschild potentials differ the most. Going to large negative values of r^* , which means to approach the black hole horizon, we see that the dashed lines in the $[a_1, b_1]$ case deviate slightly more than the ones for $[a_0, b_0]$. This should be expected, since non-zero values of $[a_1, b_1]$ become by construction more significant closer to the horizon, but less important for large r^* .

Finally, the precise match of the constructed RZ potentials with the Schwarzschild reference potential also confirms that the WKB method is well suited for the problem.

9.5 Discussion

We first discuss our findings for varying $[a_0, b_0]$ and $[a_1, b_1]$ simultaneously for reference mass $M = 1$. Afterwards, we interpret the effect of allowing different values for the mass for these combinations. The reconstructed potentials, as well as the role of rotation are discussed in the end.

From our findings in Sec. 9.4.1 we see that knowing only either the real or imaginary parts of the fundamental QNMs for $l = 2$ and $l = 3$ is less useful than knowing real and imaginary part of the same l . This is because combinations of $[a_0, b_0]$ and $[a_1, b_1]$ leaving either the real or imaginary part of the Schwarzschild result unchanged, behave quite similar for both l . Combining the real and imaginary parts is more powerful when constraining the parameters. Looking into the absolute numbers, we find that one requires a very precise knowledge of the real and imaginary parts of a given QNM in order to constrain $[a_0, b_0]$ to the already known limits coming from the PPN expansion, which is discussed in Sec. 2.3.5 and was derived in [198]. Note that this section assumes that the mass is provided without any error.

However, treating the mass M as free parameter in Sec. 9.4.2, we report combinations in Fig. 9.3, such that one obtains a similar result for the fundamental QNMs of different l . In fact, introducing an uncertainty in the mass M of around one percent allows values for a_0 and b_0 to be of order 10^{-2} , which is beyond the PPN constraints of $\sim 10^{-4}$, [198]. However, realizing such high precision in determining $[a_0, b_0]$ requires pristine knowledge of M . Achieving this in actual observations is challenging and might require combined measurements using a network

of third generation gravitational wave detectors [315]. Since the scaling of the relative errors for both l is quite similar, the combination of both fundamental modes is not of significant help. In practice, this means that the mass parameter M is clearly degenerate with respect to some combinations of a_0 and b_0 . We conclude that even small uncertainties in M can actually mimic Schwarzschild fundamental QNMs for suitable choices of $[a_0, b_0]$.

In Sec. 9.4.3 we arrived at a very similar results for combinations $[a_1, b_1]$. Note that these parameters are not connected in the same way to the PPN parameters and should, by construction of the RZ metric, be more significant close to the horizon than far away. We find a similar scaling with respect to M . Quantitatively the error contours are a bit larger compared to $[a_0, b_0]$, making these parameters eventually more difficult to be constrained by QNMs.

We also studied the role of the first overtone $n = 1$ in Sec. 9.4.4. There we find that it can be helpful in determining parameters of the metric, but the contours still follow qualitatively similar patterns. Again, without very high precision for the provided spectrum, determining the leading parameters $[a_0, b_0]$ within their PPN limits seems unlikely. However, especially for introducing changes in the scaling of the real part, the access to overtones looks very promising. The role of overtones in testing the no-hair theorem and doing parameter estimation, are ongoing research [316, 317, 318].

With the explicit demonstration of the effective potentials in Sec. 9.4.5, we have verified that the shape of the potential allows the application of the third order WKB formula. This also motivates that our findings are reasonable, because the reconstructed potential barriers agree excellently. But, since the WKB method is not an exact method, small deviations with respect to exact methods are possible. Finally, because differences between the RZ potentials and the reference Schwarzschild potential become only visible close to the horizon, it is reasonable to expect that time-evolution calculations describing scattered radiation should give almost indistinguishable results too.

Now we want to make some remarks regarding the possible application of the RZ metric in the inverse spectrum problem, where one reconstructs the perturbation potentials or metric from a given QNM spectrum, e.g. [301, 319] or our works in chapter 6, chapter 7, and chapter 8. An important question in this problem is the uniqueness of the reconstructed potential. In some of the mentioned works, Birkhoff's theorem [154] for spherically symmetric and non-rotating space-times was used. However, in this work, we do not have such a theorem if the underlying theory is not known. At the same time, it is well understood that different potentials can admit the same spectrum. Popular examples are the perturbation potentials of axial and polar perturbations described by the Regge-Wheeler [85] and Zerilli potentials [86], as shown by Chandrasekhar and Detweiler [208] and connected to the Darboux transform recently [258]. Considering only the first few parameters in the RZ metric, and demanding them to match Schwarzschild like fundamental modes, will give tight constraints on the potential around the maximum. Since the RZ parameters introduce, by construction, more significant effects close to the horizon, than far away, this puts additional constraints. Note that the potentials constructed in this work actually match the Schwarzschild potential in these regions extremely well. However, this precise overlap is not obvious, since in general, isospectral potentials can admit much stronger deviations from each other.

Finally, we want to comment on the role of rotation. Astrophysical black holes are expected to spin significantly, especially the observable ones forming via binary black hole mergers. This introduces not only a second parameter to the problem, but also complicates the structure of the metric and the perturbation equations. Dealing with this circumstance appropriately is far beyond the scope of this work, but an important aspect in the full problem. Note that the RZ metric has been extended to include rotation in [199], so our study can in principle be extended in the future. Since we find some degeneracy between the leading RZ parameters and the black hole mass, the situation might be significantly more difficult if the mass and spin are both treated as free parameters.

9.6 Conclusions

Using the spectrum of QNMs to study alternative black hole space-times is an interesting and feasible approach in exploring alternative theories of gravity. In a theory agnostic situation, where the underlying field equations

are not known, parametrized metrics can be an effective way to investigate different properties of space-time. Unfortunately, the absence of the field equations makes it impossible to predict the evolution of gravitational perturbations, which are accessible nowadays through the advanced LIGO and advanced Virgo observatories.

In this work, we assumed that some classes of alternative theories exist, in which non-rotating black hole solutions are sufficiently well approximated by the leading order terms of the parametrized metric proposed by Rezzolla and Zhidenko [198]. Since scalar perturbations evolve qualitatively similar to the ones for gravitational perturbations in general relativity, and do not directly depend on the field equations, we have motivated that at least for some alternative theories, their qualitative behavior might be well captured with the scalar test field. Although no stringent direct connection to gravitational perturbations is possible, such fields are a legitimate approach if one is aware of this limitation.

By using the third order WKB formula to compute the QNM spectrum, we have investigated some part of the multi-dimensional parameter space of the RZ metric with reasonable resolution. We showed explicitly how the leading parameters influence the fundamental mode ($n = 0$) and the first overtone ($n = 1$) for different l . We find that the parameter combinations $[a_0, b_0]$ and $[a_1, b_1]$ strongly correlate with the black hole mass M . This implies, even in the rather optimistic case in which the connection to the scalar field holds, tiny uncertainties in the black hole mass predict non-zero parameters of the metric, which are still in agreement with the pure fundamental Schwarzschild QNMs.

As we have demonstrated in Fig. 9.7, the approach carried out in this work can also be used in the inverse spectrum problem, where one tries to reconstruct perturbation potentials from the QNM spectrum. Our explicit reconstruction of potentials admitting the same fundamental modes proves that such potentials can be constrained via this method.

Our findings might put the popular approach of using the QNM spectrum in the study of black hole space-times in a delicate context. Of course, in principle the higher order parameters might be well constrained once the whole spectrum is being provided with pristine precision, but such a scenario is far away from actual observations. In the loudest event GW150914, only rough constraints on the fundamental QNM are possible [13, 305, 320]. Since we did not consider rotating black holes in this work, our work has to be extended in the future. However, besides having a second parameter to fit observations, the results of this work already indicate that the situation becomes more involved and the unique reconstruction of parameterized space-times complicated.

Finally, since parametrized metrics are also used to obtain geodesics and therefore find applications in the calculation of black hole shadows and ray tracing, it might be promising to combine both approaches. Since the lightring is closer to black hole horizon than typical extensions of an accretion disc, it might be enlightening to combine both approaches to put even tighter constraints on the parameters.

9.7 Supplementary Material

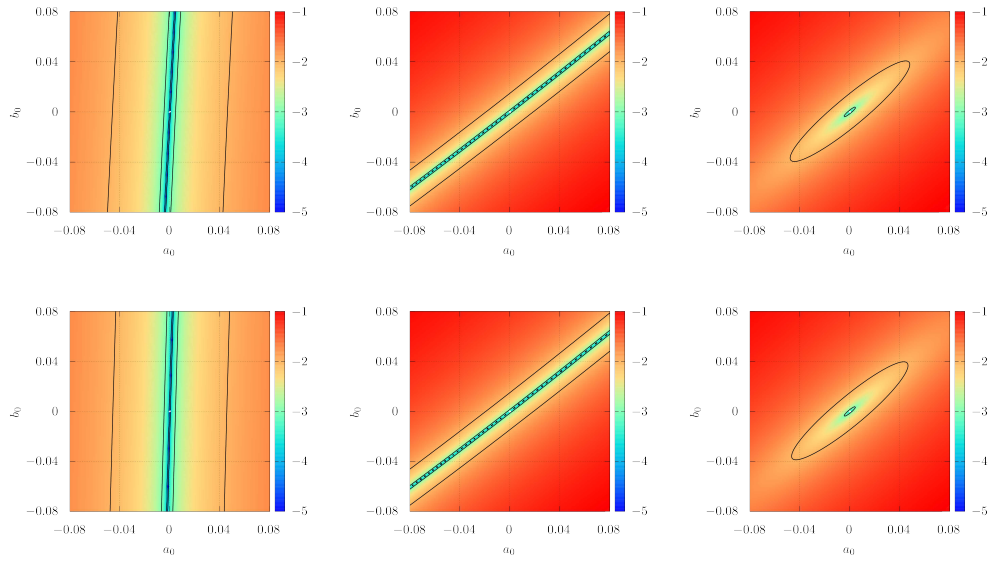


Figure 9.1: Relative errors for $n = 0$ and different l for $[a_0, b_0]$. In the following we show the logarithm $\log_{10}(x)$ of the relative errors from left to right for: the real part ω_r , the imaginary part ω_i , and the combination ω_c eq. (9.8). From top to bottom we show $l = 2$ and $l = 3$. Figures taken from [8].

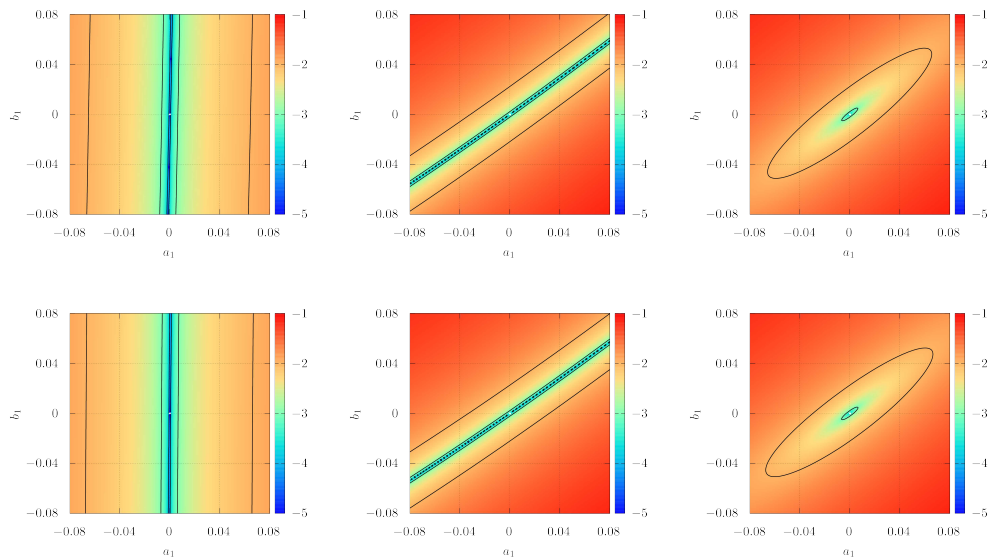


Figure 9.2: Relative errors for $n = 0$ and different l for $[a_1, b_1]$. In the following we show the logarithm $\log_{10}(x)$ of the relative errors from left to right for: the real part ω_r , the imaginary part ω_i , and the combination ω_c eq. (9.8). From top to bottom we show $l = 2$ and $l = 3$. Figure is taken from [8].

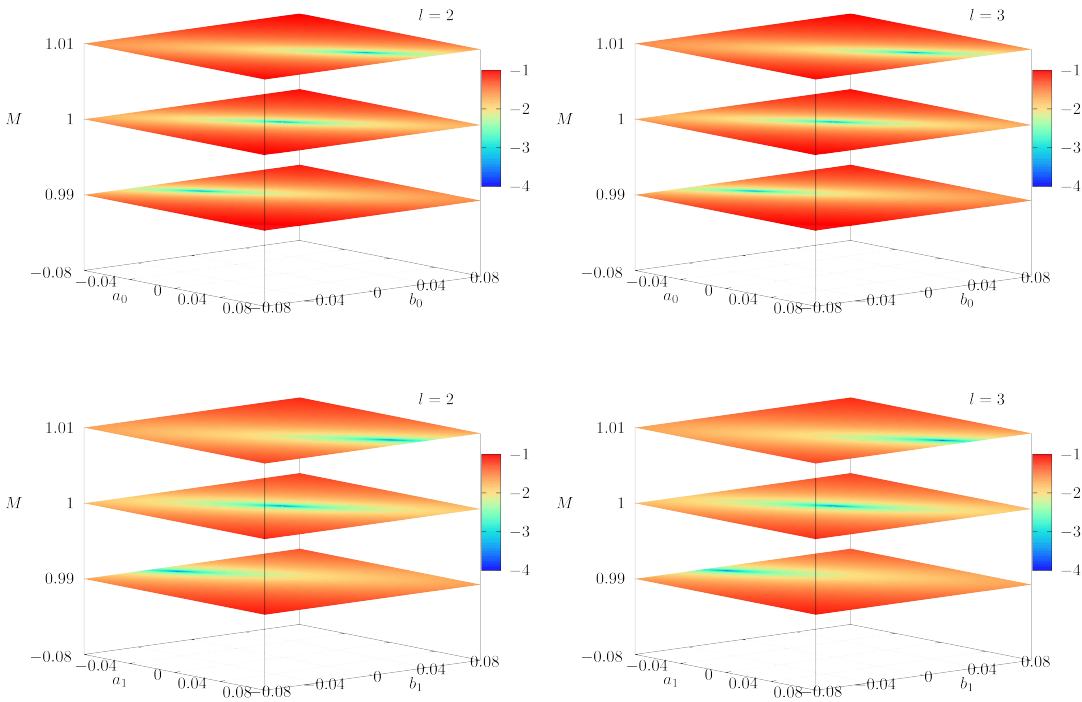


Figure 9.3: Here we show the combined relative errors ω_c for $n = 0$ and different M . The top panels are the $l = 2$ (left) and $l = 3$ (right) case for $[a_0, b_0]$, while the same l cases are shown in the bottom panels for $[a_1, b_1]$. Each layer is obtained for different mass M , while setting the non-varying parameters to the general relativity value of 0. Figures taken from [8].

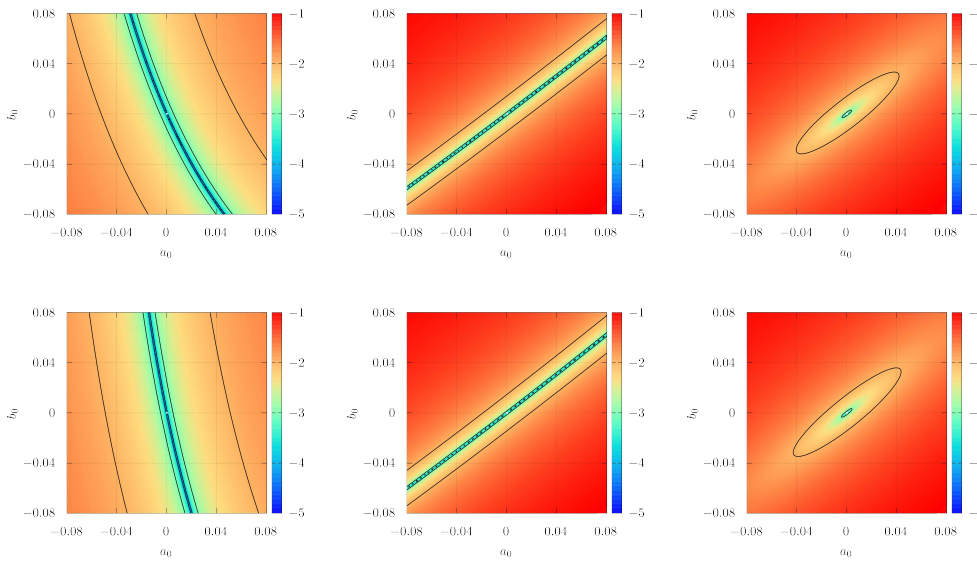


Figure 9.4: Relative errors for $n = 1$ and different l for $[a_0, b_0]$. In the following we show the logarithm $\log_{10}(x)$ of the relative errors from left to right for: the real part ω_r , the imaginary part ω_i , and the combination ω_c eq. (9.8). From top to bottom we show $l = 2$ and $l = 3$. Figures taken from [8].

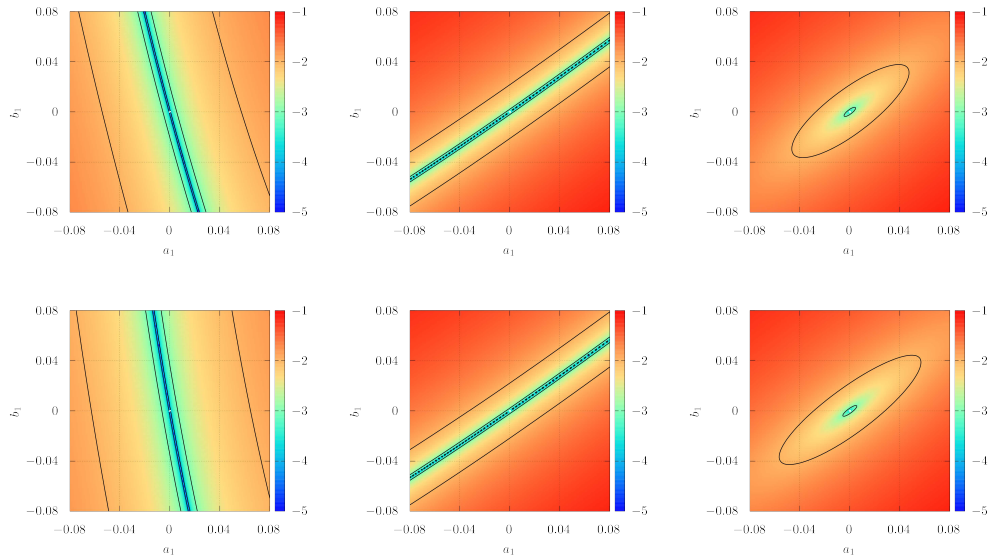


Figure 9.5: Relative errors for $n = 1$ and different l for $[a_1, b_1]$. In the following we show the logarithm $\log_{10}(x)$ of the relative errors from left to right for: the real part ω_r , the imaginary part ω_i , and the combination ω_c eq. (9.8). From top to bottom we show $l = 2$ and $l = 3$. Figures taken from [8].

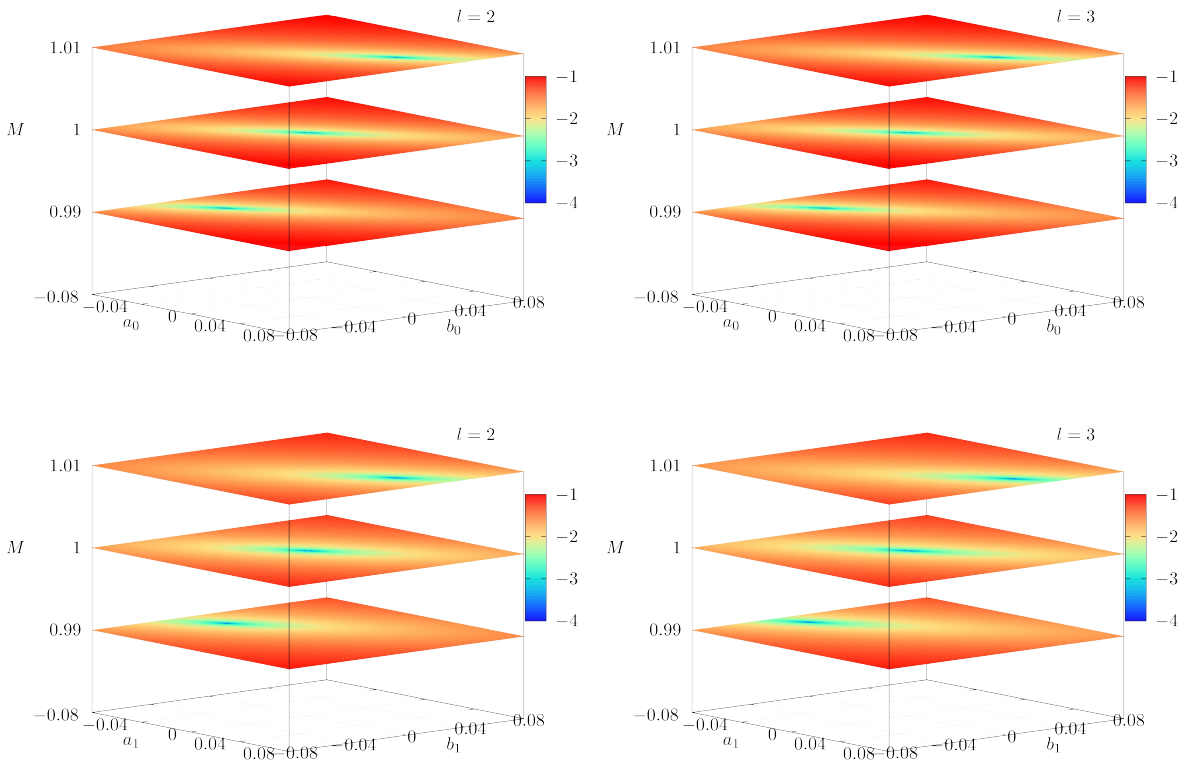


Figure 9.6: Here we show the combined relative errors ω_c for $n = 1$ and different M . The top panels are the $l = 2$ (left) and $l = 3$ (right) case for $[a_0, b_0]$, while the same l cases are shown in the bottom panels for $[a_1, b_1]$. Each layer is obtained for different mass M , while setting the non-varying parameters to the general relativity value of 0. Figures taken from [8].

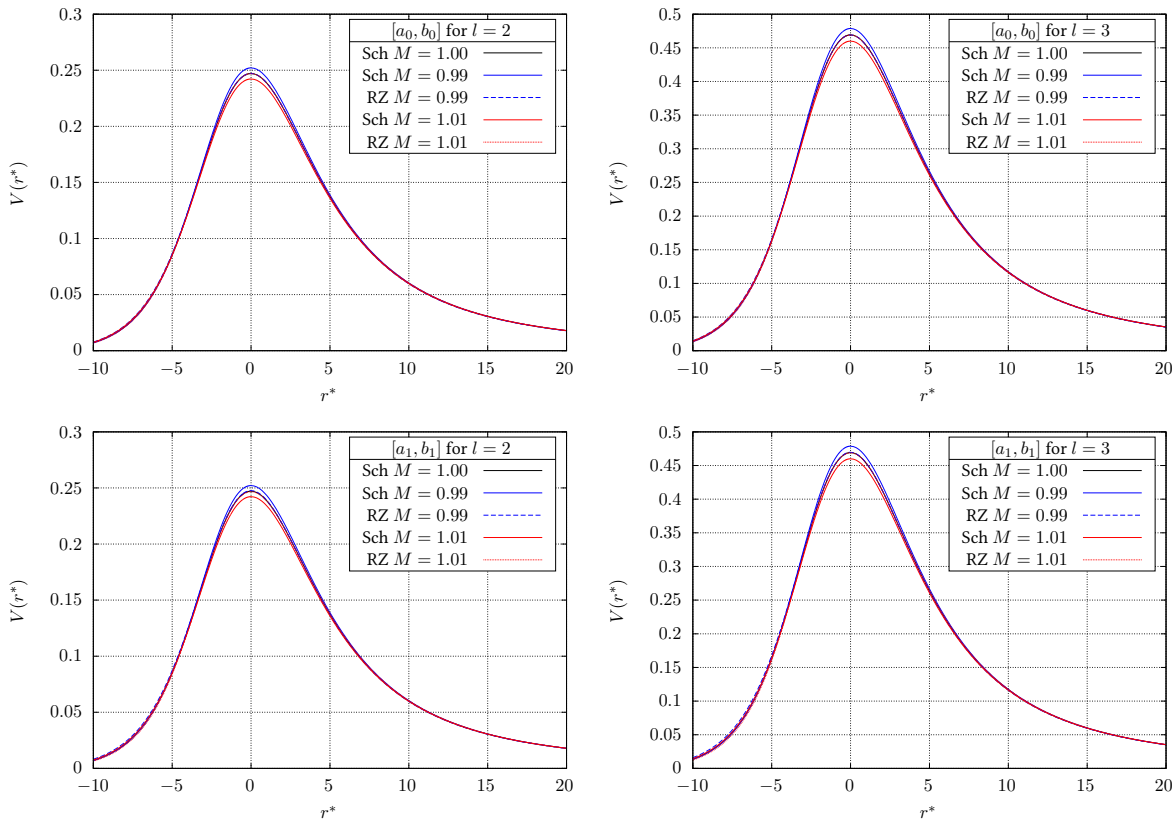


Figure 9.7: Here we show various potential barriers $V(r)$ as function of the tortoise coordinate r^* for different parameters $[M, a_0, b_0]$ (top panels) and $[M, a_1, b_1]$ (bottom panels). From left to right we consider input from $n = 0$ for the $l = 2$ and $l = 3$ cases. In each panel we show the standard Schwarzschild potentials (Sch) for different $M = [0.99, 1.00, 1.01]$ (solid lines). The dashed lines are the best matches of $[a_0, b_0]$ and $[a_1, b_1]$ for $M = [0.99, 1.01]$ in the RZ metric (dashed lines). The parameters were chosen by taking the smallest combined error $\delta\omega_c$ with respect to the $M = 1$ Schwarzschild case. To demonstrate that these modified masses change the Schwarzschild potential noticeably, we also show the Schwarzschild potentials for $M = [0.99, 1.01]$ (red and blue solid) for comparison. Note that the RZ results (dashed lines) overlap with the canonic Schwarzschild potential (black solid) around the maximum, while the other Schwarzschild cases (red and blue solid) are clearly distinguishable. Figures taken from [8].

10 | Parameter Estimation of Gravitational Wave Echoes from Exotic Compact Objects

Breakdown of Contributions

This chapter is based on the publication “*Parameter estimation of gravitational wave echoes from exotic compact objects*” by Andrea Maselli, Sebastian H. Völkel and Kostas D. Kokkotas, Phys. Rev. D 96, 064045, 2017, [3]¹. Since this is a collaborative work with Andrea Maselli, who was a postdoctoral researcher in our group at Tübingen, I will first outline our individual contributions. The types of exotic compact objects we parameterize here are inspired by ultra compact constant density stars. In our previous works, presented in chapter 5 and in chapter 6, we studied their oscillation spectra in the direct and indirect problem. By using an already existing code, Kostas D. Kokkotas provided us with the time evolution of the signal. Starting from this, Andrea Maselli and I worked in equal shares on the phenomenological parameterization of the waveforms and parameter estimation. Andrea Maselli is first author of this work because he adapted his already existing Fisher matrix code to the present problem. The writing of the text has been done by Andrea Maselli and me, while Kostas D. Kokkotas also assisted in editing the final manuscript.

Overview

Here we study the question whether the gravitational wave signal of perturbed exotic compact objects can be used to reconstruct the parameters that describe their template. Using a numerical code to simulate the waveform expected from constant density stars, as prototype of an exotic compact object, we phenomenologically parameterize the waveform with different analytical models. In order to quantify whether detected signals can be used to recover the parameters, we apply the Fisher matrix approach to the properties of current and future gravitational wave detectors. Due to the lack of realistic gravitational wave templates and related advanced data analysis techniques for such objects, our work estimates how well these parameters can, in principle, be recovered. We find that already current detectors at design sensitivity have the potential to reconstruct the main parameters, if the signals are properly described by our templates.

This paper is organized as follows. We first provide an introduction in Sec. 10.1. In Sec. 10.2 we define the analytical templates used to model the echoes, which will be used to determine the parameters’ detectability. In Sec. 10.3 we briefly describe the data-analysis procedure employed, while in Sec. 10.4 we present our numerical results, analyzing the errors on the gravitational waveforms for different interferometers. In Sec. 10.5 we summarize our conclusions.

10.1 Introduction

Gravitational wave astronomy is nowadays emerging as a new observational window, able to provide fundamental insights on some of the most energetic phenomena of our universe. The amount of incoming data produced by ground based interferometers also promises to address questions of fundamental physics with unprecedented accuracy. Among all the possible compact sources, black holes are probably the most extreme physical systems, whose existence has been definitively assessed by the advanced LIGO and advanced Virgo discoveries, see Sec. 1.3.5 for an overview. These detections mark the dawn of black hole spectroscopy, and at the same time represent the first genuine strong-field tests of general relativity [305].

¹Reprinted parts with permission from Andrea Maselli, Sebastian H. Völkel and Kostas D. Kokkotas, Phys. Rev. D 96, 064045, 2017. Copyright 2017 by the American Physical Society.

However, some crucial questions regarding the fundamental nature of black holes still remain to be addressed, as we outlined in Sec. 2.3. As an example, theoretical models predicting the existence of exotic compact objects whose compactness approaches the black hole limit, have not been completely ruled out. Such bodies may form in Nature as binary systems and merge due to gravitational wave emission. During the coalescence, these objects leave distinct signatures within the inspiral part of the signal, which has already proved to be extremely effective in discriminating between regular black holes and exotic scenarios [321, 322]. After the merger, horizonless compact objects will emit gravitational radiation until they reach a quiet and stationary state. During this process, multiple trapped w-modes may be excited, which would be visible within the gravitational wave signal by the appearance of echo-like structures, i.e. repeated pulses with characteristic frequencies and amplitudes, which differ from the black hole QNM spectrum, see Sec. 3.6 for details.

Several efforts have been already devoted to characterize the gravitational wave emission of exotic objects out of equilibrium [133, 163, 182, 263, 264, 294]. If additional structures appear within the spectrum, our ability to extract the signatures which deviates from the standard black hole picture, will strongly depend on the availability of realistic templates to be used in data searches. In this sense, the works by [323, 324] provide the first systematic attempts to construct fully reliable templates to identify the echoes.

Motivated by these results, in this paper we explore for the first time the detectability of gravitational wave signals emitted by exotic compact objects formed after binary coalescences. We consider different phenomenological templates, which are physically motivated by the analysis of perturbed ultra compact stars and the aforementioned works. The scope of this study is twofold: (i) determine the errors on the waveform's parameters which would be measured by current and future gravitational wave interferometers, (ii) investigate the dependence of such detections by the echo's parameters. Although the models employed suffer of some limitations, a complete and fully accurate description of the gravitational wave signal is nowadays not available. Nevertheless, the analysis developed in this work captures important features of the overall phenomena. Our results suggests that Advanced LIGO at design sensitivity would already be able to constrain the parameters of the echo's with good accuracy, possibly leading to infer new information on the nature of the perturbed compact object.

10.2 The ECHO Templates

The time evolution of perturbations has been discussed in Sec. 3.5.2 and involves the numerical integration of the underlying wave equation and therefore does not provide parameterized waveforms, which are more suitable for our type of parameter estimation. Using the numerical waveforms of ultra compact constant density stars, we propose different parameterized waveforms with increasing level of detail that can capture the phenomenology of exotic compact objects. This pedagogical and simple approach to the problem is justified by the fact that realistic models for exotic compact objects are not known and therefore no sophisticated waveforms exist.

The perturbation of an exotic compact object by a test particle or a wave packet will lead to the following characteristic response. The initial pulse of radiation is partially reflected by the potential barrier and will imitate the standard black hole ringdown. The transmitted part of the radiation will excite the trapped QNMs in the cavity and leak out over long times. At early times the repeated reflections will leak out as a series of recently called "echoes". Note that a similar phenomenology has already been found in earlier works [236, 237, 238].

In all our parameterized waveform models we start with the initial black hole ringdown and add to different level of detail the repeated series of echoes. The models are explained in the following and visualized in Fig. 10.1.

10.2.1 Model echoI

Our first model is given by $h_I(t) = h_{\text{QNM}}(t) + h_1(t)$, where

$$h_{\text{QNM}}(t) = \bar{\mathcal{A}}e^{-t/\bar{\tau}} \cos(2\pi\bar{f}t + \bar{\phi}) \quad (10.1)$$

describes the initial black hole QNM response, which is specified by its amplitude, frequency, phase and damping time $(\bar{\mathcal{A}}, \bar{f}, \bar{\phi}, \bar{\tau})$. The second part

$$h_{\text{I}}(t) = \sum_{n=0}^{N-1} (-1)^{n+1} \mathcal{A}_{n+1} e^{-\frac{y_n^2}{2\beta_1^2}} \cos(2\pi f_1 y_n), \quad (10.2)$$

introduces N echoes after the first mode. In this model we make the simple choice that each echo is described by the same frequency and shape (f_1, β_1) . Only the amplitude changes with $\mathcal{A}_{n+1} = \mathcal{A}_{1, \dots, N}$. The last unexplained variable is $y_n(t) = (t - t_{\text{echo}} - n\Delta t)$. Here t_{echo} describes the time shift between the first black hole like mode and the first echo. The time delay between consecutive echoes is characterized by the time delay Δt .

10.2.2 Model echoIIa

Again we describe the first oscillation with the black hole ringdown. We add more details to the echo part by introducing a second frequency f_2 . This improvement takes into account that the echo frequencies correspond to the trapped modes, which form in general a spectrum of multiple frequencies. This waveform is given by

$$h_{\text{II}} = h_{\text{QNM}}(t) + h_{\text{IIa}}(t, f_1, f_2, \beta_1) \quad (10.3)$$

with

$$h_{\text{IIa}}(t) = \frac{1}{2} \sum_{n=0}^{N-1} (-1)^{n+1} \mathcal{A}_{n+1} e^{-\frac{y_n^2}{2\beta_1^2}} \left[\cos(2\pi f_1 y_n) + \cos(2\pi f_2 y_n + \phi) \right]. \quad (10.4)$$

Here ϕ is the phase that determines the offset between the two terms at $t = 0$. Eq. (10.4) describes a beat-like structure, which is the simplest way to mimic the interference between different excited trapped modes.

10.2.3 Model echoIIb

Lastly, our third model generalizes the previous approaches by adding a different Gaussian function that takes into account the shape of the second trapped mode in the echoes

$$h_{\text{III}} = h_{\text{QNM}}(t) + h_{\text{IIb}}(t, f_1, f_2, \beta_1, \beta_2), \quad (10.5)$$

with

$$h_{\text{IIb}}(t) = \frac{1}{2} \sum_{n=0}^{N-1} (-1)^{n+1} \mathcal{A}_{n+1} \left[e^{-\frac{y_n^2}{2\beta_1^2}} \cos(2\pi f_1 y_n) + e^{-\frac{y_n^2}{2\beta_2^2}} \cos(2\pi f_2 y_n + \phi) \right]. \quad (10.6)$$

10.2.4 Comment on the Amplitudes

The amplitudes of all waveform models can not directly be related to trapped modes spectrum, but are motivated from the numerical waveform. We assume that the amplitudes $\mathcal{A}_{1, \dots, N}$ carry a fraction of the initial black hole QNM component $\bar{\mathcal{A}}$. This scaling is found in the updated version of a code for ultra compact constant density stars presented in [236]. Here the ratio between the black hole amplitude and the first echo amplitude is roughly equal to $\bar{\mathcal{A}}/\mathcal{A}_1 \sim 1/4$. Consecutive echo amplitudes then decrease as $\bar{\mathcal{A}}/\mathcal{A}_N \sim \frac{1}{4+N}$. By making this choice we reduce the number of free parameters significantly and scale them with the initial black hole like factor $\bar{\mathcal{A}}$.

10.2.5 Further Generalizations

In order to incorporate more details of the numerical waveform, the following straightforward improvements could be done in future work: (i) add different frequencies and their interference to characterize each echo; (ii) include the damping factor of each frequency (although we expect they would play a subordinate role within the

data-analysis of the waveform), (iii) introduce different functions to model the shape of the echoes, instead of the Gaussian profile used in this paper. Such improvements could potentially describe a more realistic scenario, which would ultimately depend on the nature of the ECO's perturbation. However, we believe that the gravitational wave templates presented in this section are already able to capture the most relevant features of the real process.

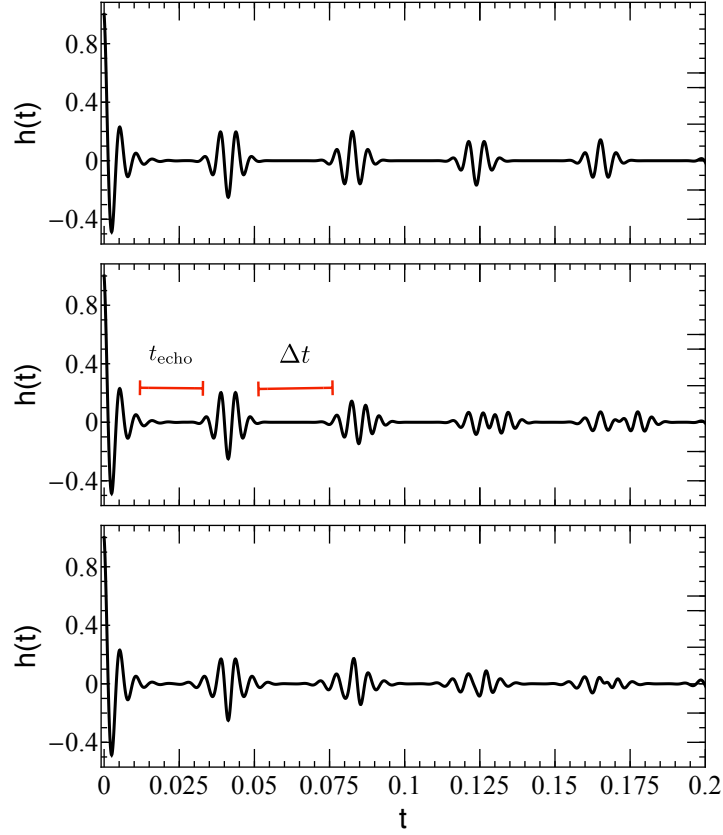


Figure 10.1: Sketch of some phenomenological waveforms used in this work. The center panel also shows the meaning of the two parameters t_{echo} and Δt , which identify the time shift between different pulses in the template. Figure taken from [3].

10.3 Data Analysis Procedure

In this work we use a Fisher matrix approach [325, 326, 327] to estimate the errors on the template parameters. If one considers a large signal to noise ratio (SNR), one can write the probability distribution of the parameters $\vec{\theta}$ of a given set of data d as expansion around the true values $\vec{\theta}_v$ as

$$p(\vec{\theta}|d) = p_0(\vec{\theta})\mathcal{L}(d|\vec{\theta}) = p_0(\vec{\theta})e^{-\frac{1}{2}(\tilde{h}(\vec{\theta})-d|\tilde{h}(\vec{\theta})-d)} \approx p_0(\vec{\theta})e^{-\frac{1}{2}\Gamma_{\alpha\beta}\Delta\theta^\alpha\Delta\theta^\beta}. \quad (10.7)$$

Here $p_0(\vec{\theta})$ describes the prior probability on $\vec{\theta}$ and $\Delta\theta^\alpha = \theta^\alpha - \theta_v^\alpha$. The Fisher information matrix $\Gamma_{\alpha\beta}$, which characterizes the curvature of the likelihood function $\mathcal{L}(d|\vec{\theta})$, is expressed in terms of the partial derivatives of the gravitational wave template with respect to the echo parameters

$$\Gamma_{\alpha\beta} = \left(\frac{\partial \tilde{h}}{\partial \theta_\alpha} \middle| \frac{\partial \tilde{h}}{\partial \theta_\beta} \right)_{\vec{\theta}=\vec{\theta}_v}. \quad (10.8)$$

$(\tilde{a}|\tilde{c})$ defines the scalar product on the waveform's space given by

$$(\tilde{a}|\tilde{c}) = 2 \int_0^\infty \frac{\tilde{a}(f)\tilde{c}^*(f) + \tilde{a}^*(f)\tilde{c}(f)}{S_n(f)} df, \quad (10.9)$$

$S_n(f)$ is the noise spectral density of the chosen detector, and $\tilde{a}(f), \tilde{c}(f)$ are the Fourier transform of the templates in the frequency domain. We use the following normalization for the Fourier transform of the templates

$$\tilde{h}(f) = \int_{-\infty}^{\infty} h(t) dt \quad , \quad h(t) = \frac{1}{2\pi} \int_{-\infty}^{\infty} \tilde{h}(f) df . \quad (10.10)$$

All the waveforms considered yield a full analytical form of $\tilde{h}(f)$, which can be easily computed by means of symbolic manipulation softwares like Mathematica. The covariance matrix of the parameters is simply given by the inverse of the Fisher, i.e. $\Sigma_{\alpha\beta} = (\Gamma_{\alpha\beta})^{-1}$, whose diagonal and off-diagonal components correspond to the standard deviations and the correlation coefficients of $\vec{\theta}$, respectively. Note that, according to the Cramer-Rao bound, the uncertainties obtained through the Fisher matrix represent a lower constraint on the variance of any unbiased estimator of the parameters. The scalar product eq. (10.9) also allows to define the SNR of the specific signal, as

$$\rho^2 = (\tilde{h}|\tilde{h}) = 4 \int_0^{\infty} \frac{|\tilde{h}(f)|^2}{S_n(f)} df . \quad (10.11)$$

In this paper we consider the detectability of echoes by current and future generation of detectors. These include Advanced LIGO with the ZERO_DET_high_P anticipated design sensitivity curve [328], the Einstein Telescope (ET) [329], LIGO-Voyager (VY) [330], Advanced LIGO with squeezing (LIGO A+) [331] and the Cosmic Explorer (CE) with a wideband configuration [332]. In the following Sec. 10.4 we will present our results on the specific parameter of the template θ_α either in terms of the absolute error σ_α , or its relative (percentage) value $\epsilon_\alpha = \sigma_\alpha/\theta_\alpha$.

10.4 Constraints on the echo's parameters

Here we present the results for the different templates of Sec. 10.2 using numerical integration of eqs. (10.8)-(10.11). For all the models we choose the frequency and the damping factor of the black hole QNM mode, as those of a non-rotating object with the same mass of the final black hole formed in the GW150914 event [305], i.e. $M \simeq 65 M_\odot$. This yields $\bar{f} \simeq 186$ Hz and $\bar{\tau} \sim 3.6 \times 10^{-3}$ s. Moreover, without loss of generality, we fix the phase of $\tilde{h}(t)$ to $\bar{\phi} = 0$, and the overall amplitude to a prototype value $\mathcal{A} = 5 \times 10^{-22}$, which roughly corresponds to a SNR of the QNM-like mode only (i.e. neglecting the contribution of the following echoes) of $\rho \sim 8$ with Advanced LIGO. This value is consistent with the best-fit parameters inferred from GW150914, O1 configuration [305]. Note that, since A represents a multiplicative factor of the total signal, our results can immediately be re-scaled to any amplitude A_{new} as

$$\Gamma_{\alpha\beta} \rightarrow \frac{\mathcal{A}_{\text{new}}}{5 \times 10^{-22}} \Gamma_{\alpha\beta} \quad \Rightarrow \quad \sigma_\alpha \rightarrow \frac{5 \times 10^{-22}}{\mathcal{A}_{\text{new}}} \sigma_\alpha , \quad (10.12)$$

and in the same way for the SNR

$$\rho \rightarrow \frac{\mathcal{A}_{\text{new}}}{5 \times 10^{-22}} \rho . \quad (10.13)$$

After the first pulse, repeated echoes are also expected to occur with a time delay Δt which depends on the nature of the exotic object [296]. The time to travel from the peak of the potential barrier to the reflective surface and back is approximate with

$$\Delta t \sim 4M |\log \delta| , \quad (10.14)$$

where $\delta \ll 1$ describes the position of the effective surface r_0 with respect to the non-rotating black hole horizon located at $2M$ in the Schwarzschild coordinate.², i.e. $r_0 = 2M(1 + \delta)$. By using eq. (10.14) we can approximate the potential well, which is responsible for the reflection of the echoes, with a box-potential specified by the

²The coordinate distance is not gauge invariant, and therefore in general the specific value of δ is not uniquely defined. However the difference with respect to the proper distance is subordinate in our calculations due to the logarithmic dependence within r_0 . Note also that the approximations for small δ are only valid for systems, where the reflecting surface is very close to the black hole horizon in the Schwarzschild coordinate. Although constant density stars can feature a similar structure, the values of δ for such objects can never be small, due to the Buchdahl limit.

coordinate width

$$x_c \simeq 2M |\log \delta|. \quad (10.15)$$

By making this assumption one can relate the frequencies in the echoes and the trapped modes inside the potential well with each other. It allows to express the gap between two consecutive modes Δf with frequencies f_{n+1}^{box} and f_n^{box} as

$$\Delta f \equiv f_{n+1}^{\text{box}} - f_n^{\text{box}} \simeq \frac{1}{4M |\log \delta|}. \quad (10.16)$$

Having fixed the first frequency of each waveform to the corresponding black hole QNM component, we can immediately derive the values of f_1 and f_2 used in the `echoI` and `echoIIa-b` templates

$$f_1 \simeq \bar{f} \quad , \quad f_2 \simeq \bar{f} - \Delta f. \quad (10.17)$$

Note that $f_2 < f_1$. It is worth to remark that these assumptions represent an approximation of the real physical scenario, in which we expect that $\bar{f} \neq f_1$ and Δf take a more complex form, which ultimately depends on the specific exotic compact object. However, for the purpose of this paper, this will not change the outcome of the data-analysis procedure. Moreover, having fixed the object mass to $M = 65M_\odot$, throughout this paper we consider three values of $\delta = (10^{-10}, 10^{-20}, 10^{-30})$, which roughly correspond to compact objects with surface corrections at Micron, Fermi and Planckian level, respectively [322].

Finally, the time between the black hole QNM-like mode and the first echo, t_{echo} could be affected by nonlinearities due to the merger phase at the end of the coalescence [133], i.e. $t_{\text{echo}} \simeq \Delta t \pm \delta t$. In the following, for each value of Δt given by eq. (10.14), we will consider different configurations by varying the coefficient δt in order to have a maximum correction of the order 10 % on t_{echo} .

Before assessing the detectability of the templates from Sec. 10.2, it is instructive to first analyze some basic features which are common to all the waveforms. In Fig. 10.2 we show the relative errors ϵ_α for the `echoI` model computed for LIGO, as a function of the number of echoes included within the template. In this particular case we assume $\beta_1 = 0.003$, and $\delta = 10^{-10}$, which corresponds to $t_{\text{echo}} = \Delta t \simeq 2.95 \times 10^{-2}$ s. From the first two panels one finds that the uncertainty on frequency and damping time of the black hole QNM component (black dots) is essentially unaffected by N , and it is therefore independent³ from the template (10.2). On the other hand, the errors on (f_1, β_1) and on the delay times $(t_{\text{echo}}, \Delta t)$ reduce as far as the number of pulses grows in time. For the particular model analyzed here, the uncertainty on both f_1 and β_1 changes approximately with 30 % between $N = 2$ and $N = 10$. Although these values seem to converge to the QNM value, this decrease saturates due to the progressive amplitude reduction of the echoes. This feature is also evident looking at the evolution of the overall SNR (right-bottom panel of Fig. 10.2), which reaches a nearly constant value of $\rho \sim 9.3$ after 12 pulses. This picture is nearly independent of the range of parameters used in this work and of the specific echo model adopted.

According to these results, we can safely consider gravitational waveforms that include 10 pulses after the black hole QNM oscillation, since larger values of N will not affect the analysis. This choice also makes our analysis more robust, since at later times, some physical effects may not be captured by our models (as the interference of multiple trapped frequencies).

³The correlation coefficients derived from the Fisher matrix between \bar{f} ($\bar{\tau}$) and the echo parameters, are also very small for all the configurations.

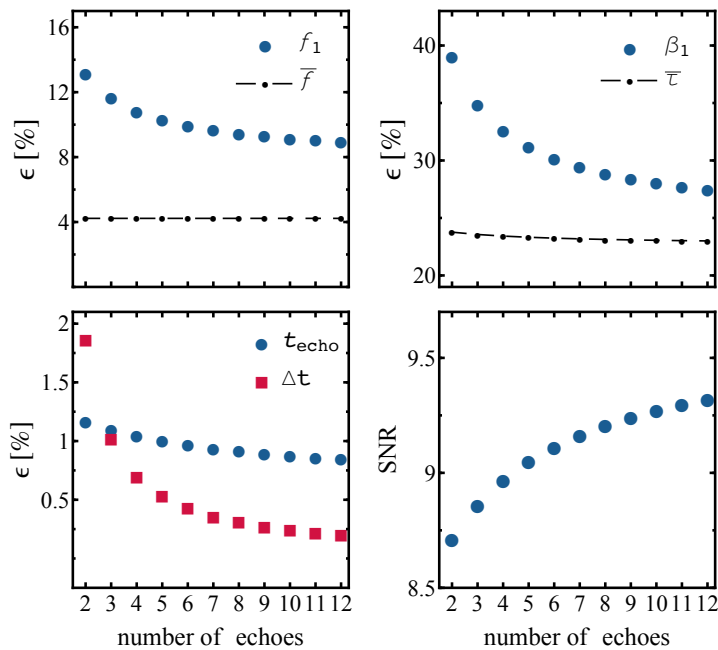


Figure 10.2: Relative (percentage) errors on the parameters of the template `echoI` as a function of the number of echoes. All the results are derived for Advance LIGO, assuming $\delta = 10^{-10}$, and $\beta_1 = 0.003$. The bottom right panel shows the change of the signal-to-noise ratio due to the increasing numbers of echoes. Figure taken from [3].

10.4.1 `echoI`

We start with our simplest waveform `echoI`, which depends on the set of parameters

$$\vec{\theta} = \{\ln \bar{A}, \bar{f}, \bar{\tau}, \bar{\phi}, f_1, \beta_1, t_{\text{echo}}, \Delta t\}, \quad (10.18)$$

which implies an 8×8 Fisher matrix. We fix the frequency and damping factor of the black hole QNM, while f_1 and the time shift Δt follow from eqs. (10.14) and (10.17). In order to explore the parameter space of different configurations, we vary the shape factor β_1 and $t_{\text{echo}} = \Delta t + \delta t$. This allows to determine the more (or less) favorable signals to be detected by gravitational wave detectors. The width of the Gaussian that describes the echoes represents the coefficient which dominantly affects the shape of the waveform and therefore leads to major changes in the parameter estimation. Moreover, we only discuss the features of the post-QNMs, since the errors on \bar{f} and $\bar{\tau}$ do not vary significantly within all the configurations. They are peaked around $\epsilon_{\bar{f}} \sim 4\%$ and $\epsilon_{\bar{\tau}} \sim 22\% - 23\%$, respectively. In Fig. 10.3 we show the uncertainties of the `echoI` parameters as a function of β_1 computed for Advanced LIGO, for a specific configuration with $t_{\text{echo}} \approx \Delta t$ and $\delta = 10^{-10}$. From both panels one can immediately see that all relative errors rapidly decrease as the shape factor grows, with variations $\gtrsim 40\%$ for ϵ_{f_1} and ϵ_{β_1} . Note that the SNR changes between $\rho \sim 8.9$ for $\beta_1 = 0.002$ to $\rho \sim 10.3$ for $\beta \sim 0.006$ with an overall increase of 15%. It is important to remark that, although these differences do exist between the various configurations, all the modes considered yield errors smaller than an $1\text{-}\sigma$ upper bound with $\epsilon_\alpha = 1$. This is particularly promising for the measurements of the time shift parameters (right panel), which can be constrained with an accuracy better than 1%.

The dependence of σ_α with respect to t_{echo} , which we vary in our dataset as $t_{\text{echo}} = \Delta t(1 \pm 0.1)$, is much milder and leads to nearly constant errors for all the parameters of the template. This can be appreciated from the contour plots of Fig. 10.4, in which curves of fixed accuracy for f_1, β_1 and Δt are given by vertical straight lines. Note that the *relative* errors on t_{echo} (bottom left) change less than 10% within the parameter space considered, even though the *absolute* error remains practically constant.

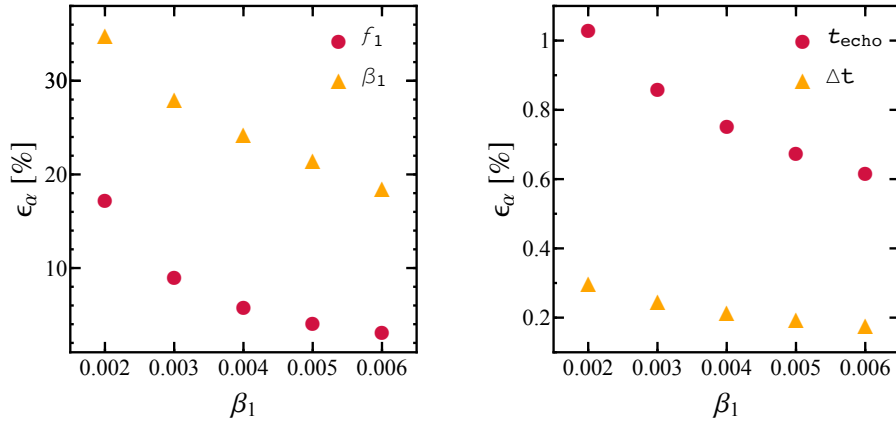


Figure 10.3: Relative (percentage) errors on the parameters of the template `eChOI` computed for Advanced LIGO, as a function of the width of the Gaussian width β_1 . Both panels refer to $t_{\text{echo}} \approx \Delta t \approx 2.95 \times 10^{-2}$ ($\delta = 10^{-10}$). Figure taken from [3].

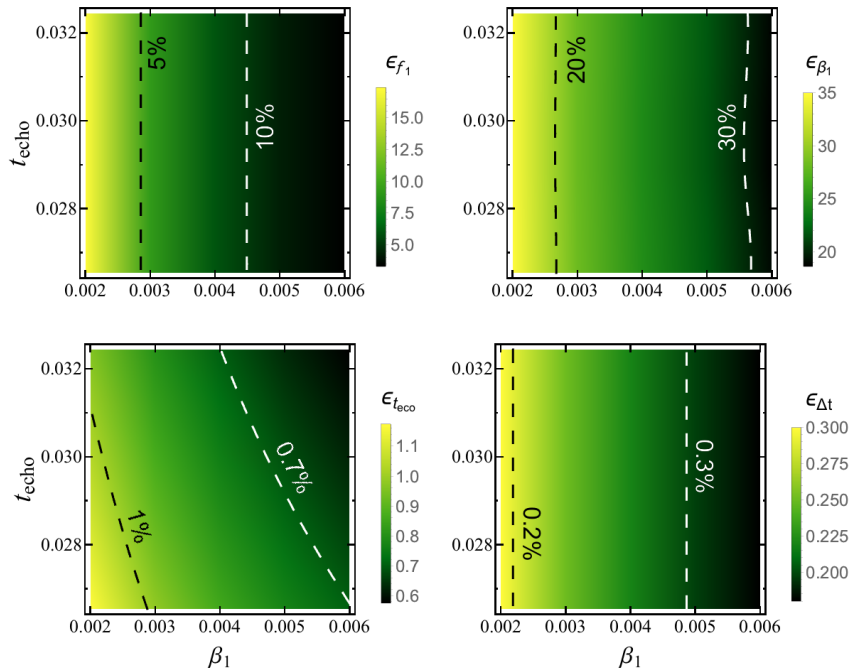


Figure 10.4: Contour plots in the $\beta_1 - t_{\text{echo}}$ parameter space for the relative errors on the `eChOI` parameters. White and black dashed curves represent configurations with fixed accuracy. The data refer to Advanced LIGO at design sensitivity. Figure taken from [3].

Although Advanced LIGO (at design sensitivity) seems already be able to set narrow bounds on some of the features of the echoes, it is interesting to investigate how these results improve as far as we consider next generation detectors. This is shown in Fig. 10.5, in which we draw the relative errors of `eChOI` for different interferometers. All the results correspond to the best-case scenario, i.e. for $\beta_1 = 0.006$. Note also that in general, for fixed β_1 , the best measurements for each detector will correspond to a different value of t_{echo} (although changing this variable does not yield significant variations). Looking at the top panel we note that the error of the echo's shape factor decrease to values of the order of $\leq 1\%$ already with LIGO A+, while for the frequency f_1 , the same level of accuracy would require at least the Einstein Telescope. As expected, the recently proposed Cosmic Explorer would lead to detect gravitational wave signals with exquisite precision, with errors being more than an order of magnitude smaller than values obtained by the current generation of detectors. Second generation interferometers are also expected to form a network of ground based detectors, as soon as Advanced Virgo and KAGRA will join the Hanford and Livingston LIGO sites. A collection of n independent interferometers will

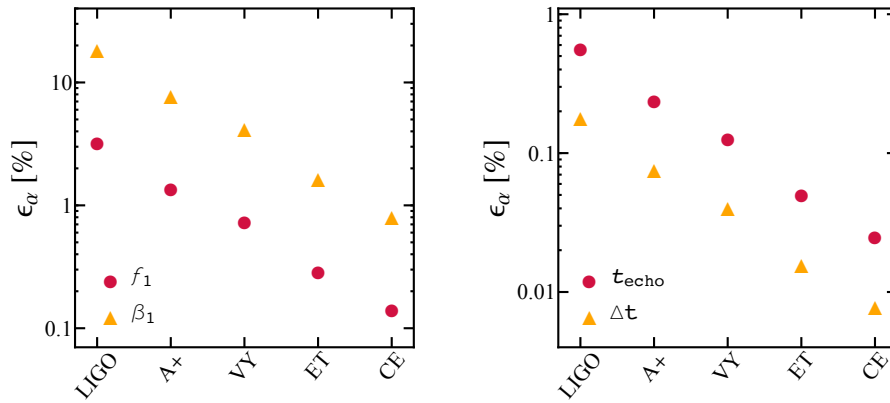


Figure 10.5: Errors on the `echoI` template for different gravitational wave interferometers. The data refer to the best case scenario with $\beta_1 = 0.006$ (and different values of t_{echo}). Figure taken from [3].

roughly reduces the error by a coefficient $1/\sqrt{n}$. Looking at Fig. 10.5 this factor would translate the network measurements at the same level of LIGO A+.

All the results presented so far are derived assuming a shift of the effective surface of the exotic compact object equal to $\delta = 10^{-10}$, which (together with the mass) determines the two time-delay factors of our template. In order to test alternative scenarios, we have considered different configurations by varying δ to 10^{-20} and 10^{-30} , without finding significant deviations from the data shown in Figs. 10.3-10.5. The parameters being mostly affected, f_1 and β_1 , lead to changes $\lesssim 9\%$ and $\lesssim 2\%$, respectively, while for the other coefficients we observe variations below 1%. The values of $\epsilon_{t_{\text{echo}}}$ and $\epsilon_{\Delta t}$ do actually change, although the corresponding absolute errors remain constant. This means that the uncertainties for the new values of δ can be simply obtained from the previous results, by rescaling

$$\epsilon_{t_{\text{echo}}}\Big|_{\delta=10^{-20}} = \epsilon_{t_{\text{echo}}}\Big|_{\delta=10^{-10}} \frac{t_{\text{echo}}(\delta = 10^{-10})}{t_{\text{echo}}(\delta = 10^{-20})}, \quad (10.19)$$

and the same for Δt .

10.4.2 `echoIIa-b`

The `echoIIa` model introduces two extra parameters: (i) a second frequency within the spectrum, which leads to a beat-like interference with the first component, (ii) a phase offset ϕ between the two echo modes. These extra parameters further enlarge the configuration space to a 10×10 Fisher matrix. This extension does not alter the estimate of \bar{f} and $\bar{\tau}$, whose errors remain unchanged compared to the values obtained for the previous template. Moreover, as already described for `echoI`, all the results are nearly degenerate with respect to t_{echo} , as changes on this parameter do not lead to sensible variations of the errors. For this reason we will only focus on the dependence of the echo's errors on β_1 .

The parameter estimation of this template shows that the results are strongly affected by the choice of ϕ . In particular the error distribution finds a minimum when the echo modes are out of phase with $\phi = -\pi/2$, while it is maximum when the two components are on phase, i.e. $\phi = 0$.

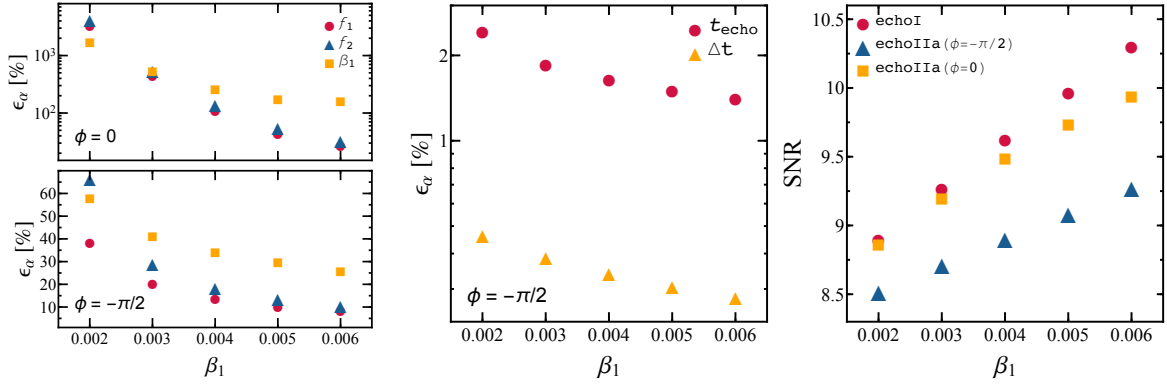


Figure 10.6: (Left and center panels) Same as Fig. 10.3 but for the parameters of the echoIIa model with phase shift $\phi = 0$ and $\phi = -\pi/2$. (Right panel) Comparison between the SNR of echoI and echoIIa as a function of β_1 . All the results refer to Advanced LIGO, assuming $t_{\text{echo}} \approx \Delta t$, with $\delta = 10^{-10}$. Figure taken from [3].

This effect is particularly relevant for (f_1, f_2, β_1) , as shown in the left panel of Fig. 10.6 in which we draw the corresponding relative uncertainties computed for LIGO, assuming $\delta = 10^{-10}$. As already seen for echoI, all the errors decrease with the growth of the shape factor, up to our best model with $\beta_1 = 0.006$. The two frequencies yield almost the same accuracy for $\phi = 0$, while for out-of-phase modes the errors on f_2 are in general larger and converge to ϵ_{f_1} for $\beta_1 \gtrsim 0.004$ only. This figure also shows that our ability to measure the width of the Gaussian function strongly depends on the phase of the echoes, as for $\phi = 0$ all of the configurations lead to errors above an upper bound $\epsilon_{\beta_1} = 1$. This picture changes dramatically if $\phi = -\pi/2$, for which the uncertainties on this parameter is of the same order of magnitude of (f_1, f_2) , and smaller than 50% for $\beta_1 > 0.002$. Variations of ϕ are subordinate on t_{echo} and Δt , for which we observe small deviations between the two cases. The center panel of Fig. 10.6 shows that even for this template the two parameters provide the best measurements, at the level of percent and below.

As expected, even for the most optimistic scenario ($\phi = -\pi/2$), the results obtained for this model are in general worse than those derived for the echoI (cfr. Fig. 10.3). This change is partially due to the larger number of parameters which, for a given configuration and detector sensitivity, dilutes the amount of information contained within the waveform. In this regard, it is also interesting to compare how the specific form of the waveform may influence the SNR of the signal (and the degeneracies between the parameters). The right panel of Fig. 10.6 shows indeed how this quantity changes as a function of β_1 for echoI and echoIIa (and two values of ϕ). The picture leads to some interesting conclusions. First, we observe that for all cases considered the second parametrization yields lower SNR. Moreover the overall growth is softer, with an increase of $\sim 9\%$ - 12% (depending on the value of ϕ) compared to a change of $\sim 16\%$ for the first template. More significantly, the values of ρ for $\phi = -\pi/2$ are always smaller than those for $\phi = 0$, which is a rather counterintuitive result, as the errors scale in the opposite direction. In this case a major role is played by the degeneracy between the parameters, as shown in Fig. 10.7 where the correlation coefficients $c_{\alpha\beta} = \Sigma_{\alpha\beta}/(\sigma_\alpha\sigma_\beta)$ between f_1 and (β_1, f_2) are plotted. For $\phi = 0$ the two components of the echoes (10.4) are described exactly by the same functional form, and all the variables are extremely correlated, as for the two frequencies for which $c_{f_1 f_2} \simeq -1$. Note that in the limit $f_1 \rightarrow f_2$ we would have an 100% degeneracy. Conversely, for out-of-phase modes with $\phi = -\pi/2$ we have a maximum break of such degeneracy which allows to set tighter constraints on the parameters. Moreover, the values of $c_{f_1 \beta}$ for $\beta = \{t_{\text{echo}}, \Delta t\}$ are always close to zero for any choice of ϕ , which is in line with the results previously described. Finally, unlike the echoI, the second template is more sensible to different values of δ . Comparing the results obtained for $\delta = 10^{-30}$ and $\delta = 10^{-10}$, assuming the optimal case $\beta_1 = 0.006$ and $\phi = -\pi/2$, we find that the absolute errors of $\{f_1, \beta_1, f_2, t_{\text{echo}}, \Delta t\}$ vary approximately of $\simeq \{23, -12, -8, -6, -41\}\%$, and therefore a scaling like that given by Eq. (10.19) is no longer valid. These differences grow dramatically for $\phi = 0$.

As last step we analyze the output of the echoIIB model, which improves the former description by adding another shape factor (β_2) to the second component of the pulses, specified by the frequency f_2 . For sake of simplicity, in this case we will fix $\delta = 10^{-10}$ and $t_{\text{echo}} = \Delta t$. Then, we span the possible configurations within

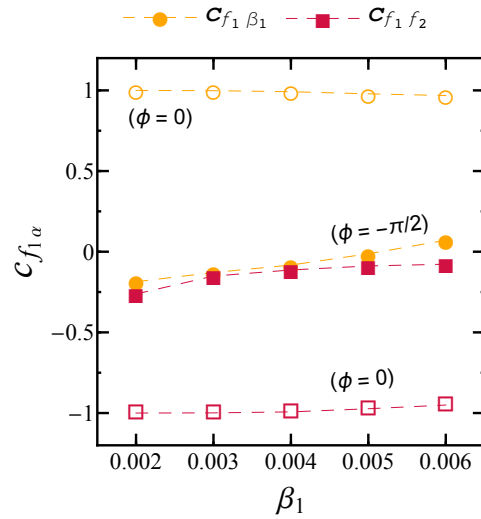


Figure 10.7: Correlation coefficients for the echoIIa template between f_1 and (β_1, f_2) , assuming $\phi = 0$ (empty dots) and $\phi = -\pi/2$ (empty dots), for LIGO with $\delta = 10^{-10}$ and $t_{\text{echo}} \approx \Delta t$. Figure taken from [3].

the $\beta_1 \times \beta_2$ parameter space, also assuming the two phase shifts considered before, i.e. $\phi = 0$ and $\phi = -\pi/2$. Fig. 10.8 shows the numerical results obtained for the latter, assuming the LIGO detector. From the top panels we observe that the relative errors on (f_1, β_1) are nearly degenerate with respect to the Gaussian width of the second component. The opposite occurs if we look at the behavior of ϵ_{f_2} and ϵ_{β_2} in the bottom plots. This feature is mainly due to the specific form of the template, such that the diagonal components of the Fisher matrix for the first mode is independent of the second one and vice versa. In both cases however, a sweet spot exists for larger values of the shape factors which yield the best results. This clearly confirms the trend observed for the echoI and echoIIa templates. Note also that the parameter's accuracy of both modes is comparable. Only few configurations, clustered around $\beta_2 \approx 0.002$, lead to errors on f_2 and β_2 exceeding the upper bound $\epsilon_\alpha = 1$. The relative uncertainties on the time shifts (not shown in the figure) are in agreement with the results obtained for the previous waveforms, with $\epsilon_{\text{echo}} \lesssim 3\%$ and $\Delta t \lesssim 1\%$ for all the points in the $\beta_1 \times \beta_2$ plane.

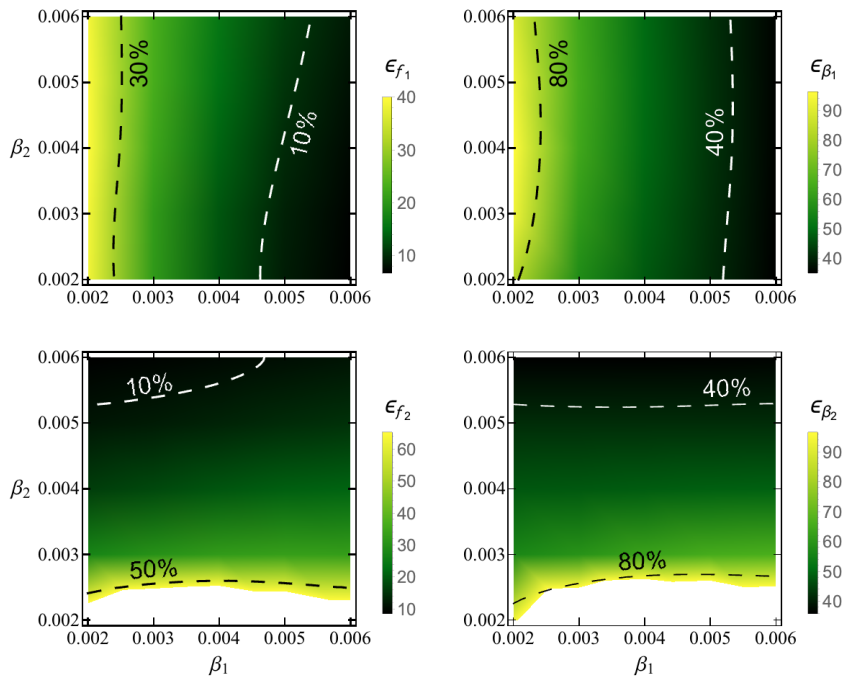


Figure 10.8: Same as Fig. 10.4 but for the parameters of echoIIb in the $\beta_1 \times \beta_2$ plane. The phase offset is fixed to $\phi = -\pi/2$. Figure taken from [3].

A phase shift $\phi = 0$ between the echo's components would, again, reduce our ability to detect frequencies and shape factors. This is shown in Figure 10.9, in which each point identifies a specific configuration for which the relative error of a certain parameter is larger than 1, i.e. for which its measurement is strictly compatible with zero. This picture rapidly improves for future detectors as demonstrated in Fig. 10.10, in which we plot the

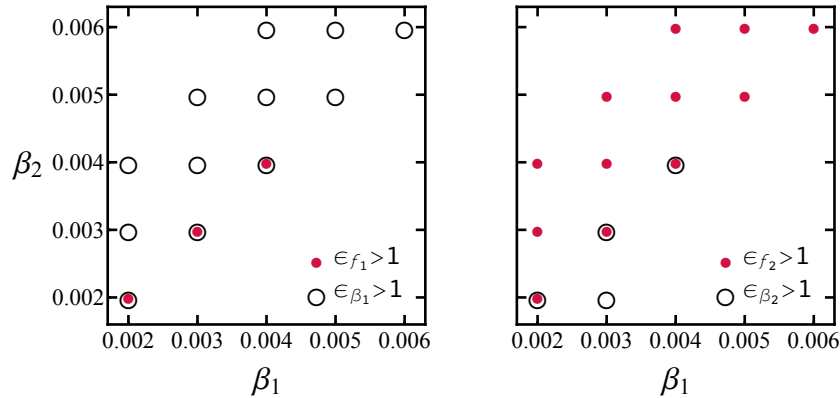


Figure 10.9: Each dot specifies a configurations in the $\beta_1 \times \beta_2$ plane with $\phi = 0$ for which the relative error $\epsilon_\alpha > 1$. Figure taken from [3].

errors corresponding to the best configurations, with $\phi = -\pi/2$. Note that the most accurate results occur when the difference between the two Gaussian widths is maximum, i.e. when $(\beta_1, \beta_2) = (0.006, 0.002)$ for ϵ_{f_1} and ϵ_{β_1} , and when $(\beta_1, \beta_2) = (0.002, 0.006)$ for ϵ_{f_2} and ϵ_{β_2} . The picture shows for example that LIGO A+ (which we remind roughly corresponds to a network of current detectors) would already constrain frequencies and shape factors with a relative accuracy around $\ll 10\%$. A third generation detector like the Einstein Telescope would be required to reduce these errors below 1%.

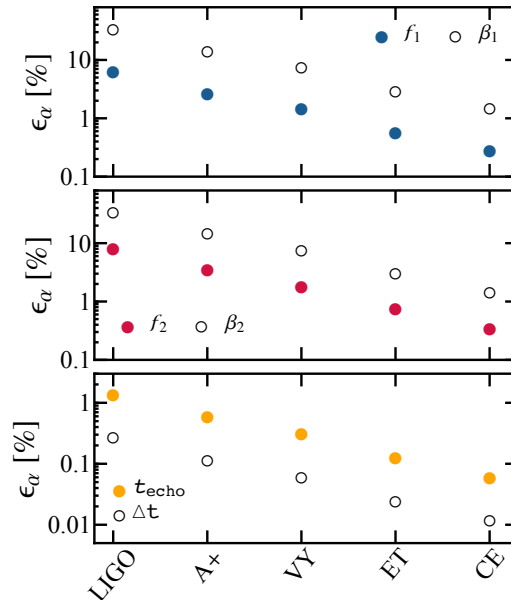


Figure 10.10: Relative errors of the echoI Ib model for the best case scenario with $\phi = -\pi/2$, computed for different interferometers. Figure taken from [3].

10.5 Conclusions

Gravitational wave astronomy is establishing itself as a new field of research capable to gain insights on a genuine strong field gravity regime, and answer open questions of fundamental physics. A key example is given by the possible existence of horizonless exotic objects whose compactness approaches the black hole limit. Such objects

may form in nature and merge within the Hubble time, mimicking the last stage of coalescence of two ordinary black holes [321]. In the postmerger phase, these objects would produce characteristic echoes, which at late time differ from the standard QNM spectrum, and can in principle be detected by laser interferometers. Although current gravitational wave data seem to show no statistical evidence of possible deviations from the standard black hole picture, it is expected that signals with larger SNR will provide new precious information. For this purpose it is mandatory to construct gravitational wave templates as accurate as possible, which allow to capture the dominant features of the process. Recent efforts have already been done to build fully analytical waveforms for data analysis strategies [323, 324]. In this paper we pursue a complementary path, trying to address for the first time the level of accuracy with which current/near future interferometers will be able to detect the echo's parameters. To this aim we have adopted phenomenological templates depending on a relatively small set of coefficients, which try to mimic the expected *true* signal with an increasing degree of realism. The numerical results obtained for all the considered models seem to suggest that even current detectors, at design sensitivity, can provide reliable estimates of all the parameters. Moreover, the analysis performed for the templates highlights some common properties, which can be described as follows:

- The SNR and the errors of realistic echo signals are expected to saturate after a certain number of repeated reflections, as the amplitude of each pulse decreases in time.
- The uncertainties on the template's parameters are mostly affected by the width of the function which shapes the echoes. In particular, larger values of this factor always lead to an increase of the overall SNR and to a reduction of the errors.
- As far as multiple frequencies are considered, the phase offset between different components of the echoes plays a crucial role, and it strongly affects the degeneracy between the parameters. Modes out of phase (in phase) lead to minimum (maximum) errors.
- Best case scenarios for all the models show that the frequencies and the shape factors of the echoes can always be measured with an accuracy smaller than 100%. A network of advanced detectors, composed of the two LIGO, Virgo and KAGRA, would reduce these values around 10%. Third generation interferometers, like the Einstein Telescope, are required to measure the same quantities at the level of percent.
- The parameters which characterize the time delay between the black hole QNM component and the subsequent echoes are measured with exquisite accuracy, with relative errors $\lesssim 3\%$ with Advanced LIGO already. Moreover changes in t_{echo} and Δt seem to slightly affect the other parameters of the waveform.
- Complex templates, in which multiple frequencies may interfere to produce the echoes, are more sensible to variations of the parameter δ which controls the shift between the objects surface with respect to a Schwarzschild black hole horizon.

A summary of the results for the most complex model can be found in Figs. 10.8-10.10. The data analysis developed in this paper may be considered as a proof of principle for future developments, and it suffers of two main limitations. The first obvious drawback is given by the lack of a semi-analytical template able to fully characterize the gravitational wave emission of perturbed exotic compact objects. The phenomenological models used here represent a first step in this direction, which provide a reliable description of the full picture, being still based on a limited numbers of parameters. Note that, unlike standard QNMs, which are solely determined by the black hole mass and spin, the echo structure is intrinsically more complex since: (i) the trapped modes spectrum crucially depends on the specific ECO considered, (ii) the shape of the echoes can be affected by the specific form of the perturbation. A second source of uncertainty, connected to the previous problem, relies on the unique identification of the echo's amplitudes. Although the assumptions employed in Sec. 10.2 are physically motivated by well known results [236], our conclusions still depend on the relative strength of the pulses, and can be considered as an optimistic scenario.

Improvements of the previous points can pursue various directions. Our current efforts are particularly devoted to investigate in detail the following aspects: (i) construct more refined models which approach realistic

ultra compact objects with larger accuracy, possibly taking into account the interference of multiple trapped modes; (ii) use a fully Bayesian analysis to perform model selection and assess the ability of ground based interferometer to distinguish between standard black hole and echo-like signals; (iii) employ realistic errors to reconstruct the ECO's scattering potential by measurements of the trapped modes, as shown in chapter 6. These extensions are already under investigation.

11 | Inverse Problem for Hawking Radiation

Breakdown of Contributions

This chapter is based on the publication “*Inverse problem for Hawking radiation*” by Sebastian H. Völkel, Roman Konoplya and Kostas D. Kokkotas, Phys. Rev. D 99, 104025, 2019, [7]¹. Since this is a joint work with Roman Konoplya, who has been collaborating with the group in Tübingen multiple times, I will first outline our individual contributions. As first author of this work, all the computations related to the inverse problem have been carried out by me. The computation of the necessary greybody factors, which are required to apply the method, has initially been computed by Roman Konoplya. Later in the project, I wrote another type of numerical code for the computation of greybody factors. We use both methods in this work. The writing was mostly done by me, with important contributions from Roman Konoplya, as well as Kostas D. Kokkotas. Both played an important role in discussions.

Overview

Hawking radiation is a widely studied phenomena arising when applying quantum field theory to the curved space-time of black holes. It can be shown that the greybody factors, which play an important part in characterizing the emitted spectrum, are related to the transmission and absorption coefficients of the associated classical perturbation potentials. This connection is the motivation for this work, which is about applying WKB theory to the inverse problem. By this we hereby mean to reconstruct the greybody factors, as well as to put some constraints on the perturbation potentials, if the spectrum of Hawking radiation, for certain types of fields, is being provided.

This chapter is organized as follows. After providing an introduction in Sec. 11.1, we describe the calculation of Hawking radiation being used in this work in Sec. 11.2. The subsequent Sec. 11.3 outlines the inverse problem methods. The applications and results of these methods are presented in Sec. 11.4 and discussed in Sec. 11.5. Our Conclusions can be found in Sec. 11.6. We provide additional material related to a simple and precise approximation of Hawking radiation in Sec. 11.7. Throughout this work we use $G = c = \hbar = k_B = 1$.

11.1 Introduction

Hawking radiation is one of the most important theoretical predictions in the application of quantum field theories to general relativity and alternative theories of gravity [119]. Despite the current lack of experimental confirmation, it fostered almost countless theoretical works on the details of the emission process (see [333, 334] and references therein). Among the most striking implications that followed, is the information loss problem [120, 121, 122, 123], that arises if one applies the pillars of modern physical theories (quantum field theories and general relativity) to the quantum aspects of black holes.

In this work we are interested in what we call the inverse problem. Assuming that the energy emission spectrum of Hawking radiation from a spherically symmetric black hole is provided, what can one learn about the black hole? It is well known that the emitted radiation is described by a black body being modified by greybody factors, which are related to the space-time of the black hole. In the following sections we outline a framework that can be applied to the greybody factors and to the entire energy emission spectra, to constrain the classical black hole perturbation potential, as well as to gain a more intuitive understanding of the individual contributions.

¹Reprinted parts with permission from Sebastian H. Völkel, Roman Konoplya and Kostas D. Kokkotas, Phys. Rev. D 99, 104025, 2019. Copyright 2019 by the American Physical Society.

The interest in the inverse problem for Hawking radiation is not a purely academic exercise, as it may seem from the first glance. The quantum corrections to the black hole metric, normally, are supposed to be negligibly small and unobservable for large astrophysical black holes, so that no information about quantum corrections should be expected from astrophysical observations of compact objects. On the contrary, behavior of miniature and primordial black holes, experiencing intensive Hawking radiation, will do strongly depend on the form of quantum corrections to gravity. Therefore, if Hawking radiation could be detectable in future experiments, this would allow us to trace back the geometry of the black hole and, at the end of the day, determine the form of quantum corrections.

We have studied the inverse problem for the QNM spectrum of spherically symmetric compact objects in multiple projects presented in Sec. 6, in Sec. 7, and in Sec. 8. There we demonstrated that once the QNMs of these objects are known, the effective potential can be reconstructed in an unique way, assuming general relativity and the validity of WKB theory. In [319] the reconstruction of the shape function from the high frequency (eikonal) QNM spectrum for a broad class of wormholes was suggested. In contrast to the aforementioned studies, which are based on the QNM spectrum, this work is based on the energy emission spectrum of Hawking radiation. Although its origin is quite different, the calculation of Hawking radiation involves the classical scattering problem related to finding the transmission coefficients, greybody factors, through the black hole potential barrier. Within WKB theory and single barriers, this problem can be inverted to reconstruct a class of potentials that admit the given transmission. In contrast to the QNM spectrum, Hawking radiation appears as a sum involving many greybody factors, which have to be recovered first. Despite the initially might expected challenges in the recovery of the individual greybody factors, we find that the problem can be split up in a multiple step approach which gives satisfactory results.

11.2 Hawking Radiation

In the following we give a short overview of the theoretical framework being used in this study.

11.2.1 Energy Emission Spectra

In this work we will assume that the black hole is in the state of thermal equilibrium with its environment in the following sense: the temperature of the black hole does not change between emissions of two consequent particles. This implies the canonical ensemble for the system. Therefore we work with the following description of the spectrum of Hawking radiation

$$\frac{dE}{dt} = \sum_l N_l |A_l|^2 \frac{\omega}{\exp(\omega/T_H) - 1} \frac{d\omega}{2\pi}, \quad (11.1)$$

where T_H is the Hawking temperature, A_l are the greybody factors, and N_l are the multiplicities, which only depend on the space-time dimension and l . Details can be found in [335] and references therein.

11.2.2 Greybody Factors and Transmission

It is well known that the greybody factors in the Hawking spectrum are related to the transmission through the black hole perturbation potentials with the corresponding spin of the field (see, for example, [336]). To obtain those, one has to solve the classical scattering problem of incoming radiation being transmitted or reflected at the potential barrier.

In this work we write the metric of a spherically symmetric black hole in the following form

$$ds^2 = -e^{2\nu} dt^2 + e^{2\lambda} dr^2 + r^2(d\theta^2 + \sin^2\theta d\phi^2). \quad (11.2)$$

The linearized perturbation equations can be reduced to the following form

$$\frac{d^2\Psi}{dr_*^2} + (E - V(r))\Psi = 0, \quad (11.3)$$

where the tortoise coordinate is defined as follows:

$$dr_* = e^{\lambda-\nu} dr. \quad (11.4)$$

We shall consider the wave equation (11.3) with the boundary conditions allowing for incoming waves from infinity. Owing to the symmetry of the scattering properties this corresponds to the scattering of a wave coming from the horizon. The scattering boundary conditions for (11.3) have the following form

$$\begin{aligned} \Psi &= e^{-i\omega r_*} + R e^{i\omega r_*}, & r_* \rightarrow +\infty, \\ \Psi &= T e^{-i\omega r_*}, & r_* \rightarrow -\infty, \end{aligned} \quad (11.5)$$

where R and T are the reflection and transmission coefficients respectively.

The effective potential has the form of the potential barrier which monotonically decreases at both infinities, so that the WKB approach [214, 218] can be applied for finding R and T . Since the wave energy E is real, the first order WKB values for R and T will be real and

$$|T|^2 + |R|^2 = 1. \quad (11.6)$$

Once the reflection coefficient is calculated, we can find the transmission coefficient for each multipole number ℓ

$$|\mathcal{A}_\ell|^2 = 1 - |R_\ell|^2 = |T_\ell|^2. \quad (11.7)$$

Various methods for the computation of the transmission and reflection, which are energy dependent functions, exist in the literature. For quick and relatively accurate evaluation of the transmission and reflection coefficients for not small values of energy one can use the 6th order WKB formula [218]. According to [218] the reflection coefficient can be expressed as follows:

$$R = (1 + e^{-2i\pi K})^{-\frac{1}{2}}, \quad (11.8)$$

where

$$K = i \frac{(\omega^2 - V_0)}{\sqrt{-2V_0''}} + \sum_{i=2}^{i=6} \Lambda_i. \quad (11.9)$$

Here V_0 is the maximum of the effective potential, V_0'' is the second derivative of the effective potential in its maximum with respect to the tortoise coordinate, and Λ_i are higher order WKB corrections, which depend on up to $2i$ th order derivatives of the effective potential at its maximum [218].

For accurate calculations of the reflection/transmission coefficients at any energies we used two numerical methods. First, the shooting method, based on numerical integration from the event horizon up to the far region and consequent matching with the required asymptotic behavior [337]. Second, a direct numerical integration of the wave equation from the transmission region backwards through the potential barrier to determine the transmission coefficients. This approach has been outlined and discussed in [338]. Both methods give similar results. From here and on, when mentioning *exact transmissions* we will mean values obtained with the numerical approaches and not WKB theory.

The semi-classical WKB treatment of the problem shows that the transmission for small energies below the barrier maximum can be approximated with the Gamow formula [283]

$$T(E) = \exp\left(2i \int_{x_0}^{x_1} \sqrt{E - V(x)} dx\right), \quad (11.10)$$

where E is the energy, $V(x)$ the potential barrier, and x_0 and x_1 the classical turning points, see also Sec. 4.3.2.

In the application of black hole perturbation theory, the coordinate x is the co-called tortoise coordinate r^* and $E = \omega^2$. Higher order WKB descriptions for the transmission exist and have been applied in this context [339]. In this work we will use eq. (11.10) as basis for inverse problem. The reason for the use of this low order simplification is that the “inversion” of the Gamow formula is well known and defines a class of so-called width equivalent potentials. We discuss this in the following Sec. 8.4.

11.3 Inverse Problem

In this section we outline the inverse method being used to reconstruct the black hole potential barrier widths for a given transmission, as well as the framework, if the energy emission spectra is provided.

11.3.1 Individual Transmissions

The inversion of the Gamow formula eq. (11.10) has been derived and discussed in [275, 285, 286] and in Sec. 4.3.2. From there it is known that providing the transmission $T(E)$ through a single potential barrier can not be used to uniquely determine its shape. In contrast, infinitely many so-called width equivalent potentials exist. A similar result exists for the Bohr-Sommerfeld rule of bound states in potential wells [274, 284]. The width \mathcal{L} of the potential barrier is given by

$$\mathcal{L}(E) \equiv x_1 - x_0 = \frac{1}{\pi} \int_E^{E_{\max}} \frac{dT(E')/dE'}{T(E')\sqrt{E' - E}} dE', \quad (11.11)$$

where E_{\max} is the maximum of the potential barrier. If it is not known, one can extrapolate it from where the transmission becomes $1/2$, which corresponds to the WKB result at the maximum of the barrier. To convert eq. (11.11) into a potential barrier one has to provide a function for one of the two turning points, $x_0(E)$ or $x_1(E)$, and invert the relation for E . Note that the provided turning point function has to exclude “overhanging cliffs” in the potential, which correspond to a multi-valued function for the potential. More details can be found in the aforementioned works [274, 275, 284, 285, 286]. The application of eq. (11.11) to individual transmission functions of black holes is shown in Sec. 11.4.

Since the Gamow formula is not valid for energies around the peak of the barrier, we extend the reconstruction process. The Pöschl-Teller potential is widely used in black hole theory to approximate calculations that involve the potential. In the form used here it is given by

$$V(x) = \frac{V_0}{\cosh(ax)^2}. \quad (11.12)$$

It describes black hole potential barriers for energies around the maximum very well. We expand the potential barrier at the peak to parabolic order and uses an analytic formula for the transmission in the fitting procedure for energies around the peak. It is straight forward to identify the Pöschl-Teller potential parameters with the two parabola parameters. This is used to approximate the peak region where the pure WKB treatment is not valid.

11.3.2 Energy Emission Spectra

The energy emission spectra is a sum over all angular contributions l , which maps the individual transmissions $T_l(E)$ in a non-trivial way in one function eq. (11.1). However, in order to apply the inverse method of Sec. 8.4, one has to find the individual transmission functions first. For this purpose we have worked out a framework that is based on some fairly general observations and explained in the following.

Modeling Individual Transmissions

The function describing the transmission through a potential barrier is by far not arbitrary. For single potential barriers studied in this work, it resembles a logistic function. We make use of this and parameterize any transmission with

$$T_{\text{fit},l}(E) = \frac{1}{1 + \exp\left(a_{l,0} + a_{l,1}E + a_{l,2}/\sqrt{E}\right)}, \quad (11.13)$$

where $a_{l,i}$ are a priori unknown constants that have to be fitted to a given energy emission spectra. The index l refers to the angular contribution. It is in principle straightforward to include higher order terms in cases where this ansatz does not yield sufficient precise results. As we show in Sec. 11.7, the interesting contribution comes around the peak and is in this sense local. Higher order terms in eq. (11.13) could be used to capture long range effects of the potential, but those are very difficult to be reconstructed from the entire spectrum.

Treatment of Energy Emission Spectra

The actual energy emission spectra will contain in principle infinitely many terms, but not all contribute in the same way. Making use of this observation simplifies the treatment of the full problem significantly. The weighting of each term with the l dependent transmission. The individual transmissions act qualitatively like a high pass filter. For a given l , the threshold is located around the barrier maximum, which in the eikonal approximation is simply proportional to

$$E_{\text{max},l} \sim l(l+1), \quad (11.14)$$

and therefore acts as a cut off for small E , but is transparent for large E . Thus, high l -terms only affect the spectra for large E , but can be neglected for small ones.

Extract Transmissions

Using the observations of the previous paragraph, it is straightforward to implement a numerical scheme that works in multiple steps. For a given transmission spectrum, one can start with the reconstruction of the lowest transmission function by fitting it to the set of parameters of our model eq. (11.13). It is important to realize that this can only be done reasonably in an interval between neighboring potential maximums. The contribution of the transmission $T_l(E)$ to the spectrum dominates only in the interval $(E_{\text{max},l-1}, E_{\text{max},l})$. For smaller or larger energies it can be well approximated with 0 or 1, respectively. Once the parameters are determined in this range, we repeat with the fitting of the next transmission $T_{l+1}(E)$ in the subsequent interval. We find it useful to define a “normalized” spectrum, where we divide out all l independent functions from the energy emission spectrum $d^2E/d\omega dt$, as described in eq. (11.1)

$$\mathcal{I}(E) \equiv \sum_l N_l |\mathcal{A}_l|^2 \equiv \sum_l I_l(E). \quad (11.15)$$

If the value of the Hawking temperature is not assumed to be known, it can be obtained from the following procedure. As it is shown in Fig. 11.1, the normalized spectrum is well described with smoothed steps whose growth scales linearly with the energy. The case we show is for Schwarzschild, but it is similar for Reissner-Nordström, as we show in Sec. 11.7.1. In contrast to this, the actually measured spectrum $I(E)$ falls off exponentially for large energies. The idea now is to find an approximation for the Hawking temperature by demanding that the normalized spectrum has to grow roughly linearly for large energies. In a second step we can read out the temperature by using the step structure. Going from the measured spectrum $I(E)$ to the normalized spectrum $\mathcal{I}(E)$

is done via

$$\mathcal{I}_{\text{rec}}(E) = \frac{2\pi}{\sqrt{E}} \left(\exp\left(\frac{\sqrt{E}}{T_{\text{H,rec}}}\right) - 1 \right) \times I(E), \quad (11.16)$$

where $T_{\text{H,rec}}$ is the reconstructed Hawking temperature. The simple functional structure of the normalized spectrum allows one to precisely determine the Hawking temperature $T_{\text{H,rec}}$, as long as the perturbation potentials have the single barrier structure we assume in this work. The number of saddle points N_s (counted from low to high energies) corresponds to the number of summed terms which are relevant up to the given energy. Contributions from higher terms at this energy value are being suppressed due to the transmission functions and therefore negligible. If one knows the full spectrum, one can determine $T_{\text{H,rec}}$ from demanding that the value of the measured spectrum has to match the sum of the multiplicities at the flattest point between $(E_{\text{max},N_s}, E_{\text{max},N_s+1})$. In Fig. 11.1 one can see that the flattest part of the normalized spectrum coincides very well with the summation of the multiplicities up to the N_s -th term. More details are being provided in the caption.

Since this work assumes that the spectrum is known with high precision and no observational errors, this identification becomes in principle arbitrary precise by going to higher energies. Therefore we continue with the exact values. It is evident that observational errors on the measured spectrum would require a special treatment and put an error on the reconstructed temperature. However, the experimental access to Hawking radiation is currently not possible, which is the reason why we do not consider this limitation here.

Strictly speaking, when dealing with gravitational perturbations of static black holes in four dimensional spacetimes, two channels of perturbations come into play: the axial (vector) and polar (scalar) ones. They are represented by the corresponding vectors and scalars relatively the 2-sphere rotation group. In addition, the multiplicity factors are, in general case, different for different channels of gravitational perturbations. Therefore, when talking here about Hawking radiation of gravitons in the vicinity of the Reissner-Nordström black hole, we simply mean this single channel of perturbations which we considered here for purely illustrative purpose. The possibility of distinguishing different channels of gravitational perturbations was considered recently in [340] and we will not touch this problem here. It is evident that there is no such a problem for emission of particles of other spin.

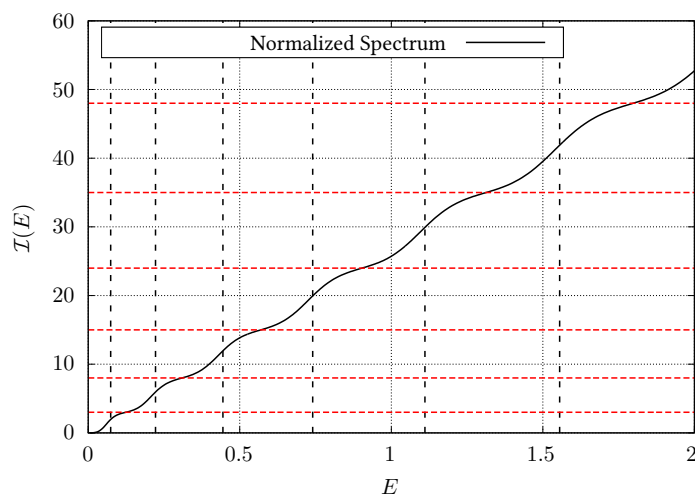


Figure 11.1: Here we show the normalized energy emission spectrum, defined in eq. (11.15), for the Schwarzschild case. The black dashed lines indicate the potential maximums of each potential barrier $E_{\text{max},l}$ and match qualitatively with the saddle points. The red dashed lines show the summation of all multiplicities up to the l -th term $\sum_i^l (2i + 1)$, starting from $l = 1$ as lowest line. This line intersects the normalized spectrum in its flattest intervals between two consecutive potential maximums $E_{\text{max},l}$. Figure taken from [7].

11.4 Applications and Results

In this section we demonstrate the results of the inverse method applied to the knowledge of different exact transmission functions as well as to several energy emission spectra. The transmissions and the energy emission spectra are obtained numerically by integration of the wave equation through the potential barrier for every given E (see, for instance, [337]). For the numerical implementation of the fitting we use the routines of CERN's ROOT Data Analysis Framework [341]. As examples to demonstrate the proposed methods, we study the vector case for the Schwarzschild and Reissner-Nordström black holes in four dimensional general relativity. The metric functions for these black holes are

$$e^{2\nu} = e^{-2\lambda} = 1 - \frac{2M}{r} + \frac{Q^2}{r^2} \quad (11.17)$$

and the parameters of the black holes are provided in TABLE 11.1. We list the equations describing the two different types of perturbation potential in Sec. 11.7.2.

Table 11.1: Parameters of the studied black holes in this work.

Model	M	Q	T_H
Schwarzschild	1	0	$1/8\pi$
Reissner-Nordström	$2/3$	$1/\sqrt{3}$	$1/6\pi$

11.4.1 Reconstructing the Greybody Factors

By fitting numerically our expansion for the transmission to the normalized energy emission spectrum eq. (11.15) we are able to reconstruct the transmissions for the first few l . Our results for this are shown in Fig. 11.2 for Schwarzschild and in Fig. 11.3 for Reissner-Nordström. To obtain the normalized spectrum we used the correct value for the Hawking temperature, as explained in 11.3.2.

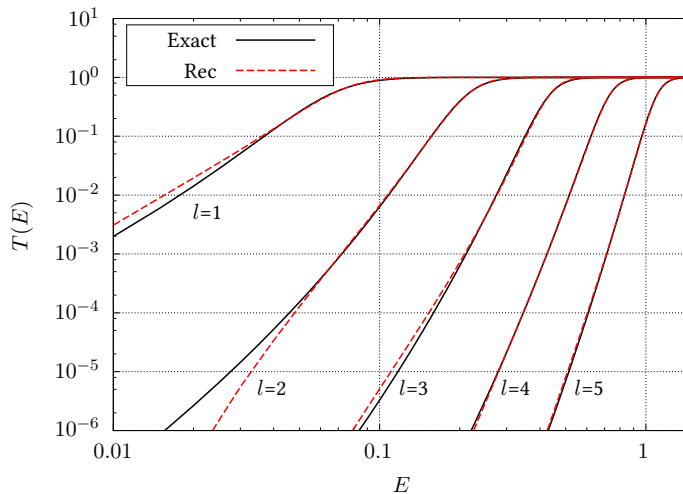


Figure 11.2: Reconstruction of the Schwarzschild transmissions $T_l(E)$ from spectrum fitting. Figure taken from [7].

11.4.2 Reconstructing the Potential Widths

By using the reconstructed transmissions, we can now approximate the widths of the potential barriers. Our results are provided for Schwarzschild in Fig. 11.4 and for Reissner-Nordström in Fig. 11.5. Note that there are two aspects to be investigated. First, the general precision of the inverse method to obtain the potential widths from a given transmission. Second, how much the results for the inversion depend on the precision with which

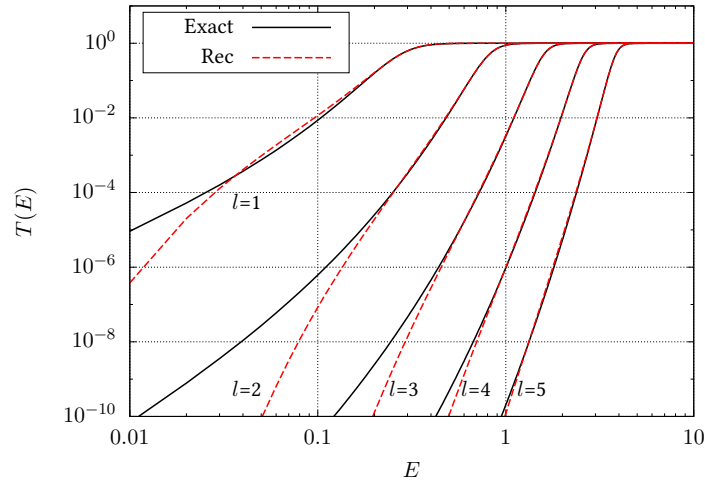


Figure 11.3: Reconstruction of the Reissner-Nordström transmissions $T_l(E)$ from spectrum fitting. Figure taken from [7].

the transmission is provided. To address both questions we show the results using the numerically precisely calculated transmission (red dashed), the fitted transmission (blue dashed), and for further discussion the pure inverse WKB result (green dashed). Since the reconstructed transmissions T_l are precise for energies from close to the potential maximum $E_{\max,l}$ to the lower maximum $E_{\max,l-1}$, it is not surprising that the exact and fitted transmissions yield comparable results there. However, we find clear deviations for smaller energies, which can be traced back to the imprecise reconstruction of the transmission in these regions, as shown in Fig. 11.2 and Fig.11.3.

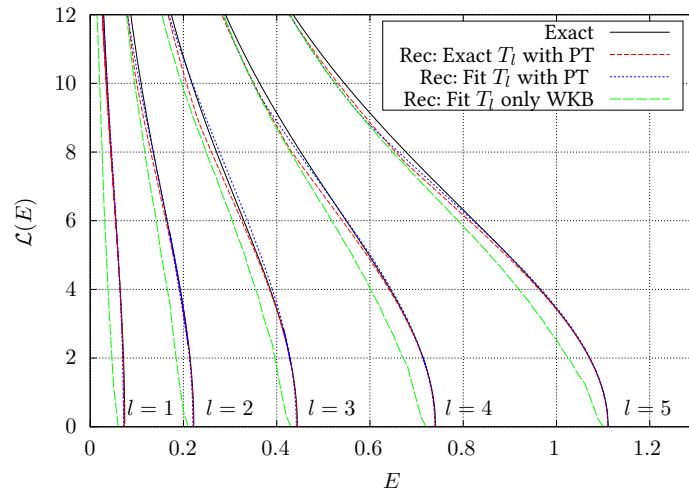


Figure 11.4: Reconstruction of the Schwarzschild potential barrier widths $\mathcal{L}_l(E)$ from given transmissions $T_l(E)$. Figure taken from [7].

11.5 Discussion

In this section we discuss our findings and relate them to inverse spectrum methods that have recently been developed for ultra compact stars and exotic compact objects, such as gravastars and wormholes [2, 5, 6, 319].

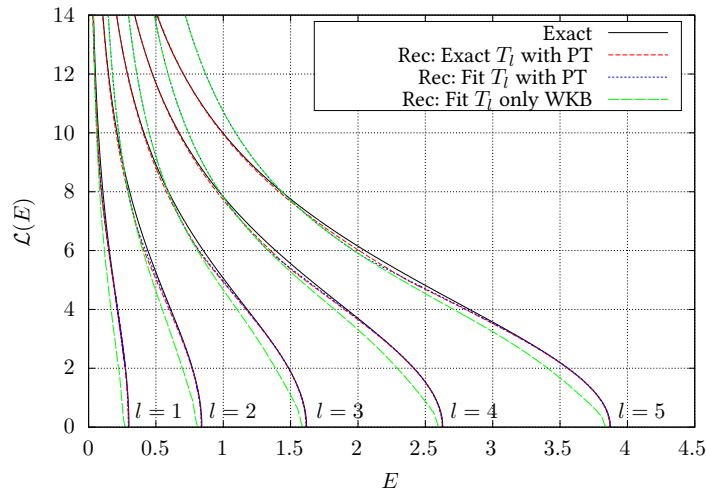


Figure 11.5: Reconstruction of the Reissner-Nordström potential barrier widths $\mathcal{L}_l(E)$ from given transmissions $T_l(E)$. Figure taken from [7].

11.5.1 Reconstructing the Greybody Factors

The individual contributions to the energy emission spectrum can be easily understood from the normalized energy emission spectrum. It intuitively demonstrates for which energies a given transmission encodes information of the potential barrier to the spectrum. We find that it only contributes on an interval around its barrier maximum. As a consequence one can only reconstruct the transmission in this interval precisely, but loses accuracy for smaller energies, where the contribution is exponentially small. In our examples the transmissions range over 10 orders of magnitude. We also find that due to the l dependency of the multiplicities and the exponential suppression in the energy emission spectrum, higher l contributions become negligible and therefore more challenging to reconstruct.

11.5.2 Reconstructing the Potential Widths

Our results for the reconstruction of potential barrier widths from the directly provided transmission functions of the Schwarzschild and Reissner-Nordström black holes show that the inverse method works very precise around the peak of the barrier and in the region far below. The method combines the parabolic transmission fit to find the Pöschl-Teller potential width at the barrier maximum and merges it with the inverted Gamow formula for small energies. Here we make two comments. First, the precision at the peak region and for energies much below the peak is very good, taking into account the fairly simple structure of the method. Second, the least precise region is where the Pöschl-Teller approximation becomes less valid, but the turning points are not too far away from each other. In case that the transmission have to be reconstructed from the spectrum, it should be expected that the reconstruction only works reliable in an interval between consecutive potential maximums, but not on the whole range.

11.5.3 Connection to Related Inverse Spectrum Problems

The here presented method for the reconstruction of transmission functions and black hole potential barrier widths has to be discussed in the context of other inverse methods that are based on gravitational wave observations. Most of them make use of the oscillation spectra of the objects, which can be for present matter or space-time itself. Relevant objects are neutron stars, black holes, and more recently exotic compact objects. Besides the extensive numerical relativity based simulations for neutron stars and black holes, there are also multiple semi-analytic approaches. In the case of neutron stars, there are well established asteroseismology relations that can be used to constrain the compactness or equation of state of neutron stars by using different types of

their fundamental oscillation modes [90, 239, 240, 342]. In addition to this, there are also spectral methods using masses and radii of neutron stars, to reconstruct their equation of state [93, 94, 95, 96, 241].

Technically closer to this work is the inverse spectrum method we presented in Sec. 6, in Sec. 7, and in Sec. 8, which constraints the perturbation potential from the QNM spectrum. The methods presented there are based on the inversion of generalized Bohr-Sommerfeld rules and the Gamow formula. As it should be expected, the inversion is in general not unique. However, additional physical assumptions about the system can overcome this limitation. In the present work, the uniqueness of the reconstructed perturbation potential is not given. In another work it was shown how the QNM spectra of some wormholes can be used to reconstruct their shape function [319] by using the higher order WKB method [214, 218].

11.6 Conclusions

In this work we have presented a semi-analytic method which uses the energy emission spectrum of Hawking radiation to reconstruct the greybody factors and from this the widths of the black hole perturbation potentials. By defining a “normalized” energy emission spectrum we were able to carry out a multi step fitting procedure to reconstruct the transmissions. The reconstruction is based on the numerical fitting of a suitable expansion of the classical transmission function and its direct identification with the greybody factors. In a second step we have combined the inversion of the WKB based Gamow formula with the analytic result for the transmission through a parabola around the peak, in order to reconstruct the potential width for small energies, as well as around the peak of the barrier. We outlined why higher l terms are highly suppressed and thus do not contribute to the spectrum and are therefore not eligible for the inversion process. After presenting the method and some general observations, we applied it to the vector case of the Schwarzschild and Reissner-Nordström black holes in four dimensions described by general relativity. In Sec. 11.7 we show that the whole problem can be extremely simplified by noting that the energy emission spectrum can be very well described with a pure analytic parabolic model for the potential barriers, which might be a very useful approximation for analytic calculations in more complicated black hole potentials.

11.7 Supplementary Material

11.7.1 Toy Model for the Energy Emission Spectrum

During this study on the inverse problem of Hawking radiation we noticed that only the region of the potential barrier around the maximum plays a dominant role in the energy emission spectrum. This simple observation can be used to work out a simple analytic toy model, for a quick and simple approximation of the spectrum. Here we present a model which is in the spirit of well known QNM calculations for black holes. It is using a parabolic expansion of the potential peak, as it is done in the Schutz-Will formula [213]. In the energy emission spectrum one sums over all l , but as being outlined in this work, not all contribute similar. For a given $T_l(E)$ one finds the following cases. Either it has negligible contribution, if $E \ll E_{\max,l}$; potential dependent contribution between 0 and 1, if $E_{\max,l-1} < E < E_{\max,l+1}$; becomes approximatively 1, if $E_{\max,l} \ll E$. We expect that the parabolic approximation for the transmission to be much more precise than the corresponding result in the QNM application. Of course both approaches can only be valid in cases where the black hole potential can be represented by a single barrier.

The transmission through a parabolic potential barrier

$$V(x) = V_{\max,l} - a_l x^2 \tag{11.18}$$

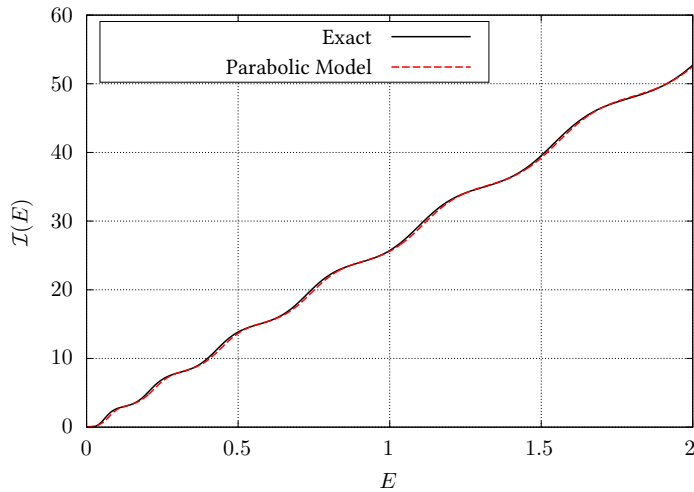


Figure 11.6: Comparison of the exact result (black solid) and parabolic approximation (red dashed) for the normalized energy emission spectrum of the Schwarzschild black hole. Figure taken from [7].

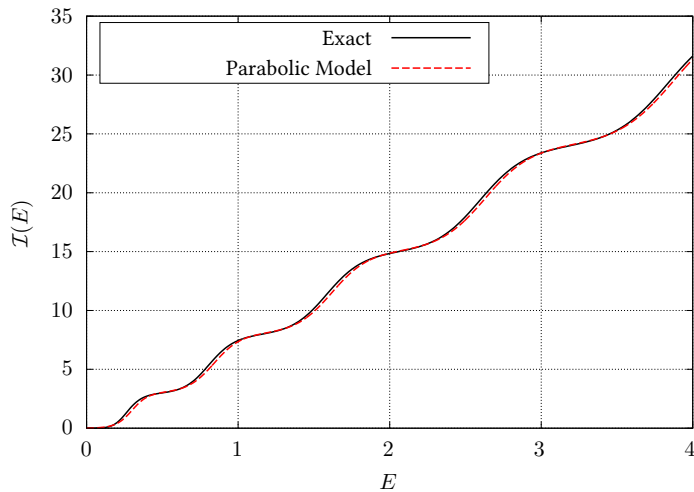


Figure 11.7: Comparison of the exact result (black solid) and parabolic approximation (red dashed) for the normalized energy emission spectrum of the Reissner-Nordström black hole. Figure taken from [7].

described by WKB theory, and valid to describe the peak of the barrier, is given by

$$T_l(E) = \left(1 + \exp \left(- \frac{\pi (E - V_{\max,l})}{\sqrt{a_l}} \right) \right)^{-1}, \quad (11.19)$$

see [343, 344] for $V_{\max,l} = 0$. The two parameters $V_{\max,l}$ and a_l have to be matched with the black hole potential at the maximum $r_{\max,l}^*$. The identifications are

$$V_{\max,l} \equiv V_{\text{BH}}(r_{\max,l}^*), \quad a_l \equiv - \frac{V''_{\max,l}}{2}. \quad (11.20)$$

The resulting normalized energy emission spectrum follows by using eq. (11.19) as approximation for the greybody factors. We show the result for Schwarzschild in Fig. 11.6 and Reissner-Nordström in Fig. 11.7. As one would naively expect from the Eikonal limit, one finds that the approximation becomes more and more precise the higher energies one considers.

11.7.2 Perturbation Potentials

In this section we provide the equations describing perturbation potentials being used to calculate the transmission and reflection coefficients in this work.

The perturbation potential describing a test electromagnetic field around the Schwarzschild black hole is given by

$$V(r) = \left(1 - \frac{2M}{r}\right) \frac{l(l+1)}{r^2}, \quad (11.21)$$

where the dependency on the tortoise coordinate is given implicitly as $r(r^*)$ and l is the multipole number of the perturbation.

The case of the Reissner-Nordström black hole is a bit more involved. In this work as a proof of principle we are only considering one of the four perturbations. The full derivation of the perturbation potential and further details can be found in [216, 345, 346, 347, 348, 349, 350]. The potential we use goes over to the pure vector perturbations of Schwarzschild eq. (11.21) in the limit of $Q = 0$. This potential can be written as

$$V(r) = \frac{\Delta}{r^5} \left(U + \frac{W(p_1 - p_2)}{2} \right), \quad (11.22)$$

with the following abbreviations

$$\Delta = r^2 - 2Mr + Q^2, \quad (11.23)$$

$$U = (2nr + 3M)W + (\bar{\omega} - nr - M) - \frac{2n\Delta}{\bar{\omega}}, \quad (11.24)$$

$$p_{1,2} = 3M \pm \sqrt{9M^2 + 8nQ^2}, \quad (11.25)$$

$$n = \frac{(l-1)(l+2)}{2}, \quad (11.26)$$

$$W = \frac{\Delta}{r\bar{\omega}^2} (2nr + 3M) + \frac{nr + M}{\bar{\omega}}, \quad (11.27)$$

$$\bar{\omega} = nr + 3M - \frac{2Q^2}{r}. \quad (11.28)$$

12 | Spectral Lines of Quantized, Spinning Black Holes and their Astrophysical Relevance

Breakdown of Contributions

This chapter is strongly based on the publication “Spectral Lines of Quantized, Spinning Black Holes and their Astrophysical Relevance” by Andrew Coates, Sebastian H. Völkel and Kostas D. Kokkotas, *Phys. Rev. Lett.* 123, 171104, 2019, [9]¹. Since this is a collaborative work with Andrew Coates, who was a postdoctoral researcher in our group at Tübingen, I will first outline our individual contributions. The work was initiated by joint discussions between the three of us on recent works [191, 192], in which gravitational wave echoes were predicted from area quantized nonspinning black holes. Andrew Coates is first author of the work because he proposed the method to calculate the spectrum. The computations had first been carried out by Andrew Coates, while I verified them afterwards. Writing and editing of the work was done in equal shares by Andrew Coates and me, while Kostas D. Kokkotas assisted in editing the final manuscript.

Overview

Here we study black hole area quantization in the context of gravitational wave physics. It was recently argued that black hole area quantization could be a mechanism to produce so-called echoes as well as characteristic absorption lines in gravitational wave observations of merging black holes. One can match the spontaneous decay of these quantum black holes to Hawking radiation calculations. Using some assumptions, one can then estimate the natural widths of these states. As can be seen from a classical paper by Bekenstein and Mukhanov, the ratio between width and spacing of nonspinning black hole states approaches a small constant, which seems to confirm the claim. However, we find that, including the effect of black hole spin, the natural widths increase. To properly address any claim about astrophysical black holes, one should examine the spinning case, as real black holes spin. Thus, the word “spinning” is key to the question of whether or not black holes should have an observable, discrete spectrum in nature. Our results suggest that it should be possible to distinguish between any scenarios for which the answer to this question is yes. However, for all of the commonly discussed scenarios, our answer is “almost certainly no”.

This chapter is organized as follows. We introduce and motivate this work in Sec. 12.1. Then the nonspinning case is reviewed in Sec. 12.2, before we continue with the spinning case in 12.3. Finally, we discuss and conclude our findings in Sec. 12.4.

12.1 Introduction

The quantum nature of black holes is among the most fascinating puzzles in theoretical physics. A particularly interesting hint about the nature of black holes comes from the seminal works on the thermodynamics of black holes [116, 117, 118, 119, 351, 352, 353], see also our historical discussion in Sec. 2.1.1. As we have no generally accepted theory of quantum gravity, nor any experimental access, following up these calculations is very challenging.

On the other hand there is a growing interest in exotic compact objects (ECOs), which could potentially mimic black holes in most astrophysical situations, see Sec. 2.3. Among the many proposed models are ultra compact

¹Reprinted parts with permission from Andrew Coates, Sebastian H. Völkel and Kostas D. Kokkotas, *Phys. Rev. Lett.* 123, 171104, 2019. Copyright 2019 by the American Physical Society.

constant density stars [88], gravastars [160, 161, 354], and wormholes [179, 180]. But, there are also proposed modifications of the physics on the horizon scale of classical black holes [355], e.g., firewalls [127].

The present work was inspired by the recent claims [191, 192] that black hole area quantization, as proposed by Bekenstein and Mukhanov [184, 185, 186], leads to gravitational wave echoes, see Sec. 3.6. As the name suggests, in the area quantization scenario, the area of black holes is quantized in some unit area of the same order as the Planck area. However, one might naively expect that, for astrophysical black holes, any change due to area quantization should be washed out. This is particularly the case if one expects to recover general relativity in the classical limit. Thus the prediction of echoes should only be relevant for small black holes, not for astrophysical ones. In order to quantify this line of thought, we extend the preexisting estimates of the natural linewidths [186] to the spinning case. The method matches the spontaneous decay of quantized black holes to the power output of Hawking radiation. For large, nonspinning black holes, there is an almost universal ratio of the width to the gap between neighboring states. This width is small in all proposed scenarios. This means that well-isolated, nonspinning black holes are likely good reflectors, if their areas are quantized. For spinning black holes, the situation is a little less clear. First of all there are more decay channels and so one would expect shorter lifetimes and hence large widths. (Specifically, the lifetime of the individual states should be shorter, not the total lifetime of the black holes.) Second, for large enough spins, the area actually grows via Hawking radiation [356]. This is a consequence of superradiance and the fact that the surface gravity is small for large a (see, e.g. [357]). These also provide the counter-intuitive behaviour that the power output grows with spin, even as the temperature decreases. We will see that the conclusion in the spinning case depends on the scale of the area quantization. In particular, for the more common suggestions this leads to no observable effect, but if the quantum of area is on the large side there will be. They should also be distinguishable where there is a detectable effect. Recently, other works appeared [358, 359], tackling this problem from a different direction (see the discussion in Sec. 12.4).

12.2 Widths of non-spinning states

For demonstrative purposes, we review the classic calculation by Bekenstein and Mukhanov in [186] the premise of which is that we can make an estimate of the natural width of nonspinning states using various assumptions:

0. Isolated black holes can only have areas an integer multiple of some unit of area.
1. The correct definition of the energy of the black hole is just Mc^2 .
2. For large black holes, the semiclassical Hawking radiation should give the correct power emitted in spontaneous decays.
3. Spontaneous decays that change the spin of the black hole by a large amount are highly suppressed. In other words, the decay of a Schwarzschild black hole should not give it a significant spin.

Assumption (0), that the area of a Schwarzschild black hole is quantized, can be written as

$$A = \alpha \ell_p^2 n = 4\pi r_s^2 = 4\pi \left(\frac{2GM}{c^2} \right)^2. \quad (12.1)$$

Here we have the Planck length $\ell_p^2 = \hbar G/c^3$ and the Schwarzschild radius r_s . The integer n labels the state of the black hole. The constant α is *a priori* not known and depends on the specific model of area quantization. The different proposals for α made in the literature range from $4 \ln 2$ to 32π or even larger [184, 185, 186, 187, 188, 189, 190]. (In principle $4 \ln q$ for integer $q > 2$ is included in the literature but $q < 10$ has been the focus.)

We now invert Eq. (12.1) to find the mass of the n th state, M_n , which gives us

$$M_n = \sqrt{\frac{\alpha n \hbar}{16\pi G}}. \quad (12.2)$$

So, if we say that assumption (1), the energy of the n state is $M_n c^2$, then the transition from n to $n - \delta n$ has an energy

$$(M_n - M_{n-\delta n}) c^2 = \hbar \omega_{n,\delta n}. \quad (12.3)$$

One can justify this by considering the relation between the Bondi mass and outgoing radiation fluxes [357].

To be able to make any quantitative predictions, we need to know the widths of these states. To do so would usually require knowledge of how these states interact with external fields etc.; in other words we would need a theory of quantum gravity. We can, however, make an estimate if we take assumption (2), i.e., that the power output by the spontaneous decay of these states matches the power output of Hawking radiation. In this case, we would have

$$P_H = \frac{\langle E_{\text{emitted}} \rangle}{\tau}, \quad (12.4)$$

where P_H is the power emitted in Hawking radiation, $\langle E_{\text{emitted}} \rangle$ is the average energy emitted in a spontaneous decay, and τ is the lifetime of the state. Using $\langle E_{\text{emitted}} \rangle = \hbar \langle \omega \rangle$, we then apply the standard relation $\tau = \hbar/\Gamma$ where Γ , is the energy width of the state. This gives us

$$P_H = \langle \omega \rangle \Gamma, \quad (12.5)$$

where $\langle \omega \rangle$ is the average transition frequency

$$\langle \omega \rangle \approx \sum_{\delta n=1}^n p(n \rightarrow n - \delta n) \omega_{n,\delta n}, \quad (12.6)$$

with $p(n \rightarrow m)$ being the probability that the state will decay from the n state to the m state, given that a decay happens. This uses the fact that, for large n and small spin parameter a , small changes in angular momentum do not make a substantial change to the transition frequency, that $\delta n = 0$ transitions increase the mass for nonspinning black holes, and assumption (3). Importantly, this average can never be smaller than $\omega_{n,1}$, which is the minimum possible transmission frequency. Underestimating $\langle \omega \rangle$ will overestimate Γ . Overestimating P_H also overestimates Γ . So if we replace $\langle \omega \rangle$ by $\omega_{n,1}$ and neglect gray body factors in P_H we will only overestimate Γ . This likely overestimate of the width is

$$\Gamma < \tilde{\Gamma} = A_{\text{eff}} \sigma_{\text{SB}} T_H^4 (\omega_{n,1})^{-1}, \quad (12.7)$$

where

$$A_{\text{eff}} = 4\pi \left(\frac{3\sqrt{3}GM(n)}{c^2} \right)^2, \quad \sigma_{\text{SB}} = \frac{\pi^2 k_B^4}{60c^2 \hbar^3}, \quad (12.8)$$

$$T_H = \frac{\hbar c^3}{8\pi GM(n)k_B}, \quad \omega_{n,1} = \frac{(M(n) - M(n-1)) c^2}{\hbar}. \quad (12.9)$$

$A_{\text{eff}} = 27A/4$ is based on estimates of the power in Hawking radiation [360], σ_{SB} is the Stefan-Boltzmann constant, and T_H is the Hawking temperature of the black hole. Tidying up and expanding for large n we arrive at

$$\tilde{\Gamma} = 9 \frac{\sqrt{n} + \sqrt{n-1}}{320n} \sqrt{\frac{c^5 \hbar \pi}{G \alpha^3}} \quad (12.10)$$

$$= \frac{9}{160} \sqrt{\frac{\pi \hbar c^5}{G \alpha^3 n}} \left(1 - \frac{1}{4n} \right) + \mathcal{O}(n^{-5/2}). \quad (12.11)$$

This shows that this estimate of the width goes to zero for large black holes (large n). Although this is in contra-

diction with the intuition gained from usual quantum systems, one can see that this must be the case. The result is a basic consequence of the fact that the total lifetime τ_{tot} of a black hole, according to Hawking radiation, scales like M^3 and thus, in the case of area quantization, $n^{3/2}$. However,

$$\tau_{\text{tot}} = \sum_{n=0}^N \tau_n \propto \sum_{n=0}^N \frac{1}{\Gamma_n}, \quad (12.12)$$

and so if Γ_n were to be a constant in n , then the lifetime would be $\tau_{\text{tot}} \propto N \propto M^2$, so Γ_n must go as $1/\sqrt{n}$. We can get a feel for how large this width is by looking at the ratio

$$\frac{\tilde{\Gamma}}{\hbar\omega_{n,1}} = \frac{9\pi}{20\alpha^2} \left(1 - \frac{1}{2n} + \mathcal{O}(n^{-2}) \right). \quad (12.13)$$

Note that this approaches a constant for large black holes. The most common proposals for α are $\alpha = 4 \ln(q)$ [184, 186, 188], with $q = 2, 3$, $\alpha = 8\pi$, or even as high as $\alpha = 32\pi$ [190]. These give ratios of around 0.2, 0.1, 10^{-3} , and 10^{-4} , respectively. Without broadening all of these values would thus lead to very different behavior from the classical black hole.

However, as already mentioned, spin can change the picture considerably [356]. For example, by looking at Fig. 3 of the same work one might expect that including the spin will reduce the lifetime of individual states.

12.3 Including the Spin

The preceding section was limited to the idealized case of nonrotating black holes. However, the most important astrophysical black holes, from an observational point of view, are expected to have non-negligible spin. Robust estimates for binary black hole mergers, which match with the LIGO and Virgo detections [55, 78, 79, 80, 297], predict values of very roughly $a \approx 0.7$ [361]. In these cases, the effect of the spin has to be taken into account and could potentially change the nonspinning result significantly. We address this issue in the following.

Along with the area, we must now also quantize the spin, as usual,

$$J = \hbar j, \quad (12.14)$$

where j is a half-integer or integer. We can define the transition frequency ω for $n \rightarrow n - \delta n$ and $j \rightarrow j - \delta j$ to be

$$\omega = \frac{c^2}{\hbar} (M(n, j) - M(n - \delta n, j - \delta j)). \quad (12.15)$$

The linearized version of this can be found in [191]. From the condition

$$j = \frac{aGM(a, n)^2}{\hbar c}, \quad (12.16)$$

one can then find $j(a)$ explicitly as a function of n and α . Next we use the results of Page [356] (removing the neutrinos), which we can then match to the rates of change of area and angular momentum. Introducing

$$f \equiv -M^2 \frac{dM}{dt} = -M^2 \dot{M}, \quad (12.17)$$

$$g \equiv -\frac{M}{a} \frac{dJ}{dt} = -\frac{M}{a} \dot{J}, \quad (12.18)$$

one finds for the rate of area change

$$\dot{A} = \frac{\hbar c^4}{G^2} \frac{A}{M^3} \left(\frac{g - 2f}{\sqrt{1 - a^2}} - g \right). \quad (12.19)$$

We can then use these expressions to find the semiclassical prediction (in this case for the rate of change of the area quantum number, i.e. \dot{n}) and match this to the quantum version in the same way as has been done for the nonspinning case like so,

$$\dot{n} = -\frac{\langle \delta n \rangle}{\tau}, \quad (12.20)$$

which gives the width

$$\Gamma = -\frac{\hbar \dot{n}}{\langle \delta n \rangle} = -\frac{\hbar \dot{n}}{r \langle \delta n_0 \rangle}, \quad (12.21)$$

where we parametrized $\langle \delta n(j) \rangle$ with r to match the nonspinning case $j = 0$ for $r = 1$. We expect $r \lesssim 1$, because for a slightly larger than 0.8, r must go negative, due to the effect of the superradiance lead to the area growing (as mentioned in the Introduction in Sec. 12.1). Furthermore, as there are more decay channels due to the spin, one could expect the lifetime of these states to be considerably lower than in the nonspinning case. If we additionally define

$$\omega_0 \equiv \omega(n \rightarrow n-1, j=0), \quad (12.22)$$

$$\omega_{\text{ref}} \equiv \omega(n \rightarrow n-1, j \rightarrow j), \quad (12.23)$$

we can finally compare the influence of the spin by looking at the ratio

$$\boxed{\frac{\Gamma \omega_0}{\Gamma_0 \omega_{\text{ref}}} = \frac{F(a)}{r}}, \quad (12.24)$$

again noting that r and $F(a)$ must become negative for large a . In the particularly interesting range of $0.6 < a < 0.8$, $F(a)$ ranges from ~ 3.5 to ~ 5.5 . This means that, for the lowest value of $\alpha (= 4 \ln 2)$, the *natural* linewidth can cause neighboring states to completely overlap. It seems likely, once one includes the effects of the black hole not being in a specific stationary state, the incoming radiation being thermal, and other environmental effects, that only for considerably larger values of α is it plausible that neighboring states are well separated. In our calculation we assumed that Hawking radiation gives the correct prediction for the rate of change of the black hole parameters. Note that a qualitatively similar conclusion for the widths was found in a recent work which instead relies on the rate of particle emission [362].

Using \dot{j} we can find the ratio of $\langle \delta j \rangle$ to $\langle \delta n \rangle$. For the same range, it varies from $\sim 0.1\alpha$ to $\sim 0.4\alpha$. If we expect the superradiant effects are not too strong for (at least the lower end of the interesting range) then one may still expect $\langle \delta j \rangle \sim 1$ which is true for most of the range $4 \ln 2 < \alpha < 32\pi$ at $a = 0.6$. We show $F(a)$ in Fig. 12.1, where one finds the maximum around postmerger spins, while it changes sign for rapidly rotating black holes. That this must turn negative can be seen from Fig. 8 of Ref. [356] and is a consequence of superradiance.

12.4 Discussion and Conclusions

Because of the lack of a fundamental theoretical framework, to estimate the width of the states one must make various assumptions: (0) area quantization is valid, (1) the energy of any given state is just its ADM mass, (2) the power output of spontaneous decays matches those of Hawking radiation, and (3) decays that significantly spin up the black hole are strongly suppressed. By including spin, we conclude that the states of black holes of astrophysical interest are very likely to strongly overlap. This is based on commonly proposed values for α . If this value is much larger, the states of astrophysical black holes could be well separated, but how this can be justified is unclear.

At this point, we want to connect our results to the expected reflectivity of astrophysical black holes. The correct method to do this for high intensity classical waves is unclear. In [358] it is claimed that the reflectivity

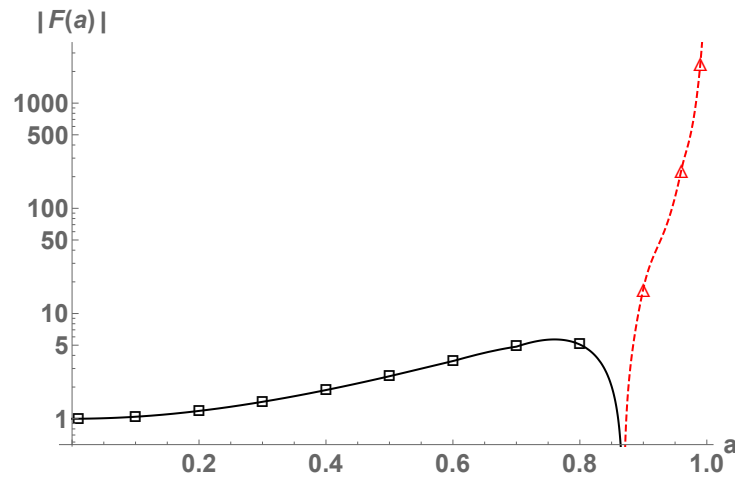


Figure 12.1: Here we show the absolute value of the enhancement factor $F(a)$, see Eq. (12.24), as a function of the spin. The black color represents positive values, whereas red is negative. The squares and triangles correspond to values of a included in Table 1 in Ref. [356], while the lines are interpolations for demonstrative purposes. Figure taken from [9].

is independent of the spacing and widths of the states and described by a Boltzmann distribution. They arrive at this conclusion via three different calculations; however, the assumptions used there seem to require additional justification. The first way they obtain their result is using the classical Einstein rate equations of a pure two-level system with well-separated states in thermal equilibrium. A solar mass black hole is in an extremely high state ($n \sim 10^{76}$) and the nearby states are all evenly spaced. Additionally, we have seen that there is likely significant overlap between them. Their second approach uses a near horizon approximation, whether this avoids trans-Planckian frequencies is unclear to us, if it does not, including them would not be uncontroversial [363, 364]. That the dissipation should appear so simply in the tortoise coordinate in particular also seems to require some more motivation. Their final calculation imposes CP symmetry and leads directly to topology changes. Given that we know CP symmetry is not realized in nature, it seems odd to apply this to an extremely nonlinear quantum gravity state. Recovering this infrared, approximate symmetry in the quantum gravity regime seems unlikely. Taking the result that occupations are well described by a Boltzmann distribution at face value, the most occupied state would be the “minimal black hole” state, which would be $\sim e^{10^{78}}$ times more occupied than the solar mass black hole state.

We want to make one last comment on the prediction of absorption lines [192]. The pure quantum mechanical treatment of black holes, which predicts a discrete spectrum, does not include the influence of the effective potential for perturbations. This potential, as shown in the same work, will trap perturbations up to the light ring. It is known that the trapped frequencies are low, while high frequency waves are only once partially being reflected when approaching the would-be horizon. However, the series of echoes at later times is built up from the frequencies of the trapped-quasinormal modes (QNMs) and is therefore discrete. In order to see absorption lines in the echo signal, the QNM frequencies have to match the black hole state frequencies. This is, in general, not the case, which might make absorption hard to detect. However, the first reflection that includes the high frequency emission is more promising to look for absorption lines, because they are less influenced by the presence of the potential barrier.

Finally, we have seen that astrophysical black holes are unlikely to reflect in the most common area quantization scenarios. Whether any quantum gravity candidates can support values of α that allow significant reflectivity remains open and is worth further investigation.

Part III

Discussions and Conclusions

13 | Discussion

In the following chapter we provide an overall discussion of the works presented in II. Since detailed and specific discussions have been provided there, we here focus on more general aspects. The status of compact objects is discussed in Sec. 13.1. In Sec. 13.2 we focus on the applicability and obtained results of the inverse WKB methods. Finally, we outline some open problems that might be interesting for future projects in Sec. 13.3.

13.1 Status of Compact Objects

The fundamental question of whether astrophysical black holes are as Einstein's theory predicts them must be ultimately answered by observations and experiments. The currently operating gravitational wave detectors advanced LIGO and advanced Virgo will be further improved in the upcoming years. The Japanese detector KAGRA is expected to start observing at the end of 2019 on. It might thus be possible to obtain more precise measurements on the fundamental QNMs and eventually a few of the overtones [315]. Arguably this would provide some of the best ways to test the nature of compact objects that form in the binary mergers of stellar mass objects [309, 313, 316, 317, 318]. With further improvements of PTAs, the space-based mission LISA [17], and other approaches, the gravitational wave search for compact objects will also be possible for much larger masses, including the upper end of supermassive black holes. For EMRIs observed by LISA, it should be possible to obtain several modes of the QNM spectrum, which would put the Kerr hypothesis and general relativity to probably one of its most challenging tests [316]. Also measurements on the absence of tidal heating and the presence of tidal deformability could provide smoking gun effects for new physics at the horizon scale [322].

On the theoretical side, it is clear that models describing ultra compact objects must be further improved to connect them with reasonable physics. While many of the current models, including those used in this thesis, are adequate to study possible smoking gun effects, such as gravitational wave echoes, the majority of them clearly requires more refined underlying physics. Especially the connection to quantum mechanically inspired objects and issues related to possible quantum effects on the horizon scale is a fascinating field of active research. We refer the reader to [84] and references therein for a comprehensive overview.

In the following we discuss gravitational wave echoes in Sec. 13.1.1, the role of rotation for ultra compact objects in Sec. 13.1.2, and the relation to possible quantum properties of black holes in Sec. 13.1.3.

13.1.1 Gravitational Wave Echoes

The probably most discussed connection between ultra compact objects and gravitational waves emitted during or after the ringdown of a binary merger are gravitational wave echoes. While this ongoing debate has been presented in Sec. 3.6, we want to discuss the connection to the inverse spectrum problem in the following.

As is known from early theoretical works [236, 237, 238], the QNM spectra of ultra compact horizonless objects is quite different from those of black holes. The waveform observed by an observer far away from the source follows from the time evolution of gravitational radiation scattered in the vicinity of the object. This means that the waveform depends on how the space-time gets excited, which requires one to know initial conditions. Computing realistic waveforms for ultra compact binary mergers is an open problem. In order to perform numerical relativity simulations, reasonable models are required, which is beyond the simple toy problems commonly discussed in the perturbative regime, in which QNMs and echoes are computed. Some caveats where waveforms might be computed precisely are EMRIs, because the space-time of the massive object can be treated with perturbative methods. These events should be observable with the future space-based mission LISA [17]. However, it is fair to say that a good template bank, as exists for black holes and neutron stars, does not exist yet. Here we

want to mention that the early inspiral part might be used to put constraints coming from the tidal deformability of the objects [321, 322], or their quadrupole moment [365].

However, since the QNM spectrum does not depend on the specific initial conditions of the time evolution, but can be formulated as boundary value problem, we think they are one of the most promising tools to study ultra compact space-times. With increasing sensitivity, it is likely that a precise measurement of the ringdown will be possible. From here QNMs can be directly extracted, without relying on the full waveform. If late time radiation shows up in some forms of echoes or similar, the extracted QNMs can in principle be used in the inverse spectrum method we studied in this work. It is clear that rotation will play an important role and requires one to extend the inverse method to describe a spinning remnant. We therefore discuss the role of rotation for ultra compact objects next.

13.1.2 Rotating Compact Objects

For technical reasons we restricted ourselves in all inverse problem works to non-rotating and spherically symmetric systems. However, astrophysical objects can have significant spin and our approximation may be violated. Since the study of rotating compact objects is challenging in and of itself, here we only want to address the stability.

While non-rotating ultra compact objects might be exotic, stability studies show that some of them can be stable in terms of mode analysis or from thermodynamically, e.g., [164, 354] for gravastars. The situation can change completely once the object is spinning so fast that the effects of rotation can not be neglected anymore. Since it is more complicated to construct solutions describing rotating ultra compact objects, fewer solutions are known. Depending on the compactness, an ergoregion forms and the objects might become susceptible to the ergoregion instability [366, 367, 368]. This was pointed out in various works on different models, including constant density stars [369], gravastars [370], and more [371, 372, 373]. These provide a strong indication that models of horizonless ultra compact objects might have fundamental problems. Because rotation is a common property of astrophysical objects, especially for neutron stars, this issue needs careful attention. Since the full treatment of the instability goes beyond the typical perturbative analysis, it is complicated to follow the complete evolution of the system. But, there are also arguments that weaken the importance of the problem. The ergoregion instability might be quenched by absorption of radiation by the compact object itself [374, 375]. One could also think that the instability exists, but will eventually produce a slowly rotating ultra compact object as stable remnant. In any case, more serious analyses are necessary for firm conclusions.

13.1.3 Prospects of Measuring Quantum Properties of Black Holes

Since many different proposals that modify the physics on the horizon scale have been reported in the literature discussing all works here is not possible, but we refer the interested reader to [84] for a recent review. Some of the concepts have been introduced in chapter 2 of this thesis. Since one work related to possible quantum properties of black holes and gravitational waves has been presented in Sec. 12, we want to first briefly discuss black hole area quantization and then another recent proposal based on the fluctuation dissipation theorem [358, 359].

As argued in recent works [191, 192], including our work [9], black hole area quantization, as proposed by Bekenstein and Mukhanov [184, 185, 186], can in principle lead to gravitational wave echoes. We have pointed out that the quantization constant α plays an important role for whether the spectrum of rotating astrophysical black holes is discrete or continuous, see also [362] for another computation of the black hole spectrum. Although we did not provide a specific waveform, it is reasonable to expect that there is a continuous range of how strong echoes appear, depending on the choice of α . The more discrete the black hole spectrum is, the more significant should echoes be. A more continuous black hole spectrum should weaken the strength of reflected gravitational waves. Quantifying the probability to not absorb, and thus reflect a graviton, could in principle be modeled with a frequency dependent reflection coefficient. If gravitational wave echoes are measured, one can thus constrain α from observations.

In two recent works [358, 359] the wave equation describing gravitational perturbations around rotating black holes was modified by an additional term, which should incorporate effects of the fluctuation dissipation theorem. The term scales with the blueshifted frequencies of gravitational waves and thus becomes important close to the black hole horizon, which is replaced by a stretched horizon. It resembles qualitatively the firewall proposal [127]. The model has one free parameter γ , which scales the strength of the new effect. The authors show that echoes can be produced and their properties depend on the free parameter.

These two examples demonstrate that quite unequal concepts of quantum black holes can in principle, produce observable effects. However, whether the free parameters of these models are of the necessary order to produce measurable effects is unknown, but can eventually be tested in future gravitational wave observations.

13.2 WKB Method for the Inverse Spectrum Problem

In this section we provide a general discussion about the WKB methods for the inverse spectrum problem that were derived in chapter 4 and applied to different compact objects in Part II. We start to review the WKB method for different types of potentials in Sec. 13.2.1, before addressing the accuracy of the reconstruction in Sec. 13.2.2.

13.2.1 The Type of Potential

The inverse problem of using an eigenvalue spectrum to reconstruct the underlying potential in the time-independent Schrödinger equation is in general not uniquely solvable. In the following we want to discuss this in the context of the here presented WKB methods.

Each of the WKB based inverse methods developed in 4.3 has been derived under some assumptions about the underlying type of potential. The standard WKB ansatz for the wave function can be valid for many different types of potentials, but the convenient, standard Bohr-Sommerfeld rule and Gamow formula can only be used for potentials with two turning points. Their main advantage is that the eigenvalue spectrum or transmission can be directly determined by integration and root finding only. The restriction here is that more involved potentials, which admit a larger number of turning points, can not easily be described. Extensions can be derived, but for some types of potentials only a part of the complete eigenvalue spectrum can be obtained. These are for example the quasi-stationary states, which are associated with semi trapped states in a classically allowed region with small imaginary part. For resonances or states with large imaginary parts, other techniques have to be used. Related methods that address this issue require the extension of the integration to the complex plane [281, 376]. However, these and similar matching methods also require information about the type of underlying potential, so a general answer, valid for every type of potential, can not be provided.

In order to solve the inverse spectrum problem, it was demonstrated that the generalized Bohr-Sommerfeld rules and Gamow formula can be used and combined to reconstruct widths $\mathcal{L}(E)$. These are a measure of the difference between two turning points, rather than the potential itself. While this result is already known for the two turning point potential well or barrier, the extension to classes of one, three and four turning point potentials revealed similar results, see Sec. 4.3. A unique reconstruction is only possible if additional information for the turning points is provided. This can either be explicitly the assumption that one of the turning points is known (spherically symmetric compact objects with Birkhoff's theorem in chapter 6 and chapter 8), or indirectly by demanding certain symmetries, e.g., that the potential is symmetric (as done for wormholes in chapter 7). In the direct spectrum problem it can happen that only a part of the spectrum is computable with the generalized Bohr-Sommerfeld rules. In these cases one can only constrain a part of the potential. This means that the reconstructed widths are only known in some region of the potential. We discuss some of the consequences in more detail in Sec. 13.2.2.

A given spectrum of eigenvalues does not directly imply the type of underlying potential. As explicitly demonstrated in chapter 7, the trapped QNM spectra of three and four turning point potentials are qualitatively similar. Thus the underlying potentials might not be distinguishable from each other in practice. It is reasonable to expect that a similar situation also emerges for potentials with more turning points. However, we argued

that further information, e.g., information from the time evolution of a scattered wave packet, might break this degeneracy. In Sec. 7.6 we emphasized that this information can in principle be used to constrain the region around the maximum of the potential barrier. Since the underlying WKB method is not exact, we want to point out that our discussion thus has limitations when it comes to the exact mathematical aspects. Since we consider them as a convenient tool for practical calculations, we discuss the important issue of the accuracy next.

13.2.2 Accuracy of the Reconstruction

In the following we discuss the accuracy of the inverse methods. To study this issue in more detail, one has to consider the different types of errors separately.

The most fundamental one is related to the underlying WKB theory. While proven to be useful and in many cases also precise, it remains an approximate method that relies on several assumptions, as discussed in Sec. 4.1. Unfortunately it is not even possible to provide a reliable measure of the error in the direct spectrum problem. Thus, studying the same for the inverse problem is even more involved. One possibility would be to check for convergence of the reconstructed properties by including higher order terms of WKB theory. One can compute these results in the direct problem. However, in the inverse problem we do not know them for the present potentials. Even if one assumes that the higher order terms are known there are issues. The WKB method itself only provides an asymptotic series, which strictly speaking can not guarantee that it converges to the correct solution. Nevertheless, we have seen in chapter 5 that higher order corrections can in practice improve the precision significantly, at least for the direct problem.

From results for the reconstruction of the potential barrier using the transmission [275], we want to note that the higher order terms reported there can be problematic. Even at leading order, the integrand to compute the widths can be quite divergent [274, 284]. At the same time, the integrals to compute the spectrum and transmission are more robust. This is also an issue if the spectrum is not provided in analytic form, as is the case for every experiment or numerical computation. If the spectrum is provided as a discrete set of numbers, it has to be interpolated. This might introduce artifacts in the reconstructed widths, such as “overhanging” cliffs [274], because widths are not monotonically increasing/decreasing functions of E .

Directly related to this aspect is also the question of how discrete spectra should be interpolated. Because there is no unique way to do so, different techniques will produce varying spectra. Since the calculation of the widths is not a simple linear process, it is not obvious how the final results differ when two different interpolations are used. Note that also the limits of integration depend implicitly on the spectrum.

Another possibility to check the accuracy of the reconstructed potential could be to compute its eigenvalue spectrum numerically and then compare it with the initial one. While this seems to be an easy solution, one should keep in mind that the reconstruction might not provide the whole potential, but only some parts. Thus one can in general not always use another numerical method, since this might depend on the potential on the full domain and will in these cases also be of limited value.

13.3 Open Problems

Among the open problems that remain after a thesis has been carried out are usually its generalization to more complicated cases. We discuss some of the issues one has to face when extending the inverse problem to rotating objects in Sec. 13.3.1, and problems in the context of alternative theories of gravity in Sec. 13.3.1.

13.3.1 Rotating Objects

Due to the technical difficulties in treating the perturbations of rotating objects in general relativity, it was a necessary and well justified assumption to solve the non-rotating inverse problem first. But, since astrophysical objects do rotate, it will be necessary to extend the methods to the rotating case. Assuming slow rotations, the presented methods could be extendable in a straightforward way. However, the general case is technically more

complicated, because the overall structure of the perturbation equations changes significantly, e.g., axial and polar perturbations couple to each other, see [248, 249] and references therein. With this more complicated structure, it is not possible to simply extend the WKB methods, or other inverse methods, that have been developed for the time independent Schrödinger equation. Things have to be derived ab initio, which makes this endeavor quite challenging. While it is true that the spectrum of rotating objects becomes more complex and thus provides more information, there are also more unknown functions in the metric that have to be constrained.

Approaches that use an efficient parametrization of the background metric in combination with full numerical methods could be more promising. Similar to the scalar field perturbations around non-rotating black holes, discussed in chapter 9, one could use a parametrized metric for axial symmetric space-times. Such metrics exist, e.g., [196, 199, 200], however the separability of the perturbation equations might not always be given, which complicates the situation. In cases where it can be separated, one might be able to reproduce a given QNM spectrum by solving the direct problem many times and by varying the parameters until convergence is found. However, whether the metric described by these parameters is a viable solution without pathologies has to be analyzed. Also, as it has been discussed in chapter 9, it is unlikely that only one unique metric describing a given, finite set of QNMs exists. This indicates that the problem might in general not admit a unique solution.

Absence of Birkhoff's Theorem and Uniqueness of the Reconstruction

Another fundamental aspect once rotation is considered, is the absence of Birkhoff's theorem [154]. We used it to provide the external space-time of a spherically symmetric object. The space-time of an axial symmetric object is in general also not described by the Kerr solution. Thus, even if a similar approach that provides the widths of turning points in some more abstract sense would be possible, the non-uniqueness might not make the reconstructed functions very useful. It might also be less clear how to relate them with physical properties of the object.

13.3.2 Compact Objects beyond General Relativity

The works in this thesis mostly focused on ultra compact objects in general relativity. While there is a lot of room for new physics in terms of exotic forms of matter as source of the energy momentum tensor, there is of course also the possibility that new types of objects exist in alternative theories of gravity. Although general relativity is the prevailing theory of gravity, a lot of interest of the community is in compact objects beyond general relativity. A review on this topic is clearly beyond the reach of this summary, but there are some aspects that should be discussed here.

The applicability of the inverse WKB methods will of course rely on the structure of the perturbation equations. If a given alternative theory yields again a time-independent Schrödinger equation, they could be applicable. However, in general this will not be the case and additional terms and couplings to additional degrees of freedom arise. In these cases one could try to follow a perturbative scheme and check whether their impact can be neglected to lowest order.

The situation becomes even more challenging once no specific alternative theory is assumed. Both, the background space-time and the way how perturbations evolve, depend on the underlying theory. In this sense one has two complicated problems at the same time. At least for qualitative studies, it can be interesting to consider test scalar fields, in a similar way as in chapter 9. The evolution of the field might indicate qualitative features. However, if the gravitational theory is not specified, inverse problems related to the QNM spectrum of actual gravitational wave observations from rotating objects are rather hopeless. There might be some hope in using a frame work that also parameterizes the gravitational theory itself.

14 | Conclusions

In this last chapter we arrive at the final conclusions. With Einstein's general theory of relativity as the underlying description of gravity [14], the space-time oscillations of black holes, neutron stars, and ultra compact alternatives were studied. The pioneering works of Regge and Wheeler in 1957 [85], Zerilli in 1970 [86], Thorne and Campolattaro in 1967 [87], and many others discussed in Sec. 3.1, settled the foundations of metric perturbation theory and QNMs. They describe the astonishing physical situation that space-time itself can undergo oscillations caused by perturbed compact objects, as motivated much earlier by Einstein himself with his approximate quadrupole formula [56]. With the technical advances of astronomical observations during the second half of the last century, it has been possible to collect overwhelming evidence that neutron stars and black holes are a part of reality and not only mathematical solutions of general relativity. The repeated direct detections of gravitational waves from merging binary black holes or neutron stars by the advanced LIGO and advanced Virgo detectors of the last years are arguably the best evidence for the existence of black holes and neutron stars [15, 55].

In Part I we provided the theory and methods used and developed in this thesis. We started with a broad overview of general relativity and gravitational wave physics in chapter 1. The compact objects studied in this work have then be introduced and discussed in chapter 2. Perturbation theory in general relativity was outlined in chapter 3. The WKB methods we used were derived in chapter 4. The results of this thesis, which had been published in a series of works [1, 2, 3, 4, 5, 6, 7, 8, 9, 10], were discussed in Part II, with exception of the more methodical work [4], which was explained in Sec. 4.4, and the proceeding article [10]. We provide a short conclusion of each work in Sec. 14.1. We discussed several general aspects of our works in chapter 13 of Part III.

In the following Sec. 14.1 we provide a concise conclusion of the individual works and show the connection between them. We start with those on the direct and inverse QNM problem in Sec. 14.1.1, before we discuss the collaborative works in Sec. 14.1.2. We finish this thesis with final remarks in Sec. 14.2.

14.1 Brief Conclusions of Individual Works

14.1.1 Works on the Direct and Inverse Quasi-Normal Mode Problem

In our first work [1], presented in Sec. 5, we demonstrated that the generalized Bohr-Sommerfeld rule [282] is a useful tool for analytic and semi-analytic calculations of the spectrum of trapped w -modes in ultra compact stars. These space-time modes are characterized by exponentially small imaginary parts, which make these modes very long lived. The models we chose are constant density stars [159], as a prototype of any ultra compact object, and gravastars [160], which were proposed as alternatives to black holes. For these models we studied in particular a full analytic approximate treatment of the perturbation potential, as well as numerical results for the exact potential, and numerical results for the next correction term of the WKB method. The computed QNMs are in good agreement with exact numerical results provided by a full numerical code presented in [233]. Our analytic result is very easy to implement and can be used as quick and approximate study of the spectrum. It can be seen as an analogue of the Schutz-Will formula [213], or similar analytic approaches [208, 209, 210, 211, 212] used for black holes, in the case of ultra compact horizonless objects.

In our subsequent works [2, 5], which we presented in Sec. 6 and in Sec. 7, we were able to invert the generalized Bohr-Sommerfeld rule to reconstruct properties of the potential from the QNM spectrum. As outlined in Sec. 4.3, we showed how the spectrum can be used to reconstruct relations between the classical turning points of the potential. In combination with Birkhoff's theorem [154] for compact stars or the assumption of symmetric wormholes, we have furthermore shown that the reconstruction of the potential is unique, within the underlying framework of WKB theory. We used the same models for ultra compact stars as in our first work, while the

wormhole model was the one proposed by Damour and Solodukhin [182]. We have furthermore argued that the spectrum of trapped w -modes might not be enough to uniquely discriminate between the 3 turning point and 4 turning point potentials. However, we argued that this should be possible with further information from the time evolution. As presentation of the inverse method to a general audience, we studied analytic spectra in a separate work [4]. Since it is not related to compact objects, but purely technical and mathematical aspects, we discussed it in Sec. 4.4.

While our previous works [1, 2, 5] have focused on ultra compact horizonless objects, but not on ordinary black holes or neutron stars, we have addressed neutron stars in [6], which is reported in Sec. 8. By considering the axial gravitational perturbations of spherically symmetric stars, one finds a technically tractable setup to study the inverse problem. Since the effective perturbation potential of ordinary neutron stars has only one turning point, the previously presented methods [1, 2, 5] can not be used. Therefore we first derived a new Bohr-Sommerfeld rule, outlined in Sec. 4.2.3. We have demonstrated that it can be used as analytic approximation to describe the real part of the normal w -mode spectrum. The inversion of this method to reconstruct the potential was demonstrated as well. Throughout the work we have used both versions of the method to connect the w -mode spectrum with underlying properties of the star. We have explicitly provided an approximation for the reconstructed g_{00} component of the metric inside the star. Furthermore, we have analytically motivated the empirically found scaling relation for the fundamental axial mode, which has been studied for neutron stars since the late 90's [90]. Also, we have predicted and confirmed with high accuracy the asymptotic spacing of consecutive overtone frequencies, in agreement with independent calculations presented in [262]. We also pointed out that this scaling changes its qualitative behavior completely, once ultra compact stars are considered. Finally, we could also reconstruct relations between the central density and central pressure. It is clear that the axial perturbations of non-rotating stars are not sufficient to capture the full physical problem, but we have proven in practice, that the QNM spectrum contains very interesting properties of neutron stars and should be studied in more detail in the future.

In another work [8], presented in Sec. 9, we studied the QNM properties of black hole space-times. Here we chose the parametrized black hole metric proposed by Rezzolla and Zhidenko [198]. We were interested in the question how unique the Schwarzschild QNM spectrum is with respect to the underlying metric. Since the metric is supposed to describe black holes beyond general relativity, gravitational perturbations can not be studied due to the lack of field equations. We argue that the scalar test field is however a natural starting point for qualitative discussions, because it only depends on the chosen metric. Then we have explicitly shown that some choices of non-zero parameters of the metric, in combination with a slightly modified ADM mass, can very effectively mimic the Schwarzschild black hole. Since real gravitational wave experiments are expected to observe only the fundamental QNMs and eventually a few overtones, it is important to understand how unique the resulting spectrum is. Although one might argue that a given combination of parameters that mimic a Schwarzschild black hole with altered ADM mass is not likely, it proofs the point that the uniqueness of the QNM spectrum of black holes requires more attention in the future. Especially with limited observational precision and only a few QNMs at hand, one might find the situation that small deviations from general relativity could unintentionally be absorbed by a different black hole mass or spin, once rotation is considered. More work is required for quantitative conclusions.

14.1.2 Collaborative Projects

In the first joint work with Andrea Maselli as first author [3], we studied the parameter estimation of phenomenological gravitational wave echo templates. The paper is described in Sec. 10. Since realistic templates are not available, we established multiple analytical waveforms, inspired by numerical time evolution calculations of ultra compact constant density stars. In order to quantify whether detected signals can be used to recover the parameters of the templates, we apply the Fisher matrix approach to current and future gravitational wave detectors. Since a more realistic treatment, as it is done for general relativity black holes, is not available at the time, our work estimates how well these parameters could be recovered. We find that already current detectors

at design sensitivity have the potential to reconstruct the main parameters, if the signals are properly described by our templates. Our work can be seen as an early proof of principle that demonstrates the importance of future gravitational wave detectors for testing the nature of compact objects.

In the joint work with Roman Konoplya as second author [7], outlined in Sec. 11, we have investigated the inverse problem of Hawking radiation [119]. As examples we chose Schwarzschild and Reissner-Nordström black holes. Since the emitted spectrum of Hawking radiation is related to the greybody factors of the classical perturbation potentials [335], it is possible to make use of the inverse WKB method for potential barriers. We have explicitly demonstrated that the greybody factors, which are being summed over in the full spectrum, can be extracted individually. We do this by a numerical fitting routine that allows to extract most details of the greybody factors. Using this as input for the inverse method for potential barriers, we have reconstructed substantial parts of the underlying widths of the perturbation potentials. Without further physical assumptions, the inverse problem in this case, has no unique answer. Since Hawking radiation of astrophysical black holes might never be observable, the here described work could be of interest for analogue gravity experiments in laboratories. While developing the numerical routine, we have obtained a simple, but relatively precise analytic approximation to compute the full spectrum of Hawking radiation. The nature of the summation of greybody factors allows to describe the full spectrum very effectively by using the results of a fitted parabola or Pöschl-Teller potential, similar to the black hole QNM computations of Schutz and Will [213], and others [208, 209, 210, 211, 212]. While the latter only work for QNMs close to the peak of the barrier, but fail completely for higher modes, the here presented approximation gives a reliable description of the whole spectrum of Hawking radiation.

In the last joint work with Andrew Coates as first author, we have studied the implications of black hole area quantization to the gravitational wave spectrum of rotating, astrophysical black holes. Our work was inspired by the recent claims [191, 192] that black hole area quantization, as proposed by Bekenstein and Mukhanov [184, 185, 186], leads to gravitational wave echoes, see Sec. 3.6. We match the spontaneous decay of these quantum black holes to Hawking radiation calculations and estimate the natural widths of these states. As in the non-rotating case described by Bekenstein and Mukhanov, we find that the ratio between width and spacing of nonspinning black hole states approaches a small constant. However, when we include the effect of the spin, the natural widths increase and we expect echo effects to be weaker. The result for this ratio is in agreement with a similar work [362] that treats the spinning case differently. Since this result depends directly on the unknown constant that measures the quantization, gravitational wave observations could in principle be used to distinguish different theories of black hole area quantization. However, for all of the commonly discussed scenarios for this constant, our answer whether gravitational wave echoes should be observable is “almost certainly no.”

14.2 Final Remarks

Compact objects are an active intersection of diverse research fields in astronomy, physics, mathematics, and philosophy. They do not only demonstrate the astonishing implications of strong field gravity described by general relativity, but have proven to be a substantial part of our universe. Coming from versatile backgrounds and scientific interests, the study of black holes, neutron stars, and various alternative models are an ongoing endeavor celebrating important success over the last years. Even more interesting, especially for young researchers, are the decades ahead of us. While the scientific proof that gravitational waves really exist has finally been made, the intriguing follow up questions concern the quantitative details of general relativity’s predictions and turning gravitational wave physics into a standard tool in modern astronomy. This has wide ranging implications, such as the micro physics of matter under extreme conditions in neutron stars, the origin of the very heavy elements in the universe, the formation of the most massive objects in the universe, hopefully new insights into dark matter and dark energy, singularities in black holes, and eventually the quantum aspects of black holes, to name a few of the many possibilities. The QNM spectrum, which has played a central role in this work, is a promising tool to extract information from a compact object. The observational confirmation of the Kerr QNM spectrum is arguably one of the most challenging tests that general relativity will have to face in the future.

Then we will ask the same question again: *Was Einstein right?*

Bibliography

- [1] S. H. Völkel, K. D. Kokkotas, A semi-analytic study of axial perturbations of ultra compact stars, *Class. Quantum Grav.* 34 (12) (2017) 125006. [arXiv:1703.08156](#), [doi:10.1088/1361-6382/aa68cc](#).
- [2] S. H. Völkel, K. D. Kokkotas, Ultra Compact Stars: Reconstructing the Perturbation Potential, *Class. Quantum Grav.* 34 (17) (2017) 175015. [arXiv:1704.07517](#), [doi:10.1088/1361-6382/aa82de](#).
- [3] A. Maselli, S. H. Völkel, K. D. Kokkotas, Parameter estimation of gravitational wave echoes from exotic compact objects, *Phys. Rev. D* 96 (6) (2017) 064045. [arXiv:1708.02217](#), [doi:10.1103/PhysRevD.96.064045](#).
- [4] S. H. Völkel, Inverse spectrum problem for quasi-stationary states, *J. Phys. Commun.* 2 (2) (2018) 025029. [arXiv:1802.08684](#), [doi:10.1088/2399-6528/aaee2](#).
- [5] S. H. Völkel, K. D. Kokkotas, Wormhole potentials and throats from quasi-normal modes, *Class. Quantum Grav.* 35 (10) (2018) 105018. [arXiv:1802.08525](#), [doi:10.1088/1361-6382/aabce6](#).
- [6] S. H. Völkel, K. D. Kokkotas, On the inverse spectrum problem of neutron stars, *Class. Quantum Grav.* 36 (11) (2019) 115002. [arXiv:1901.11262](#), [doi:10.1088/1361-6382/ab186e](#).
- [7] S. H. Völkel, R. Konoplya, K. D. Kokkotas, Inverse problem for Hawking radiation, *Phys. Rev. D* 99 (10) (2019) 104025. [arXiv:1902.07611](#), [doi:10.1103/PhysRevD.99.104025](#).
- [8] S. H. Völkel, K. D. Kokkotas, Scalar Fields and Parametrized Spherically Symmetric Black Holes: Can one hear the shape of space-time?, *Phys. Rev. D* 100 (4) (2019) 044026. [arXiv:1908.00252](#), [doi:10.1103/PhysRevD.100.044026](#).
- [9] A. Coates, S. H. Völkel, K. D. Kokkotas, Spectral Lines of Quantized, Spinning Black Holes and their Astrophysical Relevance, *Phys. Rev. Lett.* 123 (2019) 171104. [arXiv:1909.01254](#), [doi:10.1103/PhysRevLett.123.171104](#).
- [10] S. H. Völkel, K. D. Kokkotas, Hearing the Nature of Compact Objects, in: S. Cacciatori, B. Güneysu, S. Pigola (Eds.), *Einstein Equations: Physical and Mathematical Aspects of General Relativity*, Birkhäuser Basel.
- [11] Völkel, S. H. and Kokkotas, K. D., Can one hear the shape of an ultra compact object?, [CQG+https://cqgplus.com/2017/10/02/can-one-hear-the-shape-of-an-ultra-compact-object/](https://cqgplus.com/2017/10/02/can-one-hear-the-shape-of-an-ultra-compact-object/) (2017).
- [12] S. H. Völkel, K. D. Kokkotas, The Sound of Exotic Astrophysical “Instruments”, [CQG+https://cqgplus.com/2018/05/28/the-sound-of-exotic-astrophysical-instruments/](https://cqgplus.com/2018/05/28/the-sound-of-exotic-astrophysical-instruments/) (2018).
- [13] B. P. Abbott, et al., GW150914: First results from the search for binary black hole coalescence with Advanced LIGO, *Phys. Rev. D* 93 (2016) 122003. [doi:10.1103/PhysRevD.93.122003](#).
- [14] A. Einstein, Die Grundlage der allgemeinen Relativitätstheorie, *Ann. Phys.* 354 (7) (1916) 769–822. [doi:10.1002/andp.19163540702](#).
- [15] B. P. Abbott, et al., GW170817: Observation of Gravitational Waves from a Binary Neutron Star Inspiral, *Phys. Rev. Lett.* 119 (2017) 161101. [doi:10.1103/PhysRevLett.119.161101](#).
- [16] T. E. C. et al., First M87 Event Horizon Telescope Results. I. The Shadow of the Supermassive Black Hole, *ApJL* 875 (2019) 1. [doi:10.3847/2041-8213/ab0ec7](#).

- [17] P. A. Seoane, et al., *The Gravitational Universe* (2013). arXiv:1305.5720.
- [18] A. Einstein, Über einen die Erzeugung und Verwandlung des Lichtes betreffenden heuristischen Gesichtspunkt, *Ann. Phys.* 322 (6) (1905) 132–148. doi:10.1002/andp.19053220607.
- [19] A. Einstein, Strahlungs-Emission und Absorption nach der Quantentheorie, *Deutsche Physikalische Gesellschaft* 18 (1916) 318–323.
- [20] A. Einstein, Über die von der molekularkinetischen Theorie der Wärme geforderte Bewegung von in ruhenden Flüssigkeiten suspendierten Teilchen, *Ann. Phys.* 322 (8) (1905) 549–560. doi:10.1002/andp.19053220806.
- [21] A. Einstein, Zur Elektrodynamik bewegter Körper, *Ann. Phys.* 322 (10) (1905) 891–921. doi:10.1002/andp.19053221004.
- [22] I. Newton, *Philosophiæ Naturalis Principia Mathematica*, England, 1687.
- [23] C. M. Will, The Confrontation between General Relativity and Experiment, *Living Reviews in Relativity* 17 (2014) 4. arXiv:1403.7377, doi:10.12942/lrr-2014-4.
- [24] U. J. Le Verrier, *Theorie du mouvement de Mercure*, *Annales de l'Observatoire de Paris* 5 (1859).
- [25] M. P. Hobson, G. P. Efstathiou, A. N. Lasenby, *General Relativity: An Introduction for Physicists*, Cambridge University Press, 2006. doi:10.1017/CBO9780511790904.
- [26] F. W. Dyson, A. S. Eddington, C. Davidson, IX. A determination of the deflection of light by the sun's gravitational field, from observations made at the total eclipse of May 29, 1919, *Philosophical Transactions of the Royal Society of London. Series A, Containing Papers of a Mathematical or Physical Character* 220 (571-581) (1920) 291–333. doi:10.1098/rsta.1920.0009.
- [27] R. V. Pound, G. A. Rebka, Gravitational Red-Shift in Nuclear Resonance, *Phys. Rev. Lett.* 3 (1959) 439–441. doi:10.1103/PhysRevLett.3.439.
- [28] R. V. Pound, J. L. Snider, Effect of Gravity on Gamma Radiation, *Phys. Rev.* 140 (1965) B788–B803. doi:10.1103/PhysRev.140.B788.
- [29] C. W. Misner, K. S. Thorne, J. A. Wheeler, *Gravitation*, W. H. Freeman, San Francisco, 1973.
- [30] W. S. Adams, The Relativity Displacement of the Spectral Lines in the Companion of Sirius, *Proceedings of the National Academy of Sciences* 11 (7) (1925) 382–387. doi:10.1073/pnas.11.7.382.
- [31] D. M. Popper, Red Shift in the Spectrum of 40 Eridani B., *ApJ* 120 (1954) 316. doi:10.1086/145916.
- [32] J. W. Brault, *The Gravitational Red Shift in the Solar Spectrum.*, Ph.D. thesis, Princeton University (1962).
- [33] I. I. Shapiro, Fourth Test of General Relativity, *Phys. Rev. Lett.* 13 (1964) 789–791. doi:10.1103/PhysRevLett.13.789.
- [34] I. I. Shapiro, G. H. Pettengill, M. E. Ash, M. L. Stone, W. B. Smith, R. P. Ingalls, R. A. Brockelman, Fourth Test of General Relativity: Preliminary Results, *Phys. Rev. Lett.* 20 (1968) 1265–1269. doi:10.1103/PhysRevLett.20.1265.
- [35] I. I. Shapiro, M. E. Ash, R. P. Ingalls, W. B. Smith, D. B. Campbell, R. B. Dyce, R. F. Jurgens, G. H. Pettengill, Fourth Test of General Relativity: New Radar Result, *Phys. Rev. Lett.* 26 (1971) 1132–1135. doi:10.1103/PhysRevLett.26.1132.
- [36] R. D. Reasenberg, I. I. Shapiro, P. E. MacNeil, R. B. Goldstein, J. C. Breidenthal, J. P. Brenkle, D. L. Cain, T. M. Kaufman, T. A. Komarek, A. I. Zygielbaum, Viking relativity experiment - Verification of signal retardation by solar gravity, *ApJ* 234 (1979) L219–L221. doi:10.1086/183144.

- [37] B. Bertotti, L. Iess, P. Tortora, A test of general relativity using radio links with the Cassini spacecraft, *Nature* 425 (2003) 374–376. doi : 10 . 1038/nature01997.
- [38] V. M. Kaspi, J. H. Taylor, M. F. Ryba, High-precision timing of millisecond pulsars. 3: Long-term monitoring of PSRs B1855+09 and B1937+21, *ApJ*428 (1994) 713–728. doi : 10 . 1086/174280.
- [39] R. A. Hulse, J. H. Taylor, Discovery of a pulsar in a binary system, *ApJ*195 (1975) L51–L53. doi : 10 . 1086/181708.
- [40] J. H. Taylor, J. M. Weisberg, A new test of general relativity - Gravitational radiation and the binary pulsar PSR 1913+16, *ApJ*253 (1982) 908–920. doi : 10 . 1086/159690.
- [41] J. H. Taylor, J. M. Weisberg, Further experimental tests of relativistic gravity using the binary pulsar PSR 1913+16, *ApJ*345 (1989) 434–450. doi : 10 . 1086/167917.
- [42] J. M. Weisberg, D. J. Nice, J. H. Taylor, TIMING MEASUREMENTS OF THE RELATIVISTIC BINARY PULSAR PSR B1913+16, *ApJ* 722 (2) (2010) 1030–1034. doi : 10 . 1088/0004-637x/722/2/1030.
- [43] J. M. Weisberg, Y. Huang, RELATIVISTIC MEASUREMENTS FROM TIMING THE BINARY PULSAR PSR B1913+16, *ApJ* 829 (1) (2016) 55. doi : 10 . 3847/0004-637x/829/1/55.
- [44] C. S. Reynolds, Measuring Black Hole Spin using X-ray Reflection Spectroscopy, *Space Sci. Rev.* 183 (1-4) (2014) 277–294. arXiv : 1302 . 3260, doi : 10 . 1007/s11214-013-0006-6.
- [45] C. Bambi, Testing black hole candidates with electromagnetic radiation, *Rev. Mod. Phys.* 89 (2) (2017) 025001. arXiv : 1509 . 03884, doi : 10 . 1103/RevModPhys . 89 . 025001.
- [46] A. Friedmann, Über die Krümmung des Raumes, *Zeitschrift für Physik* 10 (1922) 377–386. doi : 10 . 1007/BF01332580.
- [47] A. Friedmann, Über die Möglichkeit einer Welt mit konstanter negativer Krümmung des Raumes, *Zeitschrift für Physik* 21 (1) (1924) 326–332. doi : 10 . 1007/BF01328280.
- [48] G. Lemaître, Un Univers homogène de masse constante et de rayon croissant rendant compte de la vitesse radiale des nébuleuses extra-galactiques, *Annales de la Société Scientifique de Bruxelles* 47 (1927) 49–59.
- [49] G. Lemaître, L’Univers en expansion, *Annales de la Société Scientifique de Bruxelles* 53 (1933) 51.
- [50] H. P. Robertson, Kinematics and World-Structure, *ApJ*82 (1935) 284. doi : 10 . 1086/143681.
- [51] H. P. Robertson, Kinematics and World-Structure II., *ApJ*83 (1936) 187. doi : 10 . 1086/143716.
- [52] H. P. Robertson, Kinematics and World-Structure III., *ApJ*83 (1936) 257. doi : 10 . 1086/143726.
- [53] A. G. Walker, On Milne’s Theory of World-Structure, *Proceedings of the London Mathematical Society* 42 (1937) 90–127. doi : 10 . 1112/plms/s2-42.1.90.
- [54] A. Liddle, *An Introduction to Modern Cosmology*, Wiley, 2015.
- [55] B. P. Abbott, et al., Observation of Gravitational Waves from a Binary Black Hole Merger, *Phys. Rev. Lett.* 116 (2016) 061102. doi : 10 . 1103/PhysRevLett . 116 . 061102.
- [56] A. Einstein, Über Gravitationswellen, *Sitzungsberichte der Königlich Preußischen Akademie der Wissenschaften* (Berlin), Seite 154-167. (1918).
- [57] B. S. Sathyaprakash, B. F. Schutz, *Physics, Astrophysics and Cosmology with Gravitational Waves*, *Living Rev. Rel.* 12 (1) (2009) 2. doi : 10 . 12942/lrr-2009-2.

- [58] K. D. Kokkotas, B. G. Schmidt, Quasi-Normal Modes of Stars and Black Holes, *Living Rev. Rel.* 2 (1999) 2. arXiv:gr-qc/9909058, doi:10.12942/lrr-1999-2.
- [59] H.-P. Nollert, Quasinormal modes: the characteristic 'sound' of black holes and neutron stars, *Class. Quantum Grav.* 16 (12) (1999) R159–R216. doi:10.1088/0264-9381/16/12/201.
- [60] E. Poisson, C. M. Will, *Gravity: Newtonian, Post-Newtonian, Relativistic*, Cambridge University Press, 2014.
- [61] F. Pretorius, Evolution of Binary Black-Hole Spacetimes, *Phys. Rev. Lett.* 95 (2005) 121101. doi:10.1103/PhysRevLett.95.121101.
- [62] M. Campanelli, C. O. Lousto, P. Marronetti, Y. Zlochower, Accurate Evolutions of Orbiting Black-Hole Binaries without Excision, *Phys. Rev. Lett.* 96 (2006) 111101. doi:10.1103/PhysRevLett.96.111101.
- [63] J. G. Baker, J. Centrella, D.-I. Choi, M. Koppitz, J. van Meter, Gravitational-Wave Extraction from an Inspiral Configuration of Merging Black Holes, *Phys. Rev. Lett.* 96 (2006) 111102. doi:10.1103/PhysRevLett.96.111102.
- [64] A. Buonanno, T. Damour, Effective one-body approach to general relativistic two-body dynamics, *Phys. Rev. D* 59 (1999) 084006. arXiv:gr-qc/9811091, doi:10.1103/PhysRevD.59.084006.
- [65] B. Allen, The Stochastic gravity wave background: Sources and detection, in: *Relativistic gravitation and gravitational radiation. Proceedings, School of Physics, Les Houches, France, September 26-October 6, 1995, 1996*, pp. 373–417. arXiv:gr-qc/9604033.
- [66] N. Christensen, Stochastic Gravitational Wave Backgrounds, *Rept. Prog. Phys.* 82 (1) (2019) 016903. arXiv:1811.08797, doi:10.1088/1361-6633/aae6b5.
- [67] P. A. R. Ade, et al., Detection of *B*-Mode Polarization at Degree Angular Scales by BICEP2, *Phys. Rev. Lett.* 112 (24) (2014) 241101. arXiv:1403.3985, doi:10.1103/PhysRevLett.112.241101.
- [68] P. A. R. Ade, et al., Joint Analysis of BICEP2/*KeckArray* and *Planck* Data, *Phys. Rev. Lett.* 114 (2015) 101301. arXiv:1502.00612, doi:10.1103/PhysRevLett.114.101301.
- [69] J. Weber, Gravitational Radiation, *Phys. Rev. Lett.* 18 (1967) 498–501. doi:10.1103/PhysRevLett.18.498.
- [70] J. Weber, Gravitational-Wave-Detector Events, *Phys. Rev. Lett.* 20 (1968) 1307–1308. doi:10.1103/PhysRevLett.20.1307.
- [71] J. Weber, Evidence for Discovery of Gravitational Radiation, *Phys. Rev. Lett.* 22 (1969) 1320–1324. doi:10.1103/PhysRevLett.22.1320.
- [72] A. de Waard, L. Gottardi, J. van Houwelingen, A. Shumack, G. Frossati, MiniGRAIL, the first spherical detector, *Class. Quantum Grav.* 20 (10) (2003) S143–S151. doi:10.1088/0264-9381/20/10/317.
- [73] O. D. Aguiar, The Past, Present and Future of the Resonant-Mass Gravitational Wave Detectors, *Res. Astron. Astrophys.* 11 (2011) 1–42. arXiv:1009.1138, doi:10.1088/1674-4527/11/1/001.
- [74] A. N. Lommen, Pulsar timing arrays: the promise of gravitational wave detection, *Reports on Progress in Physics* 78 (12) (2015) 124901. doi:10.1088/0034-4885/78/12/124901.
- [75] S. Kawamura, et al., The Japanese space gravitational wave antenna - DECIGO, *Journal of Physics: Conference Series* 122 (2008) 012006. doi:10.1088/1742-6596/122/1/012006.
- [76] M. Abernathy, et al., Einstein gravitational wave Telescope conceptual design study (2011).

- [77] D. Reitze, et al., Cosmic Explorer: The U.S. Contribution to Gravitational-Wave Astronomy beyond LIGO (2019). [arXiv:1907.04833](https://arxiv.org/abs/1907.04833).
- [78] B. P. Abbott, et al., GW151226: Observation of Gravitational Waves from a 22-Solar-Mass Binary Black Hole Coalescence, *Phys. Rev. Lett.* 116 (2016) 241103. doi:10.1103/PhysRevLett.116.241103.
- [79] B. P. Abbott, et al., GW170814: A Three-Detector Observation of Gravitational Waves from a Binary Black Hole Coalescence, *Phys. Rev. Lett.* 119 (2017) 141101. doi:10.1103/PhysRevLett.119.141101.
- [80] B. P. Abbott, et al., Multi-messenger Observations of a Binary Neutron Star Merger, *ApJ* 848 (2) (2017) L12. doi:10.3847/2041-8213/aa91c9.
- [81] B. F. Schutz, Determining the Hubble Constant from Gravitational Wave Observations, *Nature* 323 (1986) 310–311. doi:10.1038/323310a0.
- [82] B. P. Abbott, et al., A gravitational-wave standard siren measurement of the Hubble constant, *Nature* 551 (7678) (2017) 85–88. [arXiv:1710.05835](https://arxiv.org/abs/1710.05835), doi:10.1038/nature24471.
- [83] B. P. Abbott, et al., Gravitational Waves and Gamma-Rays from a Binary Neutron Star Merger: GW170817 and GRB 170817A, *ApJ* 848 (2) (2017) L13. doi:10.3847/2041-8213/aa920c.
- [84] V. Cardoso, P. Pani, Testing the nature of dark compact objects: a status report, *Living Rev. Rel.* 22 (1) (2019) 4. [arXiv:1904.05363](https://arxiv.org/abs/1904.05363), doi:10.1007/s41114-019-0020-4.
- [85] T. Regge, J. A. Wheeler, Stability of a Schwarzschild Singularity, *Physical Review* 108 (1957) 1063–1069. doi:10.1103/PhysRev.108.1063.
- [86] F. J. Zerilli, Effective Potential for Even-Parity Regge-Wheeler Gravitational Perturbation Equations, *Phys. Rev. Lett.* 24 (1970) 737–738. doi:10.1103/PhysRevLett.24.737.
- [87] K. S. Thorne, A. Campolattaro, Non-Radial Pulsation of General-Relativistic Stellar Models. I. Analytic Analysis for $L \geq 2$, *ApJ* 149 (1967) 591. doi:10.1086/149288.
- [88] S. Chandrasekhar, V. Ferrari, On the non-radial oscillations of a star, *Proceedings of the Royal Society of London Series A* 432 (1991) 247–279. doi:10.1098/rspa.1991.0016.
- [89] E. Berti, V. Cardoso, A. O. Starinets, Quasinormal modes of black holes and black branes, *Class. Quantum Grav.* 26 (2009) 163001. [arXiv:0905.2975](https://arxiv.org/abs/0905.2975), doi:10.1088/0264-9381/26/16/163001.
- [90] N. Andersson, K. D. Kokkotas, Towards gravitational wave asteroseismology, *Mon. Not. Roy. Astron. Soc.* 299 (1998) 1059–1068. [arXiv:gr-qc/9711088](https://arxiv.org/abs/gr-qc/9711088), doi:10.1046/j.1365-8711.1998.01840.x.
- [91] O. Benhar, E. Berti, V. Ferrari, The Imprint of the equation of state on the axial w modes of oscillating neutron stars, *Mon. Not. Roy. Astron. Soc.* 310 (1999) 797–803, [ICTP Lect. Notes Ser.3,35(2001)]. [arXiv:gr-qc/9901037](https://arxiv.org/abs/gr-qc/9901037), doi:10.1046/j.1365-8711.1999.02983.x.
- [92] K. D. Kokkotas, T. A. Apostolatos, N. Andersson, The Inverse problem for pulsating neutron stars: A 'Fingerprint analysis' for the supranuclear equation of state, *Mon. Not. Roy. Astron. Soc.* 320 (2001) 307–315. [arXiv:gr-qc/9901072](https://arxiv.org/abs/gr-qc/9901072), doi:10.1046/j.1365-8711.2001.03945.x.
- [93] L. Lindblom, N. M. Indik, A Spectral Approach to the Relativistic Inverse Stellar Structure Problem, *Phys. Rev. D* 86 (2012) 084003. [arXiv:1207.3744](https://arxiv.org/abs/1207.3744), doi:10.1103/PhysRevD.86.084003.
- [94] L. Lindblom, N. M. Indik, Spectral Approach to the Relativistic Inverse Stellar Structure Problem II, *Phys. Rev. D* 89 (6) (2014) 064003, [Erratum: *Phys. Rev. D* 93, no.12, 129903 (2016)]. [arXiv:1310.0803](https://arxiv.org/abs/1310.0803), doi:10.1103/PhysRevD.89.064003, doi:10.1103/PhysRevD.93.129903.

- [95] L. Lindblom, The Relativistic Inverse Stellar Structure Problem, *AIP Conf. Proc.* 1577 (1) (2015) 153–164. arXiv:1402.0035, doi:10.1063/1.4861951.
- [96] L. Lindblom, Inverse Structure Problem for Neutron-Star Binaries, *Phys. Rev. D* 98 (4) (2018) 043012. arXiv:1807.02538, doi:10.1103/PhysRevD.98.043012.
- [97] Kac, M., Can One Hear the Shape of a Drum?, *The American Mathematical Monthly* 73 (4) (1966) 1–23. doi:10.2307/2313748.
- [98] C. Gordon, D. Webb, S. Wolpert, Isospectral plane domains and surfaces via Riemannian orbifolds, *Inventiones mathematicae* 110 (1) (1992) 1–22. doi:10.1007/BF01231320.
- [99] R. Arnowitt, S. Deser, C. W. Misner, Coordinate Invariance and Energy Expressions in General Relativity, *Phys. Rev.* 122 (1961) 997–1006. doi:10.1103/PhysRev.122.997.
- [100] J. Michell, On the Means of Discovering the Distance, Magnitude, &c. of the Fixed Stars, in Consequence of the Diminution of the Velocity of Their Light, in Case Such a Diminution Should be Found to Take Place in any of Them, and Such Other Data Should be Procured from Observations, as Would be Farther Necessary for That Purpose. By the Rev. John Michell, B. D. F. R. S. In a Letter to Henry Cavendish, Esq. F. R. S. and A. S., *Philosophical Transactions of the Royal Society of London* 74 (1784) 35–57.
- [101] P. S. L. Place, Beweis des Satzes, dass die anziehende Kraft bey einem Weltkörper so gross seyn könne, dass das Licht davon nicht ausströmen kann, *Allgemeine Geographische Ephemeriden* (Bd. 4) (1799) 1–6.
- [102] C. Montgomery, W. Orchiston, I. Whittingham, Michell, Laplace and the origin of the black hole concept, *Journal of Astronomical History and Heritage* 12 (2009) 90–96.
- [103] K. Schwarzschild, Über das Gravitationsfeld eines Massenpunktes nach der Einsteinschen Theorie, *Sitzungsberichte der Königlich-Preussischen Akademie der Wissenschaften*, Reimer, Berlin 86 (3) (1916) 189–196.
- [104] J. R. Oppenheimer, H. Snyder, On Continued Gravitational Contraction, *Phys. Rev.* 56 (1939) 455–459. doi:10.1103/PhysRev.56.455.
- [105] A. Einstein, On a Stationary System With Spherical Symmetry Consisting of Many Gravitating Masses, *Annals of Mathematics* 40 (4) (1939) 922–936.
- [106] D. Finkelstein, Past-Future Asymmetry of the Gravitational Field of a Point Particle, *Phys. Rev.* 110 (1958) 965–967. doi:10.1103/PhysRev.110.965.
- [107] M. D. Kruskal, Maximal Extension of Schwarzschild Metric, *Phys. Rev.* 119 (1960) 1743–1745. doi:10.1103/PhysRev.119.1743.
- [108] H. Thirring, Über die Wirkung rotierender ferner Massen in der Einsteinschen Gravitationstheorie., *Physikalische Zeitschrift* 19 (1918) 33.
- [109] J. Lense, H. Thirring, Über den Einfluß der Eigenrotation der Zentralkörper auf die Bewegung der Planeten und Monde nach der Einsteinschen Gravitationstheorie, *Physikalische Zeitschrift* 19 (1918).
- [110] R. P. Kerr, Gravitational Field of a Spinning Mass as an Example of Algebraically Special Metrics, *Phys. Rev. Lett.* 11 (1963) 237–238. doi:10.1103/PhysRevLett.11.237.
- [111] E. T. Newman, E. Couch, K. Chinnapared, A. Exton, A. Prakash, R. Torrence, Metric of a Rotating, Charged Mass, *J. Math. Phys.* 6 (6) (1965) 918–919. doi:10.1063/1.1704351.
- [112] W. Israel, Event Horizons in Static Vacuum Space-Times, *Phys. Rev.* 164 (1967) 1776–1779. doi:10.1103/PhysRev.164.1776.

- [113] W. Israel, Event horizons in static electrovac space-times, *Communications in Mathematical Physics* 8 (3) (1968) 245–260. doi : 10 . 1007/BF01645859.
- [114] B. Carter, Axisymmetric Black Hole Has Only Two Degrees of Freedom, *Phys. Rev. Lett.* 26 (1971) 331–333. doi : 10 . 1103/PhysRevLett . 26 . 331.
- [115] R. Penrose, Gravitational Collapse and Space-Time Singularities, *Phys. Rev. Lett.* 14 (3) (1965) 57–59. doi : 10 . 1103/PhysRevLett . 14 . 57.
- [116] J. D. Bekenstein, Black Holes and Entropy, *Phys. Rev. D* 7 (1973) 2333–2346. doi : 10 . 1103/PhysRevD . 7 . 2333.
- [117] J. M. Bardeen, B. Carter, S. W. Hawking, The four laws of black hole mechanics, *Communications in Mathematical Physics* 31 (2) (1973) 161–170. doi : 10 . 1007/BF01645742.
- [118] S. W. Hawking, Black hole explosions, *Nature* 248 (1974) 30–31. doi : 10 . 1038/248030a0.
- [119] S. W. Hawking, Particle creation by black holes, *Communications in Mathematical Physics* 43 (1975) 199–220. doi : 10 . 1007/BF02345020.
- [120] S. B. Giddings, Black holes and massive remnants, *Phys. Rev. D* 46 (1992) 1347–1352. doi : 10 . 1103/PhysRevD . 46 . 1347.
- [121] J. Preskill, Do Black Holes Destroy Information?, in: S. Kalara, D. V. Nanopoulos (Eds.), *Black Holes, Membranes, Wormholes and Superstrings*, 1993, p. 22. arXiv : hep - th / 9209058.
- [122] D. N. Page, Information in black hole radiation, *Phys. Rev. Lett.* 71 (1993) 3743–3746. doi : 10 . 1103/PhysRevLett . 71 . 3743.
- [123] S. W. Hawking, Information loss in black holes, *Phys. Rev. D* 72 (2005) 084013. arXiv : hep - th / 0507171, doi : 10 . 1103/PhysRevD . 72 . 084013.
- [124] G. 't Hooft, Dimensional reduction in quantum gravity, *Conf. Proc.* C930308 (1993) 284–296. arXiv : gr - qc / 9310026.
- [125] L. Susskind, The world as a hologram, *J. Math. Phys.* 36 (11) (1995) 6377–6396. doi : 10 . 1063/1 . 531249.
- [126] R. Bousso, The holographic principle, *Rev. Mod. Phys.* 74 (2002) 825–874. doi : 10 . 1103/RevModPhys . 74 . 825.
- [127] A. Almheiri, D. Marolf, J. Polchinski, J. Sully, Black Holes: Complementarity or Firewalls?, *JHEP* 02 (2013) 062. arXiv : 1207 . 3123, doi : 10 . 1007/JHEP02 (2013) 062.
- [128] S. W. Hawking, M. J. Perry, A. Strominger, Soft Hair on Black Holes, *Phys. Rev. Lett.* 116 (2016) 231301. doi : 10 . 1103/PhysRevLett . 116 . 231301.
- [129] G. A. Shields, A Brief History of Active Galactic Nuclei, *Publications of the Astronomical Society of the Pacific* 111 (760) (1999) 661–678. doi : 10 . 1086/316378.
- [130] S. Gillessen, F. Eisenhauer, S. Trippe, T. Alexander, R. Genzel, F. Martins, T. Ott, Monitoring Stellar Orbits Around the Massive Black Hole in the Galactic Center, *ApJ* 692 (2) (2009) 1075–1109. arXiv : 0810 . 4674, doi : 10 . 1088/0004 - 637X/692/2/1075.
- [131] S. Bowyer, E. T. Byram, T. A. Chubb, H. Friedman, Cosmic X-ray Sources, *Science* 147 (3656) (1965) 394–398. doi : 10 . 1126/science . 147 . 3656 . 394.

- [132] J. A. Orosz, J. E. McClintock, J. P. Aufdenberg, R. A. Remillard, M. J. Reid, R. Narayan, L. Gou, THE MASS OF THE BLACK HOLE IN CYGNUS X-1, *ApJ* 742 (2) (2011) 84. doi : 10 . 1088/0004-637x/742/2/84.
- [133] J. Abedi, H. Dykaar, N. Afshordi, Echoes from the Abyss: Tentative evidence for Planck-scale structure at black hole horizons, *Phys. Rev. D* 96 (8) (2017) 082004. arXiv:1612.00266, doi:10.1103/PhysRevD.96.082004.
- [134] R. S. Conklin, B. Holdom, J. Ren, Gravitational wave echoes through new windows, *Phys. Rev. D* 98 (4) (2018) 044021. arXiv:1712.06517, doi:10.1103/PhysRevD.98.044021.
- [135] G. Ashton, O. Birnholtz, M. Cabero, C. Capano, T. Dent, B. Krishnan, G. D. Meadors, A. Nielsen, A. Nitz, J. Westerweck, Comments on: "Echoes from the abyss: Evidence for Planck-scale structure at black hole horizons" (2016). arXiv:1612.05625.
- [136] J. Westerweck, A. Nielsen, O. Fischer-Birnholtz, M. Cabero, C. Capano, T. Dent, B. Krishnan, G. Meadors, A. H. Nitz, Low significance of evidence for black hole echoes in gravitational wave data, *Phys. Rev. D* 97 (12) (2018) 124037. arXiv:1712.09966, doi:10.1103/PhysRevD.97.124037.
- [137] R. Penrose, R. M. Floyd, Extraction of Rotational Energy from a Black Hole, *Nature Physical Science* 229 (1971) 177–179. doi:10.1038/phyci229177a0.
- [138] Y. B. Zel'Dovich, , *Pis'ma Zh. Eksp. Teor. Fiz.* 14 (1971) 270, [*JETP Lett.* 14, 180 (1971)].
- [139] Y. B. Zel'Dovich, , *Zh. Eksp. Teor. Fiz* 62 (1972) 2076, [*Sov.Phys. JETP* 35, 1085 (1972)].
- [140] W. Baade, F. Zwicky, Remarks on Super-Novae and Cosmic Rays, *Phys. Rev.* 46 (1934) 76–77. doi:10.1103/PhysRev.46.76.2.
- [141] J. Chadwick, Possible Existence of a Neutron, *Nature* 129 (3252) (1932) 312. doi:10.1038/129312a0.
- [142] L. D. Landau, On the theory of stars, *Phys. Z. Sowjetunion* 1 (1932) 285.
- [143] W. Pauli, Über den Zusammenhang des Abschlusses der Elektronengruppen im Atom mit der Komplexstruktur der Spektren, *Zeitschrift für Physik* 31 (1) (1925) 765–783. doi:10.1007/BF02980631.
- [144] A. Hewish, S. J. Bell, J. D. H. Pilkington, P. F. Scott, R. A. Collins, Observation of a Rapidly Pulsating Radio Source, *Nature* 217 (1968) 709–713. doi:10.1038/217709a0.
- [145] R. Turolla, S. Zane, A. L. Watts, Magnetars: the physics behind observations. A review, *Reports on Progress in Physics* 78 (11) (2015) 116901. doi:10.1088/0034-4885/78/11/116901.
- [146] E. P. Mazets, S. V. Golenetskij, Y. A. Guryan, Soft gamma-ray bursts from the source B1900+ 14, *Soviet Astronomy Letters* 5 (1979) 641–643.
- [147] E. P. Mazets, S. V. Golenetskii, V. N. Il'Inskii, Y. A. Guryan, et al., Observations of a flaring X-ray pulsar in Dorado, *Nature* 282 (5739) (1979) 587.
- [148] R. C. Tolman, Effect of Inhomogeneity on Cosmological Models, *Proceedings of the National Academy of Sciences* 20 (3) (1934) 169–176. doi:10.1073/pnas.20.3.169.
- [149] R. C. Tolman, Static Solutions of Einstein's Field Equations for Spheres of Fluid, *Phys. Rev.* 55 (1939) 364–373. doi:10.1103/PhysRev.55.364.
- [150] J. R. Oppenheimer, G. M. Volkoff, On Massive Neutron Cores, *Phys. Rev.* 55 (1939) 374–381. doi:10.1103/PhysRev.55.374.
- [151] R. F. Tooper, Adiabatic Fluid Spheres in General Relativity., *ApJ* 142 (1965) 1541. doi:10.1086/148435.

- [152] S. Chandrasekhar, The Maximum Mass of Ideal White Dwarfs, *ApJ*74 (1931) 81. doi:10.1086/143324.
- [153] L. Rezzolla, E. R. Most, L. R. Weih, Using Gravitational-wave Observations and Quasi-universal Relations to Constrain the Maximum Mass of Neutron Stars, *ApJ* 852 (2) (2018) L25. doi:10.3847/2041-8213/aaa401.
- [154] G. D. Birkhoff, R. E. Langer, *Relativity and modern physics*, 1923.
- [155] H. A. Buchdahl, General Relativistic Fluid Spheres, *Phys. Rev.* 116 (1959) 1027–1034. doi:10.1103/PhysRev.116.1027.
- [156] J. A. Wheeler, Geons, *Phys. Rev.* 97 (1955) 511–536. doi:10.1103/PhysRev.97.511.
- [157] E. A. Power, J. A. Wheeler, Thermal Geons, *Rev. Mod. Phys.* 29 (1957) 480–495. doi:10.1103/RevModPhys.29.480.
- [158] D. J. Kaup, Klein-Gordon Geon, *Phys. Rev.* 172 (1968) 1331–1342. doi:10.1103/PhysRev.172.1331.
- [159] K. Schwarzschild, Über das Gravitationsfeld einer Kugel aus inkompressibler Flüssigkeit nach der Einsteinschen Theorie, in: *Sitzungsberichte der Königlich Preussischen Akademie der Wissenschaften zu Berlin, Phys.-Math. Klasse*, 424–434 (1916), 1916.
- [160] P. O. Mazur, E. Mottola, Gravitational Condensate Stars: An Alternative to Black Holes, *arXiv:gr-qc/0109035* (February 2002). *arXiv:gr-qc/0109035*.
- [161] P. O. Mazur, E. Mottola, Gravitational vacuum condensate stars, *Proceedings of the National Academy of Sciences* 101 (26) (2004) 9545–9550. doi:10.1073/pnas.0402717101.
- [162] M. Visser, D. L. Wiltshire, Stable gravastars – an alternative to black holes?, *Class. Quantum Grav.* 21 (2004) 1135–1151. *arXiv:gr-qc/0310107*, doi:10.1088/0264-9381/21/4/027.
- [163] C. B. M. H. Chirenti, L. Rezzolla, How to tell a gravastar from a black hole, *Class. Quantum Grav.* 24 (2007) 4191–4206. *arXiv:0706.1513*, doi:10.1088/0264-9381/24/16/013.
- [164] P. Pani, E. Berti, V. Cardoso, Y. Chen, R. Norte, Gravitational wave signatures of the absence of an event horizon: Nonradial oscillations of a thin-shell gravastar, *Phys. Rev. D*80 (12) (2009) 124047. *arXiv:0909.0287*, doi:10.1103/PhysRevD.80.124047.
- [165] P. Pani, E. Berti, V. Cardoso, Y. Chen, R. Norte, Gravitational-wave signature of a thin-shell gravastar, *Journal of Physics: Conference Series* 222 (1) (2010) 012032.
- [166] V. Cardoso, L. C. B. Crispino, C. F. B. Macedo, H. Okawa, P. Pani, Light rings as observational evidence for event horizons: Long-lived modes, ergoregions and nonlinear instabilities of ultracompact objects, *Phys. Rev. D*90 (4) (2014) 044069. *arXiv:1406.5510*, doi:10.1103/PhysRevD.90.044069.
- [167] C. Cattoen, T. Faber, M. Visser, Gravastars must have anisotropic pressures, *Class. Quantum Grav.* 22 (2005) 4189–4202. *arXiv:gr-qc/0505137*, doi:10.1088/0264-9381/22/20/002.
- [168] E. Mottola, R. Vaulin, Macroscopic effects of the quantum trace anomaly, *Phys. Rev. D* 74 (2006) 064004. doi:10.1103/PhysRevD.74.064004.
- [169] P. O. Mazur, E. Mottola, Surface tension and negative pressure interior of a non-singular ‘black hole’, *Class. Quantum Grav.* 32 (21) (2015) 215024. doi:10.1088/0264-9381/32/21/215024.
- [170] C. Posada, Slowly rotating supercompact Schwarzschild stars, *Mon. Not. Roy. Astron. Soc.* 468 (2) (2017) 2128–2139. *arXiv:1612.05290*, doi:10.1093/mnras/stx523.

- [171] C. Posada, C. Chirenti, On the radial stability of ultra compact Schwarzschild stars beyond the Buchdahl limit, *Class. Quantum Grav.* 36 (2019) 065004. [arXiv:1811.09589](https://arxiv.org/abs/1811.09589), [doi:10.1088/1361-6382/ab0526](https://doi.org/10.1088/1361-6382/ab0526).
- [172] R. A. Konoplya, C. Posada, Z. Stuchlik, A. Zhidenko, Stable Schwarzschild stars as black-hole mimickers (2019). [arXiv:1905.08097](https://arxiv.org/abs/1905.08097).
- [173] C. Chirenti, L. Rezzolla, Did GW150914 produce a rotating gravastar?, *Phys. Rev. D* 94 (8) (2016) 084016. [arXiv:1602.08759](https://arxiv.org/abs/1602.08759), [doi:10.1103/PhysRevD.94.084016](https://doi.org/10.1103/PhysRevD.94.084016).
- [174] L. Flamm, Beiträge zur Einsteinschen Gravitationstheorie, *Physikalische Zeitschrift XVII* (1916) 448–454.
- [175] H. Weyl, Feld und Materie, *Ann. Phys.* 370 (14) (1921) 541–563. [doi:10.1002/andp.19213701405](https://doi.org/10.1002/andp.19213701405).
- [176] A. Einstein, N. Rosen, The Particle Problem in the General Theory of Relativity, *Phys. Rev.* 48 (1935) 73–77. [doi:10.1103/PhysRev.48.73](https://doi.org/10.1103/PhysRev.48.73).
- [177] C. W. Misner, J. A. Wheeler, Classical physics as geometry, *Annals of Physics* 2 (6) (1957) 525 – 603. [doi:https://doi.org/10.1016/0003-4916\(57\)90049-0](https://doi.org/10.1016/0003-4916(57)90049-0).
- [178] R. W. Fuller, J. A. Wheeler, Causality and Multiply Connected Space-Time, *Phys. Rev.* 128 (1962) 919–929. [doi:10.1103/PhysRev.128.919](https://doi.org/10.1103/PhysRev.128.919).
- [179] H. G. Ellis, Ether flow through a drainhole: A particle model in general relativity, *J. Math. Phys.* 14 (1) (1973) 104–118. [doi:10.1063/1.1666161](https://doi.org/10.1063/1.1666161).
- [180] K. A. Bronnikov, Scalar-tensor theory and scalar charge, *Acta Phys. Polon.* B4 (1973) 251–266.
- [181] M. S. Morris, K. S. Thorne, U. Yurtsever, Wormholes, Time Machines, and the Weak Energy Condition, *Phys. Rev. Lett.* 61 (1988) 1446–1449. [doi:10.1103/PhysRevLett.61.1446](https://doi.org/10.1103/PhysRevLett.61.1446).
- [182] T. Damour, S. N. Solodukhin, Wormholes as black hole foils, *Phys. Rev. D* 76 (2007) 024016. [arXiv:0704.2667](https://arxiv.org/abs/0704.2667), [doi:10.1103/PhysRevD.76.024016](https://doi.org/10.1103/PhysRevD.76.024016).
- [183] S. D. Mathur, The Fuzzball proposal for black holes: An Elementary review, *Fortsch. Phys.* 53 (2005) 793–827. [arXiv:hep-th/0502050](https://arxiv.org/abs/hep-th/0502050), [doi:10.1002/prop.200410203](https://doi.org/10.1002/prop.200410203).
- [184] J. D. Bekenstein, The quantum mass spectrum of the Kerr black hole, *Lett. Nuovo Cim.* 11 (1974) 467. [doi:10.1007/BF02762768](https://doi.org/10.1007/BF02762768).
- [185] V. F. Mukhanov, ARE BLACK HOLES QUANTIZED?, *JETP Lett.* 44 (1986) 63–66, [*Pisma Zh. Eksp. Teor. Fiz.*44,50(1986)].
- [186] J. D. Bekenstein, V. F. Mukhanov, Spectroscopy of the quantum black hole, *Phys. Lett.* B360 (1995) 7–12. [arXiv:gr-qc/9505012](https://arxiv.org/abs/gr-qc/9505012), [doi:10.1016/0370-2693\(95\)01148-J](https://doi.org/10.1016/0370-2693(95)01148-J).
- [187] S. Hod, Bohr’s correspondence principle and the area spectrum of quantum black holes, *Phys. Rev. Lett.* 81 (1998) 4293. [arXiv:gr-qc/9812002](https://arxiv.org/abs/gr-qc/9812002), [doi:10.1103/PhysRevLett.81.4293](https://doi.org/10.1103/PhysRevLett.81.4293).
- [188] O. Dreyer, Quasinormal modes, the area spectrum, and black hole entropy, *Phys. Rev. Lett.* 90 (2003) 081301. [arXiv:gr-qc/0211076](https://arxiv.org/abs/gr-qc/0211076), [doi:10.1103/PhysRevLett.90.081301](https://doi.org/10.1103/PhysRevLett.90.081301).
- [189] M. Maggiore, The Physical interpretation of the spectrum of black hole quasinormal modes, *Phys. Rev. Lett.* 100 (2008) 141301. [arXiv:0711.3145](https://arxiv.org/abs/0711.3145), [doi:10.1103/PhysRevLett.100.141301](https://doi.org/10.1103/PhysRevLett.100.141301).
- [190] J. Louko, J. Makela, Area spectrum of the Schwarzschild black hole, *Phys. Rev. D* 54 (1996) 4982–4996. [arXiv:gr-qc/9605058](https://arxiv.org/abs/gr-qc/9605058), [doi:10.1103/PhysRevD.54.4982](https://doi.org/10.1103/PhysRevD.54.4982).

- [191] V. F. Foit, M. Kleban, Testing Quantum Black Holes with Gravitational Waves, *Class. Quantum Grav.* 36 (3) (2019) 035006. arXiv:1611.07009, doi:10.1088/1361-6382/aafcba.
- [192] V. Cardoso, V. F. Foit, M. Kleban, Gravitational wave echoes from black hole area quantization (2019). arXiv:1902.10164.
- [193] Y. Mizuno, Z. Younsi, C. M. Fromm, O. Porth, M. De Laurentis, H. Olivares, H. Falcke, M. Kramer, L. Rezzolla, The Current Ability to Test Theories of Gravity with Black Hole Shadows, *Nat. Astron.* 2 (7) (2018) 585–590. arXiv:1804.05812, doi:10.1038/s41550-018-0449-5.
- [194] C. Bambi, A. Cárdenas-Avenda no, T. Dauser, J. A. García, S. Nampalliwar, Testing the Kerr Black Hole Hypothesis Using X-Ray Reflection Spectroscopy, *ApJ* 842 (2) (2017) 76. doi:10.3847/1538-4357/aa74c0.
- [195] S. Nampalliwar, S. Xin, S. Srivastava, A. B. Abdikamalov, D. Ayzenberg, C. Bambi, T. Dauser, J. A. Garcia, A. Tripathi, Testing General Relativity with X-ray reflection spectroscopy: The Konoplya-Rezzolla-Zhidenko parametrization, arXiv e-prints (2019) arXiv:1903.12119 arXiv:1903.12119.
- [196] T. Johannsen, D. Psaltis, A Metric for Rapidly Spinning Black Holes Suitable for Strong-Field Tests of the No-Hair Theorem, *Phys. Rev. D* 83 (2011) 124015. arXiv:1105.3191, doi:10.1103/PhysRevD.83.124015.
- [197] S. Vigeland, N. Yunes, L. C. Stein, Bumpy black holes in alternative theories of gravity, *Phys. Rev. D* 83 (2011) 104027. doi:10.1103/PhysRevD.83.104027.
- [198] L. Rezzolla, A. Zhidenko, New parametrization for spherically symmetric black holes in metric theories of gravity, *Phys. Rev. D* 90 (2014) 084009. doi:10.1103/PhysRevD.90.084009.
- [199] R. Konoplya, L. Rezzolla, A. Zhidenko, General parametrization of axisymmetric black holes in metric theories of gravity, *Phys. Rev. D* 93 (6) (2016) 064015. arXiv:1602.02378, doi:10.1103/PhysRevD.93.064015.
- [200] G. O. Papadopoulos, K. D. Kokkotas, Preserving Kerr symmetries in deformed spacetimes, *Class. Quantum Grav.* 35 (18) (2018) 185014. arXiv:1807.08594, doi:10.1088/1361-6382/aad7f4.
- [201] R. A. Konoplya, A. Zhidenko, Quasinormal modes of black holes: From astrophysics to string theory, *Rev. Mod. Phys.* 83 (2011) 793–836. arXiv:1102.4014, doi:10.1103/RevModPhys.83.793.
- [202] S. A. Teukolsky, Perturbations of a rotating black hole. 1. Fundamental equations for gravitational electromagnetic and neutrino field perturbations, *Astrophys. J.* 185 (1973) 635–647. doi:10.1086/152444.
- [203] C. V. Vishveshwara, Stability of the schwarzschild metric, *Phys. Rev. D* 1 (1970) 2870–2879. doi:10.1103/PhysRevD.1.2870.
- [204] W. H. Press, Long Wave Trains of Gravitational Waves from a Vibrating Black Hole, *ApJ* 170 (1971) L105. doi:10.1086/180849.
- [205] M. Davis, R. Ruffini, W. H. Press, R. H. Price, Gravitational Radiation from a Particle Falling Radially into a Schwarzschild Black Hole, *Phys. Rev. Lett.* 27 (1971) 1466–1469. doi:10.1103/PhysRevLett.27.1466.
- [206] S. Detweiler, S. Chandrasekhar, On resonant oscillations of a rapidly rotating black hole, *Proceedings of the Royal Society of London. A. Mathematical and Physical Sciences* 352 (1670) (1977) 381–395. doi:10.1098/rspa.1977.0005.
- [207] S. L. Detweiler, E. Szedenits, Jr., Black holes and gravitational waves. II - Trajectories plunging into a nonrotating hole, *ApJ* 231 (1979) 211–218. doi:10.1086/157182.

- [208] S. Chandrasekhar, S. Detweiler, The quasi-normal modes of the Schwarzschild black hole, Proceedings of the Royal Society of London Series A 344 (1975) 441–452. doi : 10 . 1098/rspa . 1975 . 0112.
- [209] B. Mashhoon, Quasi-normal modes of a black hole., in: H. Ning (Ed.), Third Marcel Grossmann Meeting on General Relativity, 1983, pp. 599–608.
- [210] H.-J. Blome, B. Mashhoon, Quasi-normal oscillations of a schwarzschild black hole, Phys. Lett. A 100 (1984) 231–234. doi : 10 . 1016/0375-9601(84)90769-2.
- [211] V. Ferrari, B. Mashhoon, Oscillations of a black hole, Phys. Rev. Lett. 52 (1984) 1361–1364. doi : 10 . 1103/PhysRevLett . 52 . 1361.
- [212] V. Ferrari, B. Mashhoon, New approach to the quasinormal modes of a black hole, Phys. Rev. D30 (1984) 295–304. doi : 10 . 1103/PhysRevD . 30 . 295.
- [213] B. F. Schutz, C. M. Will, Black hole normal modes - A semianalytic approach, ApJ291 (1985) L33–L36. doi : 10 . 1086/184453.
- [214] S. Iyer, C. M. Will, Black-hole normal modes: A WKB approach. I. Foundations and application of a higher-order WKB analysis of potential-barrier scattering, Phys. Rev. D35 (1987) 3621–3631. doi : 10 . 1103/PhysRevD . 35 . 3621.
- [215] S. Iyer, Black-hole normal modes: A WKB approach. II. Schwarzschild black holes, Phys. Rev. D 35 (1987) 3632–3636. doi : 10 . 1103/PhysRevD . 35 . 3632.
- [216] K. D. Kokkotas, B. F. Schutz, Black-hole normal modes: A WKB approach. III. The Reissner-Nordström black hole, Phys. Rev. D 37 (1988) 3378–3387. doi : 10 . 1103/PhysRevD . 37 . 3378.
- [217] E. Seidel, S. Iyer, Black-hole normal modes: A WKB approach. IV. Kerr black holes, Phys. Rev. D 41 (1990) 374–382. doi : 10 . 1103/PhysRevD . 41 . 374.
- [218] R. A. Konoplya, Quasinormal behavior of the D -dimensional Schwarzschild black hole and the higher order WKB approach, Phys. Rev. D 68 (2003) 024018. doi : 10 . 1103/PhysRevD . 68 . 024018.
- [219] J. L. Dunham, The Wentzel-Brillouin-Kramers Method of Solving the Wave Equation, Phys. Rev. 41 (1932) 713–720. doi : 10 . 1103/PhysRev . 41 . 713.
- [220] K. D. Kokkotas, Normal modes of the Kerr black hole, Class. Quantum Grav. 8 (12) (1991) 2217–2224. doi : 10 . 1088/0264-9381/8/12/006.
- [221] E. W. Leaver, An analytic representation for the quasi-normal modes of Kerr black holes, Proceedings of the Royal Society of London Series A 402 (1985) 285–298. doi : 10 . 1098/rspa . 1985 . 0119.
- [222] R. Price, K. S. Thorne, Non-Radial Pulsation of General-Relativistic Stellar Models. II. Properties of the Gravitational Waves, ApJ155 (1969) 163. doi : 10 . 1086/149857.
- [223] K. S. Thorne, Nonradial Pulsation of General-Relativistic Stellar Models. III. Analytic and Numerical Results for Neutron Stars, ApJ158 (1969) 1. doi : 10 . 1086/150168.
- [224] K. S. Thorne, Nonradial Pulsation of General-Relativistic Stellar Models.IV. The Weakfield Limit, ApJ158 (1969) 997. doi : 10 . 1086/150259.
- [225] A. Campolattaro, K. S. Thorne, Nonradial Pulsation of General-Relativistic Stellar Models. V. Analytic Analysis for $L = 1$, ApJ159 (1970) 847. doi : 10 . 1086/150362.
- [226] J. R. Ipser, K. S. Thorne, Nonradial Pulsation of General-Relativistic Stellar Models.VI. Corrections, ApJ181 (1973) 181–182. doi : 10 . 1086/152040.

- [227] L. Lindblom, S. L. Detweiler, The quadrupole oscillations of neutron stars, *ApJS*53 (1983) 73–92. doi : 10.1086/190884.
- [228] C. Cutler, L. Lindblom, The Effect of Viscosity on Neutron Star Oscillations, *ApJ*314 (1987) 234. doi : 10.1086/165052.
- [229] K. D. Kokkotas, B. F. Schutz, Normal modes of a model radiating system, *General Relativity and Gravitation* 18 (1986) 913–921. doi : 10.1007/BF00773556.
- [230] Y. Kojima, Two Families of Normal Modes in Relativistic Stars, *Progress of Theoretical Physics* 79 (3) (1988) 665–675. doi : 10.1143/PTP.79.665.
- [231] S. Chandrasekhar, V. Ferrari, On the non-radial oscillations of a star. III - A reconsideration of the axial modes, *Proceedings of the Royal Society of London Series A* 434 (1991) 449–457. doi : 10.1098/rspa.1991.0104.
- [232] K. D. Kokkotas, B. F. Schutz, W-modes - A new family of normal modes of pulsating relativistic stars, *MNRAS*255 (1992) 119–128. doi : 10.1093/mnras/255.1.119.
- [233] K. D. Kokkotas, Axial Modes for Relativistic Stars, *Mon. Not. R. Astron. Soc.* 268 (1994) 1015. doi : 10.1093/mnras/268.4.1015.
- [234] M. Leins, H.-P. Nollert, M. H. Soffel, Nonradial oscillations of neutron stars: A new branch of strongly damped normal modes, *Phys. Rev. D*48 (1993) 3467–3472. doi : 10.1103/PhysRevD.48.3467.
- [235] N. Andersson, Y. Kojima, K. D. Kokkotas, On the Oscillation Spectra of Ultracompact Stars: an Extensive Survey of Gravitational-Wave Modes, *ApJ*462 (1996) 855. arXiv:gr-qc/9512048, doi : 10.1086/177199.
- [236] K. D. Kokkotas, Pulsating relativistic stars, in: *Relativistic gravitation and gravitational radiation. Proceedings, School of Physics, Les Houches, France, September 26-October 6, 1995*, 1995, pp. 89–102. arXiv:gr-qc/9603024.
- [237] K. Tominaga, M. Saijo, K. Maeda, Gravitational waves from a test particle scattered by a neutron star: Axial mode case, *Phys. Rev. D* 60 (1999) 024004. doi : 10.1103/PhysRevD.60.024004.
- [238] V. Ferrari, K. D. Kokkotas, Scattering of particles by neutron stars: Time evolutions for axial perturbations, *Phys. Rev. D*62 (10) (2000) 107504. arXiv:gr-qc/0008057, doi : 10.1103/PhysRevD.62.107504.
- [239] N. Andersson, K. D. Kokkotas, Gravitational Waves and Pulsating Stars: What Can We Learn from Future Observations?, *Phys. Rev. Lett.* 77 (1996) 4134–4137. arXiv:gr-qc/9610035, doi : 10.1103/PhysRevLett.77.4134.
- [240] O. Benhar, E. Berti, V. Ferrari, The imprint of the equation of state on the axial w-modes of oscillating neutron stars, *MNRAS*310 (1999) 797–803. arXiv:gr-qc/9901037, doi : 10.1046/j.1365-8711.1999.02983.x.
- [241] L. Lindblom, Determining the nuclear equation of state from neutron-star masses and radii, *ApJ*398 (1992) 569–573. doi : 10.1086/171882.
- [242] J. B. Hartle, Slowly Rotating Relativistic Stars. I. Equations of Structure, *ApJ*150 (1967) 1005. doi : 10.1086/149400.
- [243] J. B. Hartle, K. S. Thorne, Slowly Rotating Relativistic Stars. II. Models for Neutron Stars and Supermassive Stars, *ApJ*153 (1968) 807. doi : 10.1086/149707.

- [244] N. Andersson, A New class of unstable modes of rotating relativistic stars, *Astrophys. J.* 502 (1998) 708–713. arXiv:gr-qc/9706075, doi:10.1086/305919.
- [245] J. L. Friedman, S. M. Morsink, Axial instability of rotating relativistic stars, *Astrophys. J.* 502 (1998) 714–720. arXiv:gr-qc/9706073, doi:10.1086/305920.
- [246] S. Chandrasekhar, Solutions of Two Problems in the Theory of Gravitational Radiation, *Phys. Rev. Lett.* 24 (1970) 611–615. doi:10.1103/PhysRevLett.24.611.
- [247] J. L. Friedman, B. F. Schutz, Secular instability of rotating Newtonian stars, *ApJ*222 (1978) 281–296. doi:10.1086/156143.
- [248] N. Stergioulas, Rotating Stars in Relativity, *Living Rev. Rel.* 6 (2003) 3. arXiv:gr-qc/0302034, doi:10.12942/lrr-2003-3.
- [249] V. Paschalidis, N. Stergioulas, Rotating Stars in Relativity, *Living Rev. Rel.* 20 (1) (2017) 7. arXiv:1612.03050, doi:10.1007/s41114-017-0008-x.
- [250] M. Maggiore, *Gravitational Waves. Vol. 2: Astrophysics and Cosmology*, Oxford University Press, 2018.
- [251] T. G. Cowling, The non-radial oscillations of polytropic stars, *MNRAS*101 (1941) 367. doi:10.1093/mnras/101.8.367.
- [252] P. N. McDermott, H. M. van Horn, J. F. Scholl, Nonradial g-mode oscillations of warm neutron stars, *ApJ*268 (1983) 837–848. doi:10.1086/161006.
- [253] N. Andersson, K. D. Kokkotas, B. F. Schutz, Space-time modes of relativistic stars, *MNRAS*280 (4) (1996) 1230–1234. arXiv:gr-qc/9601015, doi:10.1093/mnras/280.4.1230.
- [254] N. Andersson, K. D. Kokkotas, B. F. Schutz, A new numerical approach to the oscillation modes of relativistic stars, *MNRAS*274 (1995) 1039–1048. arXiv:gr-qc/9503014, doi:10.1093/mnras/274.4.1039.
- [255] V. Pavlidou, K. Tassis, T. W. Baumgarte, S. L. Shapiro, Radiative falloff in neutron star spacetimes, *Phys. Rev. D*62 (8) (2000) 084020. arXiv:gr-qc/0007019, doi:10.1103/PhysRevD.62.084020.
- [256] A. DeBenedictis, D. Horvat, S. Ilijic, S. Kloster, K. S. Viswanathan, Gravastar solutions with continuous pressures and equation of state, *Class. Quantum Grav.* 23 (2006) 2303–2316. arXiv:gr-qc/0511097, doi:10.1088/0264-9381/23/7/007.
- [257] P. Bueno, P. A. Cano, F. Goelen, T. Hertog, B. Vercoocke, Echoes of Kerr-like wormholes, *Phys. Rev. D*97 (2) (2018) 024040. arXiv:1711.00391, doi:10.1103/PhysRevD.97.024040.
- [258] K. Glampedakis, A. D. Johnson, D. Kennefick, Darboux transformation in black hole perturbation theory, *Phys. Rev. D* 96 (2017) 024036. doi:10.1103/PhysRevD.96.024036.
- [259] S. Chandrasekhar, On algebraically special perturbations of black holes, *Proceedings of the Royal Society of London Series A* 392 (1984) 1–13. doi:10.1098/rspa.1984.0021.
- [260] J. Matyjasek, M. Opala, Quasinormal modes of black holes: The improved semianalytic approach, *Phys. Rev. D* 96 (2017) 024011. doi:10.1103/PhysRevD.96.024011.
- [261] H.-P. Nollert, Quasinormal modes of Schwarzschild black holes: The determination of quasinormal frequencies with very large imaginary parts, *Phys. Rev. D* 47 (1993) 5253–5258. doi:10.1103/PhysRevD.47.5253.

- [262] Y. J. Zhang, J. Wu, P. T. Leung, High-frequency behavior of w -mode pulsations of compact stars, *Phys. Rev. D* 83 (2011) 064012. doi : 10 . 1103/PhysRevD . 83 . 064012.
- [263] V. Cardoso, E. Franzin, P. Pani, Is the gravitational-wave ringdown a probe of the event horizon?, *Phys. Rev. Lett.* 116 (17) (2016) 171101, [Erratum: *Phys. Rev. Lett.*117,no.8,089902(2016)]. arXiv : 1602 . 07309, doi : 10 . 1103/PhysRevLett . 117 . 089902 , 10 . 1103/PhysRevLett . 116 . 171101.
- [264] V. Cardoso, S. Hopper, C. F. B. Macedo, C. Palenzuela, P. Pani, Gravitational-wave signatures of exotic compact objects and of quantum corrections at the horizon scale, *Phys. Rev. D* 94 (8) (2016) 084031. arXiv : 1608 . 08637, doi : 10 . 1103/PhysRevD . 94 . 084031.
- [265] A. B. Nielsen, C. D. Capano, O. Birnholtz, J. Westerweck, Parameter estimation and statistical significance of echoes following black hole signals in the first Advanced LIGO observing run, *Phys. Rev. D* 99 (2019) 104012. doi : 10 . 1103/PhysRevD . 99 . 104012.
- [266] J. Liouville, Sur le développement des fonctions et séries, *Journal de Mathématiques Pures et Appliquées* 1 (1837) 16–35.
- [267] G. Green, On the motion of waves in a variable canal of small depth and width, *Transactions of the Cambridge Philosophical Society* 6 (1837) 457–462.
- [268] H. Jeffreys, On Certain Approximate Solutions of Lineae Differential Equations of the Second Order, *Proceedings of the London Mathematical Society* 23 (1925) 428–436. doi : 10 . 1112/plms/s2 - 23 . 1 . 428.
- [269] G. Wentzel, Eine Verallgemeinerung der Quantenbedingungen für die Zwecke der Wellenmechanik, *Zeitschrift für Physik* 38 (6) (1926) 518–529. doi : 10 . 1007/BF01397171.
- [270] H. A. Kramers, Wellenmechanik und halbzahlige Quantisierung, *Zeitschrift für Physik* 39 (1926) 828–840.
- [271] L. Brillouin, La mécanique ondulatoire de Schrödinger une méthode générale de résolution par approximations successives, *Comptes Rendus* 183 (1926) 24–26.
- [272] L. Brillouin, Remarques sur la mécanique ondulatoire, *J. de Physique* 7 (1926) 353–368.
- [273] C. M. Bender, S. A. Orszag, *Advanced Mathematical Methods for Scientists and Engineers*, New York: McGraw-Hill, 1978.
- [274] J. A. Wheeler, *Studies in Mathematical Physics: Essays in Honor of Valentine Bargmann*, Princeton Series in Physics, Princeton University Press, 2015.
- [275] M. W. Cole, R. H. Good, Determination of the shape of a potential barrier from the tunneling transmission coefficient, *Phys. Rev. A* 18 (1978) 1085–1088. doi : 10 . 1103/PhysRevA . 18 . 1085.
- [276] D. Bonatsos, C. Daskaloyannis, K. Kokkotas, WKB equivalent potentials for the q -deformed harmonic oscillator, *Journal of Physics A Mathematical General* 24 (1991) L795–L801. doi : 10 . 1088/0305 - 4470/24/15/002.
- [277] D. Bonatsos, C. Daskaloyannis, K. Kokkotas, Classical potentials for q -deformed anharmonic oscillators, *Phys. Rev. A* 45 (1992) R6153–R6156. doi : 10 . 1103/PhysRevA . 45 . R6153.
- [278] D. Bonatsos, C. Daskaloyannis, K. Kokkotas, WKB equivalent potentials for q -deformed anharmonic oscillators, *Chem. Phys. Lett.* 193 (1992) 191–196. doi : 10 . 1016/0009 - 2614(92)85707 - H.
- [279] D. Bonatsos, C. Daskaloyannis, K. Kokkotas, WKB equivalent potentials for q -deformed harmonic and anharmonic oscillators, *J. Math. Phys.* 33 (1992) 2958–2965. doi : 10 . 1063/1 . 529565.

- [280] B. M. Karnakov, V. P. Krainov, *WKB Approximation in Atomic Physics*, Springer-Verlag Berlin Heidelberg, 2013. doi : 10 . 1007/978-3-642-31558-9.
- [281] N. Fröman, P. O. Fröman, *Physical Problems Solved by the Phase-Integral Method*, Cambridge University Press, 2002. doi : 10 . 1017/CBO9780511535086.
- [282] V. S. Popov, V. D. Mur, A. V. Sergeev, Quantization rules for quasistationary states, *Phys. Lett. A* 157 (1991) 185–191. doi : 10 . 1016/0375-9601(91)90048-D.
- [283] G. Gamow, Zur Quantentheorie des Atomkernes, *Zeitschrift für Physik* 51 (3) (1928) 204–212. doi : 10 . 1007/BF01343196.
- [284] K. Chadan, P. C. Sabatier, *Inverse problems in quantum scattering theory*, 2nd Edition, Texts and Monographs in Physics, Springer-Verlag, New York, 1989. doi : 10 . 1007/978-3-642-83317-5.
- [285] J. C. Lazenby, D. J. Griffiths, Classical inverse scattering in one dimension, *AJP* 48 (1980) 432–436. doi : 10 . 1119/1 . 11998.
- [286] S. C. Gandhi, C. J. Efthimiou, Inversion of Gamow’s formula and inverse scattering, *AJP* 74 (2006) 638–643. arXiv:quant-ph/0503223, doi : 10 . 1119/1 . 2190683.
- [287] G. Pei, C. Bambi, Scattering of particles by deformed non-rotating black holes, *The European Physical Journal C* 75 (11) (2015) 560. doi : 10 . 1140/epjc/s10052-015-3799-5.
- [288] Y. Kojima, N. Andersson, K. D. Kokkotas, On the Oscillation Spectra of Ultra Compact Stars, *Proceedings of the Royal Society of London Series A* 451 (1995) 341–348. arXiv:gr-qc/9503012, doi : 10 . 1098/rspa . 1995 . 0129.
- [289] R. A. Konoplya, C. Molina, The Ringing wormholes, *Phys. Rev. D* 71 (2005) 124009. arXiv:gr-qc/0504139, doi : 10 . 1103/PhysRevD . 71 . 124009.
- [290] J. Skakala, M. Visser, Quasi-normal frequencies: Semi-analytic results for highly damped modes, *Journal of Physics: Conference Series* 314 (1) (2011) 012074. arXiv : 1011 . 4634.
- [291] R. H. Price, G. Khanna, Gravitational wave sources: reflections and echoes, *Class. Quantum Grav.* 34 (22) (2017) 225005. arXiv : 1702 . 04833, doi : 10 . 1088/1361-6382/aa8f29.
- [292] A. F. Cardona, C. Molina, Quasinormal modes of generalized Pöschl–Teller potentials, *Class. Quantum Grav.* 34 (24) (2017) 245002. arXiv : 1711 . 00479, doi : 10 . 1088/1361-6382/aa9428.
- [293] N. R. Khusnutdinov, I. V. Bakhmatov, Self-action of a point charge in a wormhole space-time, *Phys. Rev. D* 76 (2007) 124015. doi : 10 . 1103/PhysRevD . 76 . 124015.
- [294] R. A. Konoplya, A. Zhidenko, Wormholes versus black holes: quasinormal ringing at early and late times, *JCAP* 1612 (12) (2016) 043. arXiv : 1606 . 00517, doi : 10 . 1088/1475-7516/2016/12/043.
- [295] K. K. Nandi, R. N. Izmailov, A. A. Yanbekov, A. A. Shayakhmetov, Ring-down gravitational waves and lensing observables: How far can a wormhole mimic those of a black hole?, *Phys. Rev. D* 95 (2017) 104011. arXiv : 1611 . 03479, doi : 10 . 1103/PhysRevD . 95 . 104011.
- [296] V. Cardoso, P. Pani, Tests for the existence of black holes through gravitational wave echoes, *Nat. Astron.* 1 (9) (2017) 586–591. arXiv : 1709 . 01525, doi : 10 . 1038/s41550-017-0225-y.
- [297] B. P. Abbott, et al., GW170104: Observation of a 50-Solar-Mass Binary Black Hole Coalescence at Redshift 0.2, *Phys. Rev. Lett.* 118 (2017) 221101. doi : 10 . 1103/PhysRevLett . 118 . 221101.
- [298] H.-P. Nollert, About the significance of quasinormal modes of black holes, *Phys. Rev. D* 53 (1996) 4397–4402. arXiv:gr-qc/9602032, doi : 10 . 1103/PhysRevD . 53 . 4397.

- [299] J. L. Blázquez-Salcedo, L. M. Gonzalez-Romero, F. Navarro-Lerida, Phenomenological relations for axial quasinormal modes of neutron stars with realistic equations of state, *Phys. Rev. D* 87 (10) (2013) 104042. [arXiv:1207.4651](#), [doi:10.1103/PhysRevD.87.104042](#).
- [300] J. L. Blázquez-Salcedo, D. D. Doneva, J. Kunz, K. V. Staykov, S. S. Yazadjiev, Axial quasinormal modes of neutron stars in R^2 gravity, *Phys. Rev. D* 98 (10) (2018) 104047. [arXiv:1804.04060](#), [doi:10.1103/PhysRevD.98.104047](#).
- [301] A. G. Suvorov, Astroseismology of neutron stars from gravitational waves in the limit of perfect measurement, *Mon. Not. Roy. Astron. Soc.* 478 (1) (2018) 167–171. [arXiv:1804.09413](#), [doi:10.1093/mnras/sty1080](#).
- [302] H.-P. Nollert, R. H. Price, Quantifying excitations of quasinormal mode systems, *J. Math. Phys.* 40 (1999) 980–1010. [arXiv:gr-qc/9810074](#), [doi:10.1063/1.532698](#).
- [303] E. Barausse, V. Cardoso, P. Pani, Can environmental effects spoil precision gravitational-wave astrophysics?, *Phys. Rev. D* 89 (10) (2014) 104059. [arXiv:1404.7149](#), [doi:10.1103/PhysRevD.89.104059](#).
- [304] R. A. Konoplya, Z. Stuchlík, A. Zhidenko, Echoes of compact objects: new physics near the surface and matter at a distance, *Phys. Rev. D* 99 (2) (2019) 024007. [arXiv:1810.01295](#), [doi:10.1103/PhysRevD.99.024007](#).
- [305] B. P. Abbott, et al., Tests of General Relativity with GW150914, *Phys. Rev. Lett.* 116 (2016) 221101. [doi:10.1103/PhysRevLett.116.221101](#).
- [306] T. P. Sotiriou, Black holes and scalar fields, *Class. Quantum Grav.* 32 (21) (2015) 214002. [doi:10.1088/0264-9381/32/21/214002](#).
- [307] A. G. Suvorov, Gravitational perturbations of a Kerr black hole in $f(R)$ gravity, *Phys. Rev. D* 99 (12) (2019) 124026. [arXiv:1905.02021](#), [doi:10.1103/PhysRevD.99.124026](#).
- [308] K. Kokkotas, R. A. Konoplya, A. Zhidenko, Non-Schwarzschild black-hole metric in four dimensional higher derivative gravity: analytical approximation, *Phys. Rev. D* 96 (6) (2017) 064007. [arXiv:1705.09875](#), [doi:10.1103/PhysRevD.96.064007](#).
- [309] O. Dreyer, B. Kelly, B. Krishnan, L. S. Finn, D. Garrison, R. Lopez-Aleman, Black-hole spectroscopy: testing general relativity through gravitational-wave observations, *Class. Quantum Grav.* 21 (4) (2004) 787–803. [doi:10.1088/0264-9381/21/4/003](#).
- [310] G. Pei, C. Bambi, Scattering of particles by deformed non-rotating black holes, *Eur. Phys. J. C* 75 (11) (2015) 560. [arXiv:1508.00344](#), [doi:10.1140/epjc/s10052-015-3799-5](#).
- [311] V. Cardoso, M. Kimura, A. Maselli, E. Berti, C. F. B. Macedo, R. McManus, Parametrized black hole quasinormal ringdown: Decoupled equations for nonrotating black holes, *Phys. Rev. D* 99 (2019) 104077. [doi:10.1103/PhysRevD.99.104077](#).
- [312] R. McManus, E. Berti, C. F. B. Macedo, M. Kimura, A. Maselli, V. Cardoso, Parametrized black hole quasinormal ringdown. II. Coupled equations and quadratic corrections for nonrotating black holes (2019). [arXiv:1906.05155](#).
- [313] K. Glampedakis, G. Pappas, H. O. Silva, E. Berti, Post-Kerr black hole spectroscopy, *Phys. Rev. D* 96 (2017) 064054. [doi:10.1103/PhysRevD.96.064054](#).
- [314] K. Glampedakis, H. O. Silva, Eikonal quasinormal modes of black holes beyond General Relativity (2019). [arXiv:1906.05455](#).

- [315] A. Maselli, K. Kokkotas, P. Laguna, Observing binary black hole ringdowns by advanced gravitational wave detectors, *Phys. Rev. D* 95 (10) (2017) 104026. [arXiv:1702.01110](#), [doi:10.1103/PhysRevD.95.104026](#).
- [316] V. Baibhav, E. Berti, Multimode black hole spectroscopy, *Phys. Rev. D* 99 (2) (2019) 024005. [arXiv:1809.03500](#), [doi:10.1103/PhysRevD.99.024005](#).
- [317] M. Breschi, R. O'Shaughnessy, J. Lange, O. Birnholtz, Inspiral-Merger-Ringdown Consistency Tests with Higher Modes on Gravitational Signals from the Second Observing Run of LIGO and Virgo (2019). [arXiv:1903.05982](#).
- [318] M. Giesler, M. Isi, M. Scheel, S. Teukolsky, Black hole ringdown: the importance of overtones (2019). [arXiv:1903.08284](#).
- [319] R. Konoplya, How to tell the shape of a wormhole by its quasinormal modes, *Phys. Lett. B* 784 (2018) 43 – 49. [doi:https://doi.org/10.1016/j.physletb.2018.07.025](#).
- [320] G. Carullo, W. Del Pozzo, J. Veitch, Observational Black Hole Spectroscopy: A time-domain multimode analysis of GW150914, *Phys. Rev. D* 99 (12) (2019) 123029. [arXiv:1902.07527](#), [doi:10.1103/PhysRevD.99.123029](#).
- [321] V. Cardoso, E. Franzin, A. Maselli, P. Pani, G. Raposo, Testing strong-field gravity with tidal Love numbers, *Phys. Rev. D* 95 (8) (2017) 084014, [Addendum: *Phys. Rev. D* 95, no. 8, 089901 (2017)]. [arXiv:1701.01116](#), [doi:10.1103/PhysRevD.95.089901](#), [doi:10.1103/PhysRevD.95.084014](#).
- [322] A. Maselli, P. Pani, V. Cardoso, T. Abdelsalhin, L. Gualtieri, V. Ferrari, Probing Planckian corrections at the horizon scale with LISA binaries, *Phys. Rev. Lett.* 120 (8) (2018) 081101. [arXiv:1703.10612](#), [doi:10.1103/PhysRevLett.120.081101](#).
- [323] H. Nakano, N. Sago, H. Tagoshi, T. Tanaka, Black hole ringdown echoes and howls, *PTEP* 2017 (7) (2017) 071E01. [arXiv:1704.07175](#), [doi:10.1093/ptep/ptx093](#).
- [324] Z. Mark, A. Zimmerman, S. M. Du, Y. Chen, A recipe for echoes from exotic compact objects, *Phys. Rev. D* 96 (8) (2017) 084002. [arXiv:1706.06155](#), [doi:10.1103/PhysRevD.96.084002](#).
- [325] A. Królak, J. A. Lobo, B. J. Meers, Estimation of the parameters of the gravitational-wave signal of a coalescing binary system, *Phys. Rev. D* 48 (1993) 3451–3462. [doi:10.1103/PhysRevD.48.3451](#).
- [326] K. Kokkotas, A. Królak, G. Tsegas, Statistical analysis of the estimators of the parameters of the gravitational-wave signal from a coalescing binary, *Class. Quantum Grav.* 11 (1994) 1901–1918. [doi:10.1088/0264-9381/11/7/023](#).
- [327] M. Vallisneri, Use and abuse of the Fisher information matrix in the assessment of gravitational-wave parameter-estimation prospects, *Phys. Rev. D* 77 (2008) 042001. [arXiv:gr-qc/0703086](#), [doi:10.1103/PhysRevD.77.042001](#).
- [328] <https://dcc.ligo.org/cgi-bin/DocDB/ShowDocument?docid=2974>.
- [329] S. Hild, S. Chelkowski, A. Freise, J. Franc, N. Morgado, R. Flaminio, R. DeSalvo, A Xylophone Configuration for a third Generation Gravitational Wave Detector, *Class. Quantum Grav.* 27 (2010) 015003. [arXiv:0906.2655](#), [doi:10.1088/0264-9381/27/1/015003](#).
- [330] <https://dcc.ligo.org/public/0120/T1500290/002/T1500290.pdf>.

- [331] J. Miller, L. Barsotti, S. Vitale, P. Fritschel, M. Evans, D. Sigg, Prospects for doubling the range of Advanced LIGO, *Phys. Rev. D* 91 (2015) 062005. [arXiv:1410.5882](#), [doi:10.1103/PhysRevD.91.062005](#).
- [332] B. P. Abbott, et al., Exploring the Sensitivity of Next Generation Gravitational Wave Detectors, *Class. Quantum Grav.* 34 (4) (2017) 044001. [arXiv:1607.08697](#), [doi:10.1088/1361-6382/aa51f4](#).
- [333] P. Kanti, Black holes in theories with large extra dimensions : a review., *International journal of modern physics A.* 19 (29) (2004) 4899–4951.
- [334] R. M. Wald, The Thermodynamics of Black Holes, *Living Rev. Rel.* 4 (1) (2001) 6. [doi:10.12942/lrr-2001-6](#).
- [335] P. Kanti, H. Kodama, R. A. Konoplya, N. Pappas, A. Zhdenko, Graviton emission in the bulk by a simply rotating black hole, *Phys. Rev. D* 80 (2009) 084016. [doi:10.1103/PhysRevD.80.084016](#).
- [336] D. N. Page, Particle Emission Rates from a Black Hole: Massless Particles from an Uncharged, Nonrotating Hole, *Phys. Rev. D* 13 (1976) 198–206. [doi:10.1103/PhysRevD.13.198](#).
- [337] K. D. Kokkotas, R. A. Konoplya, A. Zhidenko, Quasinormal modes, scattering and Hawking radiation of Kerr-Newman black holes in a magnetic field, *Phys. Rev. D* 83 (2011) 024031. [arXiv:1011.1843](#), [doi:10.1103/PhysRevD.83.024031](#).
- [338] A. Rundquist, Directly integrating the Schroedinger to determine tunneling rates for arbitrary one-dimensional potential barriers, *arXiv e-prints* (2011) [arXiv:1101.2620](#)[arXiv:1101.2620](#).
- [339] R. A. Konoplya, A. Zhidenko, Long life of Gauss-Bonnet corrected black holes, *Phys. Rev. D* 82 (2010) 084003. [doi:10.1103/PhysRevD.82.084003](#).
- [340] S. Bhattacharyya, S. Shankaranarayanan, Quasinormal modes as a distinguisher between general relativity and $f(R)$ gravity, *Phys. Rev. D* 96 (6) (2017) 064044. [arXiv:1704.07044](#), [doi:10.1103/PhysRevD.96.064044](#).
- [341] R. Brun, F. Rademakers, ROOT: An object oriented data analysis framework, *Nucl. Instrum. Meth. A* 389 (1997) 81–86. [doi:10.1016/S0168-9002\(97\)00048-X](#).
- [342] J. Mena-Fernández, L. M. González-Romero, Reconstruction of the neutron star equation of state from w -quasinormal modes spectra with a piecewise polytropic meshing and refinement method, *Phys. Rev. D* 99 (10) (2019) 104005. [arXiv:1901.10851](#), [doi:10.1103/PhysRevD.99.104005](#).
- [343] E. C. Kemble, A Contribution to the Theory of the B. W. K. Method, *Phys. Rev.* 48 (1935) 549–561. [doi:10.1103/PhysRev.48.549](#).
- [344] L. D. Landau, E. M. Lifshitz, *Quantum Mechanics: Non-Relativistic Theory*, Course of Theoretical Physics, Elsevier Science, 1981.
- [345] B. C. Xanthopoulos, S. Chandrasekhar, Metric and electromagnetic perturbations of the Reissner-Nordström black hole, *Proceedings of the Royal Society of London. A. Mathematical and Physical Sciences* 378 (1772) (1981) 73–88. [doi:10.1098/rspa.1981.0142](#).
- [346] S. Chandrasekhar, *The mathematical theory of black holes*, Clarendon, Oxford, 1983.
- [347] V. Moncrief, Odd-parity stability of a Reissner-Nordstrom black hole, *Phys. Rev. D* 9 (1974) 2707–2709. [doi:10.1103/PhysRevD.9.2707](#).
- [348] V. Moncrief, Stability of Reissner-Nordström black holes, *Phys. Rev. D* 10 (1974) 1057–1059. [doi:10.1103/PhysRevD.10.1057](#).

- [349] V. Moncrief, Gauge-invariant perturbations of Reissner-Nordstrom black holes, *Phys. Rev. D* 12 (1975) 1526–1537. doi:10.1103/PhysRevD.12.1526.
- [350] F. J. Zerilli, Perturbation analysis for gravitational and electromagnetic radiation in a Reissner-Nordström geometry, *Phys. Rev. D* 9 (1974) 860–868. doi:10.1103/PhysRevD.9.860.
- [351] S. W. Hawking, Gravitational Radiation from Colliding Black Holes, *Phys. Rev. Lett.* 26 (1971) 1344–1346. doi:10.1103/PhysRevLett.26.1344.
- [352] J. D. Bekenstein, Black holes and the second law, *Lettere al Nuovo Cimento* (1971-1985) 4 (15) (1972) 737–740. doi:10.1007/BF02757029.
- [353] W. Israel, Third Law of Black-Hole Dynamics: A Formulation and Proof, *Phys. Rev. Lett.* 57 (1986) 397–399. doi:10.1103/PhysRevLett.57.397.
- [354] M. Visser, D. L. Wiltshire, Stable gravastars: An Alternative to black holes?, *Class. Quantum Grav.* 21 (2004) 1135–1152. arXiv:gr-qc/0310107, doi:10.1088/0264-9381/21/4/027.
- [355] C. Barceló, R. Carballo-Rubio, L. J. Garay, Gravitational wave echoes from macroscopic quantum gravity effects, *JHEP* 2017 (2017) 54. arXiv:1701.09156, doi:10.1007/JHEP05(2017)054.
- [356] D. N. Page, Particle Emission Rates from a Black Hole. 2. Massless Particles from a Rotating Hole, *Phys. Rev. D* 14 (1976) 3260–3273. doi:10.1103/PhysRevD.14.3260.
- [357] R. M. Wald, *General Relativity*, Chicago Univ. Pr., Chicago, USA, 1984. doi:10.7208/chicago/9780226870373.001.0001.
- [358] N. Oshita, Q. Wang, N. Afshordi, On Reflectivity of Quantum Black Hole Horizons (2019). arXiv:1905.00464.
- [359] Q. Wang, N. Oshita, N. Afshordi, Echoes from Quantum Black Holes (2019). arXiv:1905.00446.
- [360] D. N. Page, Particle emission rates from a black hole: Massless particles from an uncharged, nonrotating hole, *Phys. Rev. D* 13 (1976) 198–206. doi:10.1103/PhysRevD.13.198.
- [361] L. Rezzolla, E. Barausse, E. N. Dorband, D. Pollney, C. Reisswig, J. Seiler, S. Husa, Final spin from the coalescence of two black holes, *Phys. Rev. D* 78 (2008) 044002. doi:10.1103/PhysRevD.78.044002.
- [362] S. Hod, The quantum emission spectra of rapidly-rotating Kerr black holes: Discrete or continuous?, *Phys. Lett. B* 749 (2015) 115–118. doi:10.1016/j.physletb.2015.07.068.
- [363] T. Jacobson, Trans Planckian redshifts and the substance of the space-time river, *Prog. Theor. Phys. Suppl.* 136 (1999) 1–17. arXiv:hep-th/0001085, doi:10.1143/PTPS.136.1.
- [364] I. Booth, B. Creelman, J. Santiago, M. Visser, Evading the Trans-Planckian problem with Vaidya spacetimes (2018). arXiv:1809.10412.
- [365] N. V. Krishnendu, K. G. Arun, C. K. Mishra, Testing the binary black hole nature of a compact binary coalescence, *Phys. Rev. Lett.* 119 (9) (2017) 091101. arXiv:1701.06318, doi:10.1103/PhysRevLett.119.091101.
- [366] J. L. Friedman, Ergosphere instability, *Communications in Mathematical Physics* 63 (3) (1978) 243–255. doi:10.1007/BF01196933.
- [367] A. Vilenkin, Exponential amplification of waves in the gravitational field of ultrarelativistic rotating body, *Phys. Lett. B* 78 (2) (1978) 301 – 303. doi:https://doi.org/10.1016/0370-2693(78)90027-8.

- [368] N. Comins, B. F. Schutz, On the Ergoregion Instability, *Proceedings of the Royal Society of London. Series A, Mathematical and Physical Sciences* 364 (1717) (1978) 211–226.
- [369] K. D. Kokkotas, J. Ruoff, N. Andersson, The w-mode instability of ultracompact relativistic stars, *Phys. Rev. D* 70 (2004) 043003. [arXiv:astro-ph/0212429](https://arxiv.org/abs/astro-ph/0212429), doi:10.1103/PhysRevD.70.043003.
- [370] C. B. M. H. Chirenti, L. Rezzolla, On the ergoregion instability in rotating gravastars, *Phys. Rev. D* 78 (2008) 084011. [arXiv:0808.4080](https://arxiv.org/abs/0808.4080), doi:10.1103/PhysRevD.78.084011.
- [371] V. Cardoso, P. Pani, M. Cadoni, M. Cavaglia, Ergoregion instability of ultracompact astrophysical objects, *Phys. Rev. D* 77 (2008) 124044. [arXiv:0709.0532](https://arxiv.org/abs/0709.0532), doi:10.1103/PhysRevD.77.124044.
- [372] P. Pani, E. Barausse, E. Berti, V. Cardoso, Gravitational instabilities of superspinars, *Phys. Rev. D* 82 (2010) 044009. [arXiv:1006.1863](https://arxiv.org/abs/1006.1863), doi:10.1103/PhysRevD.82.044009.
- [373] P. V. P. Cunha, E. Berti, C. A. R. Herdeiro, Light-Ring Stability for Ultracompact Objects, *Phys. Rev. Lett.* 119 (25) (2017) 251102. [arXiv:1708.04211](https://arxiv.org/abs/1708.04211), doi:10.1103/PhysRevLett.119.251102.
- [374] E. Maggio, P. Pani, V. Ferrari, Exotic Compact Objects and How to Quench their Ergoregion Instability, *Phys. Rev. D* 96 (10) (2017) 104047. [arXiv:1703.03696](https://arxiv.org/abs/1703.03696), doi:10.1103/PhysRevD.96.104047.
- [375] E. Maggio, V. Cardoso, S. R. Dolan, P. Pani, Ergoregion instability of exotic compact objects: electromagnetic and gravitational perturbations and the role of absorption, *Phys. Rev. D* 99 (6) (2019) 064007. [arXiv:1807.08840](https://arxiv.org/abs/1807.08840), doi:10.1103/PhysRevD.99.064007.
- [376] A. Dzieciol, N. Fröman, P. Fröman, A. Hökback, S. Linnaeus, B. Lundborg, E. Walles, *Phase-Integral Method: Allowing Nearlying Transition Points*, Springer Tracts in Natural Philosophy, Springer New York, 2013.